

Structure Prediction of Alkaline Earth Oxide Nanoclusters *In Vacuo* and on Graphene

Susanne Gudrun Elisabeth Thea Escher

A thesis submitted in partial fulfillment
of the requirements for the degree of
Doctor of Philosophy

at

University College London

Supervisor: Scott M. Woodley

Secondary Supervisor: Martijn A. Zwijnenburg

* * *

Department of Chemistry

UCL

UK

May 2019

Declaration

I, Susanne Gudrun Elisabeth Thea Escher, confirm that the work presented in this thesis is my own. Where information has been derived from other sources, I confirm that this has been indicated in the work

Abstract

Can nanoclusters be used in materials design?. Knowing the structure of nanoclusters can give insight into their properties, knowing which nanocluster sizes have only one stable structure can inform experiment and knowing their behaviour on a surface is important as they are expected to be stabilised in such an environment.

In this thesis, an evolutionary algorithm has been used in conjunction with interatomic potentials and density functional theory to elucidate the structures of $(\text{BaO})_n$ nanoclusters where $n = 1$ to 18 and 24. Then, data mining was used to find structures of strontium, calcium and magnesium oxides of the same sizes. It was found that for barium oxide clusters, sizes $n = 4, 6, 8, 10$ and 16 are the best synthesis targets as they have one especially low-energy structure and are also relatively low energy compared to other sizes. Synthesis target sizes for the other three oxides were: sizes $n = 9, 15, 16, 18$ and 24 for $(\text{MgO})_n$; sizes $n = 8, 9, 12, 16, 18$ and 24 for $(\text{CaO})_n$; and the greatest number of sizes for $(\text{SrO})_n$ clusters ($n = 8, 9, 10, 12, 13, 15, 16, 18$ and 24).

Cuboid rocksalt cuts were particularly energetically favourable for barium, strontium and calcium oxides, and therefore these cuboids were looked at in greater detail. In particular, the influence of Madelung constants on their stability is investigated, and nanowire, slab and bulk energies are extrapolated from their energies.

A set of interatomic potentials was developed to investigate the behaviour of these nanoclusters above a graphene surface, and their interaction with the surface was further looked into.

Impact Statement

Properties of a material are tuned to maximise the effectiveness and efficiency of devices, applications and processes, which are exploited in technology used in everyday life (from healthcare to leisure), in industry (from chemical processes to energy generation and storage) and in nature. Another important factor is the required quantity of the material; where the surface of a material plays an important role then the volume of material can be dramatically reduced if nanoparticles are employed as they have a high surface to volume ratio.

Nanoclusters and, more generally, nanoparticles find use in a wide range of applications. For example, they are used in catalysis, sensing, staining of cells for microscopy. In catalysis, the ability to fine-tune the clusters' properties by synthesising specific sizes of the cluster means catalytic activity can be maximised. In sensing, nanoclusters can be used to sense a wide range of compounds including gases such as carbon monoxide, copper and mercury ions, and biological entities such as DNA, RNA and proteins.

If the size of the nanocluster is used as an additional tuneable parameter, then there is a need for both an understanding between how properties change with the size of the particle and how to keep the particles from coalescing. The initial aim of my research is to model the atomic structure and properties of clusters in vacuum and then anchored on a substrate. This thesis reports the progress made and the atomic structures of hundreds of nanoclusters.

On the methodological side, this work uses a computational method, an evolutionary algorithm, for elucidating the stable, low energy, atomic structures of nanoclusters and applies it to nanocluster compositions which have the potential to be imaged to atomic resolution using microscopy techniques such as scanning transmission electron microscopy. Specifically, it has been applied to nanoclusters of barium oxide. Barium oxide features very large cations that allow these techniques to work to atomic resolution. This will in the future, when such experiments are performed, allow for direct comparison between computation and experiment and therefore validation of the computational method.

This thesis includes magnesium oxide nanoclusters, for which there are many experimental results, and comparison to those results further validate the chosen method.

To gain a better insight into the relationship between the atomic structures and their properties, the range of nanoclusters investigated is extended to include nanoclusters of other alkaline earth oxides. Given the structural diversity is already captured by the end members - magnesium and barium oxide - the initial configurations were datamined as opposed to repeating the genetic algorithm search for calcium and strontium oxide clusters. Furthermore, the structures of these alkaline earth oxide nanoclusters can be used as starting points to data mine structures of other related compounds, such as alkaline halides, which may have richer applications.

The research contained in this thesis has been communicated to the wider scientific community through several conference presentations, including the 2019 autumn meeting of the European Materials Research Society, as well as two publications with a third submitted.

Acknowledgements

First and foremost, I would like to thank my supervisor Prof. Scott M. Woodley for giving me this opportunity, staying with me through this process and providing guidance and help throughout this PhD, and my secondary supervisor Dr Martijn A. Zwijnenburg for his guidance during the first 18 months of the project as well as personal advice when it was sorely needed. I am also grateful to the postdocs in the Woodley group who helped with my project: Dr Tomas Lazauskas and Dr Matt Farrow; and to those who helped me with potential development, Dr Alexey Sokol and Dr David Mora-Fonz. Many thanks also to Prof. Volker Blum for personally solving my FHI-aims issues.

Work was made a fair bit more enjoyable by the other students in the KLB, especially Rachel, Isa, Woongkyu, Ian and Ivan.

I am also grateful to Prof. Nora de Leeuw for funding my time in South Africa and Prof. Phuti Ngoepe and Dr Hasani Chauke for hosting me there.

This project was funded through a DTA studentship from UCL and computations performed as part of this project were done on the ARCHER UK National Supercomputing Service and the UK Materials and Molecular Modelling Hub, via membership of the UK's HEC Materials Chemistry Consortium, funded by EPSRC (EP/L000202), as well as UCL chemistry clusters IB-Server and Faraday.

I need to thank those in my private life: Dylan for being my centre even when we were both exhaustingly ill, and standing by my side no matter how grumpy I grew; his family, especially Amanda and Jean, for being *my* substitute family throughout my PhD; my chickens for providing joy when I could see none; and the lovely people from UCL Barbell Club for being my primary source of social life and work-life balance. Finally, I have to thank my family for their continued love and support, and especially my mother for her unwavering belief in me.

Contents

1	Introduction	1
1.1	Dimensionality	1
1.2	Nanoclusters	2
1.2.1	Applications	2
1.2.2	Structural Motifs	3
1.2.3	Computational results for alkaline earth Oxide nanoclusters	4
1.2.4	Computational results for other, related, compounds	6
1.2.5	Experimental approaches	7
1.3	1D materials	8
1.4	2D materials and surfaces	8
1.4.1	Deposition of nanoclusters on surfaces	9
1.4.2	Graphene and Graphene Oxide	9
1.5	Alkaline Earth Oxides	11
2	Theory & Computational Methods	13
2.1	The Problem of Structure Searches	13
2.2	Local Optimisation Algorithms	14
2.2.1	Zeroth-Order Method: Monte Carlo	15
2.2.2	First-Order Method: Method of Steepest Descent	15
2.2.3	Second-Order Methods	16
2.2.4	Local Optimisation Algorithms used in GULP and FHI-aims	19
2.3	Global Optimisation	19

2.3.1	Evolutionary Algorithms	20
2.3.2	Data Mining	22
2.3.3	Monte Carlo Basin Hopping	22
2.3.4	Metadynamics	23
2.3.5	Simulated Annealing	23
2.3.6	Random Structure Searches	24
2.3.7	Particle Swarm Optimisation	24
2.4	Energy functions	24
2.4.1	Interatomic Potentials	25
2.4.2	Electronic Structure Methods	30
3	Isolated Barium Oxide Clusters	37
3.1	Introduction	37
3.2	Methods	38
3.2.1	Global Optimisation to obtain plausible, low-energy metastable configurations	38
3.2.2	Refinement of Plausible Structures	39
3.3	Results	40
3.3.1	Structures and Energies of Small $(\text{BaO})_n$ Clusters ($n = 1$ to 12)	40
3.3.2	Structures and energies of larger $(\text{BaO})_n$ clusters ($n = 13$ to 18 and $n = 24$)	42
3.3.3	Normalised Clustering Energies	44
3.3.4	Second-order energies	45
3.3.5	Dipole Moment	47
3.3.6	Coordination number	49
3.3.7	Energy Density of Local Minima	51
3.3.8	Convergence of the Evolutionary Algorithm	55
3.3.9	Change in energy rankings from IPs to DFT	56
3.4	Summary and Conclusions	59

4 Clusters of Strontium, Calcium and Magnesium Oxide	61
4.1 Introduction	61
4.2 Methods	61
4.3 Results	63
4.3.1 Structures and Energies of $(\text{SrO})_n$ clusters	63
4.3.2 Structures of Calcium Oxide Nanoclusters	66
4.3.3 Structures of Magnesium Oxide Nanoclusters	69
4.3.4 Normalised Clustering Energies	73
4.3.5 Second-Order Energy Differences	76
4.3.6 Total Dipole Moments of Clusters	80
4.3.7 Coordination Number	83
4.3.8 Energy Density of Structures	84
4.3.9 Spotlight: Multiple metastable structures of $(\text{MgO})_{12}$	92
4.3.10 Relative energies with change in cation	92
4.3.11 Bond lengths	95
4.4 Summary and Conclusions	97
5 Constructed Cuboid Clusters	101
5.1 Introduction	101
5.2 Methods	102
5.3 Results	103
5.3.1 Extrapolating energies of extended structures from nanocluster en- ergies	103
5.3.2 Extrapolation of nanowire gNCEs	105
5.3.3 Comparing different cuboids of the same size	113
5.3.4 Madelung potentials	116
5.4 Summary and Conclusions	122
6 Barium Oxide nanoclusters on Graphene	125

6.1	Introduction	125
6.2	Methods	126
6.2.1	Development of interatomic potentials	126
6.2.2	DFT calculations of barium oxide clusters on Graphene and Graphene Oxide	127
6.3	Results	127
6.3.1	Fitting of potentials for the BaO-graphene interaction	127
6.3.2	DFT Calculations of Barium Oxide Clusters on Graphene & Graphene Oxide	165
6.4	Summary and Conclusions	178
7	Summary and Conclusions	181
	Acronyms	183
	List of Figures	184
	List of Tables	189
	References	192

Chapter 1

Introduction

1.1 Dimensionality

When we think of crystalline materials, the bulk is three-dimensional because it is periodic in all three dimensions and indeed large sections of materials science are concerned with these bulk materials. Conversely, isolated molecules and atoms can be considered as zero-dimensional since they are non-periodic in all three dimensions. What lies in between? The answer is nanomaterials.

Nanomaterials can be defined as materials which are on a scale of roughly 1-100 nanometres (10^{-9} m) in one or more dimensions, although the upper bound is best defined to be a size where the material starts exhibiting properties which are different from the bulk, which can be somewhat above or below 100 nm depending on material and dimensionality.¹ A number of unique properties arise specifically from their size range. Varying the size of a system from just a few atoms to sizes where it becomes bulk-like gives an extra parameter (size) to design materials which will allow for fine-tuning properties, e.g. through a change from a band gap resulting from continuous band structure in the bulk to a usually wider HOMO-LUMO gap in small nanomaterials such as nanoclusters, surface to volume ratio and other surface effects, as well as effects which depend

¹However, computational modelling of nanomaterials with size ranges on the order of 100 nm is not computationally tractable with the methods used in this thesis.

on structure, since a reduction in size might bring with it a phase change. Due to the quite large range of the nanoscale, it leads to hundreds of potential new materials with a variety of properties for each known bulk material. Nanomaterials see use in a wide range of applications, for example in catalysis, gas sensing, hydrogen storage, medicine, photovoltaics, quantum computing, and other areas of so-called nanotechnology.

Structures can be divided up into three-dimensional (3D), two-dimensional (2D), one-dimensional (1D) and zero-dimensional (0D). This work will be focused mainly on small 0D structures called nanoclusters, and the 2D structure graphene.

1.2 Nanoclusters

Nanoclusters are small nanoparticles, structures which are confined in all three dimensions and usually have less than 100 atoms.[1] Of particular interest are nanoclusters of transition metals, especially gold and platinum[2, 3, 4]. However, to validate our method we have chosen an easier to model system, barium oxide. Barium oxide is relatively more trivial to model as there are no *d*-orbitals to consider, yet is still suitable for atomic-resolution scanning transmission electron microscopy (STEM)[5]. STEM measurements can then be directly compared to theoretical results and thus we can build a bridge between theory and experiment. The majority of this work will be about nanoclusters composed of alkaline earth oxides (barium oxide as well as strontium, calcium and magnesium oxides) with sizes below 50 atoms, most of which are less than 1nm across and therefore on the very small end of nanocluster sizes. A variety of theoretical methods as described in Chapter 2 are used here to investigate them.

1.2.1 Applications

Generally, metal oxide nanoclusters are good candidates for a wide range of applications. For example, zinc oxide and copper oxide nanoclusters find use in gas sensing[6], iron and zinc oxides in heavy metal removal from water[7], and titanium dioxide ones in

sunscreens[8]. A large variety of metal oxide nanoclusters are also used in catalysis[9, 10] due to their large surface-to-volume ratio as well as tunability of properties by variation of size. If quantum effects are present, they can also be used as *quantum dots*. Quantum dots find use in nanotechnology applications such as quantum computing[11] or photovoltaics[12]. Focusing in particular on alkaline earth oxide nanoclusters, magnesium oxide nanoparticles have found applications in catalysis of amines[9], with proposed applications also in catalysis involving formaldehyde[10] and gas sensing (carbon monoxide)[13]. MgO and CaO clusters (albeit not in their most thermodynamically favourable structures, as shall be discussed later) could be used for hydrogen storage.[14, 15] Larger (20+ nm) MgO nanoparticles have also been used to modify water capacity and hydraulic conductivity of soil[16] and decrease emissions from gasoline[17]. Charged radical forms of MgO, CaO and SrO clusters of size $n = 1$ have been proposed as catalysts for proton transfer reactions[18].

Additionally, nanoclusters are of interest in the study of nucleation and crystal growth, where they represent an early stage.[19, 20, 21]

1.2.2 Structural Motifs

It is useful to think about the structures of nanoclusters in terms of structural motifs. Some of these motifs have equivalent structures in the bulk for these semiconductors, while others only occur in other classes of materials such as zeolites[22] and in nanostructures. In binary compounds, three commonly found motifs are bubbles, barrels and rocksalt cuts, as illustrated in Figure 1.1.

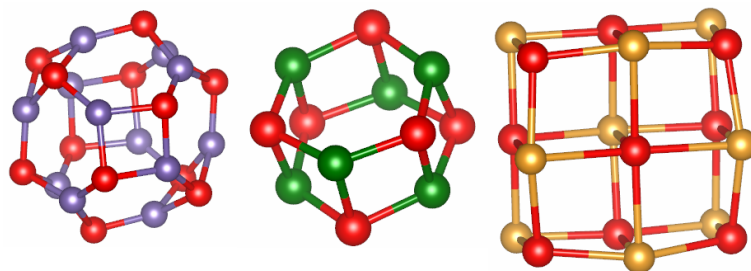


Figure 1.1: Examples of the three structural motifs: bubble (left), barrel (middle), rocksalt cut (right). All example structures were taken from Ref. [23]

Rocksalt is the bulk phase of the alkaline earth oxides, and thus rocksalt cuts would be equivalent to cuts from the bulk phase of these compounds. The barrel shapes composed of 6-membered rings can be thought to be cuts from the so-called 5-5 phase (with stacked hexagonal rings and each ion bonded to 5 of the opposite ion) which has been reported as a metastable phase for bulk alkaline earth oxides[24, 25]. Phases containing bubble motifs are primarily found in zeolites and other porous materials.

1.2.3 Computational results for alkaline earth Oxide nanoclusters

Nanoclusters of magnesium and calcium oxides have been investigated in great detail in the past. In particular, magnesium oxide clusters, which we will show can adopt all three structural motifs under certain conditions, have drawn a lot of attention, with a particular focus of many studies on the $n = 3k$ (where $k \in \mathbb{N}$) clusters, i.e. clusters where n is a multiple of 3, which can adopt both barrel and rocksalt cut structures. In the case of the barrels, a $n = 3$ unit forms a six-membered ring and the barrel structures are formed by stacking these rings atop each other. Rocksalt cuts can be built up from $n = 3$ units in multiple ways, for example by stacking 3×2 -atom units on top of each other.

Several recent studies[26, 27] have compared barrel and rocksalt motifs for clusters of all three alkaline earth oxides, comparing energetically the barrel shapes with cuboid cuts of the rocksalt structure. They generally investigated smaller clusters (with highest n ranging from 6 to 12). Because the direct competition between barrel-shaped and rocksalt cut structures is only found for $n = 3k$ clusters, it is most interesting to examine

results for those cases. Studies by Zhang et al. looked at larger $n = 3k$ clusters (up to $n = 24$) in both barrel and rocksalt cut configurations, but focused more on their dynamics [28, 29] to investigate their thermal stability.

Other computational studies on alkaline earth oxide nanoclusters[23, 30] report similar results for these more 'interesting' sizes.

This also leads to the concept of the *bulk transition size*, the size at which the rocksalt cut becomes more stable than the (in the bulk metastable) barrel-type configurations. All studies cited above agree that this is somewhere between $n = 15$ and $n = 18$ for MgO while CaO and SrO adopt bulk-like structures even at very small sizes. For BaO, ref. [26] seems to indicate that 5-5-based structures are more stable than rocksalt cuts up to $n = 12$.

The most relevant series of studies was carried out at around the same time as the work presented in this thesis. There, a tree growth-hybrid genetic algorithm[31] was employed to find tentative local minima (LM) for MgO and structures for other compounds were data mined from the magnesium oxide data. This series of studies looked at MgO, CaO, SrO, BaO and CsO nanoclusters[32, 33, 34] and showed the following: For MgO, they report barrel-like global minima (GM) structures for $n = 6, 9, 12, 15$ and 21 but cuboid rocksalt cut GMs for $n = 24$ and 36, with some other structures not fitting into either category in between. For CaO, SrO and BaO they largely predict cuboid rocksalt cut GMs where available. Generally, one can say that the bulk transition size (the size after which bulk-like structures are favoured) is higher for magnesium oxide than it is for the other three alkaline earth oxides.

A theoretical study of $(\text{CaO})_n\text{Ca}^{2+}$ clusters[35] revealed that their structures are largely the same as those of neutral calcium oxide clusters, with the extra Ca^{2+} often protruding from a corner of the structure; in the same study the results for neutral MgO and CaO clusters were again the same: in magnesium oxide, barrel-like structures were found to be lower in energy and in CaO, rocksalt cuts were the preferred structure.

1.2.4 Computational results for other, related, compounds

One compound whose clusters exhibit one of the structural motifs shown in Figure 1.1 is zinc oxide which favours bubble-shaped structures[36, 37, 23] (and, for size $n \leq 7$ clusters, rings). These are not expected to be the GM in the alkaline earth oxide clusters as based on the studies cited in section 1.2.3 and this is perhaps somewhat unsurprising as ZnO also adopts lower-coordinated structures in the bulk[38].

Compounds that might be more interesting to compare to are ones that also adopt the rocksalt structure in the bulk; the obvious choice is rocksalt (NaCl) as well as its related compounds, i.e. the alkali halides.

One paper presented density functional theory (DFT) results for barrel and rocksalt cut structures for small $(MX)_n$ clusters of alkali halides LiF, NaCl and KBr[39]; these simulations suggested that for all three the lower energy structure of the two was the barrel one at $n = 9$. The authors described elsewhere a corresponding result for $(LiF)_6$ [40]. They also investigated charged clusters and neutral ones which did not possess a 1:1 stoichiometry, but this is (for now) outside the scope of this project, although it is more useful when comparing with mass spectrometry results. Other results for alkali halides report both rocksalt cuts and various nanotubes.[41]

Typically, cations are much smaller than anions as their valence electrons are stripped. Not so in barium oxide: the cation:anion size ratio is ~ 1 [42]. Therefore, an alkali halide that is of interest in comparison to BaO in particular is KF: it too has large cations and small anions, leading to a cation:anion radius ratio of ~ 1 [42]. In the case of KF there is a preference for the bulk cut structure[23]. It appears that overall, the rocksalt cut becomes more stable compared to the barrel structure when the cation size is increased and/or anion size is decreased, in line with most of the previously discussed Group II oxide results, where the n at which the bulk transition occurs decreases with an increase in cation size.

1.2.5 Experimental approaches

Small nanoclusters such as the ones discussed here can be fabricated by laser ablation from the bulk structure[43, 44] or by nucleation in solution[45]. The former method is likely to be of more relevance to the material presented here as this investigation is about nanoclusters *in vacuo* and on surfaces rather than in solution. Larger nanoparticles can be produced by a variety of methods including chemical vapour deposition[46], vacuum annealing[47] and freeze-drying[48]. However, for the alkaline earth oxides, grain size in terms of number of atoms increases quite rapidly down the group and even MgO grains were much larger and more bulk-like than what simulations here can investigate. Some less successful attempts to fabricate MgO nanoparticles might also be worth mentioning, most notably synthesis in supercritical water[49] which can result in much smaller nanoparticles for other compounds, but fails for MgO because it is unstable in supercritical conditions[50].

In terms of structural analysis, there are several experimental pathways. Due to the uniqueness of the nanoclusters, some spectroscopic techniques such as Fourier transform-infrared spectroscopy (FT-IR) or nuclear magnetic resonance spectroscopy (NMR) do not give very straightforward answers. However, mass spectrometry can give insight into what size fragments are most stable and thus open up analysis of "magic number" clusters as well as structural motifs in general—for example, if $n = 3k$ fragments are very common, barrels composed of 6-membered rings are a likely stable motif. However, this method only shows results for charged clusters, and while a charge can be added to neutral clusters, most mass spectrometry studies of alkaline earth oxide nanoclusters involve particles that are charged to begin with. Mass spectrometric studies on the alkaline earth oxides[51] indicate especially high stability of the $n = 3k$ $(\text{MgO})_{n^+}$ fragment[52], but some $n = 2k$ $(\text{MgO})_{n^+}$ peaks have also been recorded alongside the $n = 3k$ ones[53]. For CaO, $n = 2k$ fragments seemed to appear more commonly.[54, 51, 55]

X-ray crystallography is often not an option for small nanoclusters since these techniques require a sufficiently large crystal or powder formed of smaller crystals of the same

phase. Small nanoclusters tend to conglomerate to form bulk material or larger clusters rather than crystals composed of the small cluster and in some cases are not all the same. Another promising experimental technique is atomic-resolution microscopy. Most notably, atomic resolution images of nanoclusters have been produced using transmission electron microscopy (TEM) for nanoclusters of gold[56], copper[57, 58], and similar quality results have been achieved for gold-based[59, 60] and various other nanoclusters[61] using STEM.

1.3 1D materials

1D materials are only nano-sized in two dimensions, and can therefore have both nanoparticle-like and bulk-like properties since their electrons are only confined in two out of three dimensions. They include nanowires and nanotubes. Both have drawn interest due to their tunability and applications in nanotechnology.[62] Carbon nanotubes, one of the most well-known 1D materials which are, unlike nanowires, hollow, find applications in especially strong composite materials e.g. for bicycle frames and as probe tips for atomic force microscopes[63]. Nanowires are often used in transistor technology to achieve smaller transistor sizes. In this thesis, 1D materials are relevant in that energies of alkaline earth oxide nanowires are extrapolated from nanocluster data in Chapter 6.

1.4 2D materials and surfaces

2D materials are an emergent class of materials most easily developed from the basis of layered materials. They are defined by having two parallel surfaces or interfaces which are separated by (at most) nanometres. 2D materials can be either free-standing thin films, thin films supported on a 3D material's surface or heterostructures; all 2D materials discussed in this work are free-standing thin films. 2D materials in general are of interest in that they are quite bulk-like in some respects, e.g. having a continuous band structure (which can nonetheless be fine-tuned by controlling the number of layers), while still

possessing a very high surface-to-volume ratio and surfaces/interfaces which are very close to each other, as well as exhibiting some quantum confinement effects[64] and phenomena such as the 2-dimensional electron gas. 2D materials can either be free-standing (such as free-standing graphene (FSG)) or supported by a 3D structure.

The most commonly known layered material, graphite, and its single-layer 2D equivalent, graphene, are of particular relevance here as they can act as a substrate which nanoclusters are deposited on.

1.4.1 Deposition of nanoclusters on surfaces

Nanoclusters on their own are metastable; if multiple nanoclusters are near each other and free to move, they will coalesce and form larger nanostructures or bulk material. There are several ways to stabilise them; they can be capped, suspended in solution, or anchored on a surface. In this work, the focus will be on nanoclusters *in vacuo* primarily, with a brief investigation of how they change on a single-layer graphene surface.

1.4.2 Graphene and Graphene Oxide

The discovery of graphene in 2004 by Geim, Novoselov et al.[65] drove the branching out of research on layered materials in general towards their non-bulk, few-layer forms. Graphene has many interesting properties: on the electronic side it has massless charge carriers[66], half-integer quantum Hall effect[67], absorption of visible light despite being atomically thin[68]. Mechanically pristine graphene is one of stiffest and strongest known materials[69, 70]. Graphene is best understood as a single layer formed from graphite. The graphite unit cell[71] (Figure 1.2) contains two layers in a staggered arrangement, separated by $\sim 3.3\text{\AA}$. Graphene is then a single such layer, either free-standing or supported on some other 3D compound.

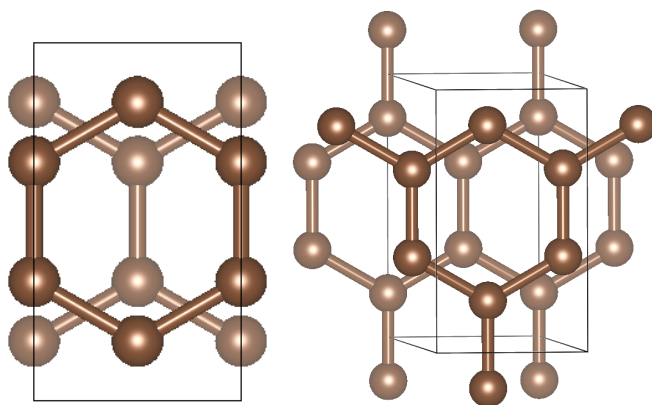


Figure 1.2: A single unit cell of graphite, viewed straight from the top, and slightly side-on, with bonds and atoms beyond the unit cell shown to illustrate how it extends.

Graphene oxide (GO) is graphene with functional groups containing oxygen[72] and generally produced from the analogous graphite oxide; in particular, GO features alcohol and epoxy groups[73], but other functional groups such as amine groups[74] may also be added to graphene. Graphene oxide exhibits transparency under electron microscopes[75] which is particularly useful for the experimental context discussed in this work. Figure 1.3 shows an example of OH-functionalised graphene.

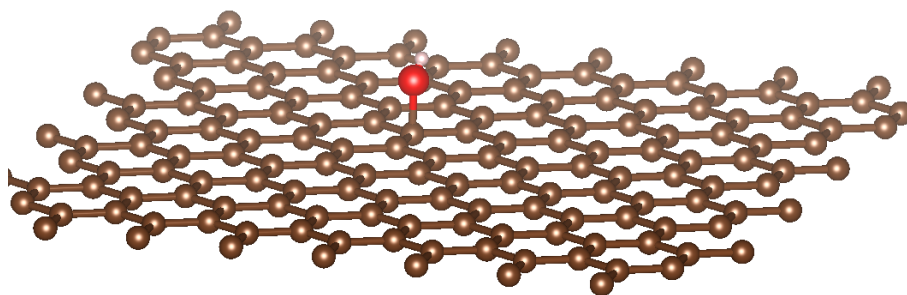


Figure 1.3: Graphene, functionalised with an OH group; structure optimised in FHI-aims using the PBEsol functional.

Graphene[76, 77, 78], graphite[58] and graphene oxide have been a popular choice for substrates for nanoclusters. Introducing defects and functional groups on graphene makes it a better substrate for nanoclusters since the clusters can be anchored (chemisorbed)

at functional group sites while they would be likely to migrate across a pristine graphene surface because they are not adsorbed strongly enough.

This thesis will focus on graphene and graphene oxide only in their role as substrates for nanoclusters, with a brief section on 2D slabs of alkaline earth oxides in Chapter 6.

1.5 Alkaline Earth Oxides

In order to put nanoclusters of the alkaline earth oxides into proper context, it is important to also look at the bulk phase of the alkaline earth oxides and their properties. This thesis will look at barium, strontium, calcium and magnesium oxides. All four are semiconducting, with band gaps tabulated in Table 1.1

	BaO	SrO	CaO	MgO
experimental band gap / eV	4.8	6.1	5.7	6.4
DFT band gap / eV	1.82	3.18	3.52	4.55

Table 1.1: Band gaps (both from experimental data[79] and our DFT calculations using the PBEsol functional) of alkaline earth oxide bulk materials.

From experimental data, it can be seen that band gap roughly decreases down the group – with all four being wide-band gap semiconductors. However, what also becomes apparent is that our methodology is not very well suited to calculating band gaps of these materials, and the band gaps (HOMO-LUMO gaps) of clusters will therefore be omitted.

Lattice parameters of all four alkaline earth oxides at standard conditions are tabulated in Table 1.2. The lattice parameter increases down the group, as expected.

	BaO	SrO	CaO	MgO
Lattice parameter (experimental) / Å	5.54	5.14	4.81	4.21
Lattice parameter (DFT) / Å	5.50	5.13	4.77	4.22

Table 1.2: Experimental Lattice parameter of BaO[80], SrO[81], CaO[82] and MgO[82] at standard temperature and pressure, and calculated equivalents using FHI-AIMS/PBESOL with 8 k-points in each direction.

As we can see from this, there is a significant difference between the smallest (MgO) and the largest (BaO). Will this difference be reflected in relative sizes of nanoclusters? Additionally, lattice parameters are least different between SrO and CaO. Will these be similar in other respects?

First ionization energies of the alkaline earth metals will be included in Table 1.3 as they shall become relevant later.

Element	Ba	Sr	Ca	Mg
Ionization Energy / eV	5.212	5.695	6.113	7.646

Table 1.3: Ionization energies of the alkaline earth metals[82].

Notice here that the ionization energies of Sr and Ca are again quite close to each other. This will influence bonding behaviour.

Chapter 2

Theory & Computational Methods

Due to the difficulties associated with experimental characterisation of small clusters, their structures are often best determined using computational techniques. Because the structure of such small clusters is strongly size-dependent, to the point where adding a single formula unit can dramatically change what structure is preferred, it is important to find and compare plausible structures for each nanocluster size. In addition, insights gained from our models can also be used in combination with experimental techniques such as NMR or lower-resolution electron microscopy to combine into a conclusive result which clarifies experimental data while simultaneously validating computational results.

2.1 The Problem of Structure Searches

To determine the structure of a nanocluster of given composition and size computationally, it is advantageous to start from as little data as possible to reduce biases and explore the cluster's PES as thoroughly as needed to find all low-energy candidate structures. There are several layers to this. First, an energy function is needed—in this work, the energy functions used will include interatomic potentials (IPs) and density functional theory (DFT). Then, any guess structure, however obtained, is locally optimised to a nearby local minimum to discover its energy, by some local optimisation algorithm. And finally, an algorithm is needed to explore conformational space, or the PES, completely enough that

all low-lying LM are found with high probability: a cluster's PES is a $(3N - 6)$ -dimensional space for any non-linear configuration, where N is the number of atoms in the cluster, and thus an exhaustive search would be prohibitively expensive.

It is assumed that the structure with the lowest energy is the most likely to be found in experiment at a temperature of 0K. This structure should be found with a sufficiently exhaustive global search algorithm paired with a sufficiently good energy function. However, global optimisation algorithms often take tens of thousands of steps to find all relevant local minima, and energy functions which are accurate enough to have a hope of ranking LM correctly tend to take hours for each local optimisation step. Therefore, a multistep approach was employed here to investigate the structure of barium oxide nanoclusters, wherein an EA was paired with IPs for the global optimisation, and the top structures for each cluster size were then used in a second step with DFT.

2.2 Local Optimisation Algorithms

Section 2.3 will cover methods to traverse large regions of a PES. This section will be concerned with, from a given starting point on the PES, finding a nearby LM. To remind ourselves again, the PES of any given three-dimensional structure is a $3N - 6$ -dimensional space. For any point on this hypersurface, a nearby local minimum can be found by use of local optimisation algorithms.

Consider an energy function f which depends on a number of independent variables $r_1 \dots r_n$. Derivatives of the energy function can give us information about the curvature of the PES as well as the forces. At a local minimum, the first derivatives of the energy function with respect to position should be zero and the second derivatives should all be positive. This is equivalent to saying that vibrational frequencies should be real (positive).

Most local optimisation algorithms will attempt to find a local minimum by going "downhill" on the PES from the starting position. They are classed based on what the highest-order derivative used is, e.g. a method only using first derivatives is a first-order method.

2.2.1 Zeroth-Order Method: Monte Carlo

It is, in principle, possible to approach a nearby local minimum without using any information about derivatives. This can be done by performing a series of small random steps consisting of moving atoms, and for each step only accepting it if it is *downhill*, i.e. lowers the total energy of a system, and otherwise discarding it and trying a different random step. If run for long enough, this will result in finding a local minimum. However, in the usual case this method is relatively inefficient.

2.2.2 First-Order Method: Method of Steepest Descent

A first-order local optimisation method is one which takes into consideration first derivatives only. One of the most commonly used first-order local optimisation methods is the method of steepest descent. In this, particles move in the direction of net force – downhill along the direction which is steepest at the starting point, that is the direction opposite to the gradient of the PES at the starting point. For a structure with N atoms, the position vector has $3N$ components:

$$r_i = \begin{bmatrix} r_{i1} \\ r_{i2} \\ r_{i3} \\ \vdots \\ r_{i3N} \end{bmatrix}$$

with $3N$ -dimensional first derivatives of the energy function $E(r_i)$, g_i which give the direction of the vector in which atoms will be moved:

$$g_i = \begin{bmatrix} \frac{\partial E}{\partial r_{i1}} \\ \frac{\partial E}{\partial r_{i2}} \\ \frac{\partial E}{\partial r_{i3}} \\ \vdots \\ \frac{\partial E}{\partial r_{i3N}} \end{bmatrix}$$

In each step, the geometry is propagated via the following equation:

$$r_{i+1} = r_i - \lambda_i g_i$$

where r_i are the positions of all atoms at step i , λ_i is the step size of step i (a positive number) and g_i is the gradient at step i . The gradient and step size are recalculated at each step. The step size is determined from the directional derivative

$$\lambda_i = \frac{(r_i - r_{i-1})^T (g_i - g_{i-1})}{\|g_i - g_{i-1}\|^2}$$

In each step, first the gradient g_i is calculated, then the direction of the step is set to $-g_i$, then the step size λ_i is calculated and finally a new point is calculated via $r_{i+1} = r_i - \lambda_i g_i$. The method is then repeated for each new point until convergence criteria are reached.

2.2.3 Second-Order Methods

The Newton-Raphson Method

In this method, the energy function is Taylor expanded about the point r_i as follows

$$E(r) = E(r_i) + (r - r_i)^T E'(r_i) + \frac{1}{2} (r - r_i)^T \cdot E''(r_i) \cdot (r - r_i) + \dots$$

The elements of g_i are collected in a column vector. Second derivatives make up the Hessian H_{jk} , which at the point $r = r_i$, can be written as:

$$H_{jk}(r)|_{r=r_i} = \left(\frac{\partial^2 E(r)}{\partial r_j \partial r_k} \right) \Big|_{r=r_i} = \begin{bmatrix} \frac{\partial^2 E(r)}{\partial r_1^2} & \frac{\partial^2 E(r)}{\partial r_1 \partial r_2} & \frac{\partial^2 E(r)}{\partial r_1 \partial r_3} & \cdots & \frac{\partial^2 E(r)}{\partial r_1 \partial r_{3N}} \\ \frac{\partial^2 E(r)}{\partial r_2 \partial r_1} & \frac{\partial^2 E(r)}{\partial r_2^2} & \frac{\partial^2 E(r)}{\partial r_2 \partial r_3} & \cdots & \frac{\partial^2 E(r)}{\partial r_2 \partial r_{3N}} \\ \frac{\partial^2 E(r)}{\partial r_3 \partial r_1} & \frac{\partial^2 E(r)}{\partial r_3 \partial r_2} & \frac{\partial^2 E(r)}{\partial r_3^2} & \cdots & \frac{\partial^2 E(r)}{\partial r_3 \partial r_{3N}} \\ \vdots & \vdots & \vdots & \ddots & \vdots \\ \frac{\partial^2 E(r)}{\partial r_{3N} \partial r_1} & \frac{\partial^2 E(r)}{\partial r_{3N} \partial r_2} & \frac{\partial^2 E(r)}{\partial r_{3N} \partial r_3} & \cdots & \frac{\partial^2 E(r)}{\partial r_{3N}^2} \end{bmatrix}_{r=r_i}$$

The second derivative gives forces and curvature of the directional vector. The step size is calculated by diagonalising the Hessian; this is possible because the Hessian is a symmetric matrix as long as the PES is smooth.

There exists a unitary matrix U which diagonalises the Hessian

$$(U^{\mathbf{T}} H^{r_i} U)_{kl} = \delta_{kl} \lambda_k$$

with δ_{kl} the Dirac delta which sets all off-diagonal elements to zero, and λ_k the diagonal matrix composed of eigenvalues of the Hessian matrix

$$\lambda_k = \begin{bmatrix} \lambda_1 & & 0 \\ & \ddots & \\ 0 & & \lambda_{3N} \end{bmatrix}$$

The Hessian will usually have $3N - 6$ non-zero eigenvalues contained in this matrix for a 3D system corresponding to its vibrational modes; the six remaining eigenvalues fall away because the system is invariant under translation and rotation in all 3 directions.

The above Taylor expansion, truncated after the second-order term, can be rewritten and unitary matrices inserted to give

$$\begin{aligned} E(r) &= E(r_i) + (r - r_i)^{\mathbf{T}} g_i + \frac{1}{2} (r - r_i)^{\mathbf{T}} \cdot H^{r_i} \cdot (r - r_i) \\ &= E(r_i) + U U^{\mathbf{T}} (r - r_i) g_i^{\mathbf{T}} + \frac{1}{2} (r - r_i)^{\mathbf{T}} \cdot U U^{\mathbf{T}} H^{r_i} \cdot U U^{\mathbf{T}} (r - r_i) \end{aligned}$$

Now, set $U^{\mathbf{T}}(r - r_i) = Q$ and $U^{\mathbf{T}} g_i = G$ to get

$$E(r) = E(r_i) + G^{\mathbf{T}} Q + \frac{1}{2} Q^{\mathbf{T}} \lambda Q$$

Then, call the m^{th} row of Q Q_m , that is $Q_m = \sum_k U_{mk}^{\mathbf{T}} (r - r_i)_k$, and correspondingly the m^{th} row of G G_m , i.e. $G_m = \sum_k U_{mk}^{\mathbf{T}} g_{ik}$ is the component of the gradient along the m^{th} eigenvector of H .

The goal is the value $r = r_{i+1}$ such that the first derivative is zero: $E'(r_{i+1}) = 0 = g$. Therefore, we minimise the energy function $E(r)$ with respect to Q_m :

$$\frac{\partial E}{\partial Q_m} = G_m + \lambda_m Q_m = 0$$

From this, it appears that Q_m contains information about the energy minimisation steps' direction and step size

$$Q_m = \frac{G_m}{\lambda_m}$$

This then gives us all the needed components for the Newton-Raphson method, i.e. the step size and the step direction. In each step, the gradient and the Hessian are computed, the step length is computed via Q_m , and then the change in coordinates is applied.

The BFGS Method

The BFGS algorithm is in principle quite similar to the Newton-Raphson algorithm, but the Hessian is not updated in every step, saving on computational cost. Instead, an approximation to the Hessian is updated during each iteration. The approximate Hessian is generated by the addition of two matrices:

$$H_{i+1} = H_i + U_i + V_i$$

Both update matrices are symmetric rank-1 matrices. The search direction comes from a formulation similar to that of the Newton-Raphson method (but with approximate second derivatives), while the step size is determined by a line search along the search direction, which is generated via the approximated Hessian.

This algorithm is preferred for materials science applications as it performs very well with the types of PES found in these applications.

2.2.4 Local Optimisation Algorithms used in GULP and FHI-aims

Both GULP and FHI-aims contain implementations of the BFGS algorithm to approximate second derivatives, which have been used throughout this project. In particular, in the GULP implementation, the Hessian is recomputed every few steps to ensure it remains close to the exact Hessian. GULP also uses a quasi-Newton-Raphson method wherein the second-order step size is used as a first guess for a line search along the search direction. Meanwhile, the implementation in FHI-aims uses the BFGS algorithm in conjunction with the standard Newton-Raphson method, assuming a harmonic potential energy surface.

2.3 Global Optimisation

Having covered local optimisation, we will now turn our attention to global optimisation algorithms which aim to traverse relevant areas of a structure's PES. In order for a global search to yield results, we require a function which measures how "good" any given structure is compared to other structures based on a chosen set of criteria. This is the cost function $\Xi(\mathbf{r})$, where \mathbf{r} is the vector of atomic positions. In this study, $\Xi(\mathbf{r})$ is simply the energy from any given energy function and therefore local minima on that energy function's PES are sought:

$$\Xi(\mathbf{r}) = E(\mathbf{r})$$

In the more general case, the cost function may also include other factors such as infrared frequencies[83, 84] or the HOMO-LUMO gap[85].

A method that performs a global search well traverses as little of the PES as necessary, avoiding regions with no low-energy basins, in order to find all relevant LM. The total number of LM will rise exponentially with the dimensionality of the PES, and therefore with the number of atoms in the system.[86] Additionally, the regions on the PES from which each minimum may be found with a simple local optimisation (basins) may vary

greatly in extent, so some minima may be much more difficult to find than others.

When exploring the PES, some structures can immediately be discarded without evaluating their energy: these are structures where two atoms are very close to each other (leading to strong repulsion and thus an unfavourable energy), and structures where the cluster has fragmented into 2 or more smaller clusters. Highlighted below are some important global optimisation methods: first ones used in this project, namely evolutionary algorithms and data mining, and then, to give a wider perspective on the field of global optimisation in a materials science context, methods used by others – Monte Carlo basin hopping, metadynamics, simulated annealing, random structure searches and particle swarm optimisation.

2.3.1 Evolutionary Algorithms

Evolutionary algorithms (EAs) are a popular method for exploring only low-energy regions of a PES[30, 87]. The most well-known type of evolutionary algorithm applied to global optimization problems is the genetic algorithm[88].

In evolutionary algorithms, concepts from natural selection are transferred to an application to find a solution that best fits the applied constraints, here the composition and number of atoms in a nanocluster.

A *population* of candidate structures that is kept at a fixed size evolves over a number of *generations* (steps of the algorithm) which can be either fixed or terminate when some convergence criterion is met, e.g. no change in the top 10 structures for a given number of generations.

The atomic coordinates for the initial population are generated randomly¹ and local optimisation to minimise the chosen energy function is performed on the member structures. After removing duplicates, the criteria for *fitness* are applied. Fitness is a measure of the quality of a trial solution; in the case of global minimization on a PES without any extra criteria, lower energy corresponds to higher fitness (cf. the cost function $\Xi(\mathbf{r})$ men-

¹Checks are made to ensure that the starting population does not contain fragmented clusters or atoms that are too close to each other

tioned previously). In order to generate the next generation, subsets of the population compete in *tournaments* to determine which will be used as *fathers* to generate new trial solutions, while *mothers* are randomly selected from the entire current population.

One mother and one father are taken to generate *offspring* by combining them in the *crossover*; in a standard GA this is done by using a binary string (genes) to represent the parent structures and the strings are cut and reassembled to make the offspring. In many modern codes, including the implementation that was used in this project, a phenotype-based[89] approach (which, lacking "genes", is not strictly a genetic algorithm) is employed, which uses the real-space structures instead of an abstract representation. More specifically, the father and mother structures are cut into two pieces and then crossover is achieved by rotating the mother's and father's pieces a random amount around the cutting plane and putting them together again along their respective cutting planes.[90] Although the cutting planes are chosen randomly, they are nevertheless constrained to preserve the atomic composition of the nanoclusters. This is achieved by ensuring the composition of the cut pieces matches. After this step, new structures are *mutated* by Monte Carlo moves of some atoms, and included in the next generation's population along with the fathers.

This method was applied to nanoclusters of barium oxide in this project and the results form the basis of Chapter 3.

Graph Theory

In the evolutionary algorithm implementation used here, duplicates were identified through a graph theoretic approach[91]: each cluster was assigned a graph based on atomic connectivity. Each graph was converted into a hashkey, that is an alphanumerical string. By comparing these hashkeys, duplicates could easily be detected and then one of each pair removed.

2.3.2 Data Mining

Having already generated a PES for barium oxide as a starting point, one goal is to use this data to also predict the structures of clusters composed of related compounds, those of the other alkali earth oxides. Therefore, data mining was also utilised in this project. It is a very quick method where one checks known structures that have the same stoichiometry (for example bulk cuts or structures taken from similar compounds) as initial configurations for local optimisation routines. Here, we used the structures found to be low-lying LM on the $(\text{BaO})_n$ PES, and scaled them down according to atomic radii sizes before re-optimising them for strontium, calcium and magnesium oxides. Data mining is also implemented in the WASP@N database[92, 93] and structures from this project were uploaded there.

2.3.3 Monte Carlo Basin Hopping

Using approaches which traverse the PES by trying to find a low energy path on it, such as molecular dynamics, leads to problems when trying to overcome energy barriers (i.e. regions of high energy between minima on a potential energy surface). One way of dealing with this is Monte Carlo (MC) methods, sequences of small random steps (with some constraints), with each step defined by small atomic displacements.

The Metropolis algorithm is then employed to introduce a notion of non-zero temperature by allowing some probability of atom moves which increase (rather than decrease) energy. This is achieved by calculating $\exp\left(-\frac{\Delta E}{k_B T}\right)$ and checking whether it is greater than a random number between 0 and 1 that is generated for each step. Since this results in a number greater than one for each $\Delta E < 0$, all energetically favourable steps are accepted. If ΔE is positive, there is some probability less than 1 that the move will be accepted.

However, the energy basins surrounding the LM are grouped into so-called *super-basins* which are surrounded by particularly high energy barriers, and in order to escape these, the method needs additional help in the form of Monte Carlo basin hopping[94].

It is possible to choose a large enough Monte Carlo step that it can pass through these high energy barriers, while still being small enough to stay within a chemically sensible region. Since this is primarily useful for finding a larger quantity of LM, the structures found by these large MC moves are immediately relaxed to a LM instead of using MC to explore individual basins.

Examples for Monte Carlo Basin Hopping being used for nanocluster applications can be found in Ref. [95, 96, 97].

2.3.4 Metadynamics

Metadynamics is based on a molecular dynamics approach. In it, as the PES is explored, regions of conformational space which have already been visited have a positive (disfavourable) energy bias potential applied to them. This method is more useful for structures which do not change too much from a known starting conformation, whereas nanoclusters often have an unknown lowest-energy conformation which might be completely unrelated to known structures such as the corresponding bulk structure. However, it has been used for some nanocluster-related applications.[98]

2.3.5 Simulated Annealing

Another possible method, simulated annealing[99], starts the chosen simulation at a high initial temperature, preventing the system from being trapped in the initial starting region and this allows the system to descend into low-energy regions of the PES as it is "cooled down", while the areas which contain accepted solutions are narrowed further the lower the temperature sinks, with the ultimate goal at arriving at only the GM when the temperature reaches absolute zero.

Simulated annealing can be applied using either molecular dynamics or MC methods; either have the ability to sample configurational space at non-zero temperatures. In calculations such as the ones being attempted here, this would terminate before 0K is reached as the energy function used in global optimization methods has to be kept relatively fast,

like IPs, and therefore might not be accurate enough to distinguish the GM in inorganic systems, so that multiple LM should be re-evaluated using a more accurate method such as DFT.

2.3.6 Random Structure Searches

For small enough systems, random structure searches may be employed. In these, structures are randomly generated and then minimised locally. This method is, however, too crude to be computationally tractable for the larger sized clusters under investigation here. With sufficient computational resources, interesting results have been achieved using random structure searches in conjunction with DFT methods for smaller systems.[100]

2.3.7 Particle Swarm Optimisation

Particle Swarm Optimisation[101, ?] treats the solutions (LM) as "particles", which are "moved" (improved) to find an optimal solution by considering their location in conformational space (the local minimum) and then moving them towards other low-lying particles (local minima).

2.4 Energy functions

Two popular energy functions used in computational materials chemistry are employed in empirical methods based on interatomic potentials, and so-called *ab initio* methods, or electronic structure, which are based on solving the Schrödinger equation for a given system.

There are other methods such as semi-empirical methods (still based on quantum mechanics, but using some empirical parameters) and coarse-grained methods (where multiple atoms are represented by one point particle), and more recently there are machine learning (neural network) based methods which, once trained, offer a very quick

way to approximate energies based on known data for other compounds[102].

This work only used IPs and DFT, which may be classed an *ab initio* method, and as such details will only be provided on those.

2.4.1 Interatomic Potentials

While electronic structure methods provide greater accuracy, they are often prohibitively expensive. Because the genetic algorithm employed in this project requires many thousands of structures to be locally minimised according to an energy function, it is therefore preferable to turn to a cheaper, yet *sufficiently* accurate method: interatomic potentials. These use concepts from Newtonian physics to model the interactions between atoms. In this project, a two-step approach using two different IP models was used in conjunction with the evolutionary algorithm. The first model employed was the rigid ion model, wherein ions are modelled first as point charges of charge Z where Z is the charge of the ion in question. This model is very robust even in disfavourable regions of a potential energy landscape, however it fails to capture polarisability of ions. Therefore, in the second step, ions are modelled as pairs of "core" point charges of charge $Z - Y$ and "shell" point charges of charge Y connected by a spring in the shell model. Although this increases the number of variables, the model can then reproduce dipoles forming. The spring between a core and corresponding shell is usually modelled as a simple harmonic spring with spring constant k as

$$E_{\text{spring}} = \frac{1}{2}kr^2$$

where r is the distance between the core and the shell of the ion. Additional checks are in place to ensure shells do not move too far from cores as this would be unphysical. In some parts of this project (when parametrising potentials), a second, higher-order term was added to discourage this from happening.

Electrostatics

In order to further minimise the cost, only two-body potentials were used. Since barium and oxygen in barium oxide are both charged and polarisable, a fundamental part of these is the Coulomb potential, which models the Coulomb interaction between all point particles (and shells, if they are present). For any pair of point charges, it is exactly

$$E_{\text{coul}}(r) = k_e \frac{qQ}{r}$$

with k_e Coulomb's constant being $1/4\pi\epsilon_0$, q and Q the charges of the two point charges, and r the distance between them. This is exact apart from the approximation of ions as (pairs of) point charges.

Image Potentials

Unique to this work, it was decided to model nanoclusters with a relatively wide HOMO-LUMO gap above a conducting surface, rather than what previous works have done, modelling narrow-gap nanoclusters above an insulating surface.[103, 104, 105] Specifically, in the graphene-BaO system, graphene is conducting. When a charged particle is situated above a conducting surface, a so-called image potential should emerge: the electrons below the metallic surface should rearrange so that the electrostatic field looks as if there were an equal but opposite charge equidistant below the surface, as shown in Figure 2.1.

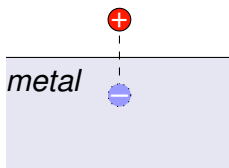


Figure 2.1: A charge above a surface generating an equal but opposite image charge.

However, the question remains whether this image potential will be the same for graphene as it is for any metal. It might be stronger, as the image charge is situated within the graphene surface and therefore closer to the charge of the barium or oxygen ion; it might

be weaker as the electrons in FSG cannot deform below the surface as they would in a 3D metal. The literature seems to be inconclusive on this. Some articles claim that there are no image potential states in graphene[106], while others claim to have measured them. Additionally, graphene is a zero-band gap semiconductor and therefore any opening of its band gap would reduce or remove the image potential effect. Our aim was to find evidence for or against mirror charges on graphene by parametrising potentials both with and without these image potential states. Because there is an opposite and equal charge for every charge above the surface, the overall effect of the image potential states should be attractive.

To model this, charges were added which are positionally dependent on Ba and O particles, and then have a Coulomb interaction with these Ba and O particles. Because graphene is not a straightforward 3D metal, the strength of the image potential may be different from what is expected. If the image potential strength varies from the expected potential where each Ba^{2+} has a " Ba^{2-} " image particle opposite it under the surface and each O^{2-} an " O^{2+} " one, the charges of these image particles can simply be altered to fit data.

Two-body potentials modelling size effects

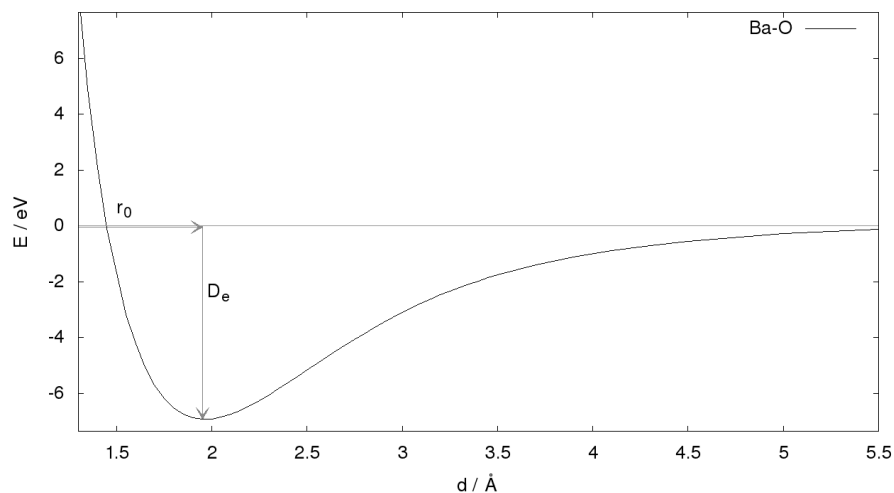


Figure 2.2: Total electronic energy of Ba-O as a function of bond distance, as calculated using the PBEsol functional in FHI-aims.

To model size effects, there are available a number of potentials which should aid in reproducing the shape shown in Figure 2.2, which shows the interaction between a single oxygen atom and a single barium atom as a function of distance, as calculated by DFT (PBEsol in FHI-aims). A number of key features are highlighted: r_0 here is the equilibrium bond distance and D_e the dissociation energy.

Three of the most commonly used potential functions of separation between two ions are named after Buckingham[107], Lennard-Jones[108] and Morse. Buckingham potentials are used to model interactions between barium and oxygen, while both Buckingham and Morse potentials are used to model the interactions of barium oxide with graphene's carbon atoms. The Buckingham potential takes the form

$$E_{\text{buck}}(r) = A \exp(-Br) - \frac{C}{r^6}$$

where A , B and C are constants which are species dependent. The first term models Pauli repulsion between electron shells in the short range, while the second term corresponds to mid- to long-range attractive interactions, i.e. van der Waals interactions. The equivalent potential where the attractive term is set to zero (that is, $C = 0$), is called the Born-Mayer potential.

The parameters of the Morse potential are more intuitive in terms of physical meaning, compared to the three parameters of the Buckingham potential, A , B and C which have much less straightforward physical meaning. The Morse potential is expressed as:

$$E_{\text{morse}}(r) = D_e(1 - \exp(-a_0(r - r_e)))^2$$

D_e is the bond dissociation energy (well depth), r_e is the equilibrium bond length and a_0 , the least straightforward parameter, can be described as

$$a_0 = \sqrt{\frac{k_e}{2D_e}}$$

where k_e is the force constant at the bottom of the well. Two of its parameters (D_e and r_e) can therefore be read straight off a plot of this potential over r and are directly representative of straightforward properties of the bond, with the third parameter still expressing properties of the bond.

The overall potential, then, is

$$\sum_i E_{\text{spring}}(r_i) + \sum_{j \neq k} \left(E_{\text{buck}}(r_{jk}) + E_{\text{morse}}(r_{jk}) + E_{\text{coul}}(r_{jk}) \right)$$

with i , j and k summed over all atoms in the cluster, and, if present, surface. In this, r_i is the distance between the core and shell of atom i ; r_{jk} is the distance between two shells; core locations are used if shells are not present. Morse or Buckingham potentials are chosen based on the species pairings.

Fitting Potentials

Barium oxide has already been modelled by Lewis et al.[109] and therefore well established IPs for it already exist. This is not the case for its interaction with a graphene surface. Therefore, potentials were fitted to model the interaction of a graphene sheet with barium oxide nanoclusters. Generally, a fit to a set of observables is performed; for each variable at least one observable is required. These observables may be obtained from experimental data or from computational results using a higher-level (*ab initio*) method. In this project, the IP parameters were refined to reproduce single-point DFT calculations of $(\text{BaO})_n$ nanoclusters approaching a graphene surface. Specifically, for each set of atomic coordinates an energy was extracted which was then fitted to. However, the dispersion correction was not applied here and this has probably led to errors in the graphene-BaO interaction energies as the exchange-correlation functional on its own does not capture dispersion effects.

GULP offers three fitting modes: `fit`, `relax fit` and `simul fit`. In the `fit` fitting mode, single-point calculations are carried out and observables compared, no atomic coordinates are altered. In the `relax fit` fitting mode, all atomic coordinates are re-

laxed and then compared to known LM structures (e.g. the experimental unit cell, or LM structures gained from DFT calculations). Finally, in the `simul fit` mode, only shells are relaxed.

The aim of the fitting is to minimise the *sum of squares* S of the observables (weighted with weights w_o as appropriate).

$$S = \sum_o w_o (f_c - f_o)^2$$

Here, o are the observables and weights and values with corresponding subscripts belong to each observable. The w_o values are chosen to weight more reliable or important data more heavily, for example to give greater weight to data closer to the equilibrium bond length in our case since that part of the curve is the most important to get right.

For the rigid ion model, fitting is relatively straightforward, with GULP providing a method in `fit` that iteratively fits any number of parameters to the given observables. Comparatively, when using the shell model, one may either use the `simul fit` mode, or for more control, use `fit` and manually perform geometry optimisations on only the shells and then reoptimise the parameters that are being fitted, doing this procedure iteratively until all the parameters remain constant. In this work, this was mostly done manually.

2.4.2 Electronic Structure Methods

Once a pool of plausible candidate structure has been generated using the EA and IPs, the energies and exact geometries of the better structures should be re-evaluated using a more accurate method. This will be a quantum mechanical method, as implemented in FHI-aims. Generally, quantum mechanical methods aim to solve a form of the electronic Schrödinger equation:

$$\hat{H}\Psi = E\Psi$$

Here, \hat{H} is the Hamiltonian operator for a system of electrons and nuclei at positions r_i and R_j , respectively.

Wavefunction Methods

In a first step, we will take the Born-Oppenheimer approximation, that is the assumption that nuclei are stationary compared to the much faster moving electrons. Then, in atomic units, the *electronic* Hamiltonian for N electrons and M nuclei can be written as

$$\hat{H}_{\text{elec}} = - \sum_{1 \leq i \leq N} \frac{1}{2} \nabla_i^2 - \sum_{1 \leq i \leq N, 1 \leq j \leq M} \frac{Z_j}{r_{ij}} + \sum_{1 \leq i \leq N, i < k \leq N} \frac{1}{r_{ik}}$$

The first term is the kinetic energy of the electrons, the second term is the attraction between electrons and nuclei, and the third is electron-electron repulsion. Z_j is the atomic number (charge) of the j^{th} nucleus.

The solution to the electronic Schrödinger equation emerging from this is the electronic wavefunction Ψ_{elec} . This depends explicitly on the electronic coordinates but only parametrically on the nuclear coordinates. The energies, then, which also parametrically depend on the nuclear coordinates, are the eigenvalues of this system. However, finding an exact solution to this with an exact wavefunction when there are multiple electrons is prohibitively expensive.

One small piece is still needed to discuss this further: Slater determinants. In order to get to a wavefunction which obeys antisymmetry (since electrons are fermions), we construct the determinant of a matrix of one-electron wavefunctions, where each electron is in turn put into each orbital.

$$\Psi = \frac{1}{\sqrt{N!}} \begin{vmatrix} \phi_1(1) & \phi_2(1) & \dots & \phi_N(1) \\ \phi_1(2) & \phi_2(2) & \dots & \phi_N(2) \\ \vdots & \vdots & \ddots & \vdots \\ \phi_1(N) & \phi_2(N) & \dots & \phi_N(N) \end{vmatrix}$$

Now, the first computational method that finds use is the Hartree-Fock method. It uses a single Slater determinant to represent the ground-state wavefunction. By the variational

principle, the best wavefunction is the one which gives the lowest possible energy,

$$E_0 = \langle \Psi_0 | \hat{H} | \Psi_0 \rangle$$

It can be shown that there is an equation which determines the optimal spin orbitals. This is called the Hartree-Fock equation.

$$\hat{F}(i)\psi(\mathbf{x}_i) = \epsilon\psi(\mathbf{x}_i)$$

where $\hat{F}(i)$ is the one-electron Fock operator,

$$\hat{F}(i) = -\frac{1}{2}\nabla_i^2 - \sum_{j=1}^M \frac{Z_j}{r_{ij}} + v^{\text{HF}}(i)$$

and where $v^{\text{HF}}(i)$ is the average potential experienced by electron i due to the presence of all other electrons. As such, the problem becomes a one-electron problem with electron-electron repulsion only treated in an average way.

In practice, this method scales as $\mathcal{O}(n^4)$ with the number of electrons, n , and is not very accurate – for example, it systematically underestimates bond distances. More accurate methods built on Hartree-Fock, which take into account electronic excitations in various ways, are available: Møller-Plesset perturbation theory (MP2, MP3), Coupled Cluster methods, and CASSCF, to name a few. All of these methods scale even worse with system size than Hartree-Fock and are prohibitively expensive for systems much beyond 10 atoms in size.

Density Functional Theory

The key idea behind DFT is that of reducing the problem to one of electron density instead of individual electrons' wavefunctions, and of then reducing the kinetic energy expression to one of non-interacting particles (Kohn-Sham DFT) – this series of changes reduces the complexity of the problem and therefore also reduces the computational cost for large

systems.

DFT shifts the problem from finding the ground state wavefunction to a functional E of the electron density $\rho(\mathbf{r}) = \sum_n |\psi_n(\mathbf{r})|^2$, where ψ_n are the single-particle wavefunctions of individual electrons, under the constraint that $\int d\mathbf{r} \rho(\mathbf{r}) = N$, and that the nuclei contribute an external potential V_{ext} . The following two theorems (the Hohenberg-Kohn theorems) show it is possible to do this:

Theorem 1. ρ uniquely determines V_{ext} .

A graphic argument for this is that with any electron density, there will be cusps at nuclear positions and integrating the electron density around each nucleus can uniquely identify that nucleus (its element). A rigorous proof for this can be found in March's paper on generalisation of Kato's theorem.[110]

Theorem 2. *By variationally minimising the energy as a functional of the electron density, both the ground state energy and corresponding ground state density can be found, i.e.*

$$E[\rho(\mathbf{r})] > E[\rho_0(\mathbf{r})] \quad \forall \rho \neq \rho_0 \quad (2.1)$$

The functional form resulting in the exact solution (the Hohenberg-Kohn functional) is unknown, but there are ways to approximate its components.

A functional describing the energy $E[\rho]$ may be decomposed into a sum of four terms:

$$E[\rho] = \int \rho(r) V_{\text{ext}}(r) d\mathbf{r} + J[\rho] + T[\rho] + E_{xc}[\rho]$$

with V_{ext} the external potential of the nuclei, J the two-electron Coulomb interaction, $T[\rho]$ the sum of single-electron kinetic energy terms and $E_{xc}[\rho]$ the many-body terms describing electron exchange, correlation, and the error in the kinetic energy approximation.

The way of expressing the kinetic energy mentioned above was proposed by Kohn and Sham in 1965[111]: Solving the problem for a fictitious system of non-interacting electrons with the same electron density ρ as the real system leads to an exact solution

for the non-interacting system. It is not an exact solution for the interacting system that is ultimately being simulated and so its error should be captured in E_{xc} .

The result can then be converged variationally with respect to nuclear positions by updating the electron density iteratively until the energy is converged. This is the self-consistent field method.

All DFT results reported here were achieved using the FHI-aims code[112] which is run by KLMC as part of KLMC's functionality. Some calculations were also redone using NWChem[113] to confirm their validity.

Implementation of DFT (FHI-aims)

Basis Set

FHI-aims uses numerical atom-centred basis sets. The basis functions are arranged in "tiers" and the user can choose from "light", "intermediate", "tight" or "very tight" basis sets and then further add or remove basis functions to adjust accuracy and ease of convergence as needed (accuracy being higher with a tighter basis set, ease of convergence with a lighter one).

Exchange-Correlation Functional Choice

PBEsol[114, 115, 116] is the functional used throughout, as it was developed for solid state and surface systems, and is unbiased and relatively cheap computationally. It has been used numerous times for nanocluster systems.[23, 117, 118]

Hybrid functionals

One way of making the exchange-correlation functional in DFT more physically meaningful is to include some amount of Hartree-Fock exchange which is exact. To validate some results, a hybrid functional, PBESOL0[119], has been used to re-calculate exact geometries as well as energies of $(\text{BaO})_n$ clusters. This functional contains 25% Hartree-Fock

exchange, that is the exchange correlation functional is

$$E_{xc}^{\text{PBESOL0}} = \frac{1}{4}E_x^{\text{HF}} + \frac{3}{4}E_x^{\text{PBESOL}} + E_c^{\text{PBESOL}}$$

Relativity

While it can be ignored in most cases, special relativity becomes somewhat relevant in this work because barium atoms have a very high atomic number and its electrons therefore have relativistic velocities. In the FHI-aims implementation of DFT used here, a scalar relativistic kinetic energy term is implemented with the approximation used being "atomic ZORA"[120, 121] which has generally held up well in energy-based benchmarks.[122] and was therefore chosen here wherever barium atoms are present.

Chapter 3

Isolated Barium Oxide Clusters

3.1 Introduction

This chapter will describe in detail structures of barium oxide nanoclusters and their stabilities. Barium has a high atomic number and forms a cation which is very close in size to the oxygen anion[42]. Barium oxide is therefore of particular interest, being suitable for atomic-resolution microscopy (TEM, STEM)[123]. Insight gained may also apply to smaller cation options which might have more promising applications, such as magnesium or calcium oxide. Group II oxides are expected to have a simple enough conformational space to make it a good candidate for computational structure searches. As such, barium oxide is especially suited to benchmark the performance of our methods against any future experimental results where the barium oxide clusters will be deposited on a surface. Recent collaborations have resulted in a study incorporating both atomic resolution STEM images and computational data from structure searches on gold nanoclusters[124], and atomic-resolution images have also been reported on their own recently for platinum[125], cobalt[126] and gold[127] nanoclusters. No comparable study has been conducted for non-metallic nanoclusters. Although these experimental results are not yet available at the time of writing this, we are aware of a leading experimental group in this field that would be interested in making a comparative study if suitable computational data were available (the group of Richard Palmer).

To get an insight into the behaviour of how clusters interact with surfaces, one can first determine their structures and properties *in vacuo* and then use these structures as a starting point for developing cluster-surface models. Therefore, searches of the energy landscapes of $(\text{BaO})_n$ clusters *in vacuo* have been completed for sizes $n = 2$ to 18 as well as $n = 24$ using an evolutionary algorithm. One important aspect of analysing this data is to look at relative stability of different structural motifs and how this influences relative size stabilities, and this will be focused on this data.

3.2 Methods

3.2.1 Global Optimisation to obtain plausible, low-energy metastable configurations

Aiming for a *sufficiently* exhaustive search of the low energy region of conformational space for $(\text{BaO})_n$, the EA implemented in KLMC[91] was employed in order to get reasonable first guesses of potential structures. Each run required specifying the number of atoms of each type (Ba, O), parameters of IPs and EA parameters (a population of 100 clusters per generation and between 100 generations for $(\text{BaO})_4$ and 1000 generations for $(\text{BaO})_{24}$). Note that more generations are necessary for larger clusters as conformational space grows exponentially with the number of atoms in the cluster. IPs[109] were chosen as the energy function because they are more efficient than DFT and expected to give reasonable results. Note that to increase our confidence in finding all low energy LM, i.e. in order to explore a sufficiently large subset of conformational space, several thousand individual geometry optimisations were necessary for each cluster size at this stage. To further reduce the cost of local optimisations and make the method more robust, each structure was optimised in two stages, first employing a rigid ion model and then starting from the first step's results, a second refinement using the shell model. In addition, structures were also constructed (cuts from the bulk phase) and data-mined from magnesium, calcium and strontium oxide results.

3.2.2 Refinement of Plausible Structures

The best, or lowest energy (as measured by our chosen IP model) structures (usually 20, but up to top 40 for the largest cluster size) resulting from this were saved for each size, and then used as starting points for higher accuracy re-optimisation using DFT (the PBEsol generalised gradient approximation (GGA) functional[114, 115, 116]) as implemented in FHI-aims. Each conformation was pre-optimised locally during which a light basis set is employed, and then these pre-optimised configurations were re-optimised with a tight basis set, i.e. first-tier improvements to basis functions for Ba atoms and first- and second-tier improvements for O atoms. This should provide an accuracy of $< 10\text{meV}$ per atom. No periodic boundary conditions were employed for this set of calculations. For larger clusters, more structures (up to top 40) were saved; this was necessary as many LM were close in energy to each other and the IPs' quality was not high enough to always rank them correctly. DFT input files were generated automatically from the EA outputs using KLMC's data mining functionality. The overall workflow is shown in Figure 3.1.

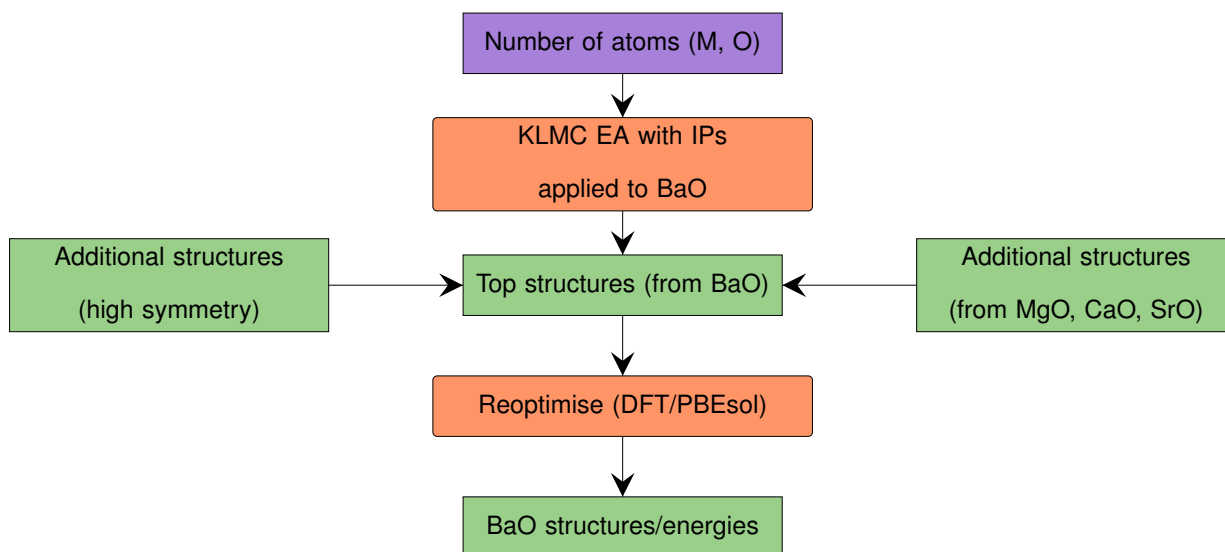


Figure 3.1: Steps in generating optimised structures and energy rankings for barium oxide nanoclusters.

Additionally, all DFT calculations were re-run while employing the PBEsol0[119] hybrid functional with the same basis set to further verify these results. As will be reported

below, they only made a significant difference when refining the $n = 24$ configurations.

3.3 Results

As described above, structure searches were performed for $(\text{BaO})_n$ clusters of sizes $n = 2$ to 18 and $n = 24$. Their structures and energies will be reported in two segments; small clusters ($n \leq 12$) and larger clusters ($n > 12$).

3.3.1 Structures and Energies of Small $(\text{BaO})_n$ Clusters ($n = 1$ to 12)

The three lowest-energy (as per DFT) structures for $(\text{BaO})_n$ ($2 \leq n \leq 12$) with their energies relative to their respective GMs are reported in Table 3.1 below. Specifically, for clusters of sizes $n = 1, 2$ and 3 only one LM was found each, the latter two forming a tetragonal ($n = 2$) and hexagonal ($n = 3$) ring with all atoms two-coordinated, as opposed to a linear stick which has terminating 1-coordinated atoms. These sticks are predicted to be unstable. LM ring conformations can also be found for larger sized clusters, but even by $n = 4$ other 3D structural motifs are found to be more stable.

For the $n = 4$ cluster, the deformed cube structure is much lower in energy than the ring; previous studies have shown that this is also the case for $(\text{MgO})_4$ and $(\text{KF})_4$ [23], which adopt the same phase in the bulk as BaO does (rocksalt). This cuboid, which is composed of $2 \times 2 \times 2$ atoms, will be referred back to as a secondary building unit (SBU) of many of the following clusters. In fact, all even- n BaO GM shown in Table 1 (left-hand side) are exclusively composed of these cubic SBUs and form larger cuboids themselves. The same holds for the $n = 9$ GM, which is the only rocksalt cut with odd n in this size range. Additionally, there exist non-cuboid rocksalt cuts, for example, the second-lowest energy structure for $n = 10$ is a non-cuboid composed of $n = 4$ SBUs.

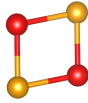


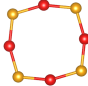
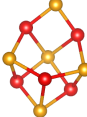
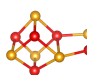
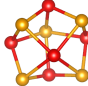
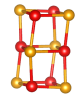
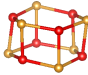
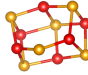
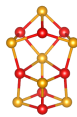
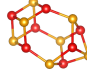
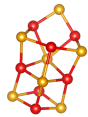
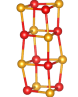
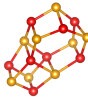
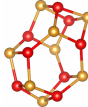
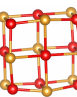
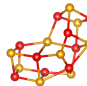
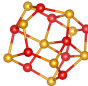
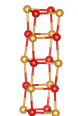
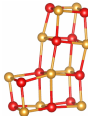
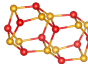
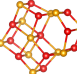
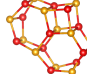
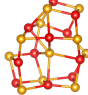
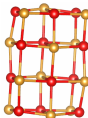
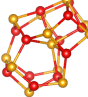
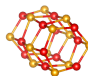
	1st	2nd		1st	2nd	3rd
n		2			3	
						
n		4			5	
						
$\Delta E/\text{eV}$	0.0	2.999		0.0	0.010	0.052
n		6			7	
						
$\Delta E/\text{eV}$	0.0	0.134	0.666	0.0	0.007	0.113
n		8			9	
						
$\Delta E/\text{eV}$	0.0	0.284	0.587	0.0	0.076	0.165
n		10			11	
						
$\Delta E/\text{eV}$	0.0	0.393	0.585	0.0	0.132	0.193
n		12				
						
$\Delta E/\text{eV}$	0.0	0.047	0.347			

Table 3.1: Lowest energy structures of $(\text{BaO})_n$ clusters for $n = 2$ to 12, as resulting from PBEsol geometry optimisations

Structural motifs that are not composed of this SBU include rings (which are only in

the top 3 for $n = 3$ and $n = 4$) and barrels (non-GM structures of $n = 6, 9, 10$ and 12). There are also configurations found to have the $n = 4$ SBUs as *part* of their structure, for example non-GM structures of $n = 8, 9$ and 11 .

The odd- n clusters which could not form bulk cuts composed of these building blocks, such as the $n = 5$ and 7 GM, all adopt relatively highly coordinated and symmetrical structures. The total number of LM found increased with n ; for $n \geq 7$, more than 20 were found by the EA and therefore, only a subset of the LM found for $n \geq 7$ were refined using FHI-aims.

3.3.2 Structures and energies of larger $(\text{BaO})_n$ clusters ($n = 13$ to 18 and $n = 24$)

Table 3.2 shows the larger BaO clusters. Again, for even- n clusters (this time on the right), specifically $n = 14, 16$ and 18 , the GM found is a cuboid rocksalt cut made up of $n = 4$ SBUs. In the case of $n = 14$, the GM is not cuboid, but still a rocksalt cut made of the same SBUs. The $n = 14$ cuboid has $7 \times 2 \times 2$ atoms, all of which are 3- or 4-coordinate, whereas the non-cuboid cut has two higher-coordinated atoms and 54 bonds compared to the cuboid's 52, indicating again that a higher coordination number seems to be preferred here overall.

The size $n = 18$ provides an interesting case as it is possible to form more than one competitive cuboid, $4 \times 3 \times 3$ and $6 \times 3 \times 2$. The $6 \times 3 \times 2$ rocksalt cut has

a higher surface area and 72 total bonds whereas the $4 \times 3 \times 3$ cut has 75 bonds.

The former is lower energy in PBEsol calculations and also in those using a hybrid functional, PBEsol0. Another factor that may affect a structure's relative stability is the formation of a dipole if layers are not charge neutral. The $4 \times 3 \times 3$ cuboid, for

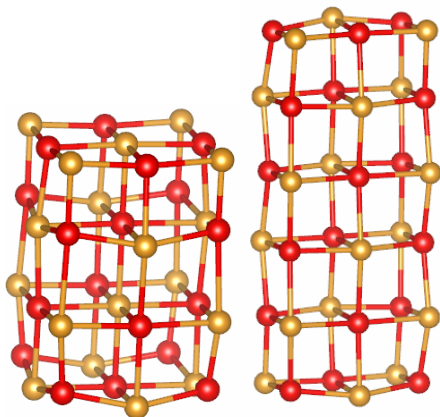


Figure 3.2: The $(\text{BaO})_{18}$ $4 \times 3 \times 3$ (left) and $6 \times 3 \times 2$ (right) bulk cut structures

example, when constructed has a dipole that atomic and electronic relaxations will try to reduce. This is due to having an even number of 9-atom layers which, since there are different numbers of barium and oxygen atoms on them, create a dipole. This will be discussed in more detail in Section 3.3.5.

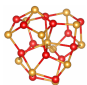
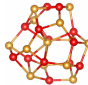
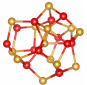
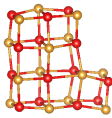
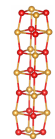
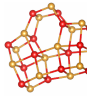
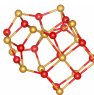
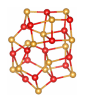
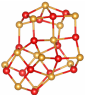
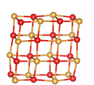
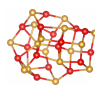
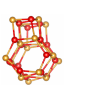
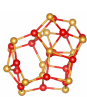
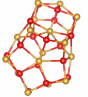
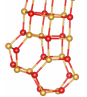
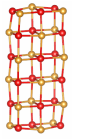
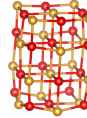
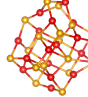
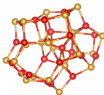
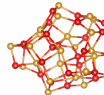
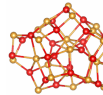
	1st	2nd	3rd	1st	2nd	3rd
n	13			14		
						
$\Delta E/\text{eV}$	0.0	0.114	0.173	0.0	0.061	0.125
n	15			16		
						
$\Delta E/\text{eV}$	0.0	0.241	0.242	0.0	0.548	0.753
n	17			18		
						
$\Delta E/\text{eV}$	0.0	0.204	0.398	0.0	0.108	0.374
n				24		
						
$\Delta E/\text{eV}$				0.0	0.001	0.189

Table 3.2: Three lowest energy structures of $(\text{BaO})_n$ clusters for $n = 13$ to 18 and 24, as resulting from PBEsol geometry optimisations

Again, for some of the odd- n clusters it is not possible to form perfect cuboid rocksalt cuts. However, the majority of odd- n LM shown in Table 3.2 contain fragments composed of $n = 4$ SBUs as well as other previously seen structural elements such as barrels.

Surprisingly, the three top structures for $(\text{BaO})_{24}$ are not rocksalt cuts

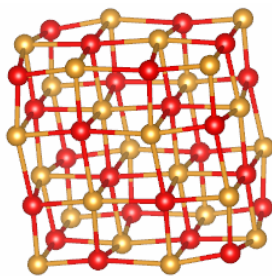


Figure 3.3: The $(\text{BaO})_{24}$ bulk cut structure, the GM as predicted by PBEsol0 calculations.

and in fact have a lower average coordination number than the rocksalt cut. All three were roughly 300 meV lower in energy than the rocksalt cut in this set of calculations. As this result was unexpected, the $(\text{BaO})_{24}$ DFT optimisations were re-run with PBEsol0. Indeed, in these calculations the rocksalt cut (Figure 3.3) was re-ranked as the global minimum;

energy rankings of all other $(\text{BaO})_{24}$ structures, including those shown in Table 3.2, were unaffected. The top 5 structures of all other $(\text{BaO})_n$ clusters were subsequently also reevaluated with PBEsol0 and none of their energy rankings changed qualitatively.

3.3.3 Normalised Clustering Energies

One measure of stability of a cluster is the normalised clustering energy[32, 128]: here, the energy of a cluster is compared to that of the smallest stoichiometric cluster, the $n = 1$ stick unit, as follows:

$$NCE(n) = \frac{E(n)}{n} - E(1)$$

This shows how energetically favourable it is for each cluster size to form from a bath of $n = 1$ units. In this and the following sections up to 3.3.6, only GM energies are going to be discussed. The NCEs for clusters of sizes $n = 4$ to 18 are shown in Figure 3.4. Here, a lower NCE implies a greater stability.

It is expected that the NCE values should slowly converge toward the bulk limit of -3.999 eV, however, the lowest NCE found for these sizes, that of $n = 16$, is -2.795 eV and therefore still 1.204 eV higher. For most sizes the value of the NCE decreases each time an extra formula unit is added. It is visible in the figure that this decrease tends to be markedly stronger when going from an odd numbered cluster to an even numbered

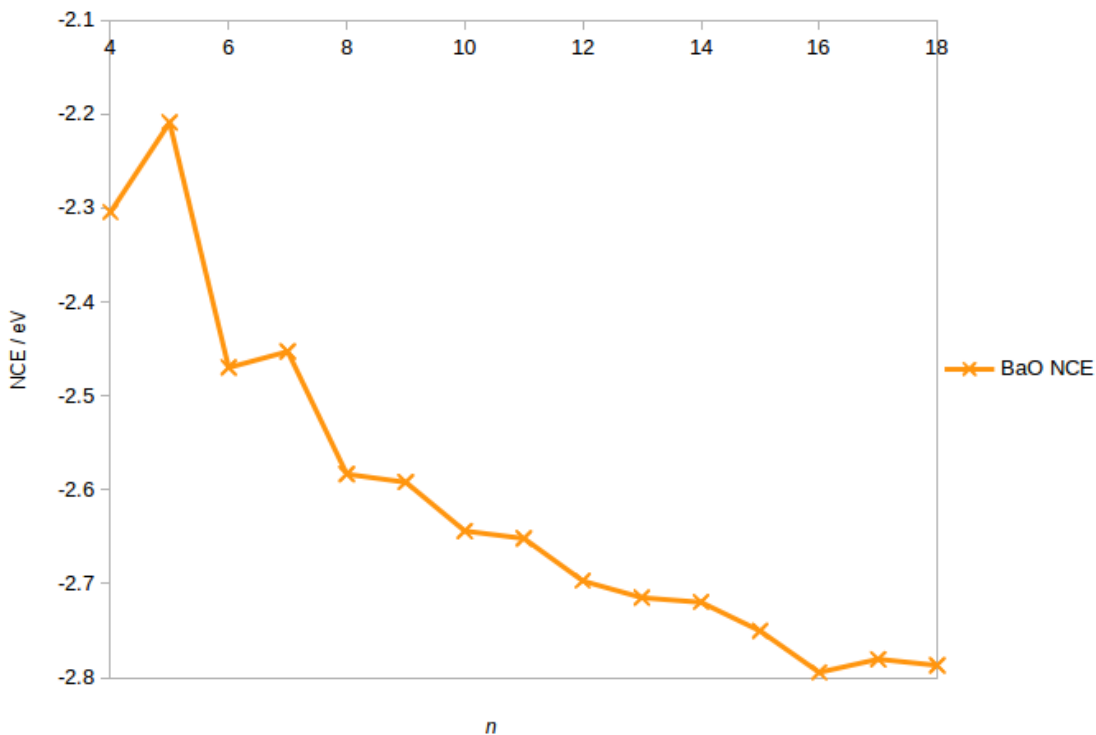


Figure 3.4: NCEs for barium oxide clusters, as resulting from PBEsol calculations.

cluster, indicating that even numbered clusters are generally more stable. For three sizes ($n = 4$, $n = 6$ and $n = 16$), the value of the NCE actually goes up when an extra formula unit is added, indicating that they are (by this measure) more stable than the next larger size and it is highly unlikely that the next larger size would form from them by addition of a single $n = 1$ cluster.

3.3.4 Second-order energies

Another useful measure of the stability of cluster sizes relative to each other can be obtained by calculating the second-order energy differences ΔE , which relate a cluster's energy to nearest neighbours' energies as follows:

$$\Delta E = E(n) - \frac{1}{2}(E(n+1) + E(n-1))$$

The term "second-order energy difference" is used because they are the centered difference approximation with second-order error to the first derivative of GM energy $E(n)$

with respect to cluster size n . Negative second-order energy differences suggest that the cluster is more stable than the average of clusters with 1 more and 1 less formula units while positive ΔE indicate relatively less stable clusters. The second-order energy difference thus provides a measure of whether or not two clusters of a given size might transfer one BaO unit.

Second-order energies for BaO clusters with $n = 2$ to 17 (i.e. all sizes where both neighbours' energies were available) are shown in Figure 3.5 and Table 3.3, along with their structures. Almost all clusters with negative second-order energies are rocksalt cuts, and all except the GM for $n = 2$ one are composed of the $n = 4$ SBUs. Not keeping with this overall trend is the $n = 13$ cluster, which has a slightly negative second-order energy, but because the value is so close to zero, this is not a very strong deviation. All other non-rocksalt GMs have positive second-order energies and are therefore less stable than their neighbours. The $n = 14$ cluster, which forms a rocksalt cut that is not cuboid, also has a positive second-order energy.

The negative values in Figure 3.5 and Table 3.3 can often be related to *magic number* sizes $n = m_i$. When clusters are created via laser ablation of a surface and then subsequently measured in a mass spectrometer, larger peaks are expected for $n = m_i$ sizes[43, 44]; these cluster sizes show a greater relative stability. Magic numbers have previously been predicted for $(\text{NaCl})_n\text{Cl}^-$ clusters, see Ref. [129].

The second-order energy of the $n = 9$ cluster is slightly positive despite it being a cuboid made up of $n = 4$ SBUs; since the main feature which distinguishes it from other such cuboids is its polar nature, this could indicate that polar clusters are less favourable. Therefore, dipole moments will be investigated in more detail.

n	2 nd -order energy difference
2	-0.573
3	0.126
4	-0.425
5	0.17807
6	-0.13903
7	0.07392
8	-0.06103
9	0.02165
10	-0.02199
11	0.01868
12	-0.01374
13	-0.006482
14	0.01284
15	0.006809
16	-0.02911
17	0.01034

Table 3.3: Second-order energy differences of $(\text{BaO})_n$ clusters for $n = 3$ to 17.

3.3.5 Dipole Moment

A number of properties strongly correlate with the sign of the second-order energies and the odd- n /even- n split. The first of these is dipole moment, as shown in Figure 3.6 and Table 3.4.

Most structures with odd n have dipole moments between 4 and 8 D while most even- n GM have negligible dipole moments (are non-polar). One data point to note is $n = 9$, which, while it is odd and has a relatively high dipole moment, is also a cuboid rocksalt cut GM, the only one that is polar. This is due to its 9-atom charged layers similar to the

$4 \times 3 \times 3$ (BaO)₁₈ isomer discussed previously.

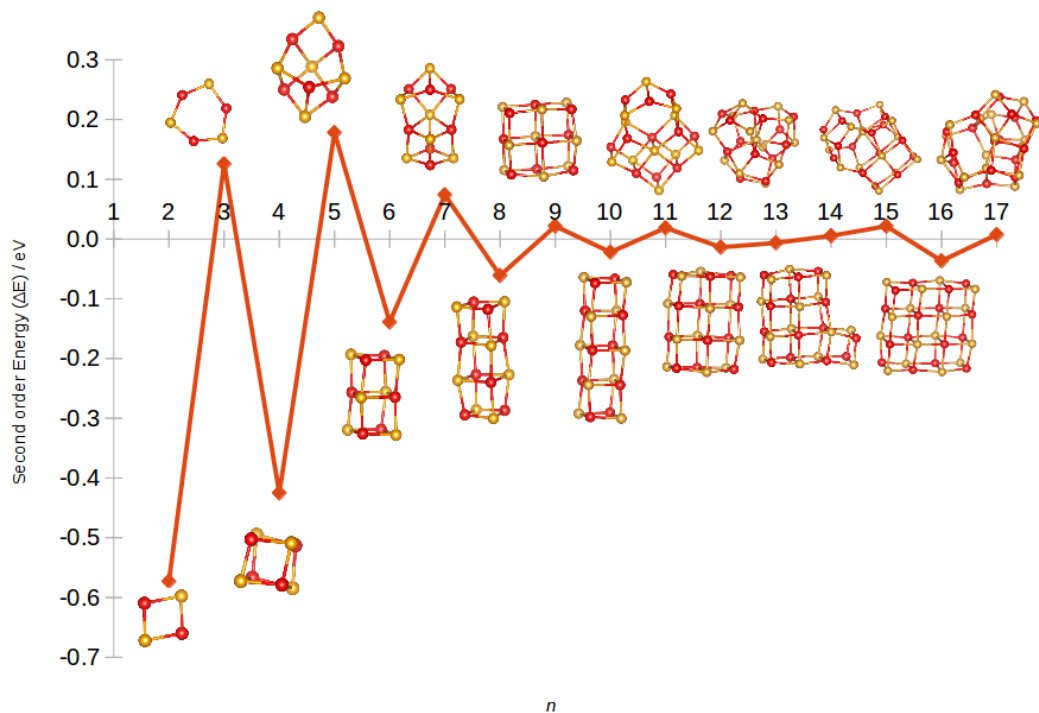


Figure 3.5: Second-order energies of BaO clusters ($n = 2$ to 17)

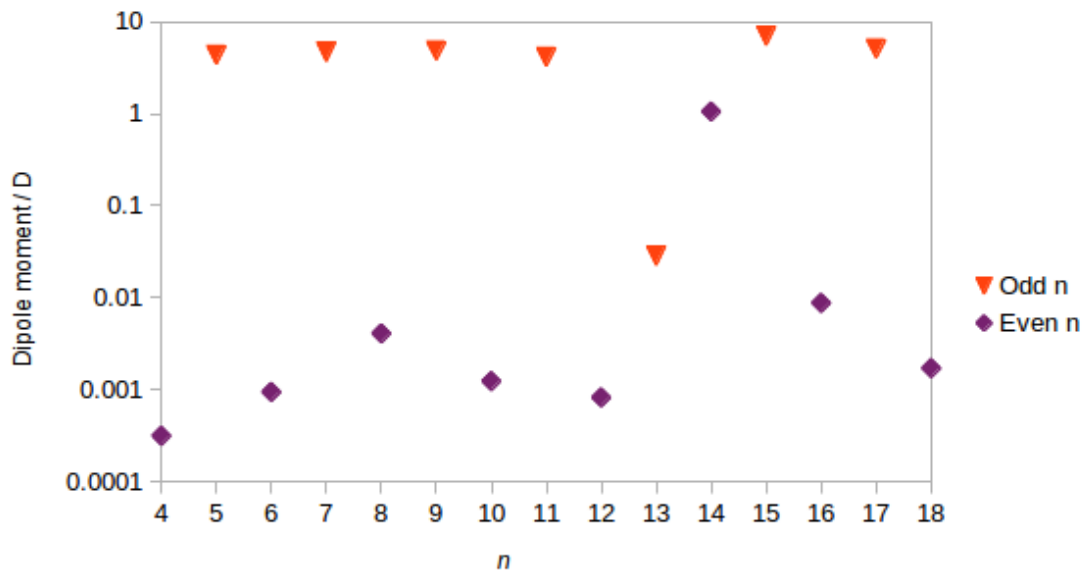


Figure 3.6: Dipole moments of BaO GM for $n = 4$ to 18, as optimised with PBEsol.

The two cluster sizes which do not follow the trend, $n = 13$ and 14 also need explana-

even n		odd n	
4	3.14E-04	5	4.38E+00
6	9.41E-04	7	4.70E+00
8	4.08E-03	9	4.87E+00
10	1.23E-03	11	4.17E+00
12	8.21E-04	13	2.86E-02
14	1.06E+00	15	7.06E+00
16	8.76E-03	17	5.13E+00
18	1.71E-03		

Table 3.4: Dipole moments of BaO GM for $n = 4$ to 18, as optimised with PBEsol.

tion. The $n = 14$ structure is in effect equivalent to the $n = 16$ one, but with four atoms removed from one edge of a non-polar cuboid rocksalt cut, creating a less symmetrical L-shaped structure. Due to the reduced symmetry, the structure acquires a dipole. The fact that this is still preferred over non-polar structures such as the $7 \times 2 \times 2$ cuboid bulk cut indicates that the assumed penalty for a dipole moment is in competition with other factors such as maximisation of coordination number (to approach the limit of 6, i.e. that found in bulk rocksalt); for $n = 14$, the dipole moment is also somewhat less severely penalised because it is, at 1.06 D, significantly smaller than those of the other polar structures discussed here (which range from 4.17 to 7.06 D); however, $n = 14$ has a second-order energy much closer to zero than other even- n rocksalt cuts, suggesting that its dipole moment is not entirely without consequence.

The non-polar nature of the $n = 13$ GM appears to be primarily because it has near-perfect threefold symmetry along multiple axes, and indeed it is relatively lower in energy with its negative second-order energy than other structures which are disordered and relatively under-coordinated, further supporting the fact that magnitude of dipole moment does play a role in energetics of these clusters.

3.3.6 Coordination number

The other property mentioned above to explain why even- n BaO clusters appear more favourable was coordination number. Coordination numbers as a function of size are shown in Figure 3.7. Since BaO adopts the rocksalt structure, we expect its coordination

number to increase and asymptotically approach that found in rocksalt, 6. There is generally a trend of increasing coordination number with increasing n , however, above $n = 6$ it only steadily increases for even n .

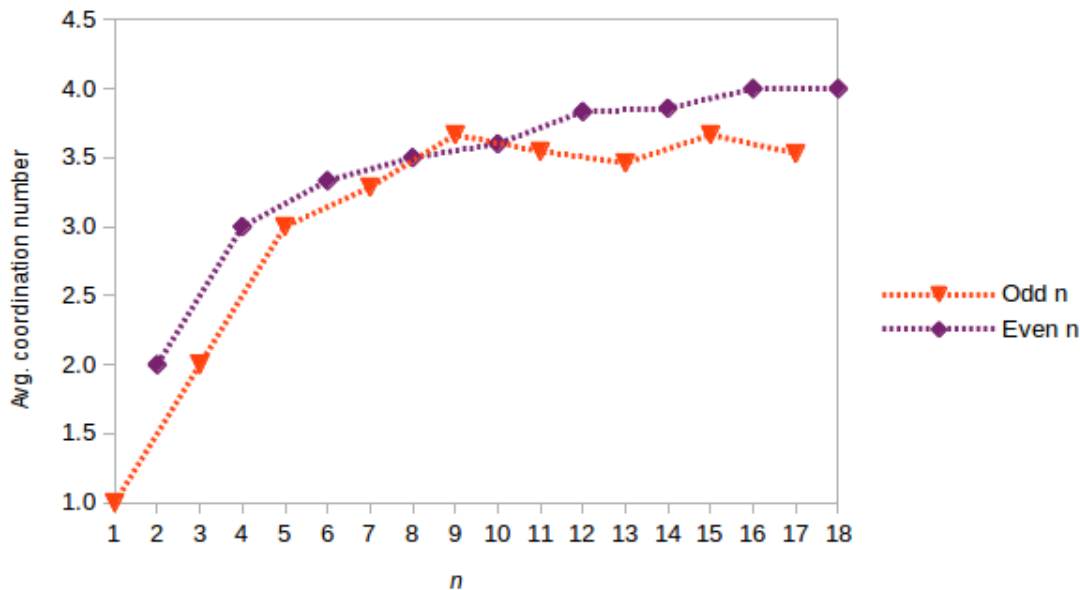


Figure 3.7: Coordination numbers of BaO cluster GM for $n = 1$ to 18, as calculated with PBEsol; bond length cutoff ~ 2.95 Å.

Assuming that coordination numbers closer to 6 are better, this also supports the second-order energy trends in that in most cases, the even- n clusters are higher coordinated than their odd- n neighbours, with $n = 9$ the only exception, since it is a rocksalt cut like the even- n structures. This gives further evidence that BaO prefers higher coordination numbers, or 6-coordinated atoms, since the even- n clusters also generally have a lower second-order energy. In this size range, the coordination number does not get very close to 6 because even at $n = 18$, the majority of atoms are still surface atoms.

Contradictory to this, an analysis of all top 20 LM shows that there is little correlation of coordination number with energy within each size: perhaps this trend is primarily collateral to the trends of rocksalt cut preference and preference for non-polar structures. This is shown for the example of $n = 16$ (where a cuboid rocksalt cut exists in Figure 3.8: While one can generally say that lower energy structures tend to have no bonds, the correlation is nowhere near strong enough to predict the relative energy of a structure

from its number of bonds.

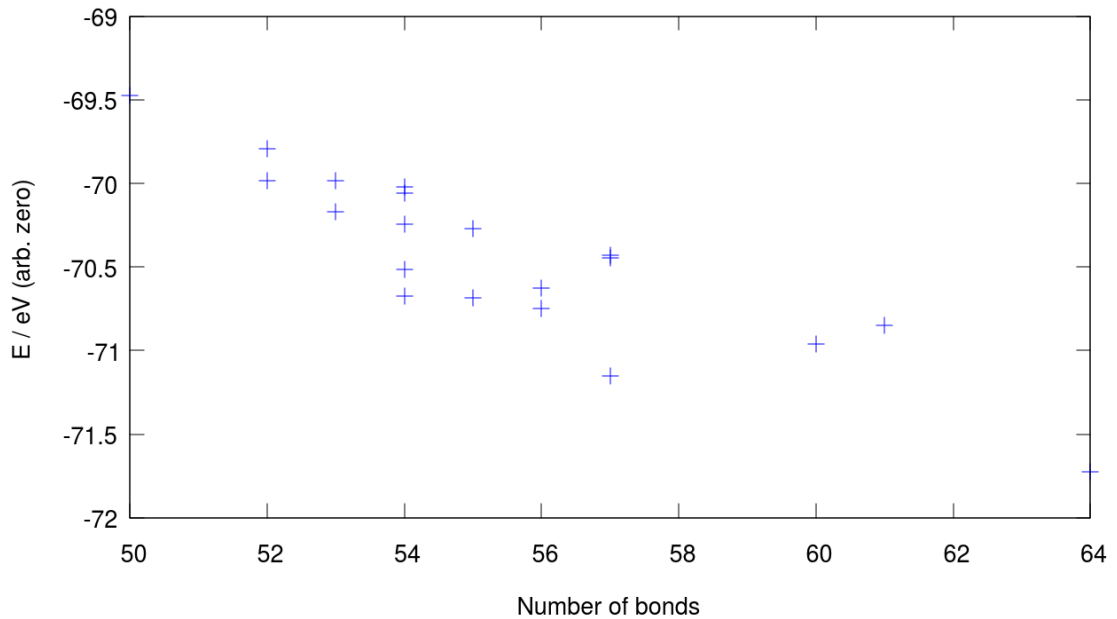


Figure 3.8: Energy as a function of the total number of bonds for $n = 16$ structures.

3.3.7 Energy Density of Local Minima

The previous data all assumed a temperature of 0K. In order to get a more detailed idea which structures are most likely to be found at non-zero temperature, it is important to combine the stability of a cluster relative to its neighbours with a notion of how likely it is to adopt the GM structure rather than perhaps another one that is very close to it in energy. For this, Figure 3.9 was created. For each size, n , the likelihood of finding a particular LM configuration will depend upon the temperature of the system and the LM's energy difference from the GM. Gaussian smearing corresponding to a temperature of 100K (cf. the paper by Haertelt et al.[83] where a 100K source temperature was used) was applied to the energies of each n 's LM (green lines) and additionally, energy per formula unit was directly compared to the $n - 1$ GM (red mark). Assuming a bath of $n = 1$ BaO units, LM to the right of this mark are more likely to fragment to the smaller global minimum, while ones to its left are more likely to grow from it.

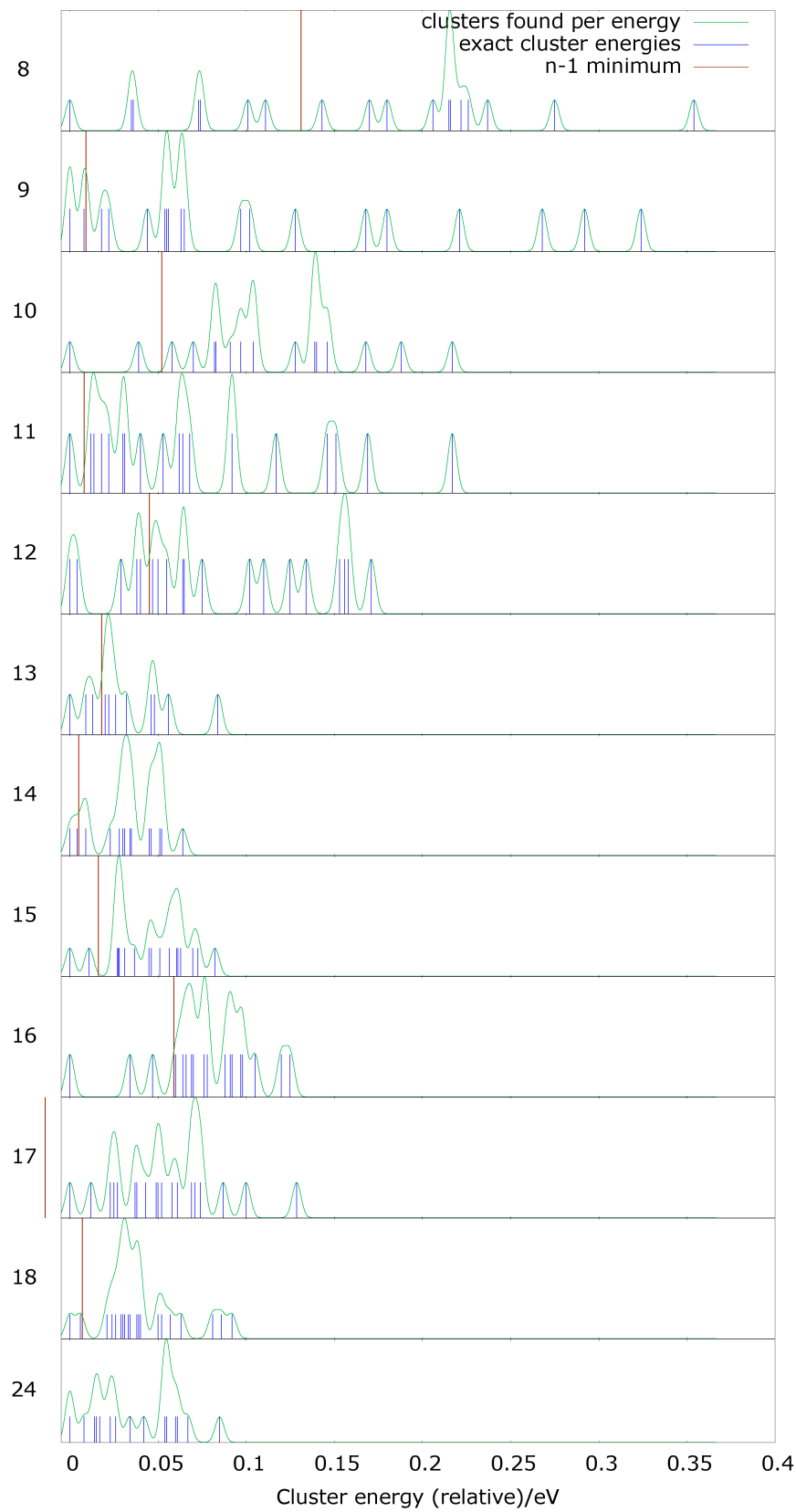


Figure 3.9: Density of LM for BaO clusters for $n = 8$ to 18 and 24 at 100K. Blue impulses indicate cluster energy per formula unit, green lines indicate smeared energies, and red divisions mark $n - 1$ cluster energies..

The further to the right the $n-1$ mark is, the more likely it is that a size n cluster is found and the more stable the size n GM is to fragmenting into an $n-1$ cluster and a $n=1$ unit. This can be seen on Figure 3.9 by the position of the red line. The figure only includes clusters with $n \geq 8$. By this measure, the $n=8$ cluster is the most relatively stable, followed by $n=10, 12$ and 16 ; this is in line with their second-order energies being the lowest, which is an expected result because the second-order energies strongly depend on the relative energy of the $n-1$ GM.

It is also useful compare the energies of the other LM of size n to the energy of the $n-1$ GM: each cluster size shown here has 5 or less LM that are relatively more stable than the $n-1$ GM. Typically, there are more LM that fulfill this criterion where n is even. In the case of $n=17$, not even the GM is lower in energy than the $n=16$ GM, meaning it is highly likely that all $n=17$ clusters will fragment. For $n=10$, two structures lie to the left of the $n=9$ GM and both are bulk cuts composed of $n=4$ SBUs; the same holds for the two structures of $n=14$ that are to the left of the $n=13$ GM, but is not a trend that holds for all even- n candidate structures as for example $n=12$ has 5 structures to the left of the $n=11$ line, only one of which is a rocksalt cut.

More importantly, there are some n where only one structure is found to be both thermally accessible (i.e. much lower energy than other LM) and lower energy than the $n-1$ GM. These should prove to be good target structures to try and synthesize because confirming that only one structure is found in these cases would lend validity to the methodology here. Examples of this are $n=8, 10$ and 16 , all of which are bulk cuts and also magic number clusters. For $n=9, 12, 14, 18$ and 24 it is likely that multiple configurations will be found experimentally as their LM are very close to each other in energy. However, some degree of skepticism is warranted in the case of the $n=24$ result since it differed when a different functional was used; the hybrid functional result would suggest this is a further size with only one thermally accessible minimum and thus a good synthesis target structure.

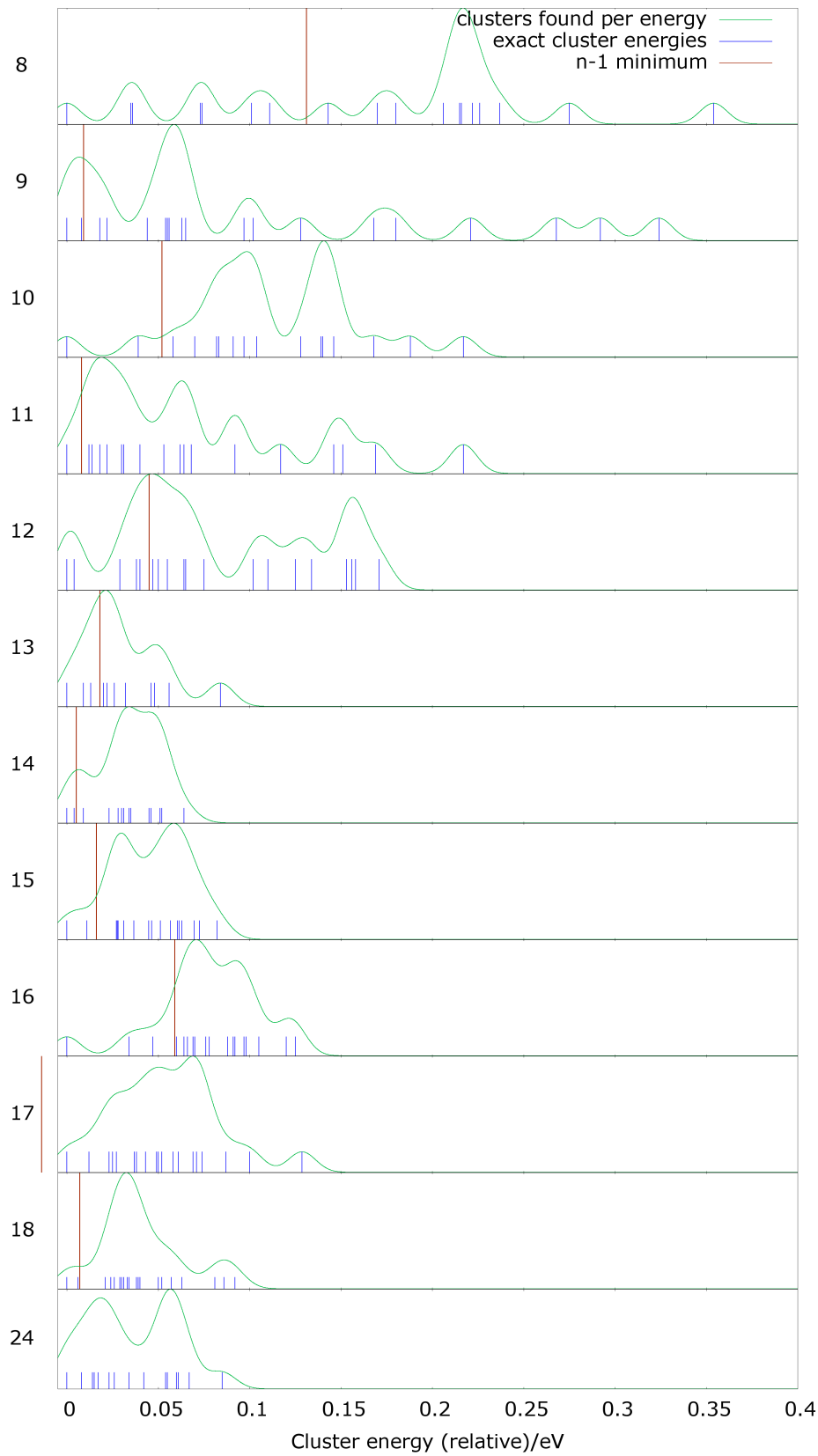


Figure 3.10: Density of LM for BaO clusters for $n = 8$ to 18 and 24 at 300K. Blue impulses indicate cluster energy per formula unit, green lines indicate smeared energies, and red divisions mark $n - 1$ cluster energies.

Investigating $n = 10$ in detail, only two structures are to the left of the red line: these are both structures composed exclusively of $n = 4$ SBUs, while the next lowest structure is composed of hexagonal barrel elements adjacent to each other. This is not universally the case; for example, for $n = 12$ and $n = 15$ both the rocksalt cut and the barrel are below the $n = 1$ GM in energy, with $n = 12$ also featuring some other structures that meet this criterion. Overall, these two structural motifs seem to both be favoured over alternatives, even if this holds more so for the $n = 4$ SBU than the $n = 6$ barrel shape.

Since some experiments use a source at room temperature, this plot has been re-done for 300K (Figure 3.10). It is clearly visible from this plot that while even more LM become thermally accessible for some sizes, $n = 8, 10$ and 16 remain sizes for which there is only one thermally accessible structure.

3.3.8 Convergence of the Evolutionary Algorithm

Being a nondeterministic method, there is no guarantee that the EA found all LM, and there is no obvious convergence criterion. However, by tracking whether new low-energy structures are found, it is possible to gain some confidence that all low-lying LM are present after a number of EA steps.

Figure 3.11 shows the top 10 structures found at each EA step for $n = 15$, one of the larger sizes of clusters investigated here and therefore one of the larger conformational spaces to explore. The black lines indicate energies of top 10 local minima, while the red line constitutes a running average energy of the top 10. What we can see from this is that the IP GM is found after less than 10 steps for this size, the second lowest after ~ 200 steps and all other LM are found after approx. 300 steps. The calculation was run for a total of 800 steps, which is more than twice what appears to be required and is therefore assumed to be a safe length of time to run the EA.

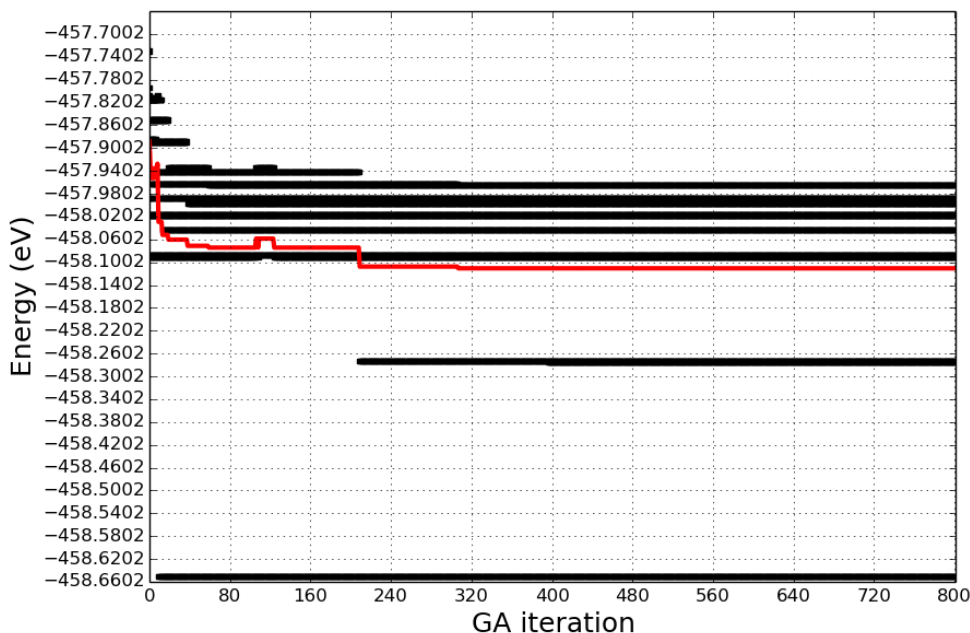


Figure 3.11: Top 10 structure as the EA progresses (and running average energy in red)

3.3.9 Change in energy rankings from IPs to DFT

For the example case of $n = 13$, energy rankings for IPs and DFT and the changes between them are plotted in Figure 3.12 in order to test the quality of our IP, i.e. to see if the IP landscape was sufficiently able to predict the GM or other low-lying LM from the top 20 structures alone. A number of the IP LM were found to be unstable on the DFT landscape and so collapsed to DFT LM already found by relaxing a lower energy IP LM.

On first glance, there appears to be a large discrepancy between the IP and DFT calculations as the much higher energy IP LM are missing from this map, i.e. this mapping is a small snapshot of a much larger energy landscape, it can be argued that the IP is *sufficiently good* to find structures which are close enough to the true LM that they will converge toward them: the goal is not to find exact LM, but rather to find structures within the potential wells of relevant LM. Taking the top 20 structures is clearly necessary for this size as the IP-ranked 20th-lowest LM became 3rd lowest in DFT. In particular, the IP suffers from predicting erroneous LM. A lot of structural diversity is lost by multiple IP structures converging to the same DFT LM, indicating that some DFT LM (here: especially the second-lowest LM, which was found five times) have particularly large wells.

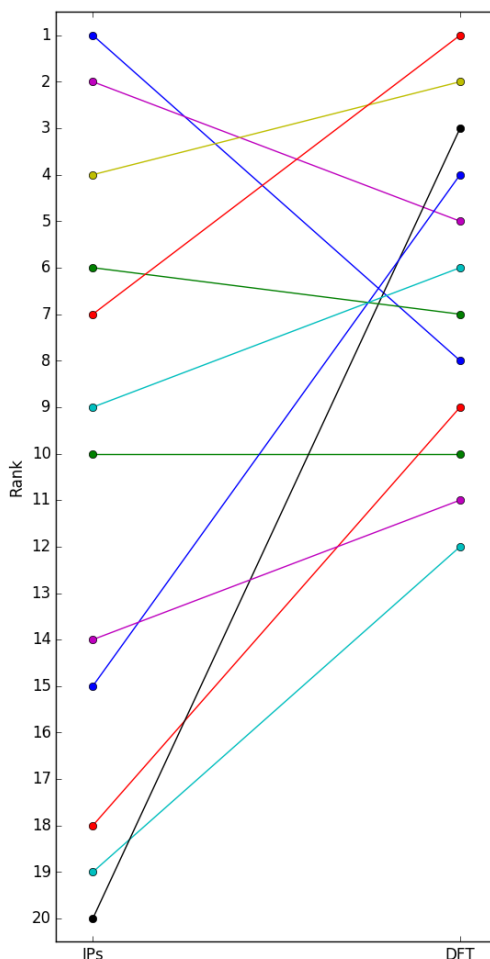


Figure 3.12: Relative energy rankings of IP (left) and DFT (right) structures of $n = 13$ clusters; where structures changed significantly during the DFT geometry optimisation, the line is still drawn.

The loss of structural diversity was worst for the chosen example of $n = 13$ and in general worse for structures with several low-lying LM so small structural changes are more likely to influence rank. Consequently, such problematic sizes are also those which are not recommended as synthesis targets. After this EA calculation on $n = 13$, two additional (rocksalt cut) structures were added manually. One of them was found to be 0.95 eV (0.073 eV per formula unit) above the GM in energy, while the other converged to the same second-lowest LM as several other structures, a non-cuboid structure.

In order to test how IPs performed for more important, relatively low energy sizes, the same procedure was repeated for $n = 16$. The result of this is shown in Figure 3.13. Notice that the top 3 DFT structures are found within the top 10 IP structures, with the worst change in rank being the 16th lowest IP structure which results in the 5th lowest DFT structure—that is to say, the IP performs much more favourably for this arguably more important case, $n = 16$ being the size which is preferred by several of the measures detailed above.

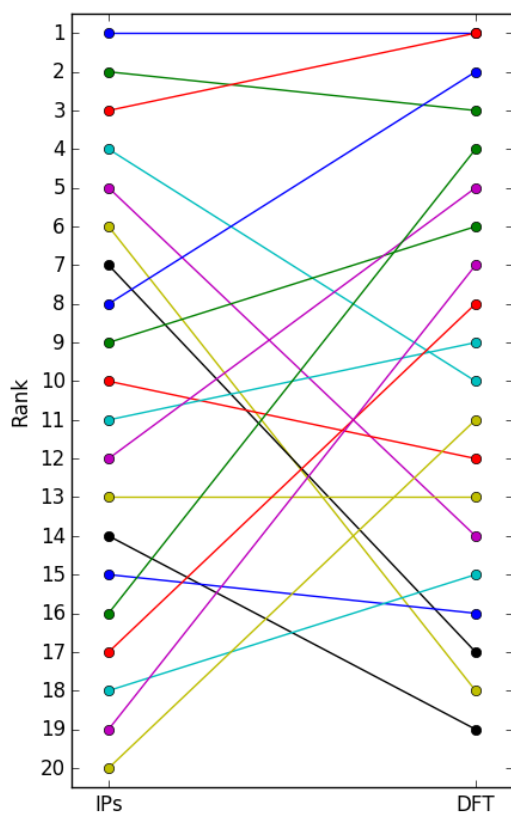


Figure 3.13: Relative energy rankings of IP (left) and DFT (right) structures of $n = 16$ clusters.

3.4 Summary and Conclusions

The structures and stabilities of $(\text{BaO})_n$ nanoclusters with $n = 1$ to 18 and 24 were investigated. It was found that clusters which adopted structures akin to cuboid cuts from the rocksalt (bulk) phase, or at least composed of $n = 4$ cuboid secondary building units were the most stable; this generally corresponds to even- n structures. It was also found that non-polar structures were favoured over polar ones, with the $n = 9$ cuboid rocksalt cut structure as well as the $n = 18$ polar $3 \times 3 \times 4$ -atom structure being disfavoured compared to $n = 8$ and 10, and the $6 \times 3 \times 3$ -atom $n = 18$ structure, respectively. On the other hand, the amorphous but less polar $n = 13$ GM is relatively lower in energy, while the other, polar, non-cuboids are in general higher energy than non-polar cuboids. Another trend found that is reflected in energies is that of coordination number; clusters composed of atoms with coordination numbers closer to that of atoms in the bulk phase, 6, were generally more stable than clusters with smaller average coordination numbers. In summary, structures which are relatively stable and thus deemed "magic number" sizes most likely to show up in mass spec in non-size-selected experiments are $n = 4, 6, 8, 10$ and 16.

In the next piece of analysis, these structures were further filtered by which of them have no additional LM close enough in energy to the GM that they would occur at 100 and 300K, respectively. At both temperatures, this narrows the best choice clusters down further to $n = 8, 10$ and 16. The GM of $n = 16$ is additionally exceptionally stable in terms of its NCE.

Given more computer resources, we could have examined larger clusters as well as reevaluating more IP LM using DFT. One other possible area of research is looking at these clusters of barium oxide with defects. In fact, ongoing work in our group is looking at these clusters with one barium atom replaced by lead. We hope that experimental work on these clusters will also emerge in the future.

Chapter 4

Clusters of Strontium, Calcium and Magnesium Oxide

4.1 Introduction

Barium oxide clusters have applications mainly as an imaging target to compare to experiment. In comparison, clusters of the smaller-cation alkali earth oxides have been investigated more frequently for more practical applications. Nanoclusters of these three oxides are promising for applications such as catalysis[9, 10, 18] and heavy metal capture[7]. This chapter will describe structures of strontium, calcium and magnesium oxide and their energy rankings, as well as comparing them to each other and barium oxide clusters to investigate the effect of cation size on structure. They will be presented in "reverse" order, from the bottom of the periodic table to the top, i.e. in the order strontium oxide – calcium oxide – magnesium oxide, as the cations become more and more dissimilar from the barium cation in this order.

4.2 Methods

In Chapter 3, I used an evolutionary algorithm in conjunction with interatomic potentials to elucidate structures of barium oxide nanoclusters. With these barium oxide

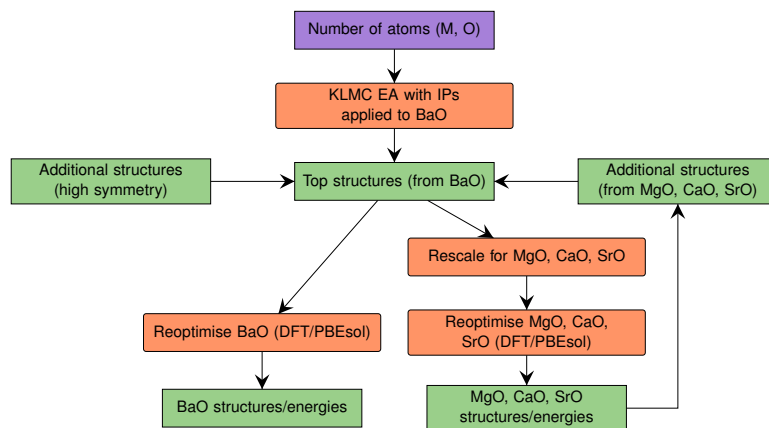


Figure 4.1: Steps in generating optimised structures and energy rankings for alkaline earth oxide nanoclusters.

structures[130] as a starting point, data mining, as implemented in KLMC, was used to scale down structures based on ionic radii as a simple way to transfer between potential energy landscapes of different compounds. Starting from these data-mined structures, geometry optimisations were performed using the two-step DFT approach in FHI-aims[112]: with a light basis set and convergence criteria first, and then with a tight basis set and convergence criteria to get more accurate geometries and energies. The flowchart from Figure 3.1, now expanded, includes steps to gain insight into $(\text{SrO})_n$, $(\text{CaO})_n$ and $(\text{MgO})_n$ cluster structures and is shown in Figure 4.1.

Similar data-mining approaches have been used to generate nanocluster structures of materials with wurtzite or sphalerite bulk phases[131] as well as bulk materials[132] such as alkali metal oxides[133]. They do not cover as much as conformational space as separate EA searches would, but can be sufficient to find the most relevant structures for synthesis targets. Here, the resulting structures of calcium and magnesium oxide especially will be extensively compared to other results for these clusters in order to confirm their veracity.

Dipole calculations were also carried out for $n = 18$ clusters in FHI-aims.[112]

4.3 Results

4.3.1 Structures and Energies of $(\text{SrO})_n$ clusters

Small Clusters ($n \leq 12$)

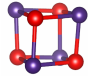

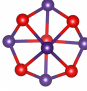
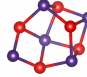
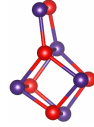
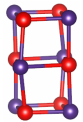
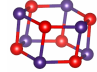
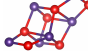
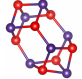
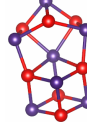
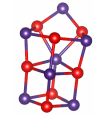
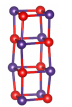
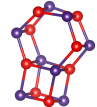
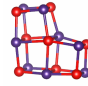
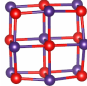
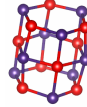
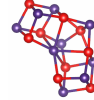
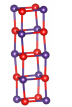
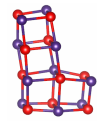
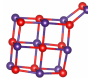
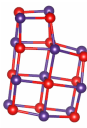
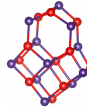
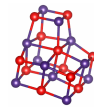
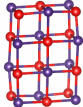
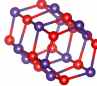
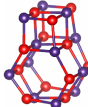
	1st	2nd		1st	2nd	3rd
n	4			5		
						
$\Delta E/\text{eV}$	0.0	3.520		0.0	0.058	0.064
n	6			7		
						
$\Delta E/\text{eV}$	0.0	0.349	2.461	0.0	0.065	0.175
n	8			9		
						
$\Delta E/\text{eV}$	0.0	0.519	0.583	0.0	0.429	1.143
n	10			11		
						
$\Delta E/\text{eV}$	0.0	0.502	0.965	0.0	0.035	0.252
n	12					
						
$\Delta E/\text{eV}$	0.0	0.627	0.770			

Table 4.1: Three lowest energy structures of $(\text{SrO})_n$ clusters for $n = 4$ to 12, as resulting from PBEsol geometry optimisations

Table 4.1 shows tentative top-3 lowest energy structures of small ($n = 4$ to 12) strontium oxide clusters. We will again be using the $n = 4$ cuboid structure as a SBU as a descriptor for structures of other, larger, clusters. The general trend for even- n clusters is the same as was found for barium oxide clusters: the GM are all cuboid rocksalt cuts, with some non-cuboid rocksalt cuts as additional LM. The $n = 4$ SBU can be found in even more LM than it was for $(\text{BaO})_n$ clusters, for example the third-lowest energy LM for $n = 8$ is an L-shape composed of $n = 4$ SBUs, and the third-lowest $n = 10$ LM is the cuboid rocksalt cut $n = 9$ GM with two atoms added to one corner.

For odd n , different structural motifs are observed and there is greater divergence from $(\text{BaO})_n$ structures. For example, the $(\text{SrO})_5$ GM has higher connectivity (16 bonds) than the $(\text{BaO})_5$ GM (15 bonds), and the 3-layered barrel appears in the top 3 for $(\text{SrO})_9$, with more barrel-like motifs and less amorphous structures overall. However, as with barium oxide clusters, the $n = 9$ GM is again the cuboid rocksalt cut. New here are two non-cuboid rocksalt cut structures for $n = 11$; the $n = 11$ GM is equivalent to the $n = 12$ GM with two atoms removed from one side, while the third-lowest $n = 11$ LM is a $3 \times 3 \times 3$ cuboid which has been cut diagonally along the (1 1 1) direction.

Large clusters ($13 \leq n \leq 18, n = 24$)

Table 4.2 shows the 3 lowest energy structures of the larger ($n = 13$ to 18 and 24) strontium oxide clusters. All even- n GM are again rocksalt cuts, with the $n = 14$ GM the only non-cuboid; while there is a cuboid available, it is formed of $2 \times 2 \times 7$ atoms and therefore heavily under-coordinated. While the cuboid rocksalt cuts discussed throughout only have (1 0 0) exposed surfaces, the $n = 14$ GM also features an exposed (1 1 0) surface.

There are more rocksalt cuts found for odd n . First, there are both the GM and 3rd-lowest LM for $n = 13$ rocksalt cuts which are $3 \times 3 \times 3$ cuboids with one corner atom removed. The $n = 13$ GM has oxygen as its central atom, and the 3rd-lowest LM strontium. The 0.76 eV energy difference may be because the GM structure has strontium

atoms at its corners and the angles around strontium atoms are larger than in the perfect cuboid, leading to a structure that is closer to spherical (which is assumed to be favoured); in comparison, when strontium is in the centre, the corner atoms are oxygen and therefore at acute angles. For a more in-depth discussion of bond angles and how they change with cation size, see Section 4.3.6. The exposed new surface is a (1 1 1) surface. The 2nd-lowest LM is actually an only slightly deformed version of the 3rd-lowest LM, with a ring opening up on the opposite side to the missing atom, again making the structure closer to spherical. The $n = 15$ GM is similar to the $n = 14$ one in that it has a (1 1 0) newly exposed surface compared to the perfect cuboids. From the following sections, it will become apparent that strontium oxide is unique in this strong preference for non-cuboid rocksalt cuts.

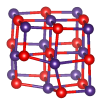
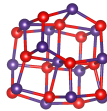
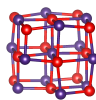
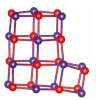
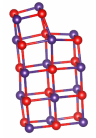
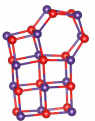
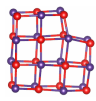
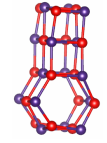
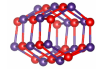
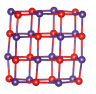
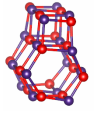
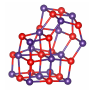
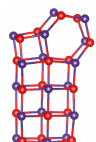
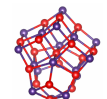
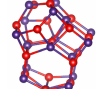
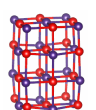
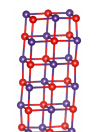
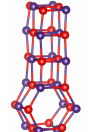
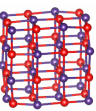
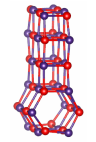
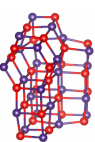
	1st	2nd	3rd	1st	2nd	3rd
n	13			14		
						
$\Delta E/\text{eV}$	0.0	0.684	0.759	0.0	0.112	0.155
n	15			16		
						
$\Delta E/\text{eV}$	0.0	0.394	0.687	0.0	0.997	1.250
n	17			18		
						
$\Delta E/\text{eV}$	0.0	0.408	0.424	0.0	0.535	1.232
n				24		
						
$\Delta E/\text{eV}$				0.0	1.921	2.810

Table 4.2: Three lowest energy structures of $(\text{SrO})_n$ clusters for $n = 10$ to 18 and $n = 24$, as resulting from PBEsol geometry optimisations

4.3.2 Structures of Calcium Oxide Nanoclusters

Small Clusters ($n \leq 12$)

Table 4.3 shows the structures of small clusters of $(\text{CaO})_n$ with $n = 4$ to 12. GM for even- n clusters are the same as they are for $(\text{BaO})_n$ and $(\text{SrO})_n$ clusters, with some variation in other low-lying LM compared to $(\text{BaO})_n$ and $(\text{SrO})_n$ clusters. In particular there are the

same non-cuboid rocksalt cut LM as were seen for $(\text{SrO})_n$, with only one new structure which also contains $n = 4$ SBUs in the third-lowest $n = 6$ LM. Odd- n GM are more open than they were in $(\text{SrO})_n$ for $n = 5$ and 7, while for larger sizes $n = 9$ and 11 the structures are largely the same as $(\text{SrO})_n$ ones, including the rocksalt cuts.

Large clusters ($13 \leq n \leq 18, n = 24$)

Table 4.4 shows structures of $(\text{CaO})_n$ clusters with $n = 13$ to 18 and 24. Almost all GM are again rocksalt cuts, with even- n GM being cuboids (where low-energy cuboids are feasible), and the same cuts as seen in $(\text{SrO})_n$ otherwise. Interestingly, even the $n = 14$ cuboid rocksalt cut makes it into the top 3 despite being heavily undercoordinated: as it is a $7 \times 2 \times 2$ -atom cuboid, atoms in this structure can have at most 4 bonds and are thus quite far away from bulk-like character. Similarly, for $n = 16$ and $n = 24$, additional non-cuboid rocksalt cuts are observed in the top 3; the $n = 16$ one is cut from the $3 \times 3 \times 4$ ($n = 18$) structure by removing one of the edges (compared to the $2 \times 4 \times 4$ $n = 16$ GM), while the $n = 24$ third-lowest LM is a highly irregular cut taken from the $3 \times 4 \times 5$ $n = 30$ cuboid cut (cf. the $n = 24$ GM is the $3 \times 4 \times 4$ cuboid cut). Additionally, a new structure featuring a barrel composed of 8-atom rings is observed as the third-lowest LM for $n = 17$. $n = 17$ is also the only cluster size where no rocksalt cut was found; however, all top 3 structures contain $n = 4$ SBUs and the top 2 structures feature them for the majority of their structure (28 and 30 out of 34 atoms, respectively).

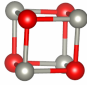


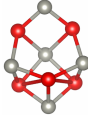
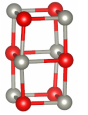
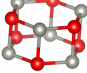

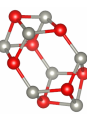


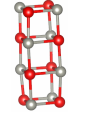
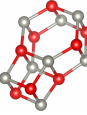
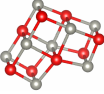
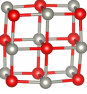
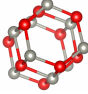
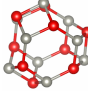
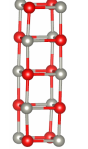

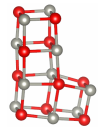
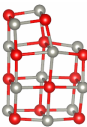
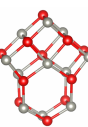
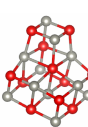
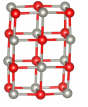
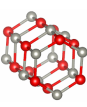
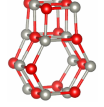
	1st	2nd	3rd	1st	2nd	3rd
n		4			5	
						
$\Delta E/\text{eV}$	0.0			0.0	0.010	0.097
n		6			7	
						
$\Delta E/\text{eV}$	0.0	0.378	2.033	0.0	0.341	0.357
n		8			9	
						
$\Delta E/\text{eV}$	0.0	0.570	0.625	0.0	0.443	1.452
n		10			11	
						
$\Delta E/\text{eV}$	0.0	0.531	0.566	0.0	0.073	0.314
n		12				
						
$\Delta E/\text{eV}$	0.0	0.657	0.843			

Table 4.3: Three lowest energy structures of $(\text{CaO})_n$ clusters for $n = 4$ to 12, as resulting from PBEsol geometry optimisations

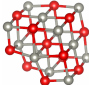
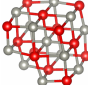
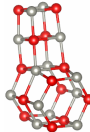
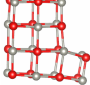

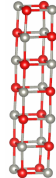
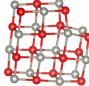
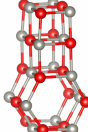
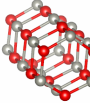
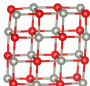
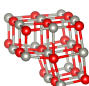
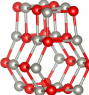
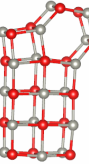
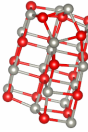
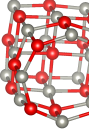
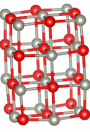
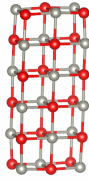
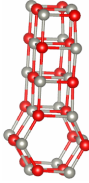
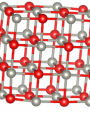
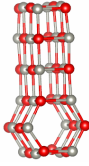
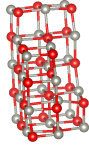
	1st	2nd	3rd	1st	2nd	3rd
n	13			14		
						
$\Delta E/\text{eV}$	0.0	0.616	1.274	0.0	0.184	0.598
n	15			16		
						
$\Delta E/\text{eV}$	0.0	0.585	0.724	0.0	1.006	1.042
n	17			18		
						
$\Delta E/\text{eV}$	0.0	0.211	0.316	0.0	1.015	1.761
n				24		
						
$\Delta E/\text{eV}$				0.0	2.583	3.493

Table 4.4: Three lowest energy structures of $(\text{CaO})_n$ clusters for $n = 13$ to 18 and $n = 24$, as resulting from PBEsol geometry optimisations

4.3.3 Structures of Magnesium Oxide Nanoclusters

Small Clusters ($n \leq 12$)

Finally, structures of magnesium oxide clusters do look significantly different from the other three; small clusters are shown in Table 4.5. For even n , only $n = 4$ and 10

have cuboid GM. Where available ($n = 6, 9$ and 12) the GM are barrels composed of 6-membered rings, and otherwise most GM are a combination of barrels and $n = 4$ SBUs.

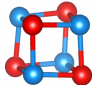

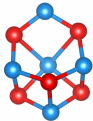
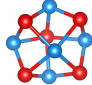
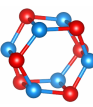
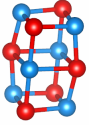
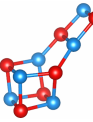
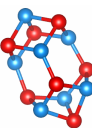
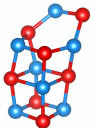
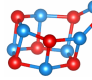
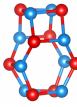
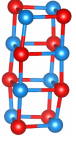
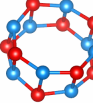
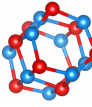
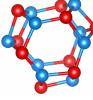
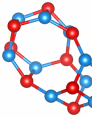
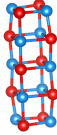
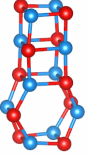
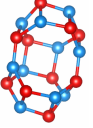
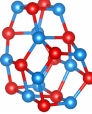
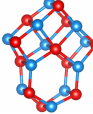
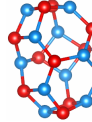
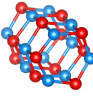
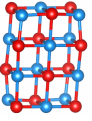
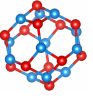
	1st	2nd	3rd	1st	2nd	3rd
n		4			5	
						
$\Delta E/\text{eV}$	0.0	1.090		0.0	0.607	1.152
n		6			7	
						
$\Delta E/\text{eV}$	0.0	0.267	2.403	0.0	0.505	0.515
n		8			9	
						
$\Delta E/\text{eV}$	0.0	0.048	0.481	0.0	0.823	2.173
n		10			11	
						
$\Delta E/\text{eV}$	0.0	0.188	0.345	0.0	0.012	0.027
n		12				
						
$\Delta E/\text{eV}$	0.0	0.365	0.597			

Table 4.5: Three lowest energy structures of $(\text{MgO})_n$ clusters for $n = 4$ to 12 , as resulting from PBEsol geometry optimisations

The cuboid rocksalt cuts all still appear in the top 3 (except for $n = 9$), but aren't GMs when more open barrel-incorporating structures are available. Also noteworthy is that many low-lying LM are bubbles (e.g. $n = 9$ and 12, as well as the $n = 8$ GM), that is they are even more open and under-coordinated compared to the rocksalt phase.

Large clusters ($13 \leq n \leq 18, n = 24$)

The three most stable structures for $(\text{MgO})_n$ clusters with $n = 13$ to 18 and 24 are shown in Table 4.6. There is less of a clear image on whether rocksalt cuts or barrels are preferred.

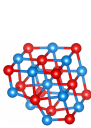
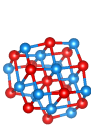
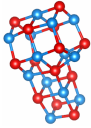
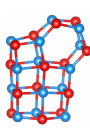
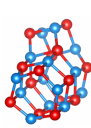
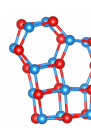
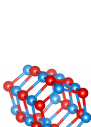
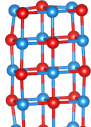
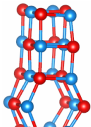
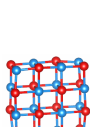
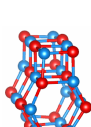
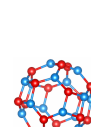
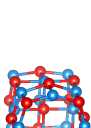
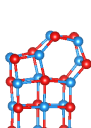
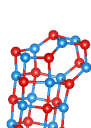
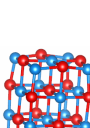
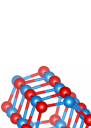
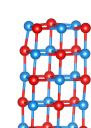
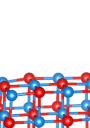
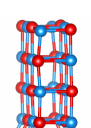
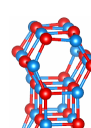
	1st	2nd	3rd	1st	2nd	3rd
n		13			14	
						
$\Delta E/\text{eV}$	0.0	0.342	0.753	0.0	0.055	0.136
n		15			16	
						
$\Delta E/\text{eV}$	0.0	0.323	0.576	0.0	0.385	1.830
n		17			18	
						
$\Delta E/\text{eV}$	0.0	0.683	0.743	0.0	0.833	1.097
n					24	
						
$\Delta E/\text{eV}$				0.0	2.242	2.530

Table 4.6: Three lowest energy structures of $(\text{MgO})_n$ clusters for $n = 13$ to 18 and 24, as resulting from PBEsol geometry optimisations

Rocksalt cut GMs are present for some sizes where barrels are not available, such as $n = 13$ and $n = 16$. However, where both rocksalt cuts and barrels are available ($n = 15$, $n = 18$ and $n = 24$) things become less clear. The preferred structure for $n = 15$ is the barrel, but for $n = 18$ the rocksalt cut is preferred – this means that the *bulk transition size*, the size beyond which bulk-like structures are preferred, is between those two. For $n = 24$, the GM is again the rocksalt cut, with the two next lowest LM structures

composed of barrels and $n = 4$ SBUs. Indeed, many other low-lying LM are rocksalt cuts (e.g. the second-lowest LM of $n = 13$ and 15 as well as the third-lowest for $n = 18$), barrels (second-lowest $n = 18$ LM) or combinations of the two (second- and third-lowest for $n = 14$; third-lowest $n = 15$; second-lowest $n = 16$, second- and third-lowest $n = 17$). The $n = 14$ GM is also a combination of $n = 4$ SBUs and one barrel. Other structures of note are the $n = 17$ GM, which is partially composed of $n = 4$ SBUs and partially of 8-membered rings, and was seen previously as a CaO LM, and the third-lowest $n = 16$ LM which is a bubble, and the only bubble found in these larger sizes.

4.3.4 Normalised Clustering Energies

Presented here are the normalised clustering energies[32, 128] (NCE) of clusters as a measure of relative stability of the clusters. As in Chapter 3, these are based on the following expression, which takes the difference of the energy of a cluster from that of the GM for $n = 1$. the linear stick configuration:

$$NCE(n) = \frac{E(n)}{n} - E(1)$$

This provides the stabilisation energy gained by each cluster to form from a bath of $n = 1$ units. A lower NCE means more stabilisation. Only GM energies are discussed as the data for GMs is the most relevant for applications such as guiding experiment.

The NCEs for GM clusters of sizes $n = 4$ to 18 are shown in Figure 4.2.

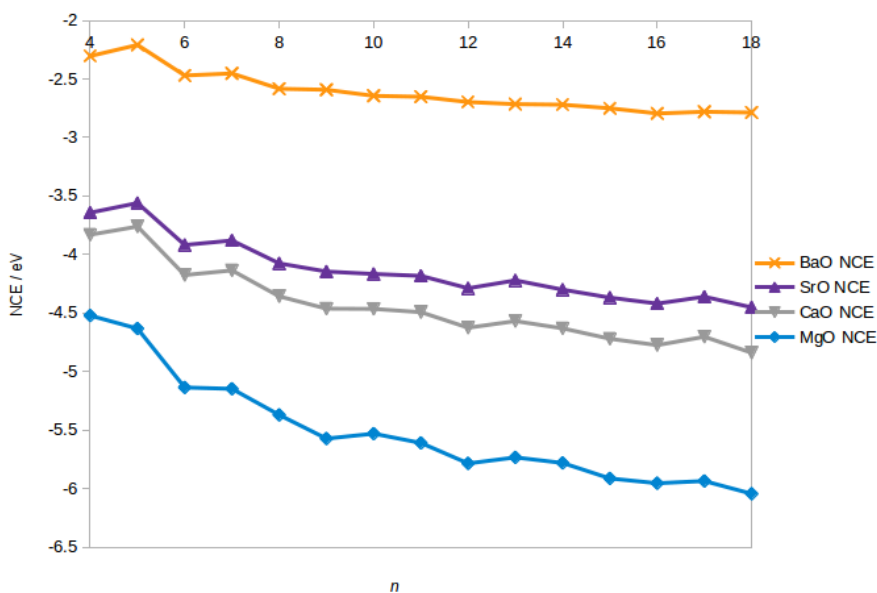


Figure 4.2: NCEs for GM clusters of all 4 compounds, as resulting from PBEsol calculations.

The first obvious trend, as reported earlier for barium oxide, is that the NCEs of nanoclusters decrease with an increase in cluster size, toward the bulk limit. A second observation from the overall plot is that NCEs increase with cation size: this is expected since a smaller cation is associated with stronger bonding and thus clustering is more energetically favourable. The difference between the average NCE for all cluster sizes is larger between BaO and SrO than it is between SrO and CaO, or between CaO and MgO, and by far the smallest between SrO and CaO. The ratios for averages, that is taking the mean NCEs of all GM clusters and then comparing them to the BaO value, are 1.00:1.58:1.70:2.11 for BaO:SrO:CaO:MgO. Corresponding ratios for the bulk generalised normalised clustering energy (gNCE) are 1.00:1.38:1.51:1.88. One can infer from this that the NCEs of $(\text{MgO})_n$ clusters are closer to its bulk value gNCE at these sizes. NCEs of $(\text{MgO})_n$ also approach the bulk value most quickly (in that larger size clusters have markedly lower NCEs), while NCEs of $(\text{BaO})_n$ clusters approach its bulk gNCE most slowly. Indeed, the averages of NCEs of these cluster sizes are between 73 and 75% of bulk values for SrO, CaO and MgO while they are 65% of the bulk value for BaO. Similarly, the $n = 18$ NCEs are between 80 and 81% of bulk values for SrO, CaO and MgO

and much lower, at 70% of the bulk value for BaO. This confirms that NCEs of $(\text{BaO})_n$ clusters converge much more slowly toward the bulk limit compared to very similar values for the three other alkali earth metal oxides.

When looking at NCEs of individual clusters, we can see that the plots for SrO and CaO follow quite similar progressions with very similar features. For example, NCEs for $n = 5$ are the highest in both compounds, and $n = 16$ ones are exceptionally low compared to similar sizes. These features are also present in the BaO plot, but much less pronounced: the BaO NCE plot has fewer features with smaller differences in NCEs between different cluster sizes. This can be partially attributed to the fact that the values of the NCEs themselves are smaller by a factor of more than 1.5 compared to the other three compounds. The graph of NCEs as a function of size for MgO has some features that differ, mirroring the trend in GM structures. Structures with notably low NCEs include $n = 6, 9, 12$ and 16 , again going from barrel shapes to a cuboid as clusters grow larger.

Since it is so notable how close NCEs of calcium and strontium oxide clusters are, and we know that their ionization energies[82] are also very close to each other, the same plot has been repeated, but reporting $\frac{\text{NCE}}{\text{Ionization Energy}}$ —this is shown in Figure 4.3. We immediately notice from this that values for MgO, CaO and SrO are largely the same, with BaO values being far less negative. The most ready explanation for this is that relativistic effects change bonding in BaO, an effect that has been previously observed in other cases[134, 135]. Comparing the three similar plots for MgO, CaO and SrO, it is apparent that some features are different in the case of MgO; for example, $n = 10$ is a maximum for MgO but not for CaO or SrO.

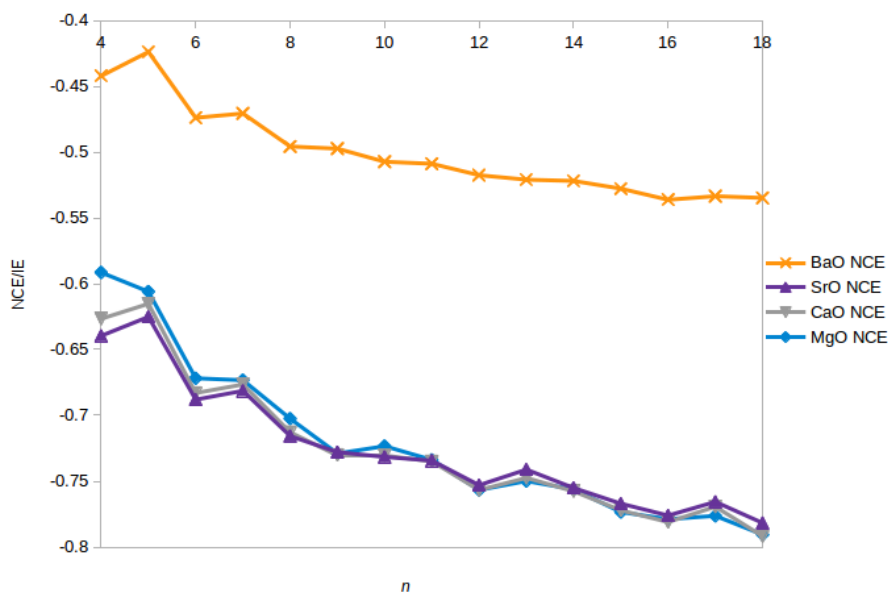


Figure 4.3: NCE/IE for clusters of all 4 compounds, as resulting from PBEsol calculations.

4.3.5 Second-Order Energy Differences

Second-order energy differences, ΔE , give a measure of stability of a cluster size relative to neighbouring sizes. The second-order energy differences are discussed here again and, as in Chapter 3 defined as

$$\Delta E = E(n) - \frac{1}{2}(E(n+1) + E(n-1))$$

where ΔE is the second-order energy difference and $E(n)$ is the energy of the GM of size n . These give a measure of how stable a GM cluster is compared to its nearest neighbours in size; a negative second-order energy difference corresponds with a more relatively stable cluster.

For reference, all second-order energy differences are shown in Table 4.7.

Second-Order Energy Differences for BaO, SrO and CaO clusters

Figure 4.4 shows second-order energy differences for the GM of BaO, SrO and CaO clusters on one plot. Cluster sizes with negative second-order energy differences were

$n / \Delta E/\text{eV}$	MgO	CaO	SrO	BaO
5	0.1962	0.2421	0.2202	0.1781
6	-0.2460	-0.2273	-0.1981	-0.1390
7	0.1059	0.1311	0.1169	0.0739
8	-0.0106	-0.0583	-0.0630	-0.0610
9	-0.1221	-0.0515	-0.0244	0.0217
10	0.0609	0.0127	-0.0023	-0.022
11	0.0477	0.0524	0.0450	0.0187
12	-0.1134	-0.0946	-0.0868	-0.0137
13	0.0498	0.0593	0.0737	-0.0065
14	0.0421	0.0134	-0.0060	0.0128
15	-0.0454	-0.0173	-0.0082	0.0068
16	-0.0301	-0.0628	-0.0552	-0.0291
17	0.0639	0.1041	0.0753	0.0103

Table 4.7: Second-order energy differences for GM cluster energies of sizes $n = 5 - 17$.

similar across the three, so ball-and-stick models only of representative SrO structures are overlaid on the plot.

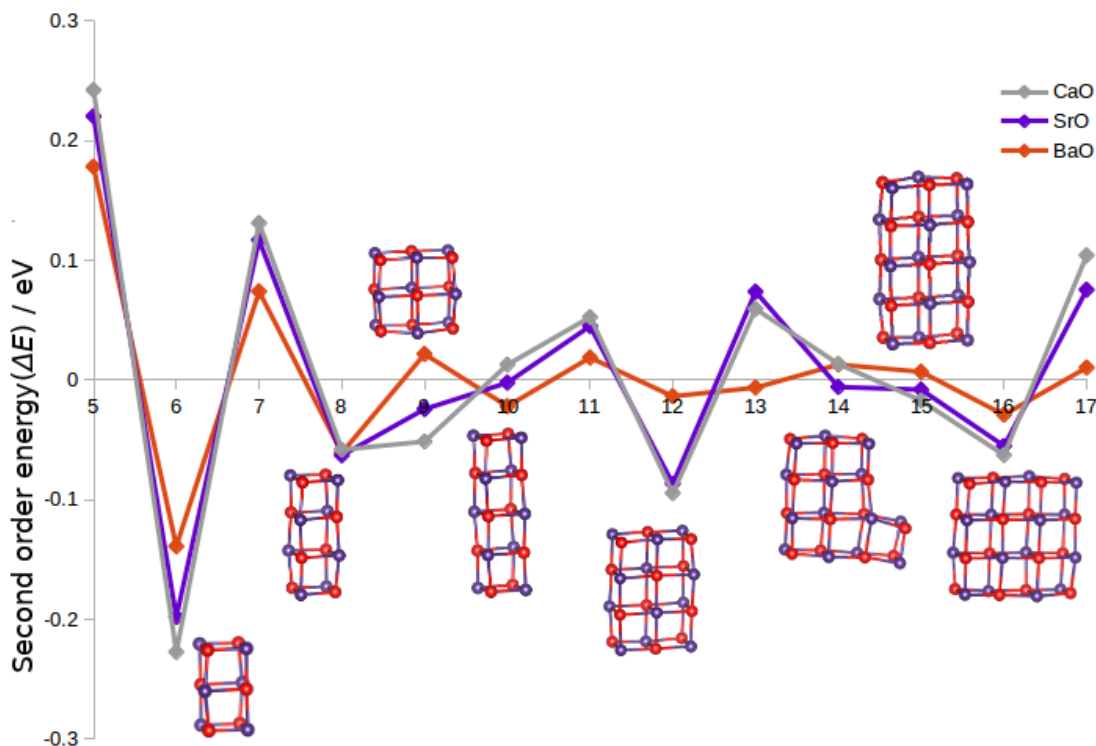


Figure 4.4: Second-order energies of BaO, SrO and CaO GM clusters ($n = 5$ to 17). Ball-and-stick models are shown for those clusters where the second-order energies are negative, and representative SrO structures.

All stable cluster sizes are rocksalt cuts. Second-order energies are markedly higher in magnitude for CaO and SrO than they are for BaO, perhaps related to stronger bonding in these two compounds. Exceptionally low second-order energies are found for all three $n = 6, 8$ and 16 clusters. Additionally it is found that for SrO and CaO, the $n = 12$ clusters also have very low second-order energies, i.e. they are exceptionally stable. This appears to go hand in hand with an exceptionally *less stable* $n = 13$ structure, which for SrO and CaO is a rocksalt cut with a "missing corner". There are some other differences: The $n = 9$ structure, which has a positive second-order energy in the case of $(\text{BaO})_9$ has negative second-order energy differences for the other two and in fact these second-order energies decrease with a decrease in cation size – this will become relevant later on, when we consider polarity of these clusters and polarisability of the cations. As $n = 9$ second-order energies straddle zero, the second-order energy of $n = 10$ clusters shows the reverse of this behaviour: it increases with a decrease in cation size. Similarly to the $n = 9$ case, the second-order energy of the (also polar) $n = 15$ cluster decreases with a decrease in cation size and is only negative for SrO and CaO. Using second-order energies as the criterion, magic number clusters of both are $n = 6, 8, 12$ and 16.

Second-Order Energy Differences for MgO clusters

Second-order energy differences of magnesium oxide clusters are shown in Figure 4.5. This is separated from the three other compounds because the general features of the plot in this figure, as well as the structures of low second-order energy GM of magnesium oxide clusters, are sufficiently different that it warrants its own plot.

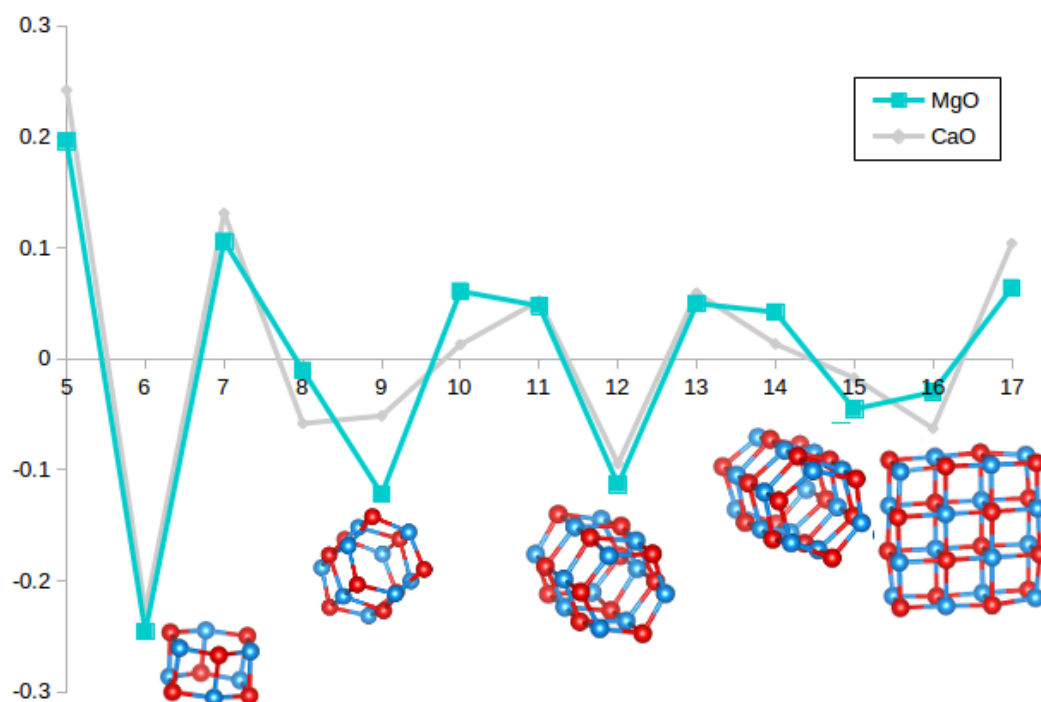


Figure 4.5: Second-order energies of MgO clusters ($n = 5$ to 17), overlaid with the second-order energies of CaO clusters to highlight the difference.

For these MgO clusters, generally every third cluster has a markedly negative second-order energy: $n = 6, 9, 12$ and 15 are all exceptionally stable and therefore magic number clusters, with GM structures that are barrel-shaped. However, $n = 16$ also has a second-order energy which is negative and is thus also a magic number cluster. The fact that both $n = 15$ and $n = 16$ have a negative second-order energy may indicate that the bulk transition probably happens in this size range.¹ The $n = 8$ second-order energy is also *slightly* negative; this indicates that structures which incorporate 6-membered rings might be generally preferred by MgO at small sizes, even where they are not "pure" barrel structures. Overall, this plot might look similar to those for BaO, SrO and CaO because $n = 6, 12$ and 16 are minima; however it is different because $n = 9$ and 15 are also clear minima and the underlying structures are barrels, not rocksalt cuts.

¹Together with the data for larger clusters found by Chen et al[58], it appears that this is much less well delineated; the $n = 21$ GM is again a barrel shape, possibly because the cuboid rocksalt cut is polar.

4.3.6 Total Dipole Moments of Clusters

Does the dipole moment play a further role in relative stabilities of cuboid rocksalt cuts at sizes $n = 9, 15$ and 18 ? For sizes $n = 9$ and 15 , there is only one possible cuboid configuration each: these configurations are polar because they have 3×3 - and 3×5 -atom layers, respectively. These layers will always have either one more cation or one more anion, leading to charges on the layers and therefore an overall dipole. Based on second-order energies previously discussed, these configurations become more stable the smaller the cation is. In the case of $n = 18$, there are two possible rocksalt cut configurations which are (meta)stable: the $6 \times 3 \times 2$ -atom configuration is non-polar but has a relatively high surface area and fewer bonds (a total of 69), while the $4 \times 3 \times 3$ -atom configuration has a total of 71 bonds and less surface atoms, but is polar because of its 3×3 -atom faces. This configuration is more stable for MgO, CaO and SrO, but less stable than the alternative for BaO.

When using a model of formal point charges for ions, the distance between layers is paramount in determining the magnitude of the dipole of a cluster: with charges in individual layers being the same across all compounds, a larger distance between layers would lead to a greater dipole. Thus, one would naïvely expect the dipole moment to be greatest for BaO and smallest for MgO. To look into this more, dipole moments for the $4 \times 3 \times 3$ -atom configuration of all four compounds were calculated. These are reported in Table 4.8.

Cluster	(MgO) ₁₈	(CaO) ₁₈	(SrO) ₁₈	(BaO) ₁₈
Dipole moment/ D	16.2	14.9	13.7	6.0

Table 4.8: Dipole moments of $n = 18$ $4 \times 3 \times 3$ cuboid clusters of MgO, CaO, SrO and BaO as calculated using the PBEsol functional in FHI-aims

Contrary to the initial assumption, the dipole moment for the $n = 18$ polar cuboid configuration actually decreases with increasing cation size. The change in expected behaviour is caused by the relative ability of the cations to reduce the total expected dipole.

As we go down the group, cations become more polarisable and will compensate for the dipole by deforming their electron cloud. In fact, polarisability of cations increases down the group as the valence electrons are further away from the nuclei, almost doubling each time, with Ba^{2+} cations having by far the largest polarisability[136], so its orbitals can deform more easily and more mixing will occur. Thus, the dipole across the cluster is more readily reduced in the case of barium oxide clusters compared to the other alkaline oxide clusters of the same configuration. Therefore, the relative stability of these structures is not directly related to dipole, but instead might be related to an energetic penalty imposed because of this polarisation effect on the cations. However, other factors should be considered: perhaps the penalty for under-coordinated atoms is lower in the case of $(\text{BaO})_n$ clusters, for example.

Cation-anion-cation bond angles

The degree of polarisation can be related to the acuteness of cation-anion-cation (M–O–M) bond angles in nanoclusters, as reported for clusters of ZnO and LaF_3 [37, 91]. M–O–M bond angles for $n = 2$ to 4 GM structures were compared to those found in the corresponding idealised shapes: 90° for the $n = 2$ square and $n = 4$ cube, and 120° for the $n = 3$ hexagon. The results are presented in Figure 4.6

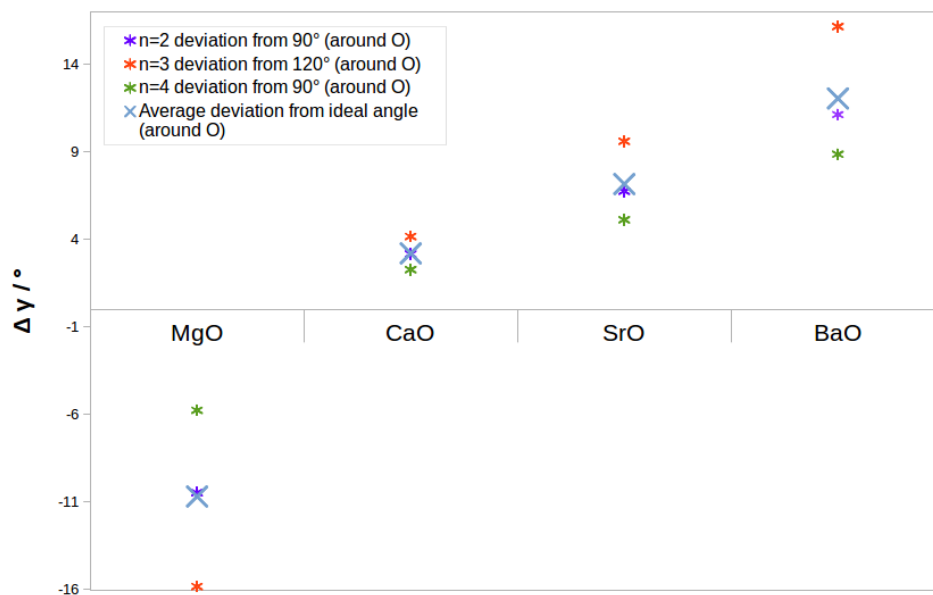


Figure 4.6: Deviation from ideal M–O–M angle for $n = 2$ to 4 DFT $(MO)_n$ GM configurations compared to perfectly symmetric squares, hexagons and cubes, where M labels group II cations.

In general, we see the largest deviation from idealised angles for $n = 3$, where the angle is largest, and the smallest deviation for $n = 4$ where the angle is most constrained. For magnesium oxide, Mg–O–Mg angles were smaller than the idealised angles. For all three others, the angles were larger than the idealised one; in the case of CaO, all three angles deviated by 2 to 4°, with these M–O–M angles growing larger (and consequently O–M–O angles becoming smaller) as the size of cation increases.

This result is as expected based on the effect of polarisabilities. For magnesium oxide, polarisability of the anion is much higher than that of the cation, and therefore the anion is more likely to form an acute angle. As the cation size is increased, the relative polarisability of the cations increases, and therefore larger cations are more likely to move out than smaller ones. This effect is most even in CaO, i.e. there is little puckering either way in CaO.

4.3.7 Coordination Number

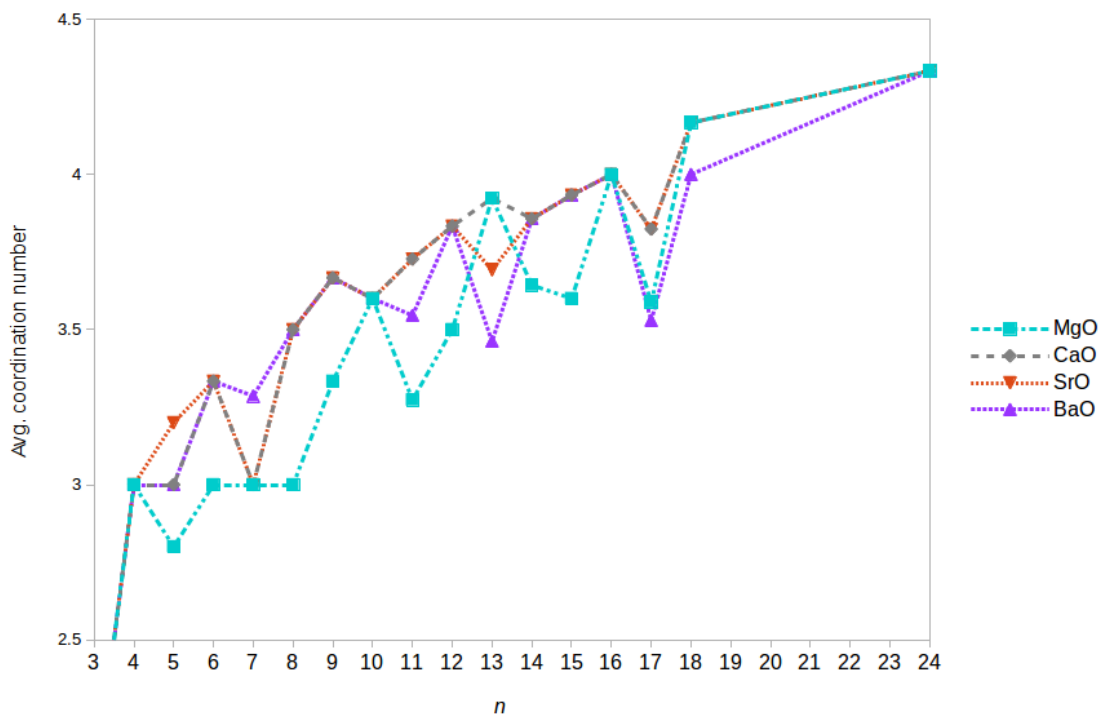


Figure 4.7: Coordination numbers of alkali earth oxide cluster GM for $n = 1$ to 18 and 24, as calculated with PBEsol; bond length cutoffs selected appropriately for each compound.

Is there a correlation between coordination number and cation type? Average coordination numbers per atom of all GM clusters are shown in Figure 4.7. For all four compounds, average coordination number generally increases with nanocluster size, to slowly approach the bulk limit of 6 as expected. However, at these nanocluster sizes the average coordination number is still quite far away from 6, with the highest, the $n = 24$ value, still below 4.5.

In general, a similar trend to that of BaO reported earlier – higher coordination numbers where cuboid rocksalt cuts are found – is also seen in SrO and CaO, with no clear trend otherwise. Coordination numbers are generally smaller for MgO clusters below size $n = 16$, as expected from their structures.

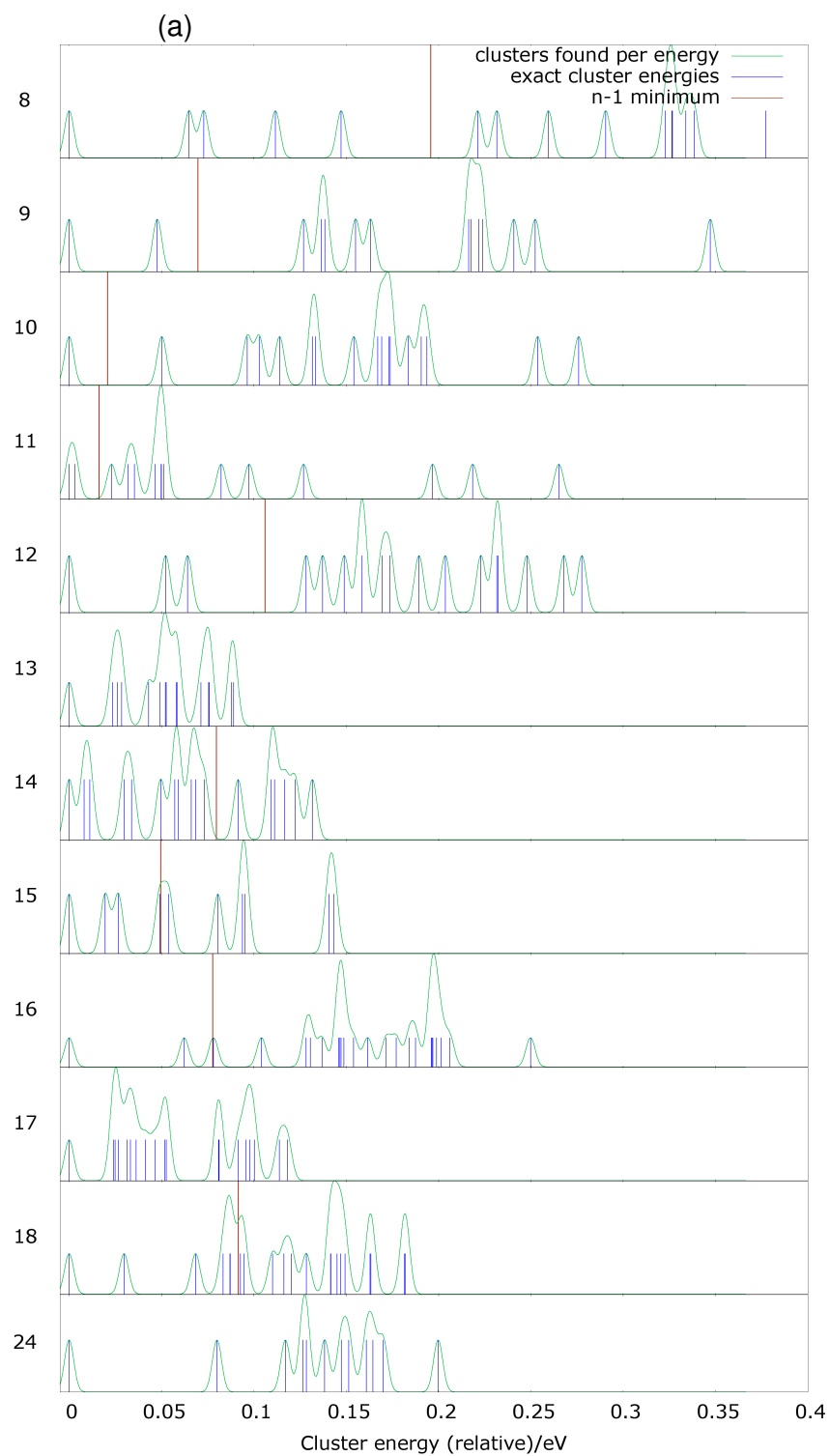
4.3.8 Energy Density of Structures

Compared to barium oxide clusters, all three other alkali earth oxide had a larger number of synthesis target cluster sizes where only one unique structure is expected to be stable for that size. Density of structure plots at 100K and 300K are presented in the following subsections.

Strontium Oxide nanoclusters

Figure 4.8 shows the density of structures for strontium oxide clusters of sizes $n = 8$ to 18 and 24 at 100K (1) and 300K (2). First, cluster sizes which are less stable than the next smaller size can be discarded immediately as they are unstable to decomposition. In this case, this criterion is met by $n = 17$, which was also less stable than $n = 16$ per formula unit in barium oxide, and $n = 13$. Therefore, these two can be discarded immediately. If there is only one impulse under the leftmost peak in Figure 4.8, it means that only one structure is likely to be found at a given temperature. At 100K, most of the remaining sizes are actually ones where only one structure is likely to be found: this is true for $n = 8, 9, 10, 12, 15, 16, 18$ and 24. Perhaps these would be good targets for a larger study at this temperature. At 300K, things look slightly different – $n = 8, 9, 12, 16$ and 24 remain synthesis targets². The $n = 10$ structure is found to be very close in energy to the $n = 9$ one and thus it is possible that it could decompose at this temperature. For $n = 18$, there are now two thermally accessible structures and for $n = 15$ three: the second-lowest $n = 18$ minimum is the non-polar rocksalt cut while for $n = 15$, the other structures actually both feature a barrel motif, with the third-lowest LM the barrel structure which is the GM for $(\text{MgO})_{15}$. All clusters which fulfill the criterion of only one structure being found are cuboid rocksalt cuts.

²Cluster sizes which are (a) more stable than the next smaller cluster size, and (b) where only one structure is likely to be found in experiment



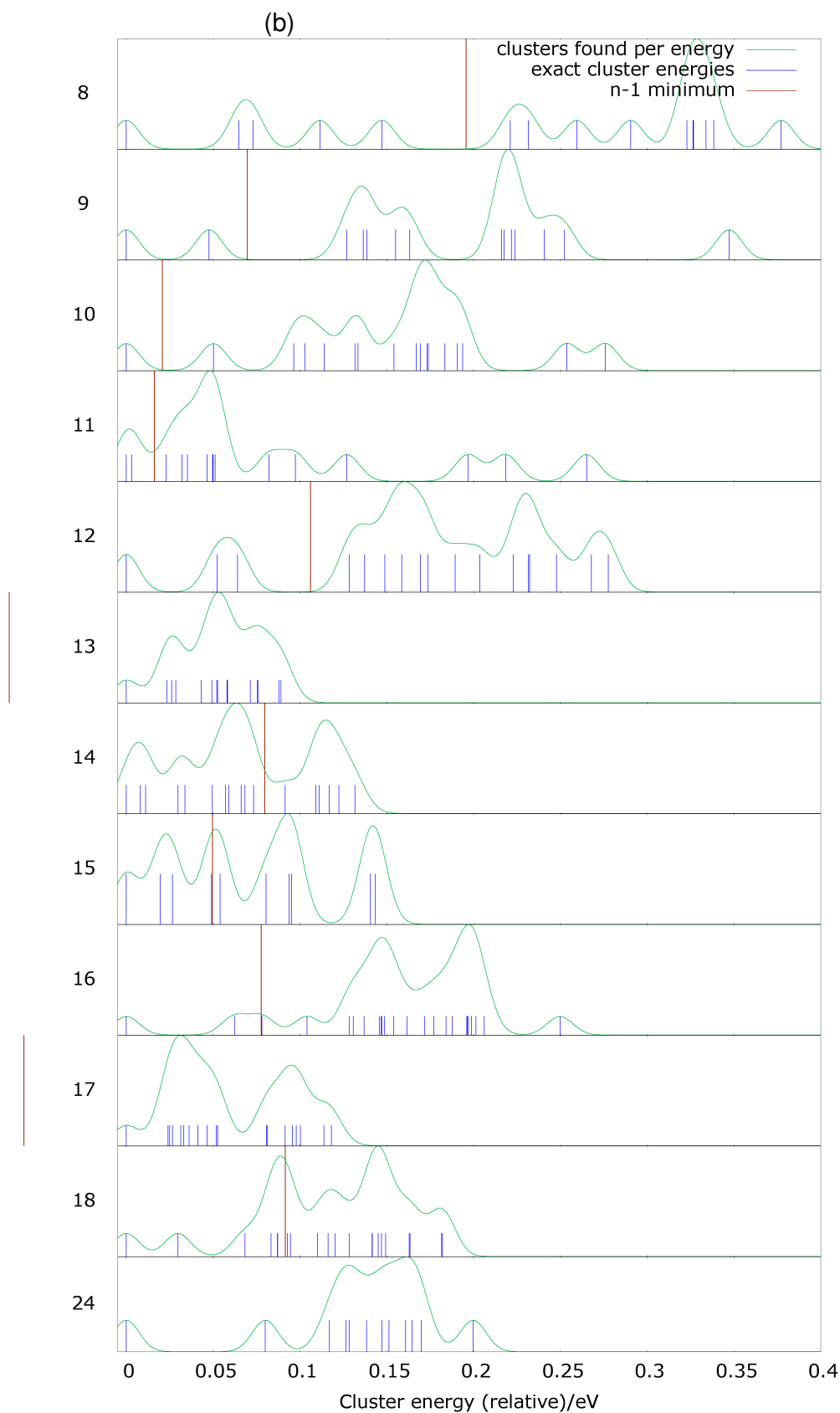
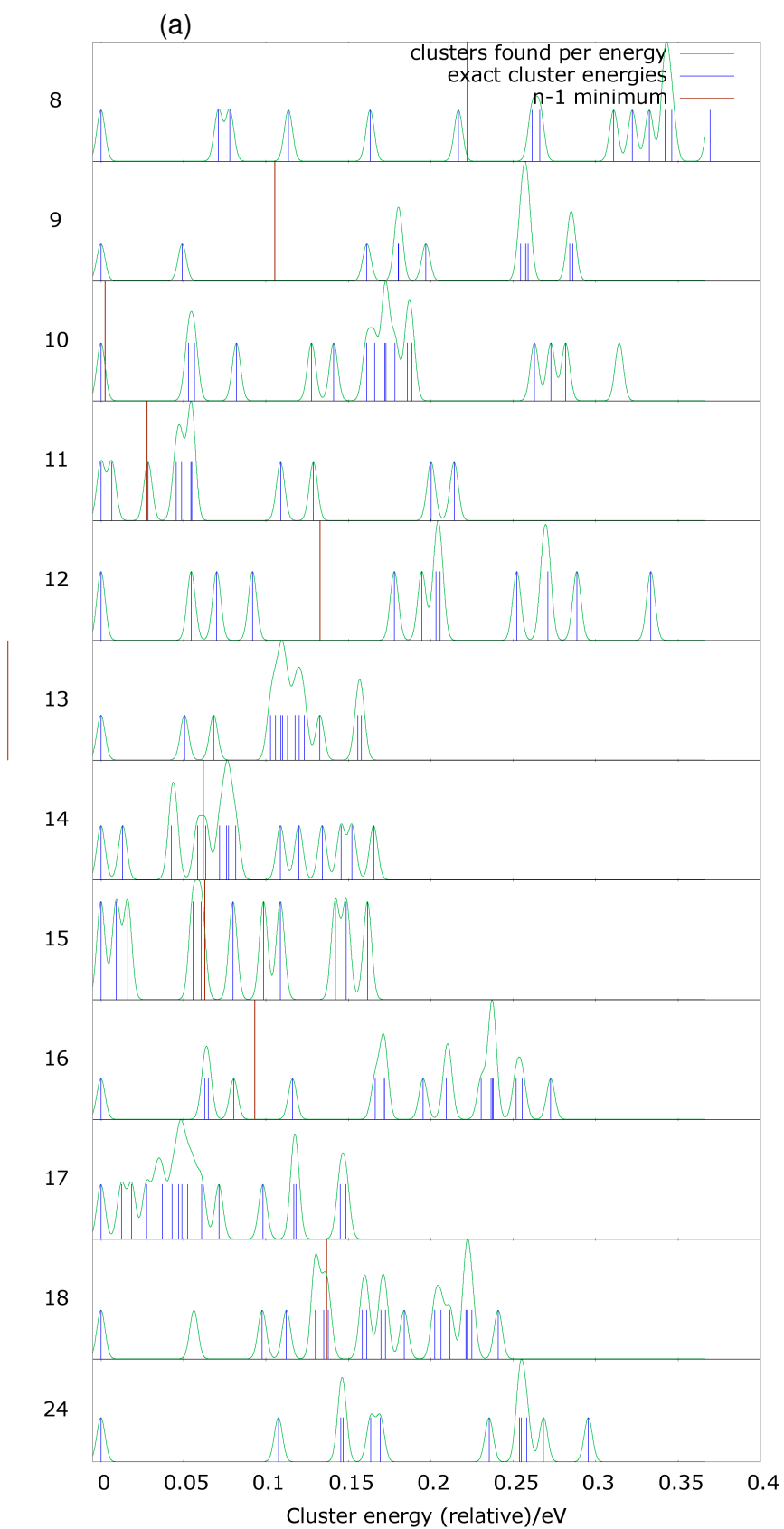


Figure 4.8: Density of LM for SrO clusters for $n = 8$ to 18 and 24 at 100K (a) and 300K (b). Blue impulses indicate cluster energy per formula unit, green lines indicate smeared energies, and red divisions mark $n - 1$ cluster energies.

Calcium Oxide nanoclusters



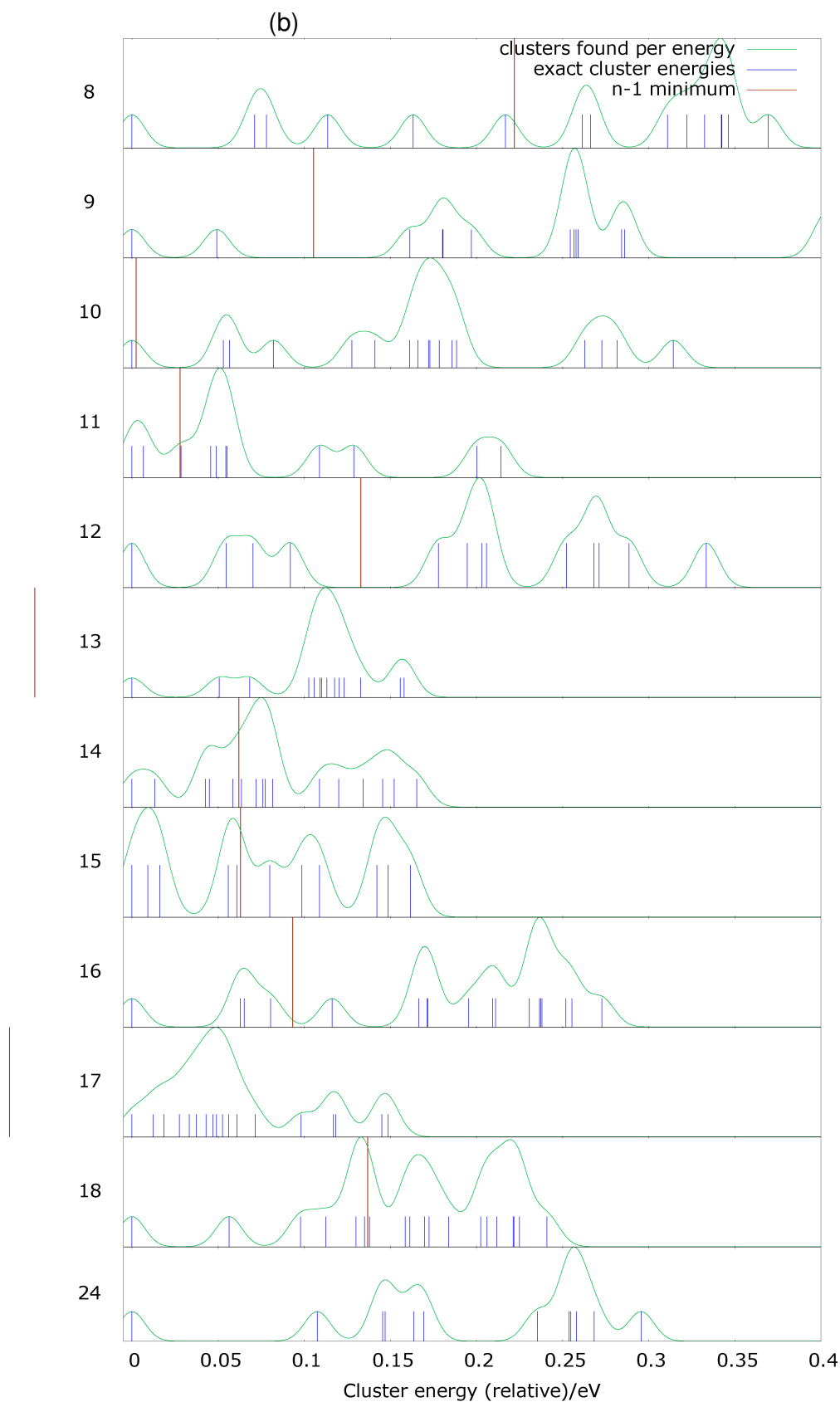
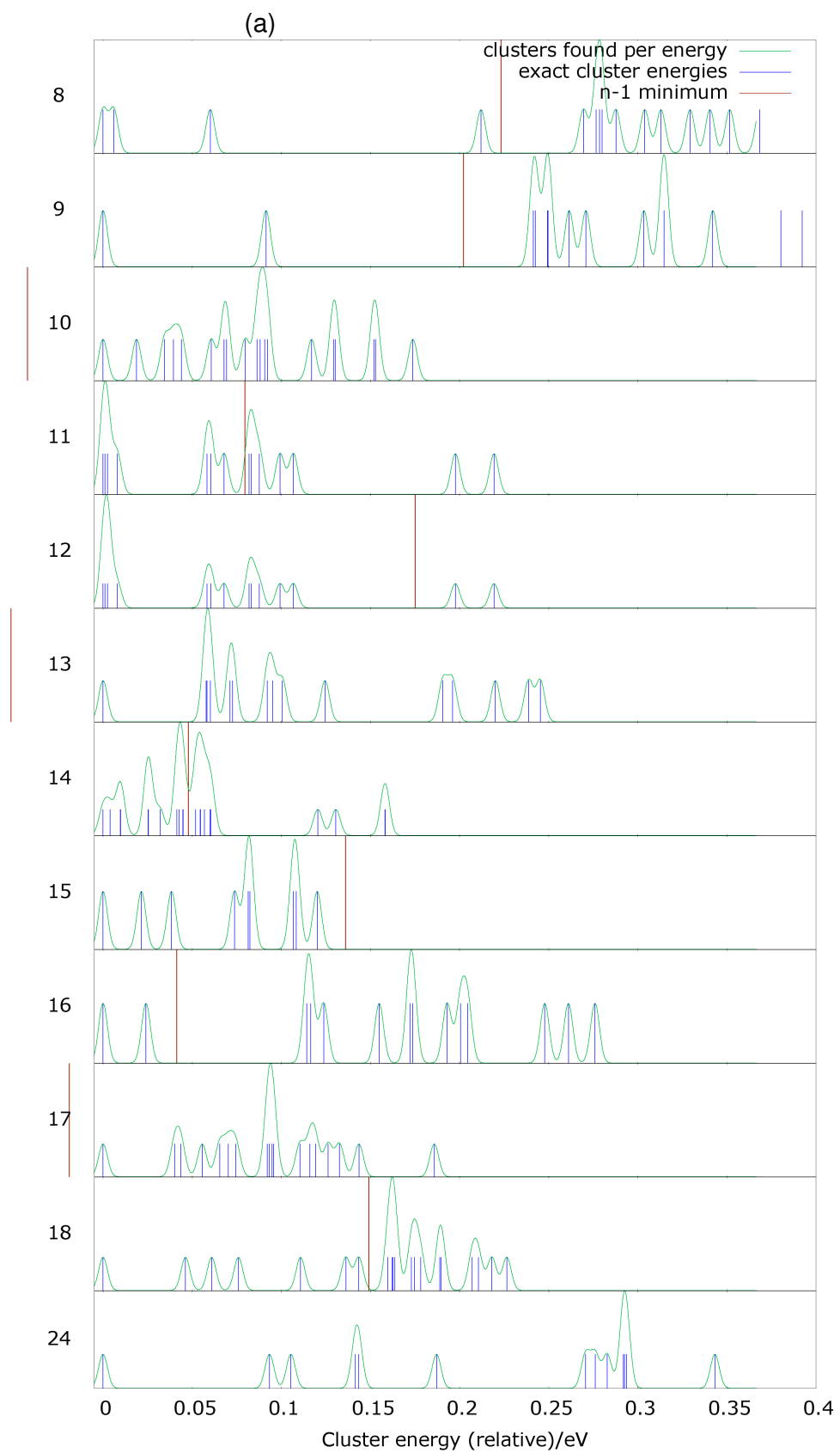


Figure 4.9: Density of LM for CaO clusters for $n = 8$ to 18 and 24 at 100K (a) and 300K (b). Blue impulses indicate cluster energy per formula unit, green lines indicate smeared energies, and red divisions mark $n - 1$ cluster energies.

In Figure 4.9 we can see the density of structures for calcium oxide clusters of sizes $n = 8$ to 18 and 24 at 100K (first figure) and 300K (second figure). Again, $n = 17$ and 13 GM are higher in energy per formula unit than $n = 16$ and 12 ones, respectively, and therefore should be discarded as unstable. Additionally, the $n = 10$ GM is almost identical in energy to the $n = 9$ one, again making decomposition a possibility. At 100K, of the other sizes, ones where only one structure is likely to be found at 100K are: $n = 8, 9, 12, 14, 16, 18$ and 24. At 300K, $n = 8, 9, 12, 16, 18$ and 24 remain – increasing the temperature results in the only non-cuboid becoming relatively less stable enough that an additional structure is likely to be found for its size. Compared to $(\text{SrO})_n$ clusters, the differences are that there is one less cuboid rocksalt cut (the polar $n = 15$ one) fulfilling the criteria whilst one non-cuboid becomes a valid synthesis target at 100K.

Magnesium Oxide nanoclusters

Figure 4.10 shows the density of structures for magnesium oxide clusters of sizes $n = 8$ to 18 and 24 at 100K (left) and 300K (right). Based on this, three sizes can be discarded for being less stable than the next smaller size ($n = 10, 13$ and 17). Of the remaining sizes, valid synthesis targets at 100K are $n = 9, 15, 16, 18$ and 24 and all of these except $n = 15$ and 16 remain viable targets at 300K. These are barrels below the bulk transition size at $n = 15 - 16$ and cuboid rocksalt cuts above it. At the bulk transition size, the second-lowest energy clusters are the rocksalt cut for $n = 15$ and a structure featuring barrels for $n = 16$; since we expect both motifs to be similar in energy at these sizes, it is unsurprising that these sizes would yield significant amounts of both structures at 300K. A perhaps more surprising result is $n = 12$, where several structures are very low energy. This will be looked at in more detail in Section 4.3.9.



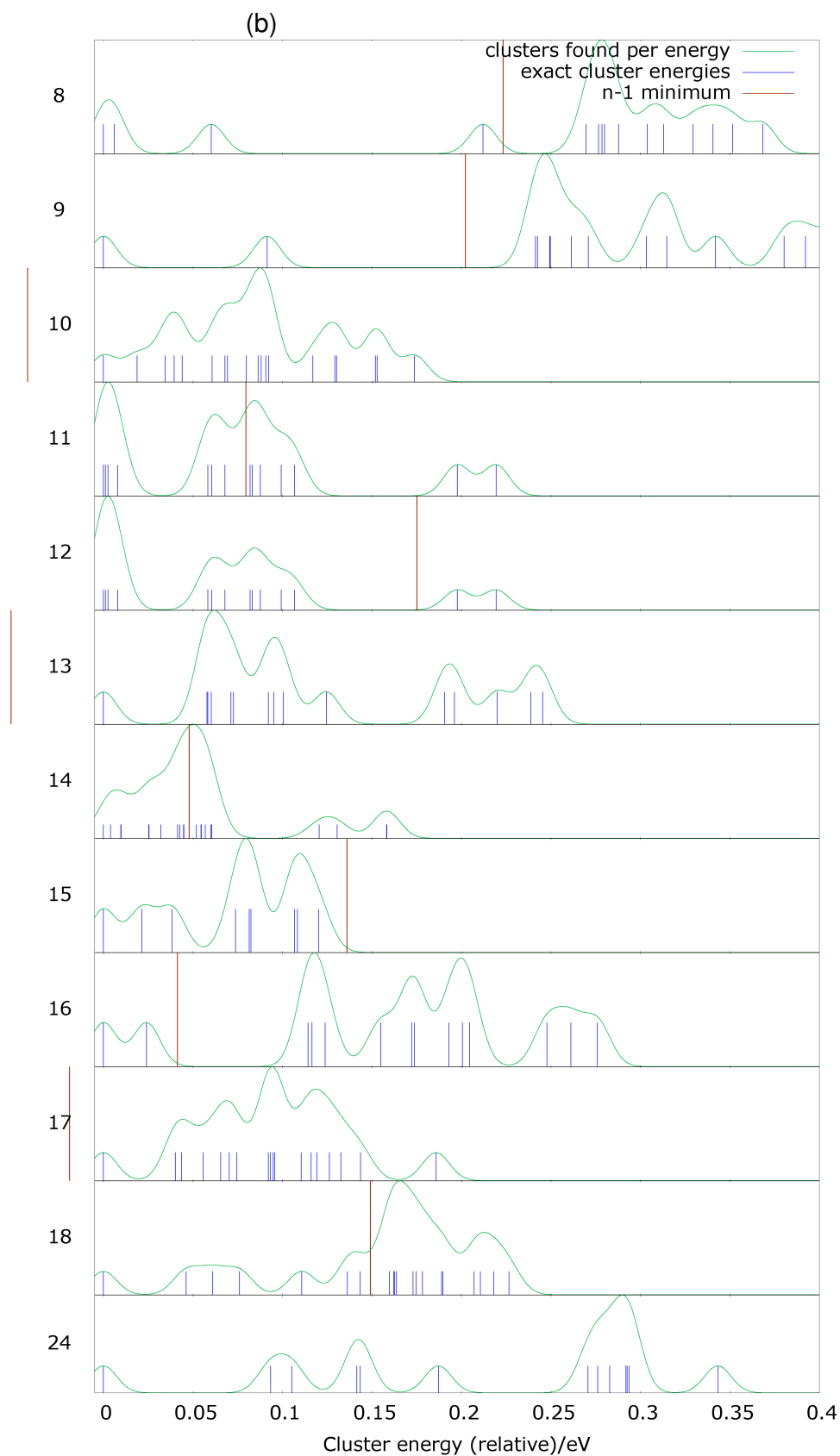


Figure 4.10: Density of LM for MgO clusters for $n = 8$ to 18 and 24 at 100K (a) and 300K (b). Blue impulses indicate cluster energy per formula unit, green lines indicate smeared energies, and red divisions mark $n - 1$ cluster energies.

4.3.9 Spotlight: Multiple metastable structures of $(\text{MgO})_{12}$

While it is not predicted to be the best synthesis target for getting one unique cluster in a size-selective synthesis, $(\text{MgO})_{12}$ is interesting for different reasons. It has four very different LM which should be thermally accessible at both 100K and 300K. If, in size-selective synthesis at appropriate temperatures, all 4 are detected in significant amounts, this would confirm our result that they are all very close to each other in energy.

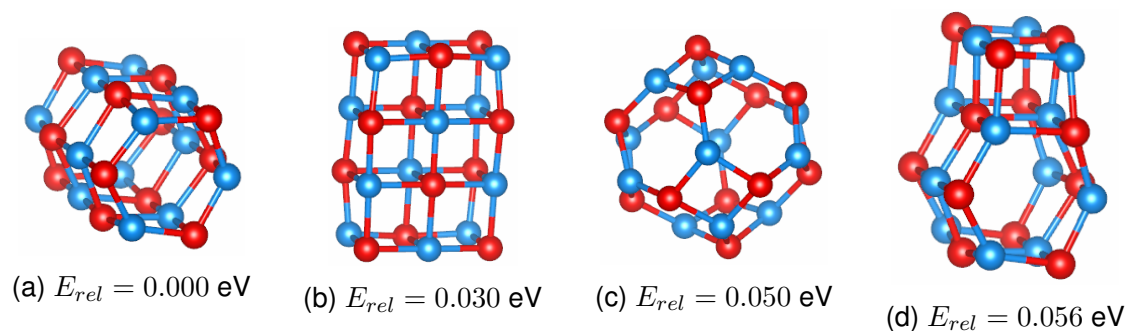


Figure 4.11: The four low-lying LM of $(\text{MgO})_{12}$, as resulting from geometry optimisations using the PBEsol functional.

Figure 4.11 shows the four low-lying LM structures. The three lowest in energy, as shown in Subfigures 4.11a, 4.11b and 4.11c, are representative of three archetypal cluster motifs which can be found for a variety of 1:1 compounds[23]: a barrel, a cuboid rocksalt cut and a bubble (which is also a truncated octahedron). The fourth low-lying LM is a structure which contains both barrel and cuboid ($n = 4$ SBU) motifs. This again shows that in the case of small $(\text{MgO})_n$ clusters, multiple motifs are similar in stability.

For the other three group II oxides, the cuboid rocksalt cut is significantly lower in energy than the other three structures. In the next section, we will look at how relative energies of structures change with change in cation size for $n = 12$.

4.3.10 Relative energies with change in cation

In the previous section, we looked at $n = 12$ clusters of magnesium oxide. Here, we will look at $n = 12$ clusters which have been datamined for all four compounds. Firstly, with Figure 4.12, we will observe how relative energy rank changes with changes in cation,

when optimised from BaO geometries. This plot shows for each starting BaO structure the rank of the structures it optimised to for SrO, CaO and MgO, even where the structure changed significantly upon optimisation. Therefore, it doesn't show the true energy rank of actual structures; it only shows how many $(\text{BaO})_{12}$ structures are required before a certain structure for one of the other alkali earth oxides is found. Figure 4.13 shows energies, rather than just ranks, and we distinguish where structures have changed during optimisation to become a different structure altogether.

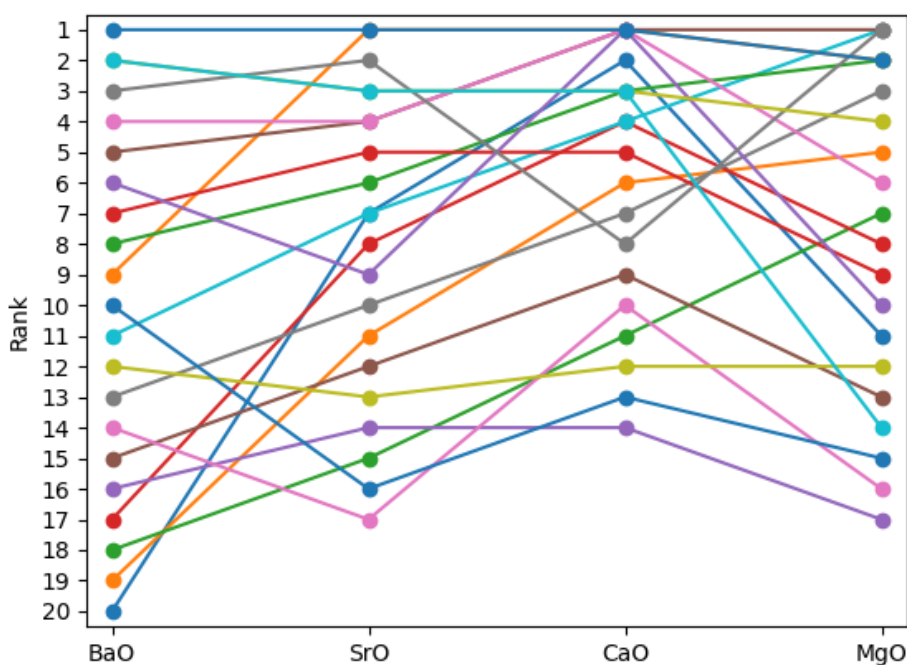


Figure 4.12: Energy ranking of structures resulting from rescaling and reoptimising $(\text{BaO})_{12}$ structures, plotted with respect to change in cation. Here, the number 1 structure is the GM, with number 2 the second-lowest LM and so on.

Looking closely at Figure 4.12, only the top 5 BaO structures are required to find all GM, but when investigating multiple low-lying LM for all four oxides, it becomes necessary to include more BaO structures: for example, the second-lowest LM for CaO is resultant from the structure ranked #20 in BaO's list of LM. Although there appears no guarantee that important LM have not been missed, we do believe that all important LM have been found. One can point to the literature to suggest that at least the top 3 appear to have

been found for all four oxides and all sizes using this method, in particular with recent papers by Chen et al. and this work reproducing each other's results.[31, 32, 33, 34] However, even if the lowest-lying LM are there, the overall density of LM is bound to be lower for SrO, CaO and MgO than it was for BaO because there are simply less than 20 LM that were found. While I could have re-run the evolutionary algorithm for the three smaller alkali earth oxides in order to find a larger number of higher-energy LM, the most important structures and pieces of information were found with the data mining alone and therefore it was left at that.

Data in Figure 4.13 are again of $n = 12$, but linked by which structure they actually are, not by which BaO origin structure they converged from, and this better highlights when structures found for BaO were found to be unstable for the other three oxides. It shows that some cluster shapes simply do not exist for all four oxides. Particular attention should be paid to the three quintessential motifs, the rocksalt cut, barrel and bubble which were discussed in Section 4.3.9 for $(\text{MgO})_{12}$: the rocksalt cut is a low-energy LM for all four compounds (second-lowest for MgO) and the barrel is a low-energy GM (top 3) for all four compounds. The bubble is the third-lowest in energy for MgO and is still found, albeit high energy, for CaO and SrO, but disappears completely in the case of BaO.

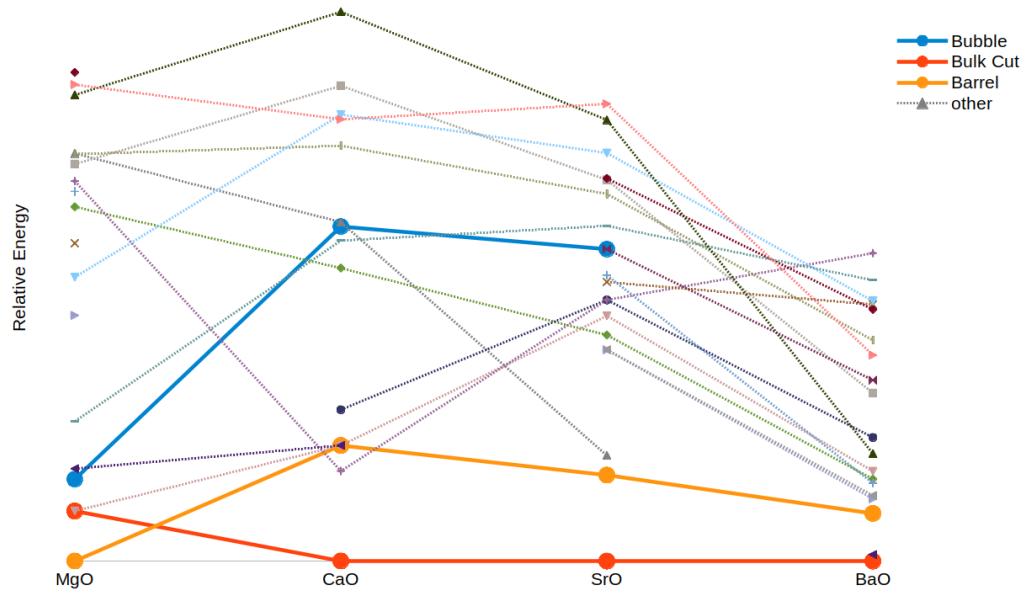


Figure 4.13: Energies relative to their respective GM of structures of $(\text{MgO})_{12}$, $(\text{CaO})_{12}$, $(\text{SrO})_{12}$ and $(\text{BaO})_{12}$, as calculated using DFT (PBEsol).

Another trend noticeable from this plot is that the energies of the BaO clusters are much closer to each other: this is most likely because some clusters of the other compounds which were middling in energy have not been found using this data mining approach. However, this is not of too much concern since these missing clusters are not particularly low in energy and the majority of this work is concerned with particularly low-energy structures.

4.3.11 Bond lengths

Recall from the Introduction of this thesis the bulk lattice parameter data for MgO, CaO, SrO and BaO bulk materials. Half of the lattice parameter in the rocksalt structure is one M-O bond. How much do the bond lengths in our cuboid clusters diverge from the bulk value? A few select sizes and their *lowest energy* cuboid structures were looked at in detail; $n = 4, 12, 16, 18$ and 24 —note that these sizes are all expected to be especially stable sizes. Also note that the lowest energy cuboid for $n = 18$ is a different shape in

the case of BaO, and thus different results are expected for this size and compound.

n	BaO	SrO	CaO	MgO
bulk	2.770	2.570	2.405	2.105
4	2.3998	2.2758	2.1429	1.9595
12	2.5368	2.3928	2.2413	2.0118
16	2.5580	2.4079	2.2545	2.0179
18	2.5610	2.4356	2.2741	2.0280
24	2.6122	2.4469	2.2844	2.0344

Table 4.9: Bond lengths in bulk BaO[80], SrO[81], CaO[82] and MgO[82], as well as selected cluster sizes.

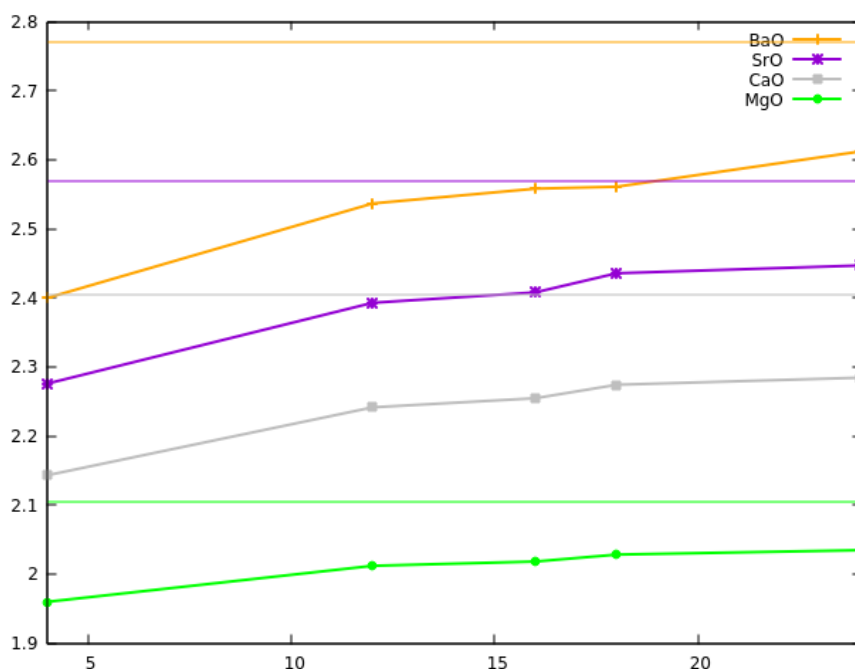


Figure 4.14: Average bond lengths (\AA) of cuboid clusters of sizes $n = 4, 12, 16, 18$ and 24 , as well as the expected asymptotes (bulk bond lengths).

The shortest bond lengths are reported for the $n = 4$ cluster; these are only between 87 and 93% of the bulk bond lengths. In general, bond lengths are shorter for smaller clusters, and gradually increase as cluster size increases. This increase is very small beyond $n = 12$, e.g. the change from $n = 18$ to 24 is $\sim 0.01\text{\AA}$ for SrO, CaO and

MgO and 0.05\AA for BaO. However, bond lengths are still more than 0.1\AA below the bulk value at $n = 24$ for Ba, Sr and Ca oxides and not much below that for MgO, indicating that clusters will have to be much larger than this to adopt structures with bulk-like bond lengths. Another thing to note is that, for BaO, the $n = 16$ to 18 jump is much smaller while the $n = 18$ to 24 jump is much larger, suggesting that the $6 \times 3 \times 2$ cluster has bond lengths which are closer to smaller clusters, while conversely (as in the cases of SrO, CaO and MgO) the $4 \times 3 \times 3$ cluster is more bulk-like when it comes to its bond lengths; this is in line with the expectation that the $4 \times 3 \times 3$ cluster will be more bulk-like as it has more non-surface atoms.

4.4 Summary and Conclusions

Structures and stabilities of $(\text{SrO})_n$, $(\text{CaO})_n$ and $(\text{MgO})_n$ nanoclusters with $n = 4$ to 18 and 24 were investigated with the intention of comparing them to each other as well as to results for $(\text{BaO})_n$ clusters. Clusters of strontium and calcium oxide, like barium oxide ones, generally showed a preference for adopting structures which were cuts from the rocksalt phase. For CaO_n and SrO_n more non-cuboid cuts were found than for barium oxide. However, these tended to not be the most stable structures when compared to other sizes. Magnesium oxide clusters adopted barrel-like structures up to and including the size of $n = 15$, after which the rocksalt cuts become more favourable, where both structural motifs stay competitive until larger sizes. It was found that polar structures such as the $n = 9$ rocksalt cut or the $n = 18$ $4 \times 3 \times 3$ rocksalt cut, were most polar for MgO, where the cation is least polarisable to minimise the dipole, but the energy penalty for being a polar cluster seemed largest for BaO. At least partially as a consequence of preference in motifs, it was found that average coordination numbers for MgO clusters tended to be smaller.

Analysis of all the LM that were investigated in this study to see if multiple structures are likely to be found for each size reveal the patterns represented in Figures 4.15 and

4.16. Red squares indicate that only one structure is likely to be found in size-selective synthesis, while yellow squares indicate sizes for which multiple structures are likely to be found at each temperature. Black squares indicate sizes which are likely to be unstable to decomposition into an $n - 1$ cluster and a $n = 1$ unit. These graphics could be used by experimentalists to guide choice of sizes to synthesise when attempting to isolate one single structure.

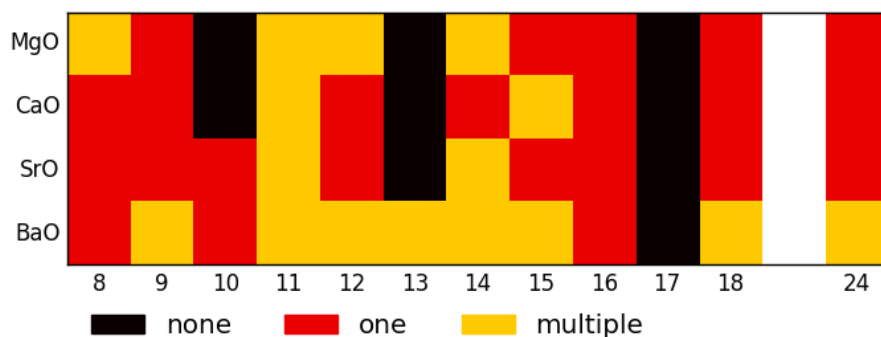


Figure 4.15: Number of LM likely to be found in experiments at 100K for each alkali earth oxide and each cluster size.

Given more resources and time, I would have extended this study to include larger clusters to get an idea of when they become more bulk-like in e.g. bond lengths. Future work may also include looking at cross-doped versions of these clusters (e.g. doping MgO with Ca^{2+} in place of a Mg^{2+} ion), as well as with other elements of similar size. Additionally, further comparison of our results with experiment should be sought.

Also, investigation of these cluster on surfaces or in solution is of interest as these *in vacuo* structures are not stable as they are.

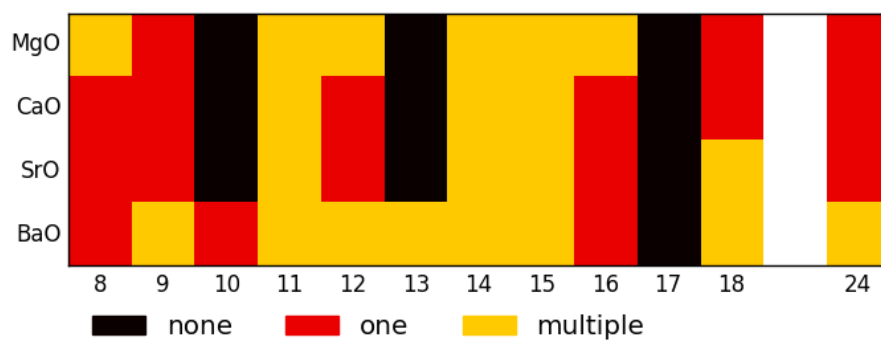


Figure 4.16: Number of LM likely to be found in experiments at 300K for each alkali earth oxide and each cluster size.

Chapter 5

Constructed Cuboid Clusters

5.1 Introduction

As already reported in previous chapters, cuboid rocksalt cuts with exposed $[1\ 0\ 0]$ faces are often particularly stable configurations for the alkali earth oxide nanoclusters. This chapter is inspired by works by Chen et al.[32, 33, 34] which looked at normalised clustering energies (NCEs) of a variety of alkali earth oxide clusters and extrapolated bulk energies from them. We will investigate and report the NCEs of cuboids, and then follow on to extrapolate energies of 1D nanowires, 2D slabs and 3D bulk material from them. This allows for direct comparison of nanowires and slabs with vacuum-free calculations of 0D and 3D materials while normal FHI-aims calculations produce an energy difference due to the presence of the vacuum, making a direct comparison impossible. 1D materials' applications include a wide range of fields such as energy storage[137], catalysis[138, 139], touch screens[140], transistors[141] and biosensing[142]. 2D materials are primarily of interest here as substrates but have seen use in photovoltaics[143] and biomedical applications[144].

Additionally, this chapter will look into the effects of shape on cuboid energy for a number of sizes: are more cube-like or more needle-like nanoclusters more stable? It will also investigate this, and the reasons for relative stabilities.

5.2 Methods

Atomic configurations and energies of smaller clusters were taken from the data generated for Chapters 3 and 4. Larger clusters were constructed using one 8-atom unit cell as a basis and then adding atoms systematically layer-by-layer in the spreadsheet package LibreOffice Calc. Structures were refined using DFT (PBEsol) in FHI-aims with a tight basis set and the BFGS local geometry optimisation algorithm. Where convergence was difficult, some extra basis functions were added to the metal, up to third-tier basis functions, and then the resulting structure was reoptimised with the original basis set. This was so that energies remain comparable between different clusters. In retrospect, it would have been more efficient to *reduce* the number of basis functions for ease of convergence and then increase it again in a second step.

The normalised clustering energies are, as in previous chapters,

$$NCE(n) = \frac{E(n)}{n} - E(1)$$

It is expected that there is a linear relationship between the NCE of a cluster and $\frac{1}{n}$. Following this, the energy of an infinitely long nanowire should be where $n \rightarrow \infty$, i.e. where $\frac{1}{n} = 0$. If a linear fit is possible, it will be to a function of the form:

$$y = ax + b$$

where b is the vertical axis intercept and therefore the value of the function where $n \rightarrow \infty$, i.e. that of the infinitely long nanowire. This same process can be repeated taking nanowire energies as a starting point to extrapolate slab energies, and finally, taking slab energies to extrapolate bulk energies. Through this process of linear fits, generalised NCEs (gNCEs) of nanowires, slabs and bulk material were extrapolated from the NCEs of nanoclusters. Plots and extrapolations were produced in gnuplot using the fit function which uses an implementation of the nonlinear least-squares (NLLS) Marquardt-Levenberg algorithm[145, 146].

Bulk energies were calculated in FHI-aims using a minimal unit cell, the PBEsol functional with a tight basis set, and 8 k-points along each dimension.

Madelung potentials were calculated using the `pot` keyword in GULP. This calculates the electrical potential U_i of all ions of the lattice felt by the ion at position r_i :

$$U_i = \frac{e}{4\pi\epsilon_0} \sum_{j \neq i} \frac{z_j}{r_{ij}}$$

where z_j is the charge of the ion at position j and r_{ij} is the distance between the ions at positions i and j . This, multiplied by the charge of the ion at r_i , gives the electrostatic energy at the site, and therefore a measure of how (de)stabilised that ion is by this electric potential.

5.3 Results

5.3.1 Extrapolating energies of extended structures from nanocluster energies

In this chapter, cuboid clusters of magnesium, calcium, strontium and barium oxides in sizes ranging from $2 \times 2 \times 3$ atoms ($n = 6$) up to $n = 40$ are considered. While a $2 \times 2 \times 2$ cuboid-like structure was found for all four compounds, this structure was, when optimised, generally too deformed to be considered bulk-like and extrapolations are only concerned with sufficiently bulk-like structures; in particular, the $2 \times 2 \times 2$ cuboids all displayed much shorter bond lengths than larger clusters or, indeed, the bulk (at only about 90% of the bulk bond length), as well as bond angles that particularly strongly deviated from the 90 deg expected for the true cube.

When plotting the NCEs of clusters against n as seen for $2 \times 2 \times N$ clusters in Figure 5.1, we can already make some observations about the four alkali earth oxides.

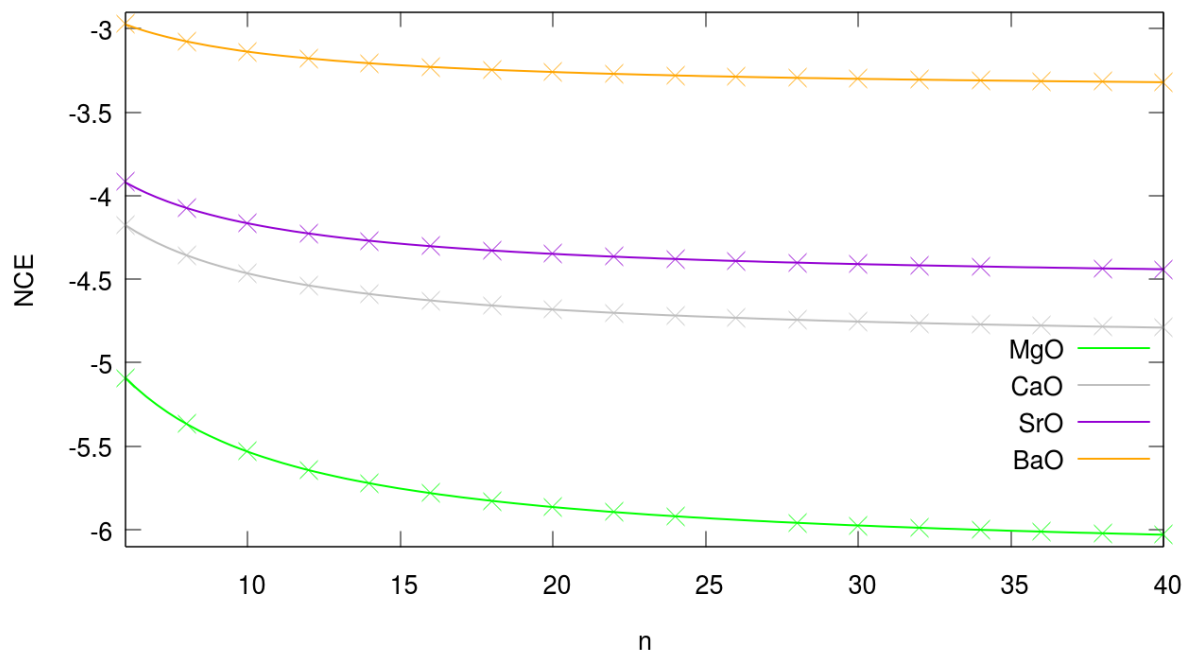


Figure 5.1: NCEs of $2 \times 2 \times N$ cuboid clusters as a function of n .

For example, the NCEs are lowest for MgO and become higher going down the group - this is in line with bonding generally being stronger with a smaller cation. Additionally, SrO and CaO NCEs are relatively close to each other compared to the more outlying cations. This is in line with their ionisation energies being the most similar, whilst their ionic sizes are more dissimilar and thus less correlated to NCEs. The other thing to notice is that there is an inverse proportional relationship between the NCEs and n , which is easier to see if the data is plotted as a function of $\frac{1}{n}$.

Therefore, in a next step, NCEs are plotted as a function of $\frac{1}{n}$ (Figure 5.2). One immediately notices *multiple* straight lines for each compound. Each of these straight lines corresponds to a different diameter nanorod, e.g. $2 \times 2 \times N$ or $2 \times 4 \times N$. The diameters of nanorods included here are: 2×2 , 2×3 , 2×4 , 2×5 , 2×6 , 3×3 , 3×4 and 4×4 . Some of these, separated out, can be seen in Figure 5.3.

It is immediately visible from Figure 5.3 that the first two linear fits (for 2×2 - and 3×3 -base nanorods) are much better than the third (for 4×4) as points visibly deviate from the fitted line in the third case, where $4 \times 4 \times 3$ energies are visibly higher than the fit would predict for all four alkali earth oxides. The highest asymptotic standard error in the

vertical axis intercept, as calculated in the fit by gnuplot, is 0.036% for SrO in the 2×2 dataset, while the highest error is 2.249% for CaO in the 4×4 dataset. It was later found that there was an error in calculating the energies of $4 \times 4 \times 4$ clusters in particular which caused the bad fit in the 4×4 extrapolation.

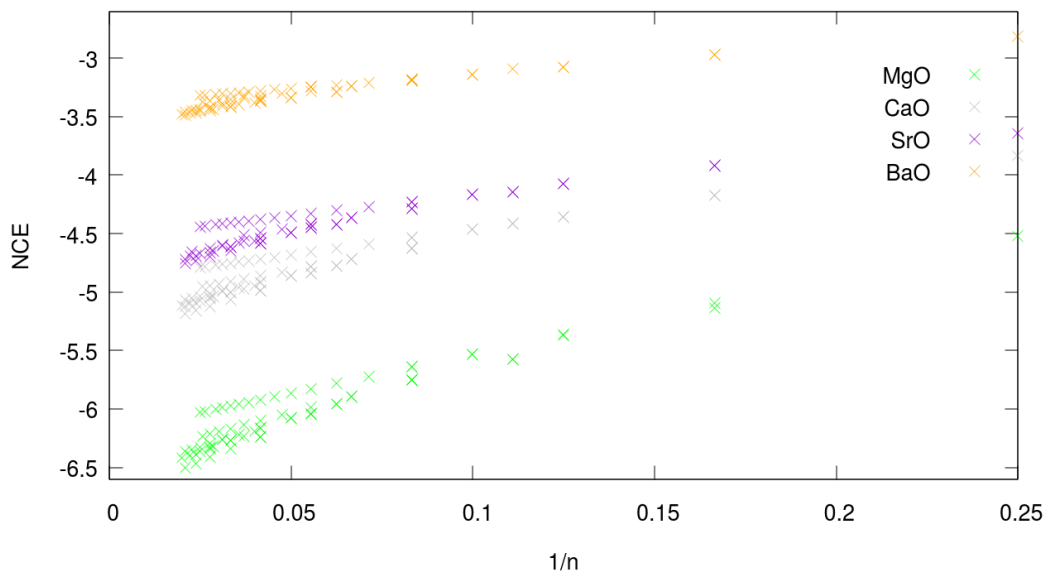


Figure 5.2: NCEs of a variety of cuboid nanocluster as a function of $\frac{1}{n}$

5.3.2 Extrapolation of nanowire gNCEs

In the following step, each of these nanorod diameters was separated out and a linear fit found for each diameter of nanorods. Example plots are shown for 2×2 (representative of the regular case), 3×3 and 4×4 in Figure 5.3.

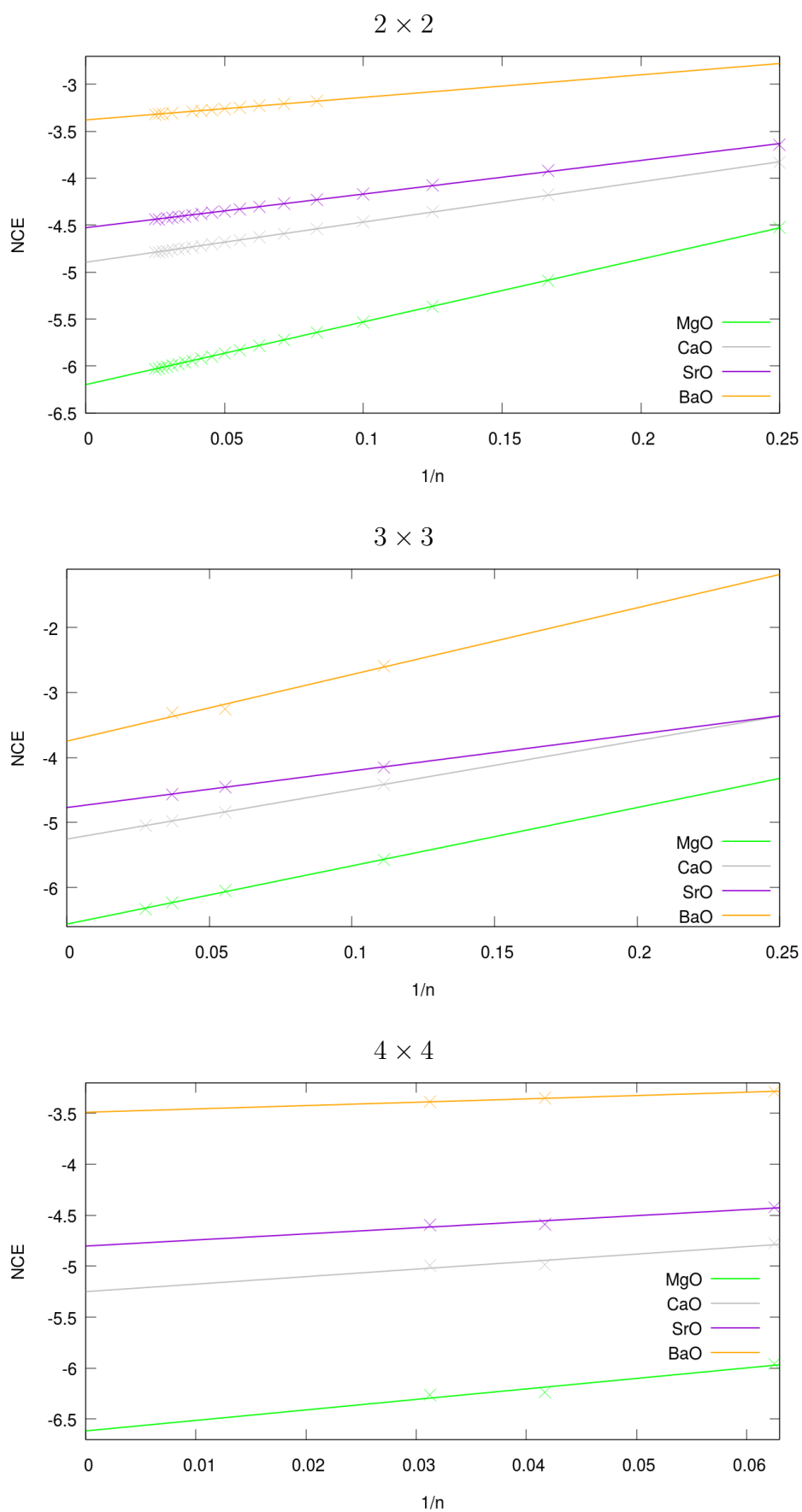


Figure 5.3: DFT (PBEsol) NCEs of 2×2 (top), 3×3 (middle) and 4×4 (bottom) nanorods as a function of $1/n$.

Even in the 2×2 dataset, longer nanorods tend to fit the line better, perhaps due to the fact that larger clusters will be more bulk-like. This may partially explain why the 4×4 data set provides a poorer fit, as only clusters up to $N = 4$ are included in it, however it was also discovered later that there was an error in the $4 \times 4 \times 4$ calculations for all compounds, specifically. Out of all the datasets considered here (including the ones not shown in these plots), only the $4 \times 4 \times$ and 3×3 datasets have less than 5 data points because only clusters up to $n = 40$ were investigated; however, the nanorods in the 3×3 data set are longer since the third coordinate has to be even to ensure neutral clusters. Additionally, the 3×3 clusters are generally expected to be higher energy as they will all be polar. Polar clusters have been shown in Chapter 3 to be higher in energy generally. An additional point of the $3 \times 3 \times N$ dataset is that the slope of the SrO data is lower than expected in the usual case; this may be because SrO penalises polar clusters less (see Chapter 4).

To extrapolate energies of nanowires from the nanorod data, the vertical axis intercept is used here (as this is where $\frac{1}{n} = 0$ and therefore $n \rightarrow \infty$). These extrapolated values, including errors, are tabulated in Table 5.1.

To illustrate what we mean by nanowire, see Figure 5.4. A nanowire here is the equivalent of a nanorod, but infinitely extending in one dimension.

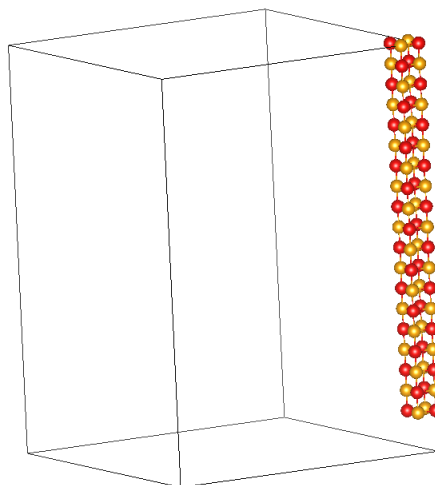


Figure 5.4: A BaO nanowire in a unit cell.

As expected, nanowires with a larger diameter have a lower gNCE, while nanowires with similar cross-sectional areas such as 9-atom 3×3 and 8-atom 2×4 are very close to each other in energy. It also becomes apparent here that the data of 4×4 nanowire is indeed off as its energy is markedly higher than the energy of the 4×3 nanowire, and its error values are also much higher than those of the other nanowire extrapolations, especially for MgO, CaO and SrO. This is because of the previously mentioned error in the $4 \times 4 \times 4$ calculations. It might therefore be necessary to discard this data point as the values are wrong and the errors are large and it is therefore unreliable; for example a 0.13 eV error (as in the case of MgO) in one of three points would dramatically alter the fit.

hline	MgO	CaO	SrO	BaO
$N_x \times N_y$	gNCE / eV	gNCE / eV	gNCE / eV	gNCE / eV
2×2	-6.198 ± 0.001	-4.896 ± 0.001	-4.528 ± 0.002	-3.380 ± 0.000
2×3	-6.421 ± 0.005	-5.098 ± 0.010	-4.679 ± 0.007	-3.446 ± 0.006
2×4	-6.560 ± 0.003	-5.207 ± 0.003	-4.783 ± 0.003	-3.525 ± 0.007
2×5	-6.638 ± 0.003	-5.272 ± 0.003	-4.840 ± 0.006	-3.561 ± 0.008
2×6	-6.683 ± 0.024	-5.314 ± 0.004	-4.878 ± 0.007	-3.582 ± 0.006
3×2	-6.421 ± 0.005	-5.098 ± 0.010	-4.679 ± 0.007	-3.446 ± 0.006
3×3	-6.563 ± 0.018	-5.256 ± 0.004	-4.771 ± 0.009	-3.749 ± 0.123
3×4	-6.746 ± 0.014	-5.368 ± 0.011	-4.908 ± 0.014	-3.545 ± 0.020
4×2	-6.560 ± 0.003	-5.207 ± 0.003	-4.783 ± 0.003	-3.525 ± 0.007
4×3	-6.746 ± 0.014	-5.368 ± 0.011	-4.908 ± 0.014	-3.545 ± 0.020
4×4	-6.616 ± 0.133	-5.250 ± 0.118	-4.803 ± 0.083	-3.491 ± 0.005

Table 5.1: Generalised NCEs for infinitely long nanowires of cross-section $N_x \times N_y$, as extrapolated from plots such as in Figure 5.3

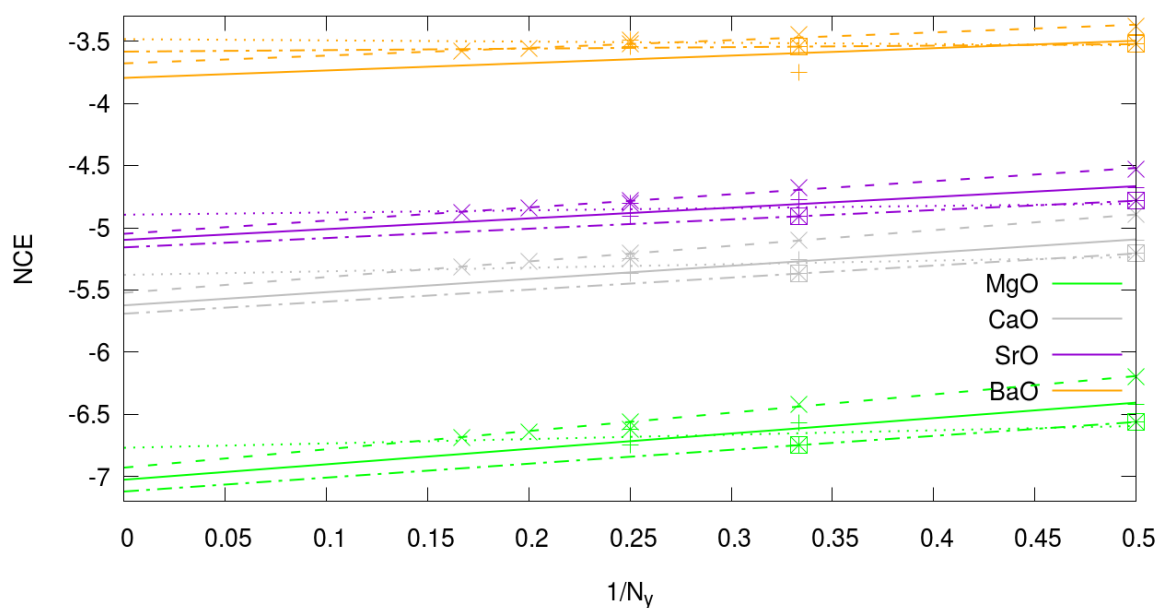


Figure 5.5: Extrapolation of gNCEs (from nanowire gNCEs) of slabs of thickness 2 atoms (dashed), 3 atoms (solid), 4 atoms (dotted), and 4 atoms with 4×4 data removed (dot-dashed).

From this extrapolated nanowire data, one can then further extrapolate data for slabs of material by the same procedure. From the data presented here, it should be possible to extrapolate energies for 2-, 3- and 4-atom thick slabs.

The $N = 2$ and 3 lines in Figure 5.5 look relatively similar to those we saw in the nanowire extrapolation. As expected, extrapolated energies are lower for the $N = 3$ slab than for the $N = 2$ slab (see Table 5.2). The third, dotted line, for $N = 4$, looks different: slopes are near-zero and, in the case of BaO, actually positive, and it is clearly visible that the line does not fit the data points, with 4×4 data being higher than the fit line in all 4 compounds. As explained previously, the 4×4 data point was removed due to the erroneous $4 \times 4 \times 4$ value, and the 4-atom thick slab fitted without it. Note that, since this was fitted to two data points only, errors are unknown for this particular fit. However, this data seems to fit in much better with that of the 2- and 3-atom thick slabs.

	MgO	CaO	SrO	BaO
Size	gNCE / eV	gNCE / eV	gNCE / eV	gNCE / eV
2	-6.927 ± 0.012	-5.522 ± 0.004	-5.048 ± 0.013	-3.679 ± 0.020
3	-7.024 ± 0.125	-5.623 ± 0.038	-5.097 ± 0.102	-3.796 ± 0.397
4	-6.767 ± 0.249	-5.378 ± 0.221	-4.895 ± 0.186	-3.485 ± 0.0711
4 (less data)	-7.119	-5.690	-5.157	-3.585

Table 5.2: Generalised NCEs for infinitely extending slabs of varying thickness, as extrapolated from plots in Figure 5.5

From this slab data, one can now also fit bulk energies in a final step. This is illustrated in Figure 5.6. It is also possible to attempt to directly fit all clusters' data in order to extrapolate the bulk energy. This is shown in Figure 5.7. The question is: which method yields more accurate results?

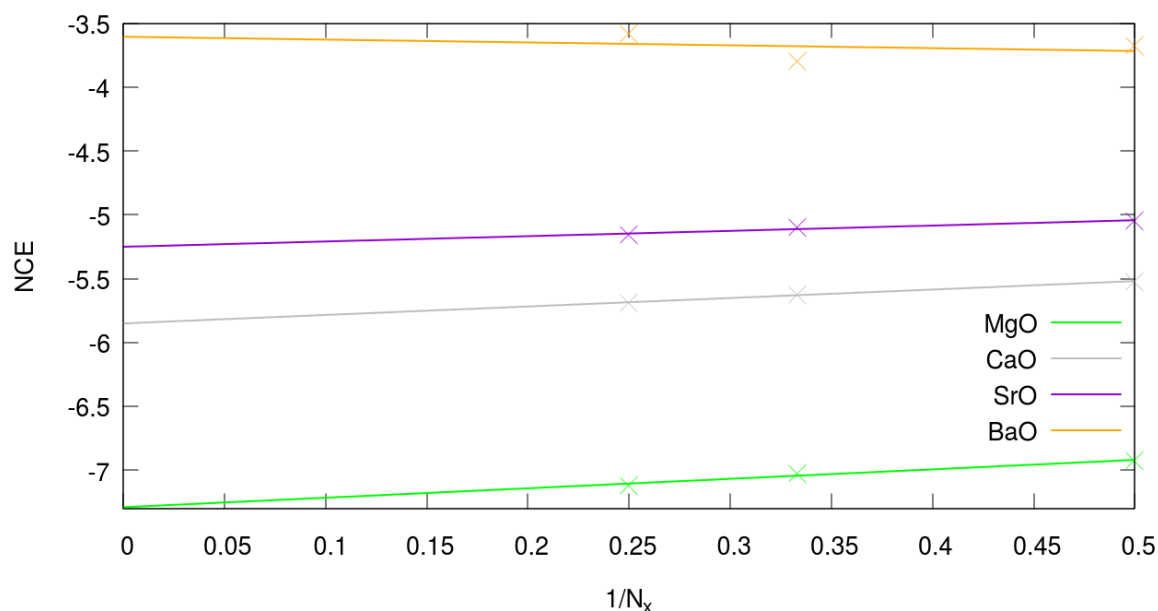


Figure 5.6: Generalised NCEs for infinitely extending slabs, as used to extrapolate bulk energy, following the three-step method.

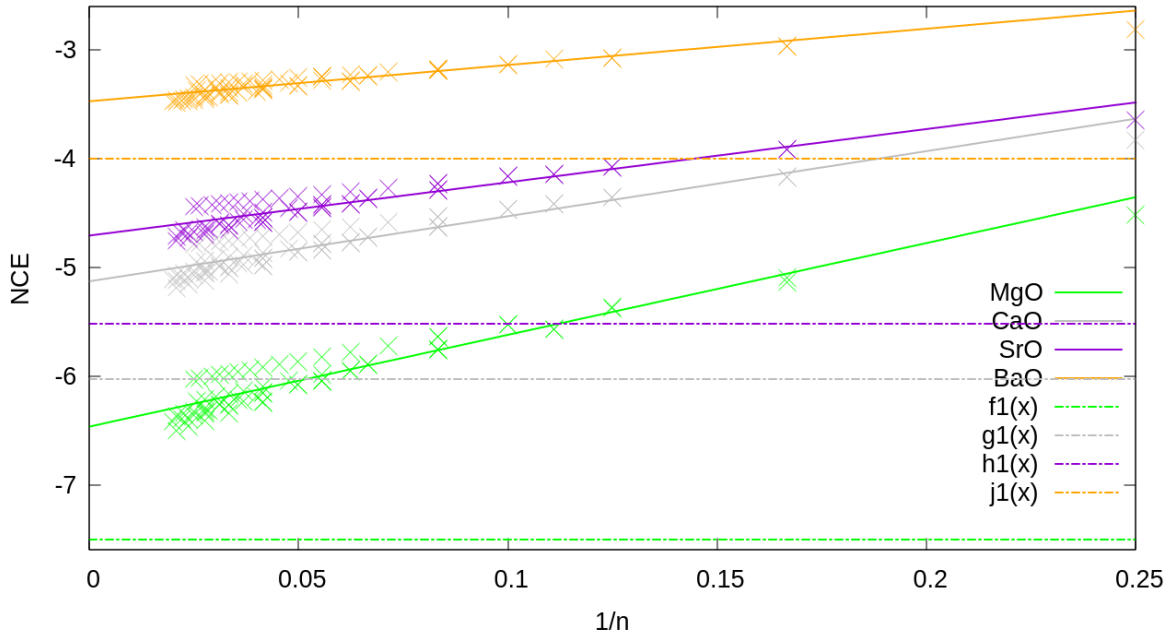


Figure 5.7: Fitting to all nanocluster energies to extrapolate bulk energy using the one-step method – the dashed lines indicate the DFT bulk energies, i.e. the limit we expect.

The results from both methods are tabulated together with DFT bulk energies in Table 5.4. Errors in the fit appear lower for the one-step method at first glance, however this is primarily as it was fitted to a larger number of data points (hundreds, compared to 3 for the 3-step fit’s last step). However, the errors relative to the DFT gNCEs are much larger than the errors in the fit in both cases, for example the MgO fit of the 3-step method has a fit error (uncertainty) of 0.052 eV while the actual result of the fit is 0.21 eV higher than the DFT result.

	MgO	CaO	SrO	BaO
Method	gNCE / eV	gNCE / eV	gNCE / eV	gNCE / eV
Three-step method	-7.29071 ± 0.05168	-5.8512 ± 0.01824	-5.25109 ± 0.03985	-3.60591 ± 0.3007
One-step method	-6.46613 ± 0.02342	-5.13019 ± 0.01976	-4.7095 ± 0.01818	-3.47495 ± 0.01611
DFT data	-7.50569	-6.03149	-5.51680	-3.99788

Table 5.3: Generalised NCEs for bulk materials as extrapolated from nanoclusters via the three-step method, the one-step method, and from DFT energies.

DFT data of the bulk structures were obtained using the same functional and basis sets as the cuboid calculation, with 8 k-points along each dimension. When comparing

to the DFT data, the three-step fit does markedly better: The highest error in the three-step method with reference to DFT data is 9.8% and occurs for BaO, while the lowest is 2.8% for MgO. In the one-step method, errors range from 13.1% for BaO to 14.9% in the case of CaO, i.e. all errors are higher, and for the three smaller cations they are significantly so. Therefore, the three-step method is better at reproducing DFT results. The next section will investigate if this can be improved by only including GM structures, rather than constructed cuboids.

It is also possible to use intermediate results to draw direct comparisons between different-dimensional nanostructures: for example, the NCE of a $4 \times 4 \times 4$ cluster, -6.25 eV, is notably lower than the gNCE of our thinnest 1d structure, the $2 \times 2 \times N$ nanowire, which is -6.20 eV.

One-step method using Global Minima

	MgO	CaO	SrO	BaO
Method	gNCE / eV	gNCE / eV	gNCE / eV	gNCE / eV
From cuboids	-6.466 ± 0.023	-5.130 ± 0.02	-4.710 ± 0.018	-3.475 ± 0.016
From GMs	-6.408 ± 0.049	-5.052 ± 0.052	-4.639 ± 0.045	-2.942 ± 0.031
DFT data	-7.506	-6.031	-5.517	-3.998

Table 5.4: Generalised NCEs for bulk materials as extrapolated from nanoclusters via the three-step method using cuboids, using GMs, and from DFT energies.

Figure 5.8 shows that it is also possible to fit linearly to GM structures in the same fashion as all the fits above - but how good is the result? When we compare the energies extrapolated from all cuboids in the 1-step method (Figure 5.7) with the new ones extrapolated from GMs, we find that the GM extrapolation actually performs marginally worse than that from cuboids. This is at least partly because for some sizes, even the GMs are high-energy and non-cuboid, but overall it seems like the three-step approach would still perform the best.

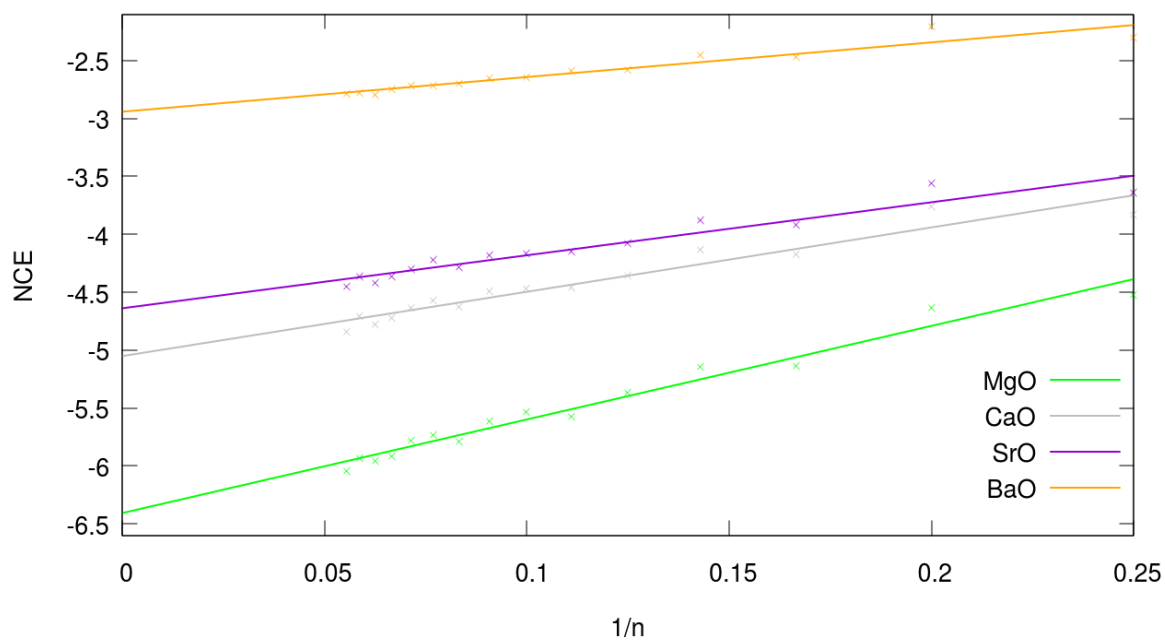


Figure 5.8: NCEs of GM clusters as a function of $\frac{1}{n}$

5.3.3 Comparing different cuboids of the same size

This is somewhat of a continuation of themes in earlier chapters: how do energies vary between different shaped cuboid cuts of the same size? Comparisons were drawn for sizes $n = 24, 27, 28, 30, 32$ and 36 . Their energies relative to the lowest of each size are tabulated in Tables 5.5 and 5.6.

$n/$ MO	structures; energies / eV/MO			
24	$2 \times 2 \times 12$	$2 \times 3 \times 8$	$2 \times 4 \times 6$	$3 \times 4 \times 4$
MgO	0.319	0.140	0.079	0.000
CaO	0.271	0.126	0.068	0.000
SrO	0.208	0.097	0.042	0.000
BaO	0.090	0.046	0.00000	0.017
27	$2 \times 3 \times 9$	$3 \times 3 \times 6$		
MgO	0.095	0.000		
CaO	0.085	0.000		
SrO	0.054	0.000		
BaO	0.000	0.022		
28	$2 \times 2 \times 14$	$2 \times 4 \times 7$		
MgO	0.259	0.000		
CaO	0.219	0.000		
SrO	0.179	0.000		
BaO	0.100	0.000		

Table 5.5: Energies of cuboid structures of sizes $n = 24, 27$ and 28 .

To minimise surface area and maximise bulk-like character, it is expected that clusters will adopt as close to spherical a shape as possible. In the case of cuboid rocksalt cuts, the closest shape to the sphere is a cube (where all side lengths are the same). In some cases, "closeness to a cube" is ambiguous, and is therefore defined here as a large cross-sectional area along the smallest surface plane. For almost all MgO, CaO and SrO cluster sizes and one BaO size, structures which are closer to a cube are lower in energy. For example, for the ($n = 30$) $2 \times 5 \times 6$ cluster this value is $2 \times 5 = 10$, while for the $3 \times 4 \times 5$ cluster of the same size it is $3 \times 4 = 12$; the latter is therefore closer to a cube in shape, and indeed lower in energy. There are still other considerations such as whether a cluster is polar or not. We know from other published data[32, 33, 34] that in the case of polar lowest-energy cuboids such as for $n = 27$, it is possible that the true

GM is non-cuboid. Since this chapter only deals with constructed clusters, a comparison which also accounts for non-cuboids is not included.

$n/$ MO	structures; energies / eV/MO					
30	$2 \times 2 \times 15$	$2 \times 3 \times 10$	$2 \times 5 \times 6$	$3 \times 4 \times 5$		
MgO	0.366	0.173	0.074	0.000		
CaO	0.311	0.154	0.064	0.000		
SrO	0.242	N/A	0.038	0.000		
BaO	0.115	0.064	0.000	0.024		
32	$2 \times 2 \times 16$	$2 \times 4 \times 8$	$4 \times 4 \times 4$			
MgO	0.273	0.000	0.002			
CaO	0.231	0.000	0.004			
SrO	0.190	0.000	0.012			
BaO	0.107	0.000	0.022			
36	$2 \times 2 \times 18$	$2 \times 3 \times 12$	$2 \times 4 \times 9$	$2 \times 6 \times 6$	$3 \times 3 \times 8$	$3 \times 4 \times 6$
MgO	0.402	0.201	0.118	0.076	0.086	0.000
CaO	0.342	0.177	0.101	0.065	0.076	0.000
SrO	N/A	N/A	0.071	0.040	N/A	0.000
BaO	0.134	0.079	0.021	0.000	N/A	0.023

Table 5.6: Energies of cuboid structures of sizes $n = 30, 32$ and 36 .

One exception to the trend where the more cube-like structures are lower in energy are the $n = 32$ clusters, where the $2 \times 4 \times 8$ structure (with a smallest cross-sectional area of 8) is preferred over the $4 \times 4 \times 4$ structure (smallest cross-sectional area of 16) in all four oxides, although this is only by a few meV per formula unit (at most 22.2 meV/MO in the case of BaO). This is the only size where the structure which is closest to the cube is not preferred by MgO, CaO and Sr, while for BaO, some other structure is preferred in nearly every case, with the exception of $n = 28$ where the most cube-like structure is not very close to a cube at all at $2 \times 4 \times 7$ atoms, and its $2 \times 2 \times 14$ alternative has the very extreme smallest cross-sectional area of 4 atoms. It has to be noted that even where BaO prefers

other structures, it is always by ~ 20 meV/MO: a smaller margin than is usually seen in the other three oxides.

5.3.4 Madelung potentials

One way to elucidate relative stability of individual ions is to look at the Madelung potential at ionic sites. If the Madelung potential *times* the ionic charge is lower, this corresponds with more stabilisation at the ionic site. Because Madelung potentials for all sites were found to be stabilising here, only their absolute values will be taken into consideration henceforth.

Madelung potentials for ionic sites in the bulk materials were calculated in GULP and are reported below, to compare to nanocluster Madelung potentials. Only the values at O^{2-} sites are reported as the Madelung potentials at Ba^{2+} cation sites have the same absolute value in the bulk. These are tabulated in Table 5.7. The magnitude of the potential is largest in MgO and gets smaller when the cation becomes larger; this is simply because here, the charge of the ions is kept the same (± 2) while the distance between them increases with increasing cation size.

Compound	MgO	CaO	SrO	BaO
U / V	23.909	20.927	19.583	18.169

Table 5.7: Madelung potentials at O^{2-} sites, calculated using GULP

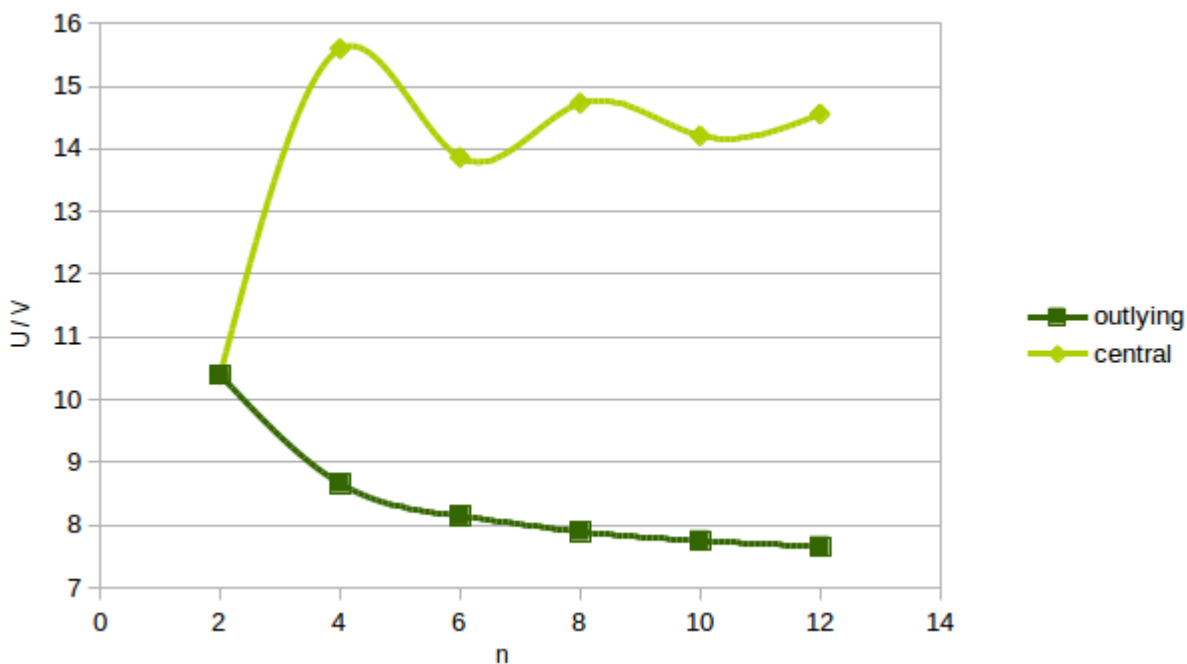
The 1D case

Figure 5.9: Madelung potential at the most outlying and central ion sites in chains of alternating Ba^{2+} and O^{2-} ions of different lengths, calculated using the rigid ion model in GULP.

In a next step, a simplified model of these nanoclusters was used: a linear chain of alternating Ba^{2+} and O^{2-} ions, at the bulk bond distance, that was lengthened 2 at a time (to preserve charge neutrality). First, this was done without any optimisation, with cores only. In this model, it was found that for the most outlying ions, the absolute value of the Madelung potential got smaller with more ions added, approaching some number below 7.6. For the ions closest to the centre of the chain, the potential oscillated about ~ 14.3 . These are shown in Figure 5.9. In this model, Ba^{2+} and O^{2-} are equivalent as they are spaced evenly and their charges are of equal magnitude. Geometrically, results for the other three oxides should be equivalent, just scaled according to bond distance.

When shells are added and relaxed, the system becomes asymmetrical. Specifically, for the most outlying ion sites, the magnitude of the Madelung potential is slightly higher at the Ba^{2+} site than at the O^{2-} site, while in the case of the middle sites, the same is true at very small sizes and it reverses slowly for larger sizes. Overall, we again see a

steady decrease in the Madelung potentials of outlying sites with growing chain length, and an oscillation about ~ 14.4 at central sites. This is shown in Figure 5.10.

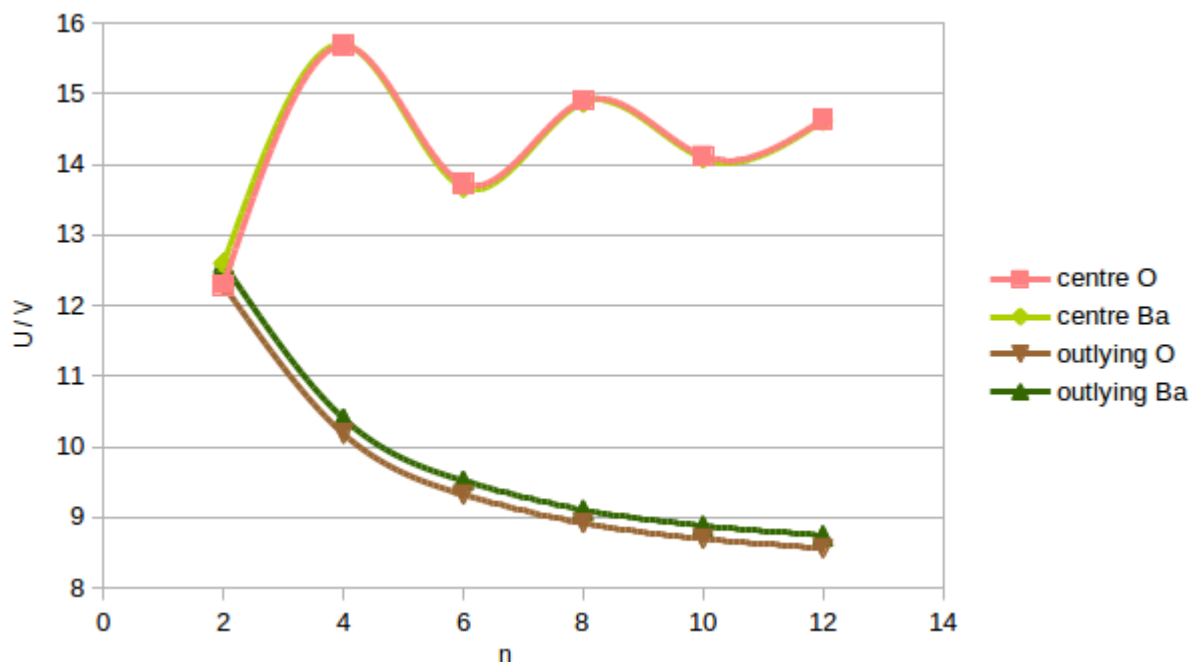


Figure 5.10: Madelung potential at outlying and central ions in chains of alternating Ba^{2+} and O^{2-} ions of different lengths, as calculated using the shell model in GULP.

The 3D case: cuboids

For calculating the Madelung potential at ionic sites in the cuboids presented above, DFT (PBEsol) geometries were used as the starting point and the rigid ion model was employed. Values reported here will be: the Madelung potential at outlying (corner) sites, the Madelung potential at a most central atom, and the average absolute value of the Madelung potential for each cluster. For each oxide, different length nanorods of 2×2 base are considered: $2 \times 2 \times 6$, $2 \times 2 \times 8$, $2 \times 2 \times 12$ and $2 \times 2 \times 16$. Notice that the last is a $n = 32$ nanocluster. To complement this, the two other $n = 32$ cuboids ($2 \times 4 \times 8$ and $4 \times 4 \times 4$) are also considered here to help explain their relative energies for the different compounds. We will look in detail again at the most outlying atoms, the central atoms, and finally the average magnitude of Madelung potentials taken from all ionic sites.

In particular, we will look at the extreme cases of barium and magnesium oxide, with

the other two oxides lying in between in behaviour.

The Madelung potentials at outlying and central sites for barium oxide cuboids are shown in Figure 5.11. As expected from what we know about puckering in these nanoclusters (see Chapter 4), the stabilisation about barium ions is stronger than the stabilisation about oxygen ions: angles about oxygen ions open up in barium oxide nanoclusters, so they become closer to each other, destabilising overall, while angles about barium ions become more acute, they therefore move further from each other, and are relatively stabilised. Indeed, the magnitude of the Madelung potential becomes larger than it is in the bulk on these sites.

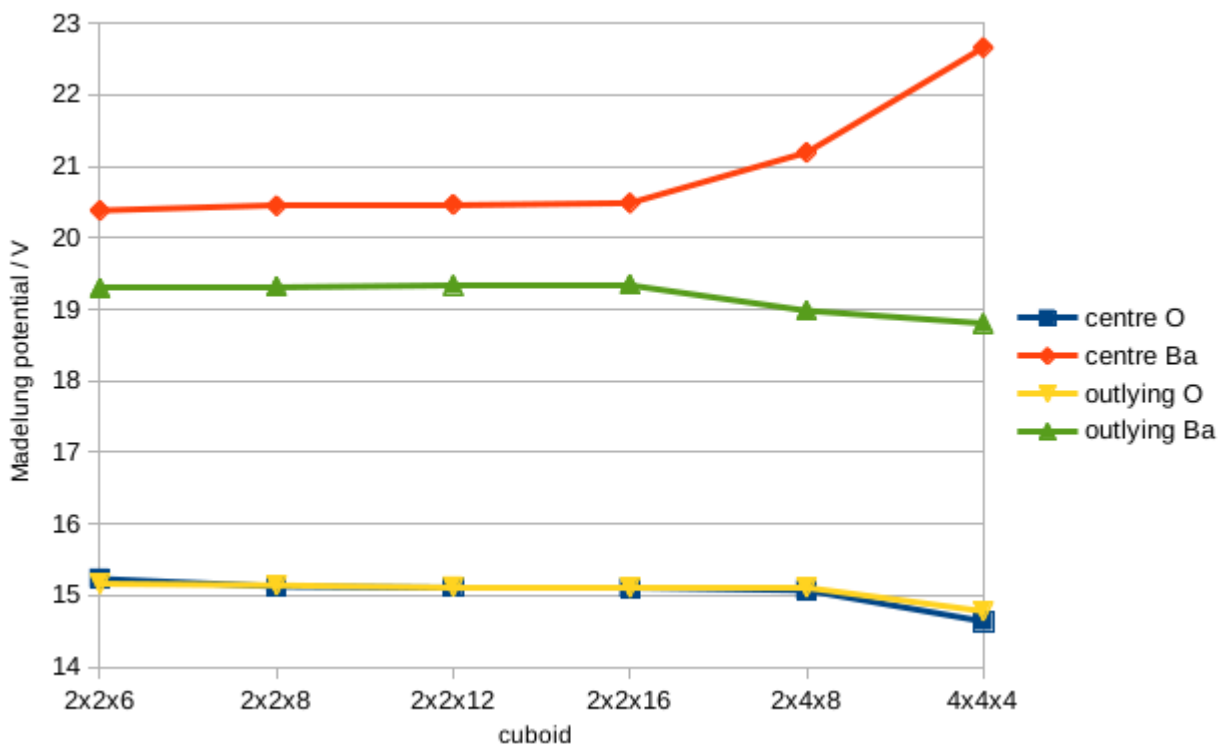


Figure 5.11: Madelung potential magnitudes at outlying and central ions in cuboid barium oxide clusters, as optimised by DFT.

Absolute values of Madelung potentials for both outlying and central sites are roughly the same for different lengths of $2 \times 2 \times N$ nanorods, but change when the structure is expanded along a different dimension. In that case, the Madelung potential for central Ba atoms becomes much stronger, while the Madelung potentials for the three other sites under investigation weaken slightly. The Madelung potential of central and outlying O^{2-}

is almost identical, while for Ba^{2+} , the central atom is significantly more stabilised than the outlying one.

The equivalent plot for magnesium oxide cuboids is shown in Figure 5.12. Most notably, the Madelung potential is stronger than in barium oxide, as expected due to what we know from the bulk and about bond lengths. Here, oxygens (which have more acute angles about them) are more stabilised, even when compared to the bulk, and magnesium cations are relatively destabilised, as the angles about them widen.

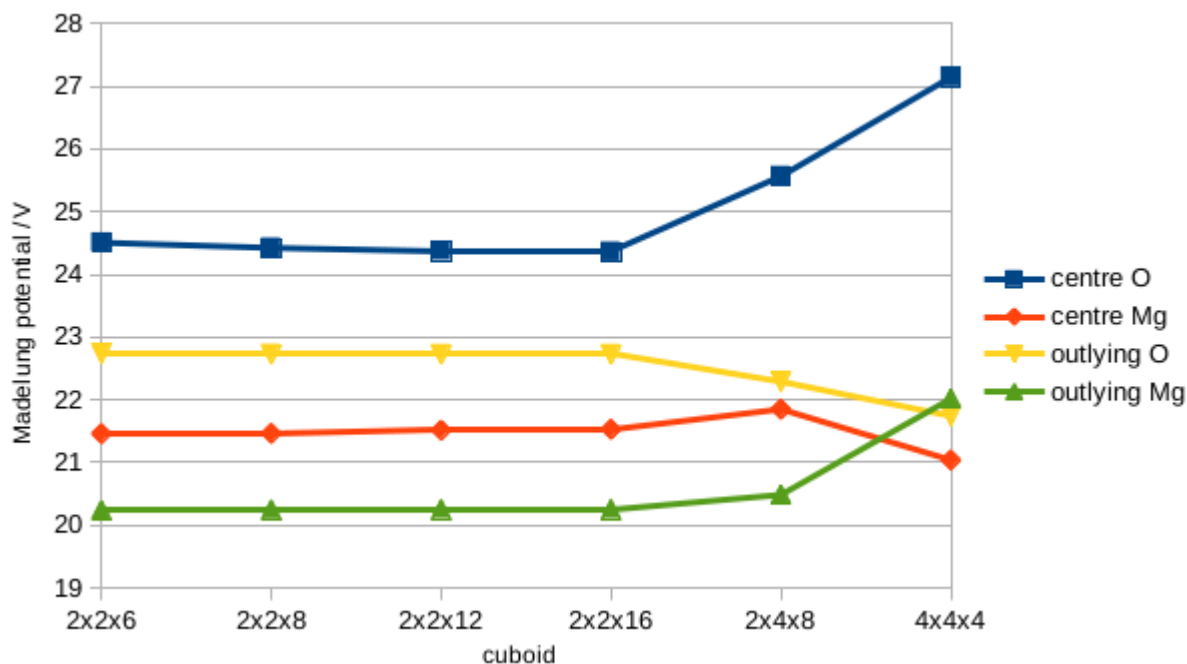


Figure 5.12: Madelung potential magnitudes at outlying and central ions in cuboid magnesium oxide clusters, as optimised by DFT.

Going from $2 \times 2 \times 16$ to $4 \times 4 \times 4$, Madelung potentials at the central O^{2-} and outlying Mg^{2+} sites, while they decrease at outlying O^{2-} and central Mg^{2+} sites; in fact, for the $4 \times 4 \times 4$ cluster, the Madelung potential of the outlying oxygen anion site is lower than that of the outlying Mg cation site, breaking with the general trend of Madelung potentials at Mg^{2+} sites being stronger.

The Madelung potentials of sites in $(\text{CaO})_n$ and $(\text{SrO})_n$ clusters lie somewhere between these two, with Madelung potentials at cation sites slightly stronger than those at oxygen sites for both.

Finally, we will look at the average value of the magnitude of the Madelung potential at ionic sites in all of these nanoclusters to see how strong overall stabilisation due to electrostatics is. These are shown in Figure 5.13 and Table 5.8.

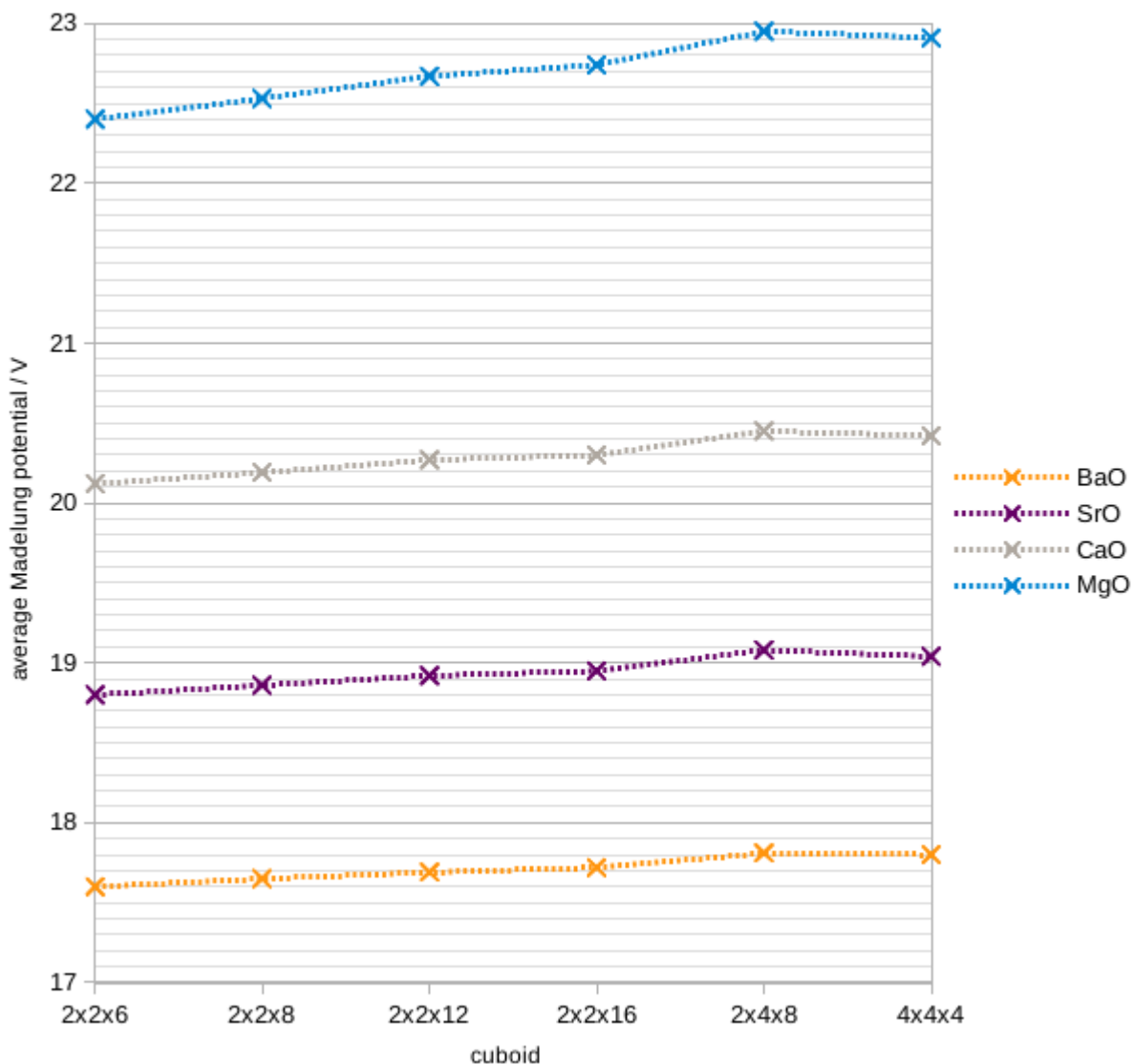


Figure 5.13: Average Madelung potential magnitudes at ionic sites in cuboid alkali earth oxide clusters, as optimised by DFT.

It can be seen clearly from the figure that in all 4 cases, the average magnitude of the Madelung potential at ionic sites increases when the length of a 2×2 -base nanorod is increased; this effect is strongest in magnesium oxide nanorods. It is also clearly visible that the $2 \times 2 \times 16$ cuboid has a lower average Madelung potential magnitude than the $2 \times 4 \times 8$ one in all 4 cases. What is slightly less clear from the figure, but can be

	MgO	CaO	SrO	BaO
$2 \times 2 \times 6$	22.40	20.12	18.8	17.60
$2 \times 2 \times 8$	22.53	20.19	18.86	17.65
$2 \times 2 \times 12$	22.67	20.27	18.92	17.69
$2 \times 2 \times 16$	22.74	20.3	18.95	17.72
$2 \times 4 \times 8$	22.95	20.45	19.08	17.81
$4 \times 4 \times 4$	22.91	20.42	19.04	17.80

Table 5.8: Average Madelung potentials across all ionic sites for MgO, CaO, SrO and BaO cuboids.

gleaned from the table, is that the average Madelung potential value at ionic sites actually *decreases* when going from $2 \times 4 \times 8$ to $4 \times 4 \times 4$ cuboids in all 4 cases - probably due to the error in $4 \times 4 \times 4$ calculations being geometrical in nature. This result is also in line with energy rankings of these $n = 32$ cuboids, where the $4 \times 4 \times 4$ cuboid was erroneously reported to be higher in energy (less stable) than the $2 \times 4 \times 8$ for all alkali earth oxides.

5.4 Summary and Conclusions

Geometry optimisations were performed for cuboid rocksalt cuts of MgO, CaO, SrO and BaO of sizes up to 80 atoms. It was found that there was a linear relationship between $1/n$ over the size of the clusters and their normalised clustering energy. This relationship was exploited to extrapolate generalised normalised clustering energies of 1D, 2D and 3D structures in a three-step method. Extrapolated energies were then compared to bulk energies from DFT calculations, and it was found that through this three-step method accurate bulk energies could be extrapolated, while a direct extrapolation from cluster energies led to less accurate results.

The energies of the cuboid nanoclusters were then examined in more detail. It was found that in most cases, for a given size the preferred cuboid was likely to be that which maximised volume and minimised surface area, i.e. the one closest to a cube geometrically, with the exception of BaO, where more oblong structures are preferred.

Madelung potentials were then calculated for strings of alternating Ba^{2+} and O^{2-} ions as well as selected cuboid rocksalt cuts of MgO, CaO, SrO and BaO. It was found that

for the string of ions, Madelung potentials of outlying ion sites become smaller the larger the structure, while those of central ion sites oscillate about some value. For the cuboids, it was found that neither outlying nor central ion sites have Madelung potentials which change much when a nanorod is lengthened; they do change when the nanocluster is grown in other dimensions instead of becoming a thin, long nanorod. It was also found that there is some correlation between the average magnitude of the Madelung potential at ionic sites with the energy rankings of different-dimensional cuboids of the same size.

Chapter 6

Barium Oxide nanoclusters on Graphene

6.1 Introduction

In practice, small nanoclusters such as the ones discussed herein are only metastable *in vacuo* as they will coalesce to form larger nanostructures or bulk material. Therefore, they are usually kept in some environment that stabilises them: they may be capped; suspended in some solution; or anchored on a surface, e.g., by defects in the surface. For this study, it was decided to investigate the barium oxide nanoclusters from Chapter 3 on a surface, namely graphene. In this form, they can be investigated experimentally, as well as used for potential applications such as catalysis.

Graphene is a commonly used substrate to deposit nanoclusters onto[147, 148], with defects in the graphene surface as well as functional groups on it (such as in graphene oxide (GO)) acting as anchoring points for the nanoclusters[149]. Titanium oxide nanoclusters on defective graphene have previously been investigated computationally using density functional theory (DFT)[76, 78, 150]. When functionalised as GO, it has the additional advantage of being transparent to electron microscopes, allowing for optimal imaging of the nanoclusters themselves.

The main challenge in a study of this BaO-graphene system, then, is to develop a

fast and computationally inexpensive method to calculate properties of the system and perhaps simulate its dynamics. This has been attempted here. Additionally, some static modelling of nanoclusters on defective graphene and (a model for) GO has been conducted.

6.2 Methods

This chapter is divided into two parts: In the first part, interatomic potentials were developed to model the interaction of barium oxide nanoclusters with a graphene surface. In the second part, DFT calculations were carried out to investigate how these nanoclusters interact with both pristine graphene and graphene oxide.

6.2.1 Development of interatomic potentials

In the first part of this chapter, attempts at developing interatomic potentials to model the interaction of barium oxide nanoclusters with graphene are presented. Details of the potential development will be shown in Section 6.3.

As experimental data was not readily available, all potentials are fitted to DFT data, which was collected using the FHI-aims code and the PBEsol GGA functional with a tight basis set, without the dispersion correction (which led to a potential for errors in cluster-surface interaction energies). Single point calculations were performed for this part. During the fit, the graphene sheet and the clusters were each kept at the same geometry and only their relative position was varied. As such, only the potential to be fitted (plus a constant term) was used during those calculations.

A range of potential types was tested; both the rigid ion model and the shell model, and both Morse and Buckingham/Born-Mayer potentials. Combinations of these were trialled with and without the presence of image charges.

6.2.2 DFT calculations of barium oxide clusters on Graphene and Graphene Oxide

In the second part of this chapter, clusters were first modelled approaching a fixed graphene surface, and then approaching a graphene surface functionalised with an alcohol group, respectively.

Calculations on the pristine graphene surface involved geometry optimisation of the cluster using the PBEsol functional, with a light basis set in a first step, and then refinement using a tight basis set.

Due to time and computer time constraints, calculations on graphene oxide involved the following steps: the functionalised graphene surface was optimised using first a light, and then a tight basis set and the PBEsol functional. Then, the cluster was positioned above the surface at a distance of 2.8\AA . The geometry was then optimized using a light basis set and PBEsol. Due to aforementioned time constraints, the structures resulting from this were not re-optimised using a tight basis set, instead only a single point calculation was run to make them comparable with our previous calculations which used a tight basis set.

6.3 Results

6.3.1 Fitting of potentials for the BaO-graphene interaction

Setup of the DFT calculations

Potentials were here fitted to DFT data gained from single-point calculations. As such, it was first necessary to find a suitable unit cell size for these DFT single-point calculations. After checking that in general, FHI-AIMS calculated properties (such as the band structure) of both graphite and graphene correctly, this involved finding a suitable size of the cell in the direction of the graphene plane (x and y directions in the unit cell) and a suitable separation between graphene sheets (z direction in the unit cell). This is illustrated

in Figure 6.1: the xy -plane is in the plane of the graphene sheet, with the z -direction perpendicular to it.

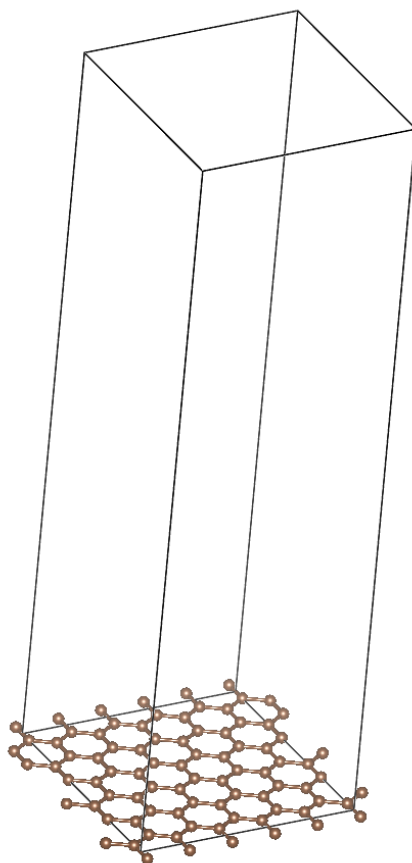


Figure 6.1: Example of a graphene cell, with large separation between graphene layers.

The z direction was investigated second. For this, calculations were set up with one 4-atom graphene primitive cell per unit cell while z was varied. The z length was varied from 2 Å to 60 Å. Overall, this looks as expected (see Figure 6.2, and for a breakdown in different distance ranges, Figure 6.3). In the short range ($< 3.5\text{Å}$), this looks like a standard repulsive potential (see Fig. 6.3a). From experimental data of graphite, we know that there should be a weak attractive force between graphite layers at a separation of about 3.3Å . However, in graphite the layers are arranged in a staggered (out-of-phase) manner (please refer back to Figure 1.2 for an illustration of this), and so we expect that with planes stacked in-phase here, the separation at which there is an attractive minimum is slightly larger because atoms are closer to each other at the same separation. Indeed,

what is found is a weak attractive interaction of less than -10 meV/4C with a minimum at just over 4\AA separation (Figure 6.3a). In the range of $6-10\text{\AA}$ (Figure 6.3b), some unexpected fluctuations can be observed. These are less than 0.05 meV/4C. We will nonetheless investigate what is causing these fluctuations. Moreover, we will investigate why there are also slight fluctuations around 40\AA .

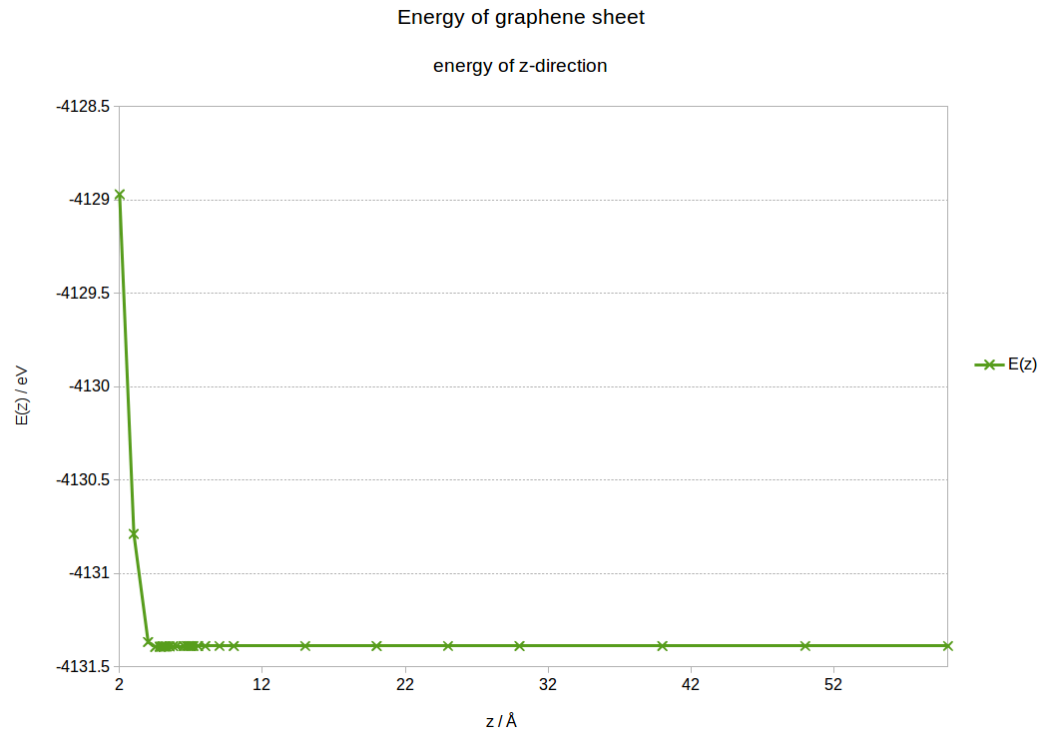
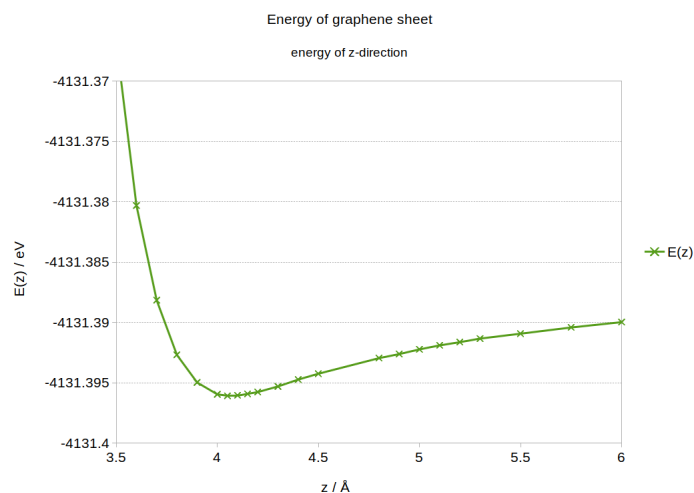
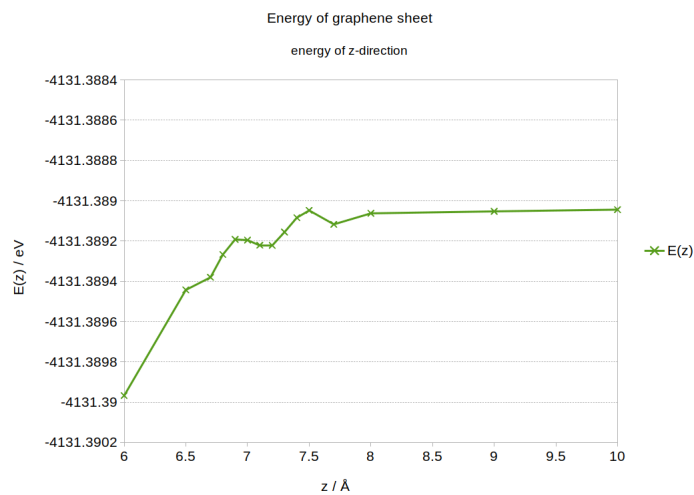


Figure 6.2: Energies of a 1×1 graphene sheet in a 3D periodic unit cell as a function of separation between sheets, as calculated using FHI-aims/PBEsol.

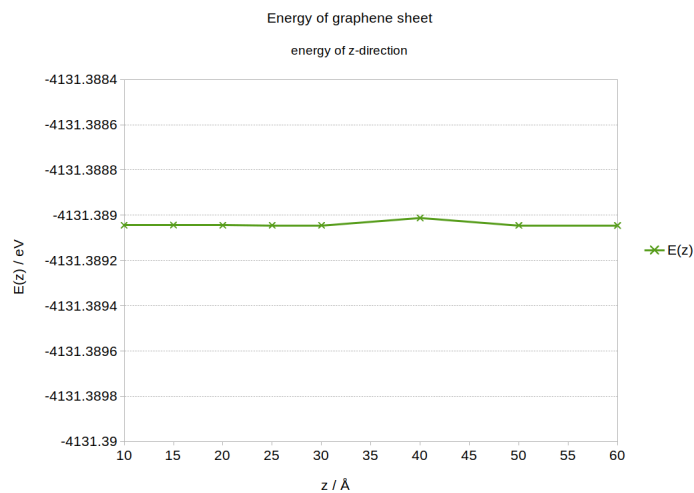
In order to investigate these fluctuations, calculations on the long range were run for the same unit cell with a larger basis set (up to second-tier improvements), and with a cell larger in the xy direction (Figure 6.4). Fluctuations with the larger unit cell are much less significant; however, the energy appears to be uniformly decreasing at this range which is contrary to expectation but can probably be safely ignored as this effect is $\sim 2\text{ }\mu\text{eV}/4\text{C}$. Additionally, the energies are all about $0.8\text{ meV}/4\text{C}$ higher.



(a) The weakly attractive short range, around the minimum



(b) Slightly longer range



(c) Long range – note fluctuation at 40 Å.

Figure 6.3: Energies of a 1×1 graphene sheet in a 3D periodic unit cell, different length ranges, as calculated using FHI-aims/PBESol.

When the basis set size was increased, fluctuations in the energy were reduced significantly; the difference between $z = 10$ and $z = 60$ values was also $\sim 2 \mu\text{eV}$. However, there were some convergence problems and FHI-aims had to be run with `override_illconditioning` set to `True` to get results for this because with large basis sets, ill-conditioned matrices arise. For this calculation, the larger basis set might at first seem like the better option as it will result in more accurate energies overall while also keeping fluctuations low, but there are convergence difficulties, and in subsequent calculations, where there is a nanocluster atop the surface, a larger xy -plane will be necessary, which is sufficient to eliminate this error.

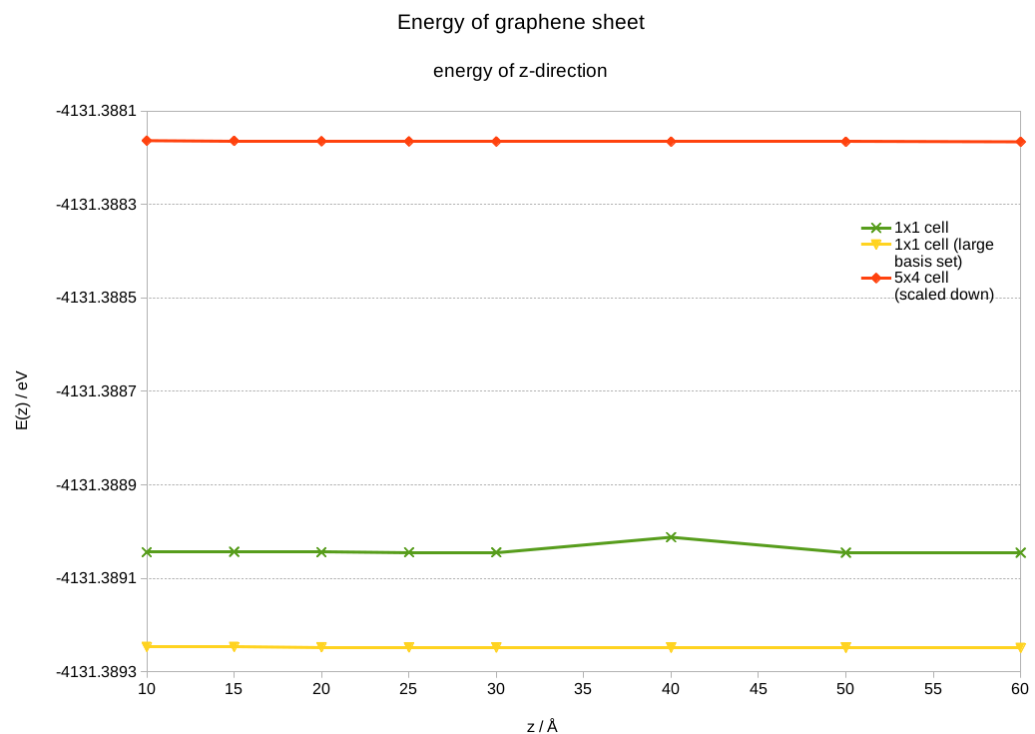
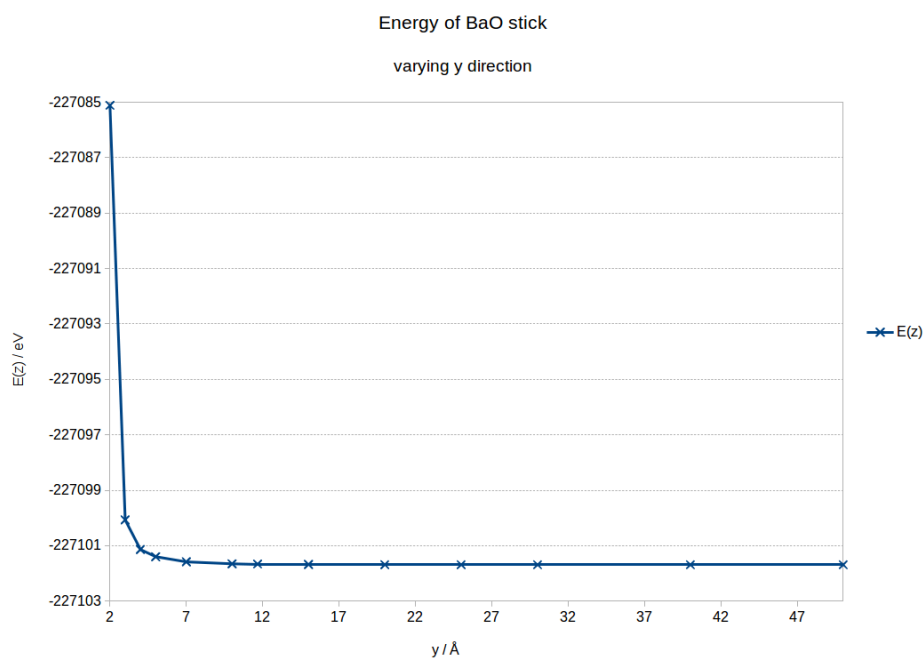
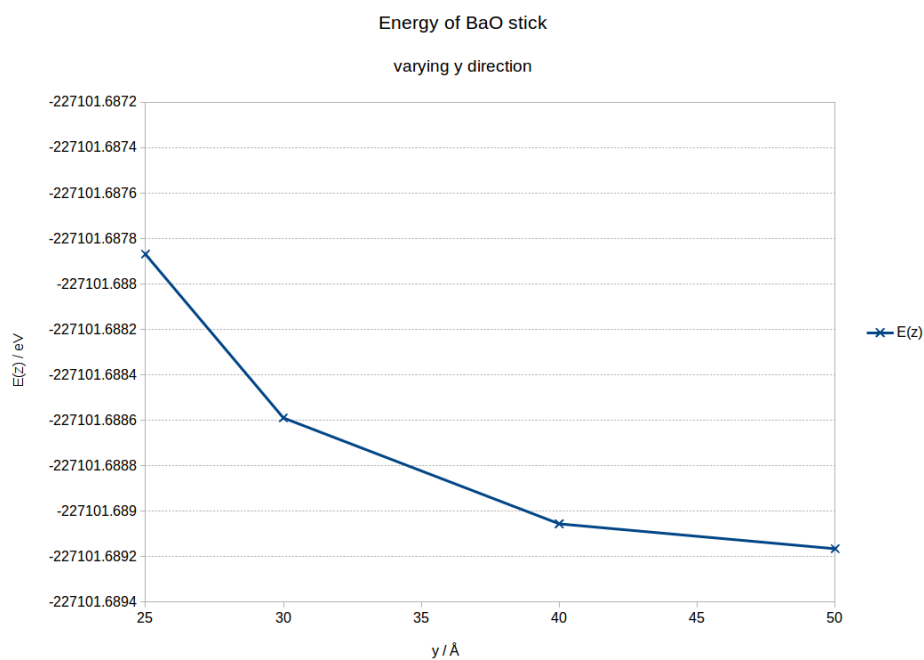


Figure 6.4: Energies of a 1×1 and 5×4 graphene sheet in a 3D periodic unit cell, with the z -length varied.



(a)



(b) Long range only

Figure 6.5: Energies of $(\text{BaO})_1$ in a $50\text{\AA} \times y \times 50\text{\AA}$ unit cell without graphene, where y is varied

Next, we try to find the extent of xy -plane for a nanocluster in an otherwise empty unit cell that is large enough that the interactions of the cluster with its periodic images are sufficiently small. Two directions (z and one of the directions of the xy -plane, y) are

kept fixed at 50 \AA , with the assumption that this is sufficiently large to have only minimal interaction with images of the cluster in adjacent cells along these axes. First, a stick – $(\text{BaO})_1$ at equilibrium bond length – is chosen. This will also be the first "model cluster" for potential parametrisation. Here, the interaction can be reasoned to be repulsive at any separation as like charges are always nearer each other than opposite charges. Indeed, this appears to be the case – see Figure 6.5.

From Figure 6.5 it is apparent that the forces in this system do seem to be repulsive at all length ranges (Subfigure 6.5a), but that the difference in interaction energy drops to about 0.1 meV between 40 and 50 \AA . Therefore, 40 \AA seems an appropriate choice.

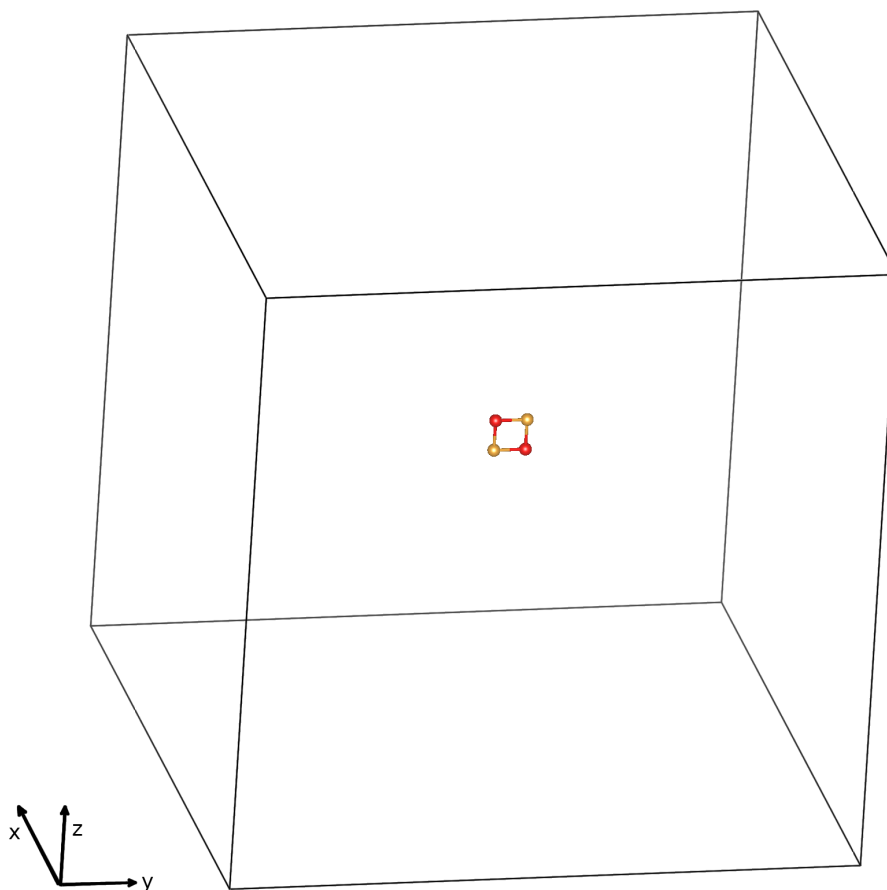


Figure 6.6: $(\text{BaO})_2$ square in a $50 \text{ \AA} \times y \times 50 \text{ \AA}$ unit cell, where y is varied.

Because this dominance of repulsive Coulomb interactions is not always found, the calculation was repeated with a square of ions, $(\text{BaO})_2$, at the equilibrium bond distance

for the $(\text{BaO})_1$ stick (i.e. not the optimised $(\text{BaO})_2$ cluster). This is situated in the xz plane with bonds parallel/perpendicular to the z -direction, while the y -coordinate is varied. Again, the energy change drops below 0.1 meV between 40 and 50 Å. However, there is now an attractive range with the minimum at ~ 3.5 Å and a well depth of ≈ 780 meV (likely more if the structure had been allowed to relax fully).

Ba-O stick on graphene: no image charges

A set of DFT single-point calculations was employed in order to get energies, which were then used to parametrise interatomic potentials, to model the interaction of graphene with barium oxide clusters. For this, clusters were simulated at different distances from the surface and different orientations. In a first attempt, the $n = 4$ cuboid cluster was used, however this did not immediately yield usable potentials. To step back, we reduced the problem to the $n = 1$ Ba–O stick, where one atom only is strongly interacting with the surface. And so, to start with, one potential at a time may be parametrised¹: Ba–C, or O–C, respectively. The stick was therefore positioned above the surface orthogonal to it in the "top" position (see Figure 6.7b) above the surface.

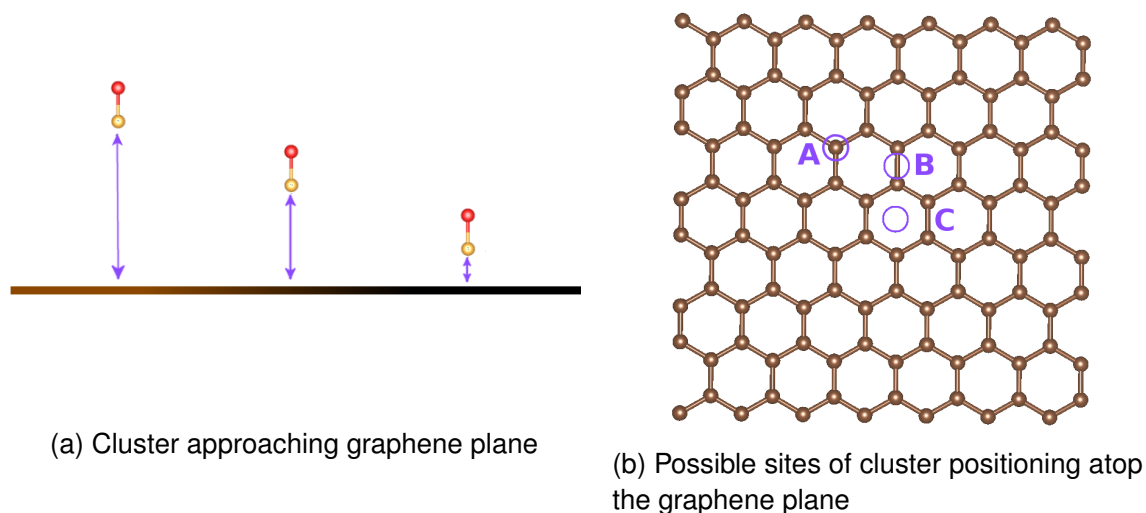


Figure 6.7: Model of the BaO stick above graphene: (a) varying the distance between the stick and graphene (b) above one of three possible sites on graphene: "top" atop an atom (A), "int" interstitially (B), or "centre" over the centre of a ring (C).

¹This is while keeping the system closer to $(\text{BaO})_n$ clusters than it would be using just Ba^{2+} and O^{2-} above the surface.

Distances between the surface and the nearer ion ranged from 2.2 Å to 10.0 Å; however, 6.5 Å is the upper end of the range where FHI-aims does not experience convergence problems (in the case of oxygen nearest the surface) or large fluctuations which appear unphysical (in the case of barium nearest the surface), so two different types of potentials each were tested, both including and omitting distances above 6.5 Å, keeping in mind that they should be less important for these short-range potentials. To begin with, only a single potential was fitted for each case, under the assumption that only the atom closest to the surface has a significant repulsive contribution to the energy due to charge overlap. Electrostatics were included, and to simplify the model in these initial potential parametrisations the rigid ion model was used so the charges were as detailed in Table 6.1.

Element		Charge
Ba	core	+2.0
O	core	-2.0
C	core	+0.0

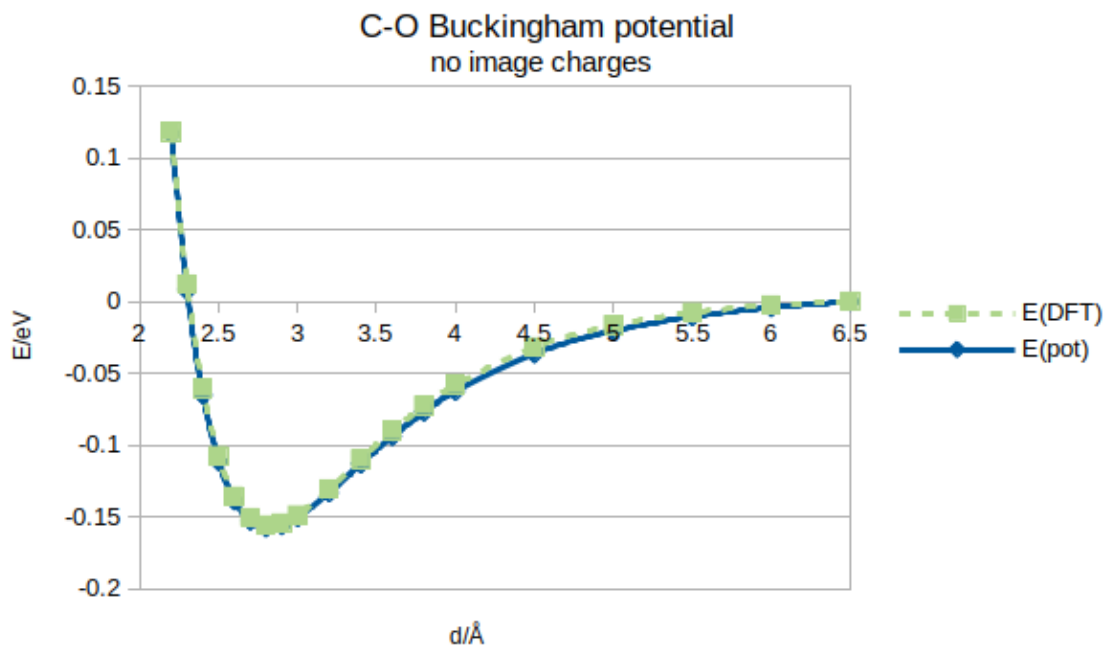
Table 6.1: Charges of barium, oxygen and carbon in the rigid ion model

The simplest case, then, is only considering one potential for the nearer ion and the Coulomb term, as well as a constant to be able to adjust the asymptote, as the zero of DFT energies is expected to be different from the zero of IP energies. We know the electrostatic term, and need to only model size effects. Both Buckingham and Morse potentials were parametrised in each case. Interactions here are between charged and non-charged species and attempting to fit both types of potential allows us to see whether these interactions are more covalent or ionic in character. The sum of squares S was noted down for each case, see Table 6.2.

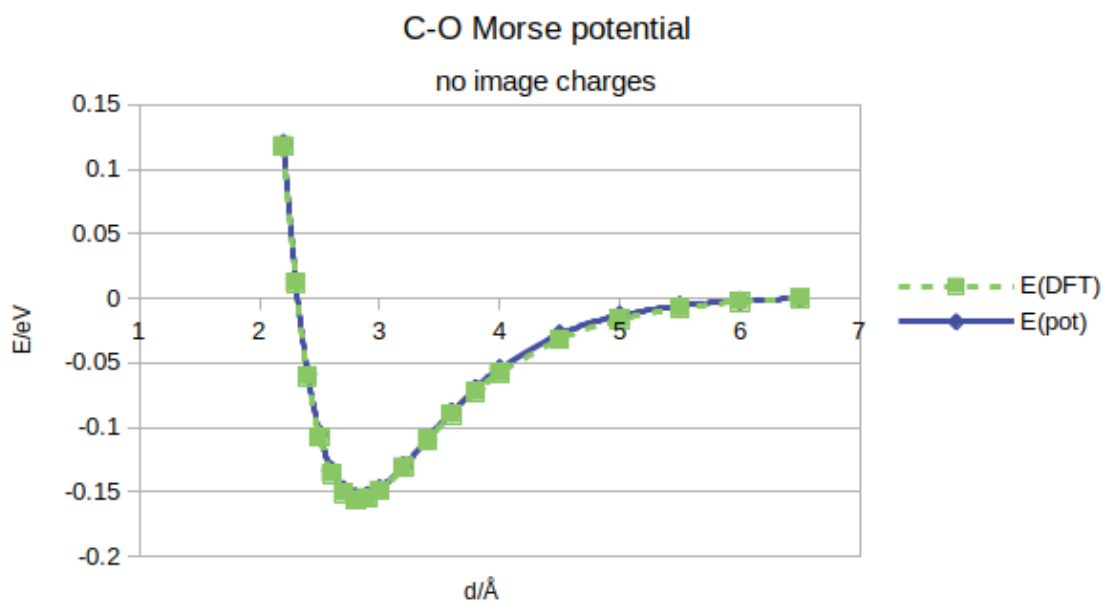
Potential form	Pair	S
Buckingham	O-C	0.000697
Morse	O-C	0.000317
Buckingham	Ba-C ($\leq 6.5\text{\AA}$)	0.006048
Morse	Ba-C ($\leq 6.5\text{\AA}$)	0.002659
Buckingham	Ba-C ($\leq 10.0\text{\AA}$)	0.011506
Morse	Ba-C ($\leq 10.0\text{\AA}$)	0.059547

Table 6.2: Sums of squares S for different single potentials of carbon interacting with oxygen and barium

Looking at the potentials and the DFT data they have been fit to together shows that agreement is very good. The energies are shown in Figures 6.8 (C–O potentials) and 6.9 (C–Ba potentials) and it is difficult to even distinguish most of the IP curves from DFT ones with the naked eye. Absolute errors for each are shown in Figure 6.11. The C–O errors are all below 3meV in magnitude, whilst the C–Ba errors are below 12meV in magnitude in the case of the Buckingham potentials, but the Morse potentials reach errors as high as 40meV in the long range. All potentials replicate the data they were fitted to very well. Table 6.2 shows that the Morse potential performs better in both scenarios. However, when the data that was excluded for the Ba-down potential ($d > 6.5\text{\AA}$) was included, it becomes apparent that the Buckingham potential performs much better, as this is where the high error in the Morse potential appears. In particular, in the long range of the Ba-down case the Morse potential approaches zero much too quickly and indeed approaches the wrong asymptote.

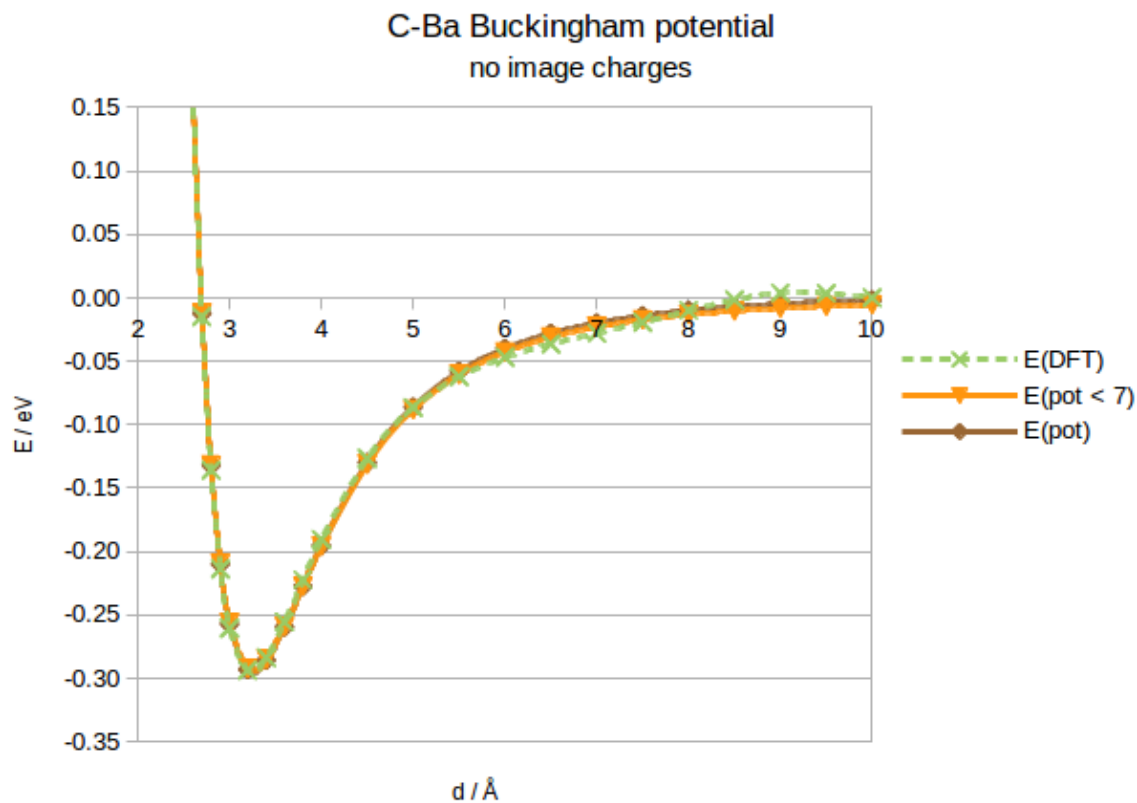


(a) C–O Buckingham potential

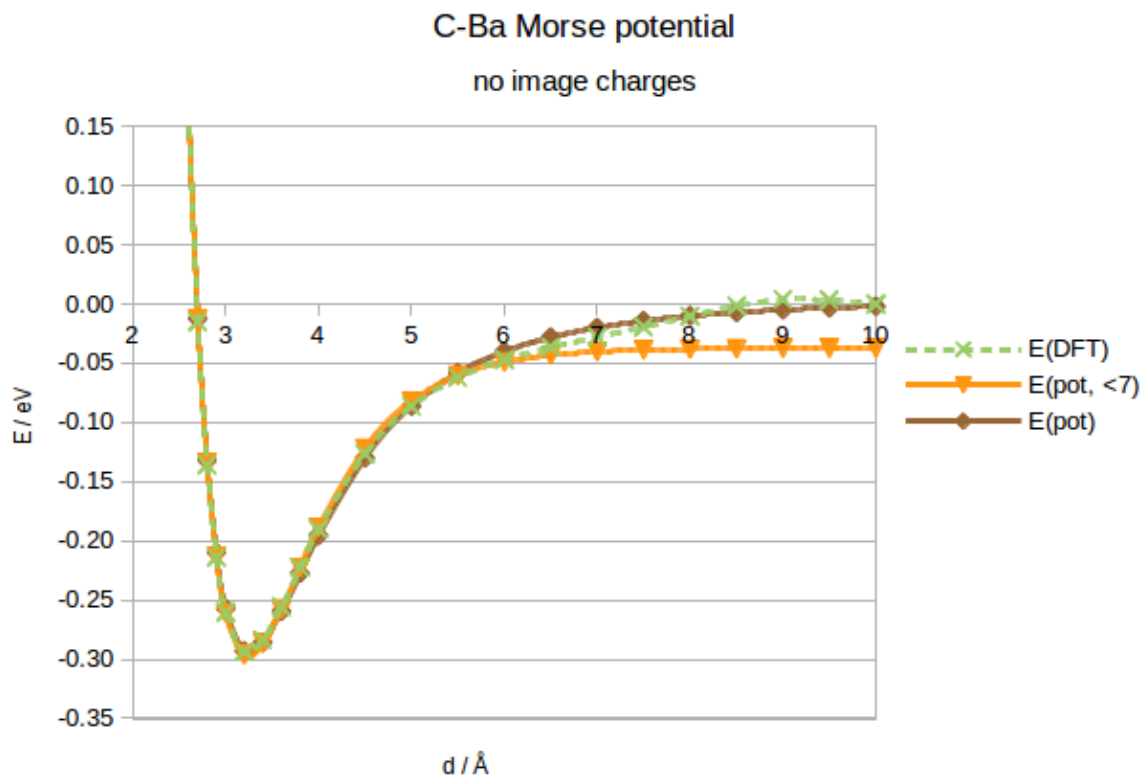


(b) C–O Morse potential

Figure 6.8: Single O-C potentials generated from the Ba-O stick approaching graphene, compared to DFT data

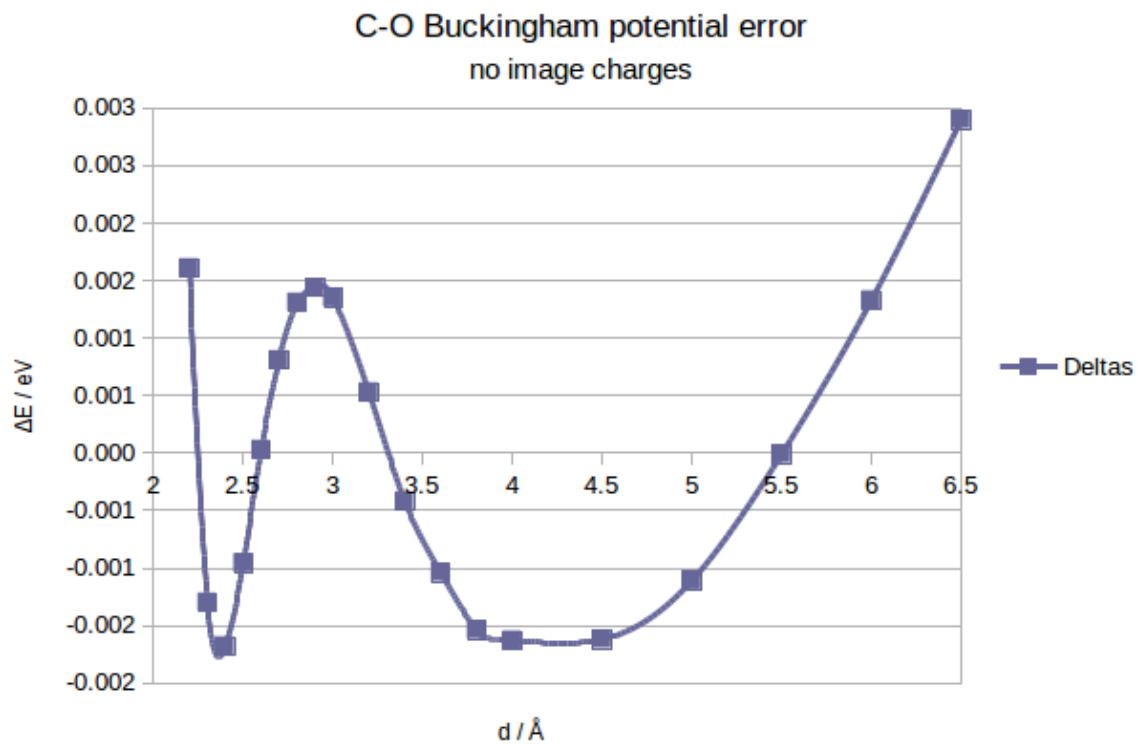


(a) C–Ba Buckingham potential

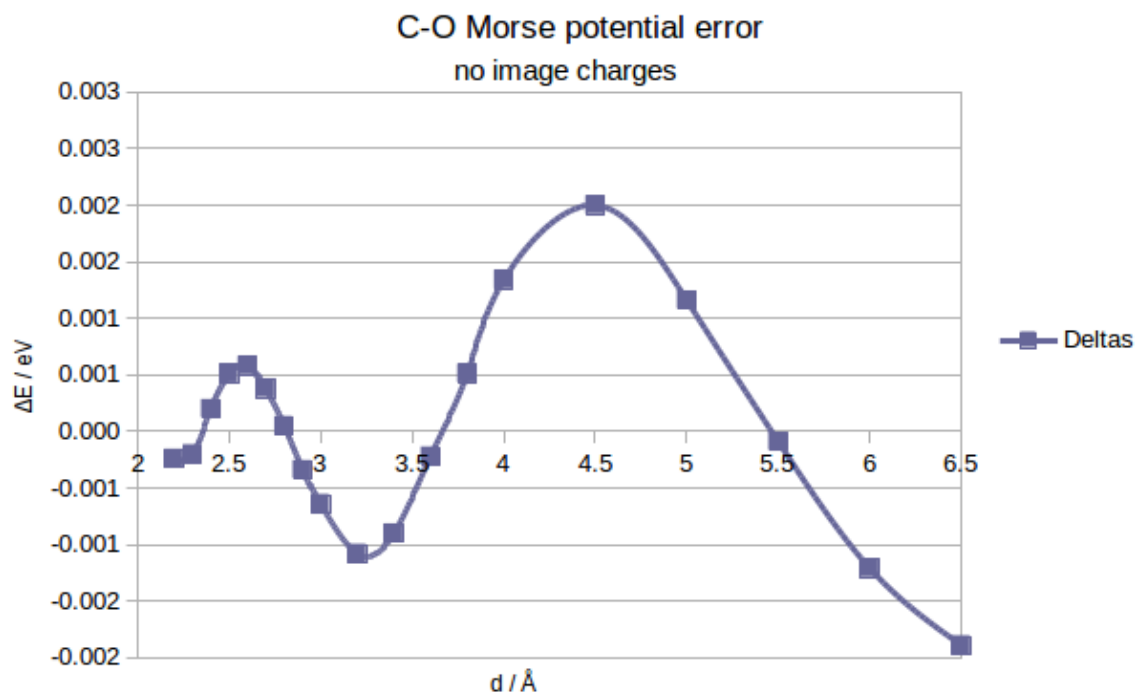


(b) C–Ba Morse potential

Figure 6.9: Single Ba-C potentials generated from the Ba-O stick approaching graphene, compared to DFT data

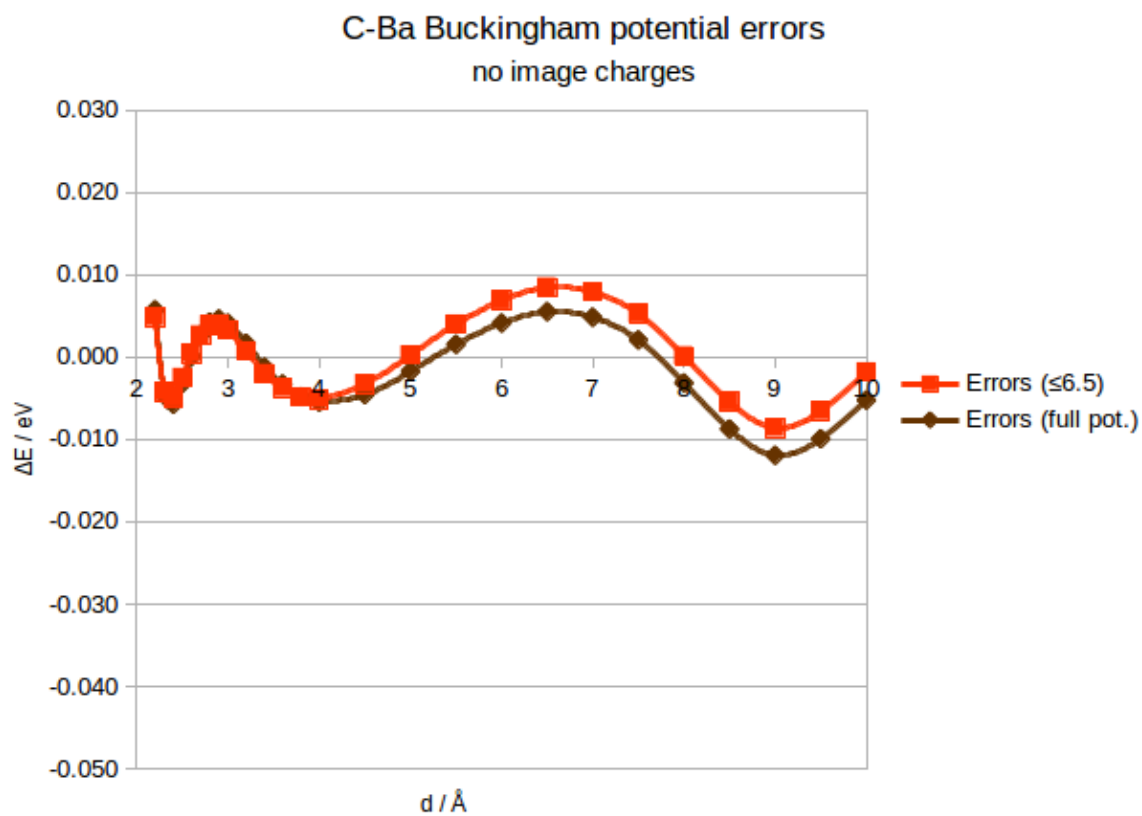


(a) C–O Buckingham potential error

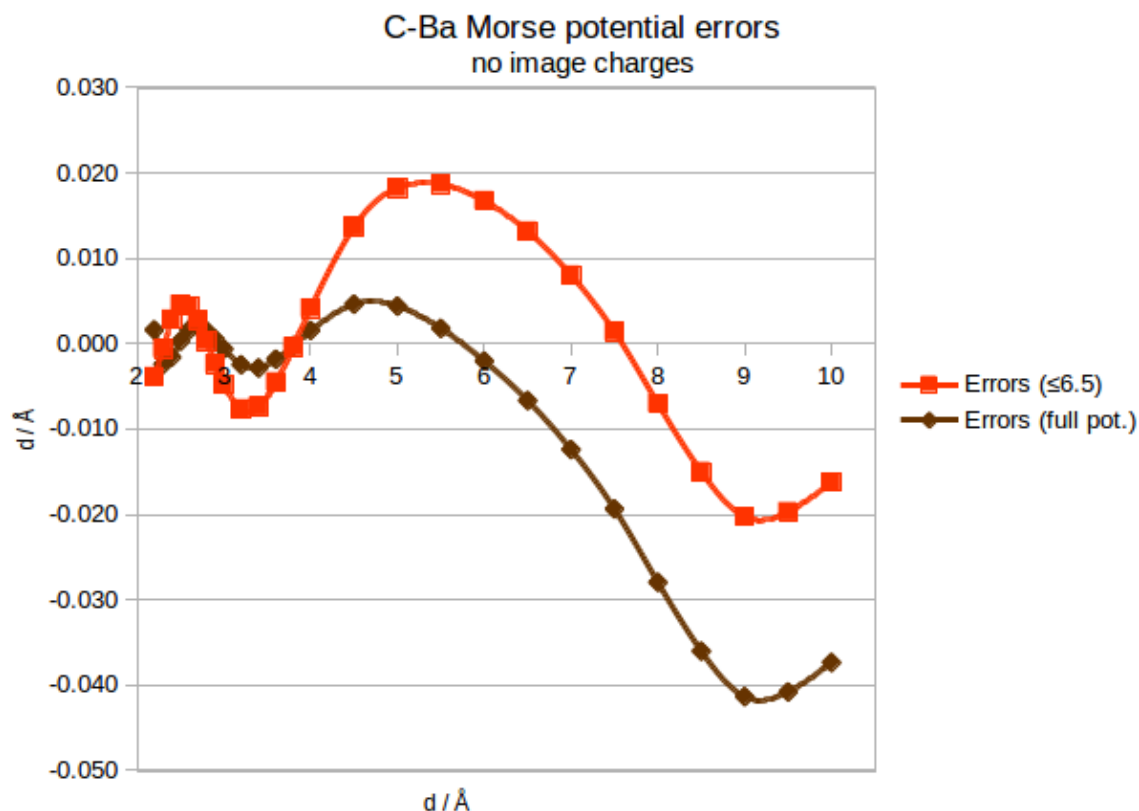


(b) C–O Morse potential error

Figure 6.10: Errors in single O–C potentials generated from the Ba–O stick approaching graphene, relative to the DFT data they were parametrised against



(a) C–Ba Buckingham potential error



(b) C–Ba Morse potential error

Figure 6.11: Errors in single Ba–C potentials generated from the Ba–O stick approaching graphene, relative to the DFT data they were parametrised against

The parameter values of the potentials used as a starting point going forward are as shown in table 6.3 (with sums of squares S cited).

O core – C core Morse		Ba core – C core Buck	
S	0.000317	S	0.011506
D_e / eV	0.013369	A / eV	151.821156
$a / \text{\AA}^{-1}$	1.571146	$\rho / \text{\AA}$	0.094453
$r_0 / \text{\AA}$	3.281059	$C / \text{eV \AA}^6$	75.768208

Table 6.3: Parameter values of single potentials (C–O and C–Ba) to model the approach of the Ba-O stick toward graphene

In the next step, instead of using one potential per orientation, two potentials (C–Ba and C–O) were fitted simultaneously. When combining 2 potentials to model the curves for each of the orientations, we expect to improve the accuracy of the "main" potential (for the element facing the graphene surface), whilst receiving fairly unreliable values for the further away element which is not accurately captured in the short range here – this will be improved upon in the next step.

O nearest the surface		s.sq.	0.000192
O core – C core Morse		Ba core – C core Buck	
D_e / eV	0.007422	A / eV	151.821156
$a / \text{\AA}^{-1}$	1.659252	$\rho / \text{\AA}$	0.094453
$r_0 / \text{\AA}$	3.400141	$C / \text{eV \AA}^6$	75.768208
Ba nearest the surface		s.sq.	0.002961
O core – C core Morse		Ba core – C core Buck	
D_e / eV	15073.052564	A / eV	2656.310036
$a / \text{\AA}^{-1}$	1.733533	$\rho / \text{\AA}$	0.313498
$r_0 / \text{\AA}$	-3.345021	$C / \text{eV \AA}^6$	78.120996

Table 6.4: Parameters of pairs of potentials when optimised for one orientation. The potentials which are likely to be unreliable are greyed out.

As can be seen in Table 6.4, these potentials still differ greatly, and the potentials for the atom that is further away from graphene have changed significantly from the previous potentials, whereas the ones for the closer atom are at least still within the same order of magnitude. Additionally, very large changes in these further away potentials led to very small improvements in the sum of squares during the development of the pairs of potentials as expected, so the data sets were simply too insensitive to changes in these potentials to optimise them well, so the next step was to combine both orientations, using the "closer atom" potentials as a starting point. From the sums of squares we can see that having a second potential to account for the second ion improves fit quality.

Next, a pair of potentials was fitted to both orientations simultaneously, with resulting values shown in Table 6.5, and their percentage difference from the initial potentials shown in Table 6.6.

Ba core – C core Buck		O core – C core Morse	
A / eV	3065.95055	De / eV	0.006452
ρ / Å	0.307204	a / Å ⁻¹	1.679617
C / eVÅ ⁶	90.663526	r ₀ Å	3.420378

Table 6.5: Parameters of pairs of potentials when optimised for both orientations.

Ba core – C core Buck		O core – C core Morse	
A	2.514 %	D _e	51.739 %
ρ	0.397 %	a	6.904 %
C	2.733 %	r ₀	4.246 %

Table 6.6: Absolute difference in parameters of potentials optimised for both orientations compared to those optimised for one orientation.

Most notably, there is a $\sim 50\%$ change in the value of D_e in the C–O potential, but a large percentage corresponds to a very small change here as D_e , representing the very shallow well depth, is very close to zero. More generally, the difference in parameters for

the O–C potential is also more pronounced, see Table 6.6. This could be indicative of previous calculation difficulties in the "O down" configuration of our model system. The sum of squares for both orientations is 0.006747, so still sufficiently low to be considered a good fit.

The data from these best $n = 1$ potentials compared to DFT data for both orientations is shown in Figure 6.12. Again, it is difficult to see a difference between the potential data and the DFT data with the naked eye, in line with the very small sums of squares.

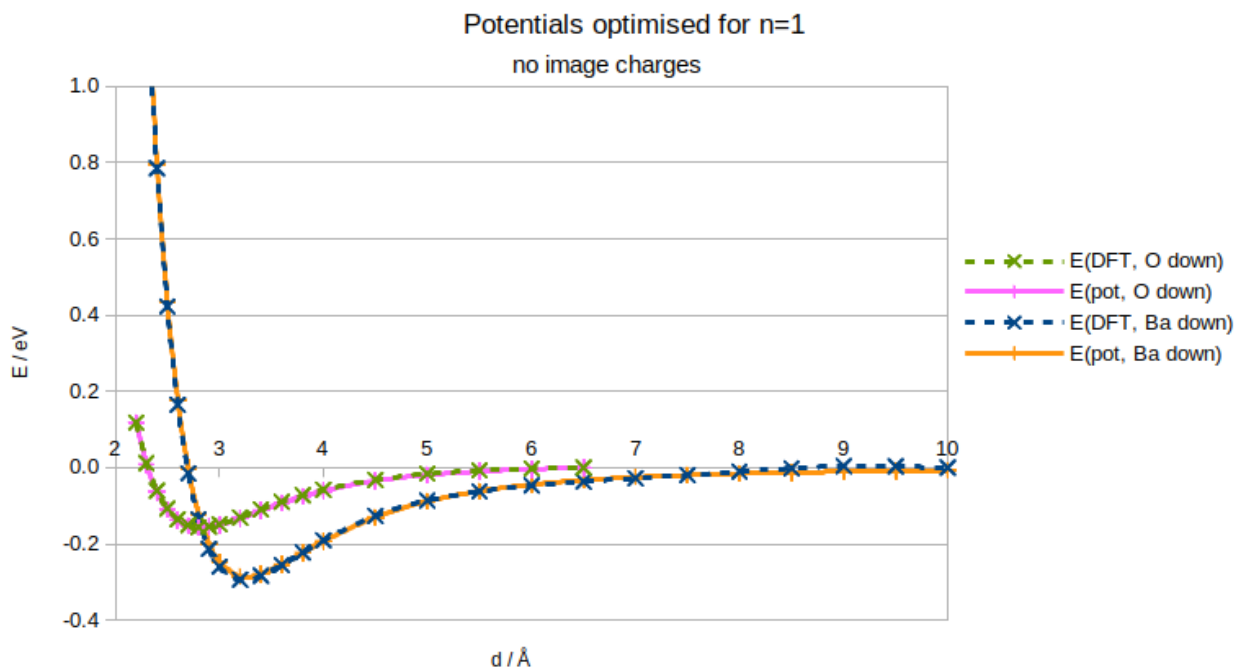
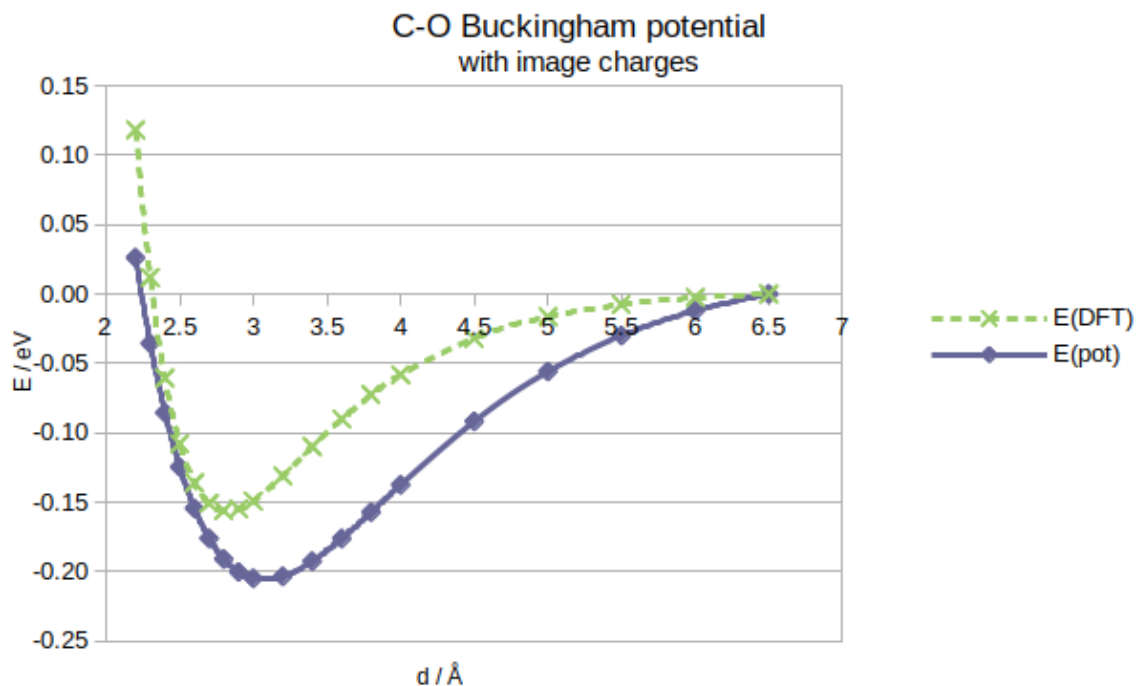


Figure 6.12: Potentials fitted to both orientations of the Ba–O stick, as compared to DFT data for this system.

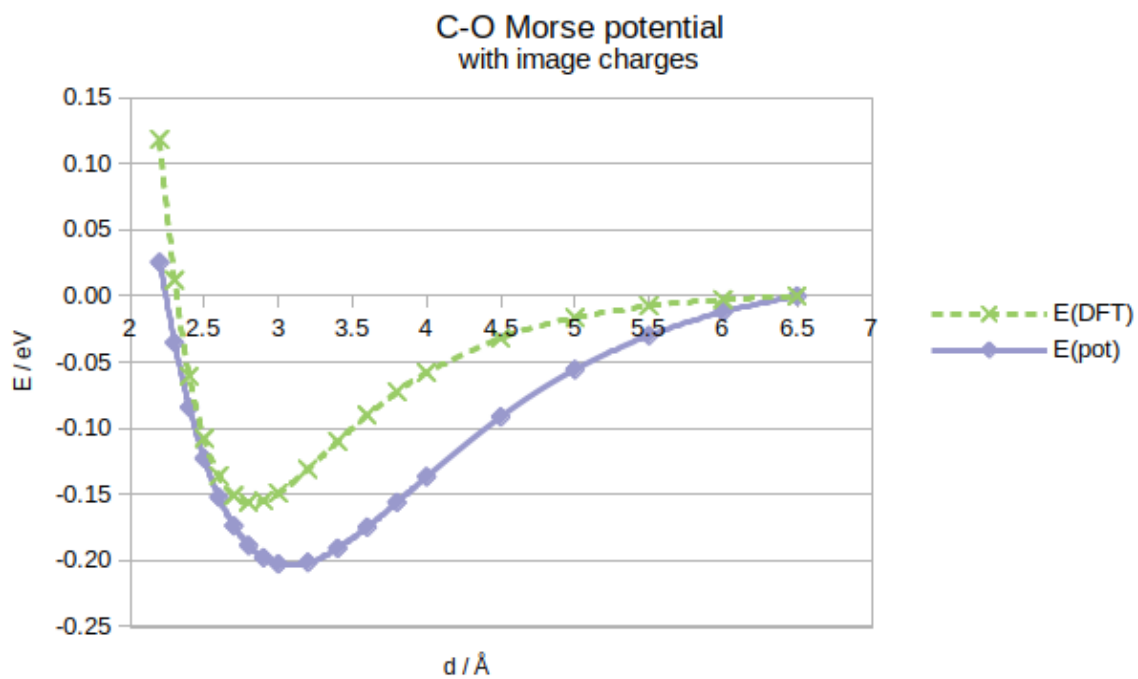
Image charges

One possible physical improvement to this model is the addition of image charges. When a charged or polar particle is present above a metallic (i.e. conductive) surface, we can expect a change in the electrostatic potential as if there were another particle of equal and opposite charge mirrored below the surface. In terms of potentials, for each ion in our nanocluster we now try adding another ion of equal and opposite charge below the surface. It is important that this ion is the "mirror image" of the ion above the surface.

Hence we constrain this image charge to move with the real ion, with x - and y -coordinates of both ions being equal, and, holding the surface fixed at $z = 0$, their z coordinates equal but with opposite sign.

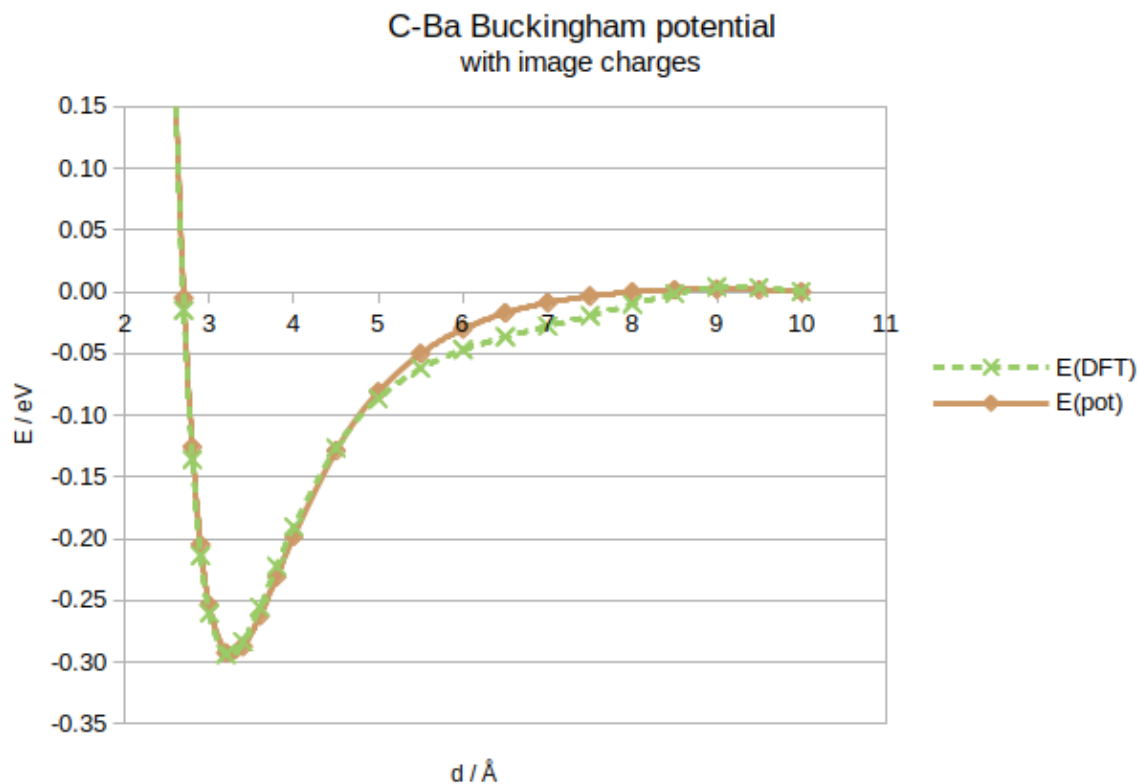


(a) C–O Buckingham potential

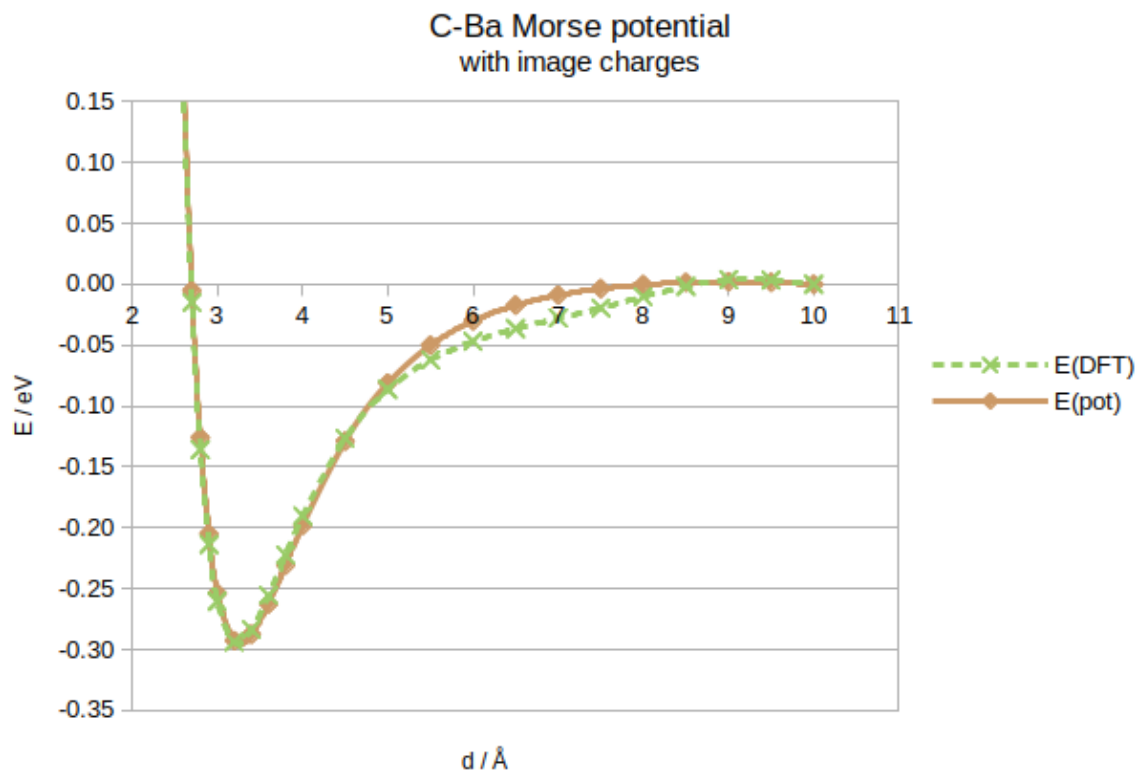


(b) C–O Morse potential

Figure 6.13: Single O–C potentials generated from the Ba–O stick approaching graphene, with image charges, compared to DFT data

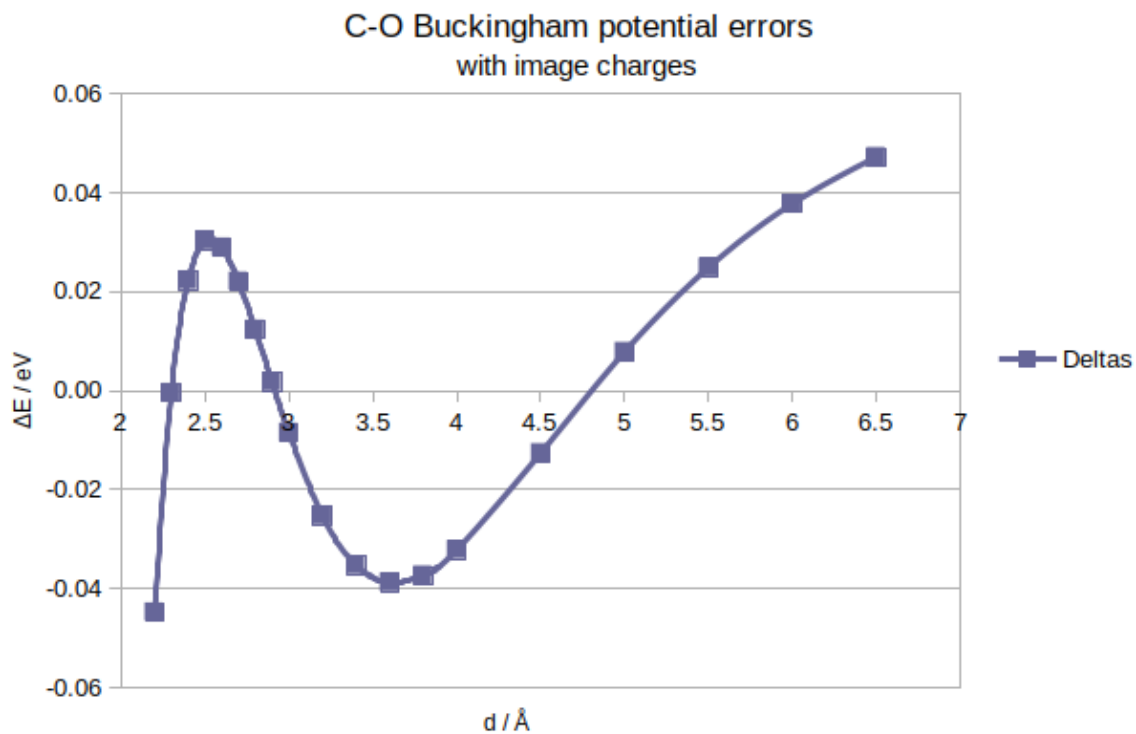


(a) C–Ba Buckingham potential

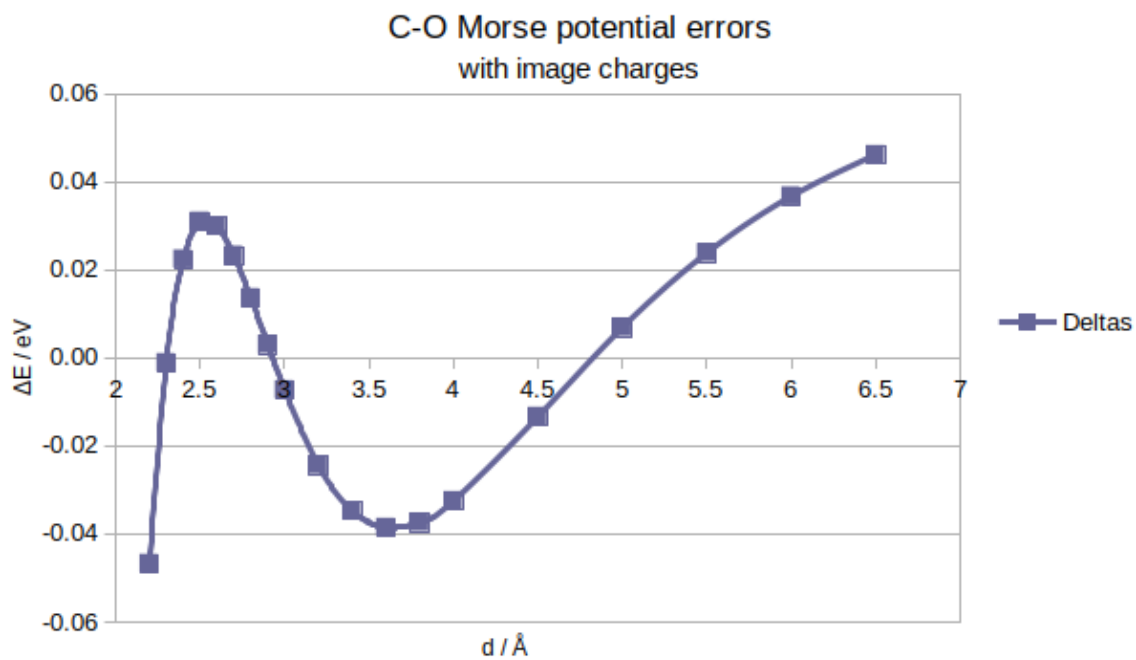


(b) C–Ba Morse potential

Figure 6.14: Single Ba–C potentials generated from the Ba–O stick approaching graphene, with image charges, compared to DFT data

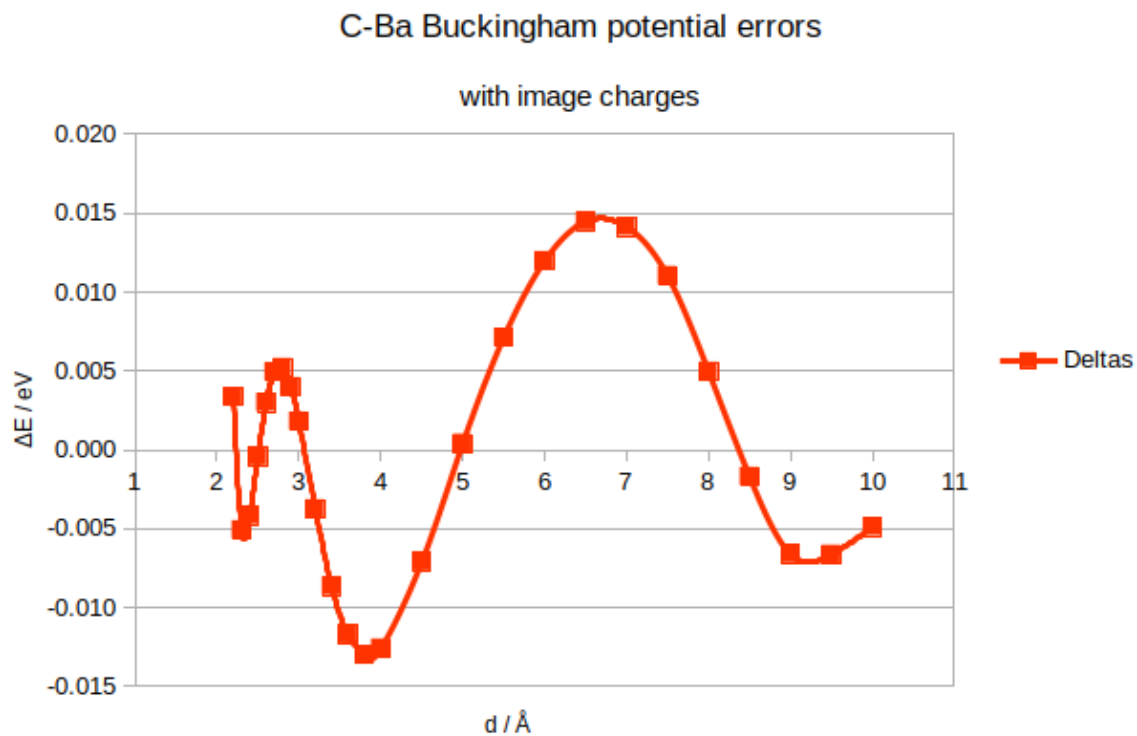


(a) C–O Buckingham potential

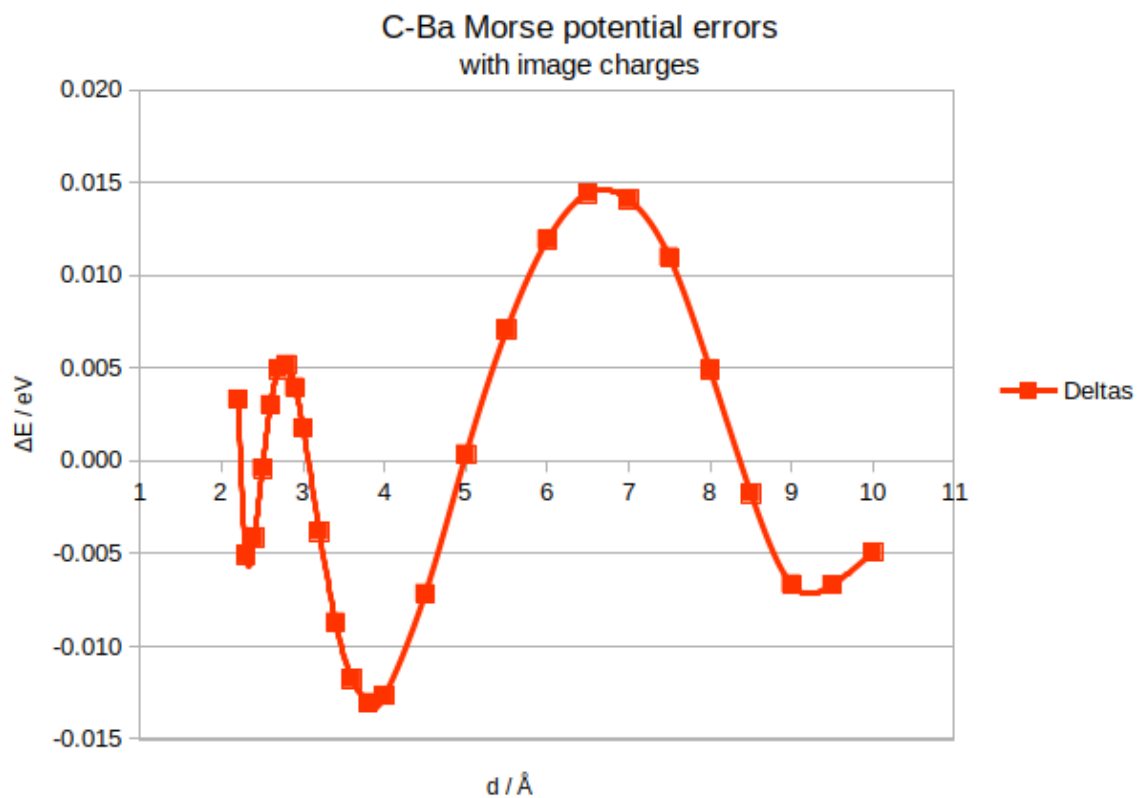


(b) C–O Morse potential

Figure 6.15: Errors in single O–C potentials generated from the Ba–O stick approaching graphene, with image charges, compared to DFT data



(a) C–Ba Buckingham potential



(b) C–Ba Morse potential

Figure 6.16: Errors in single Ba–C potentials generated from the Ba–O stick approaching graphene, with image charges, compared to DFT data

As before, the parameters for the potentials are developed separately, and then put together with both potentials optimised for each orientation. The results for separate potentials are shown in Figures 6.13 and 6.14. The most striking observation is that the C–O potentials are very strongly mismatched from DFT data, with their minimum at too large an interatomic distance, the asymptote at too high a value, and being generally too spread out. This effect appears to be nearly identical for both Buckingham and Morse potentials. The C–Ba potentials have much smaller errors and are too narrow instead of too spread out, with their minima appearing to be at slightly too close an atomic separation. If we now plot the errors of each potential (shown in Figures 6.15 and 6.16), it will indeed become apparent that the errors of the two different functional forms are very similar to each other.

These two potentials were then further refined with equivalent steps to those without image charges. The fit of the final potentials to DFT data is shown in Figure 6.17. These potentials fit DFT data much better than the initial ones. However, we can still see a difference between the energies as calculated using our new IPs compared to DFT energy with the naked eye, so it looks like this fit is markedly worse than that without image charges. Indeed, values for these potentials are captured in Table 6.7. Note that here, both are purely repulsive (Born-Mayer) potentials because all attractive interactions are captured by electrostatics and image potential terms. The sum of squares of this fit is 0.016197, about three times that of the fit without image potentials.

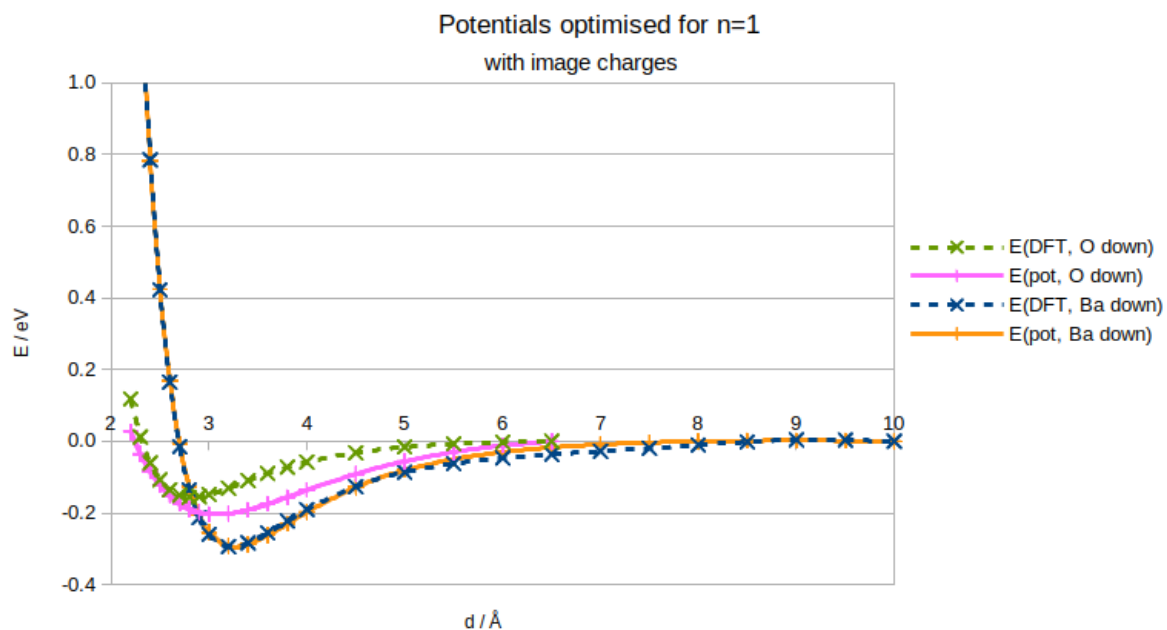


Figure 6.17: Potentials fitted to both orientations of the Ba–O stick, as compared to DFT data for this system, with image charges.

Ba core – C core Buck		O core – C core Buck	
A / eV	2634.553852	De / eV	42.466122
$\rho / \text{Å}$	0.304224	$a / \text{Å}^{-1}$	0.488378
$C / eV \text{ Å}^6$	0.0	$r_0 / \text{Å}$	0.0

Table 6.7: Parameters of potentials optimised for both orientations of the Ba–O stick above graphene, with image charges.

Testing these potentials

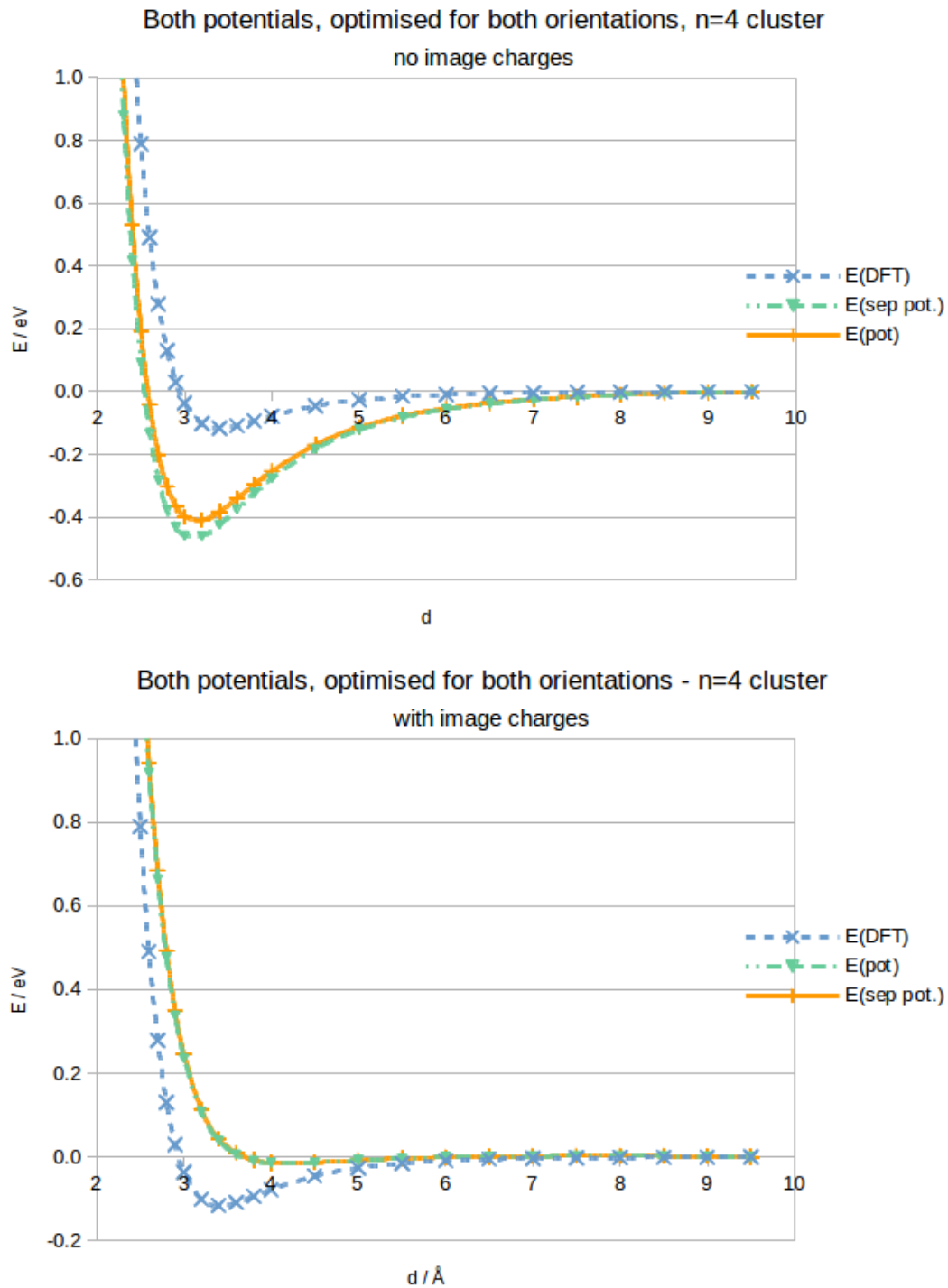


Figure 6.18: $n = 1$ potentials when applied to a $n = 4$ cluster approaching the graphene surface.

Both sets of potentials were tested on the $n = 4$ cuboid cluster above the graphene surface with its centre in the "top" position, with a barium atom closest to the surface. Re-

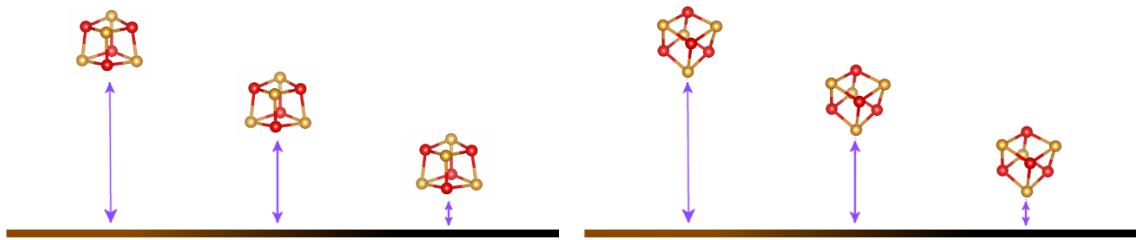
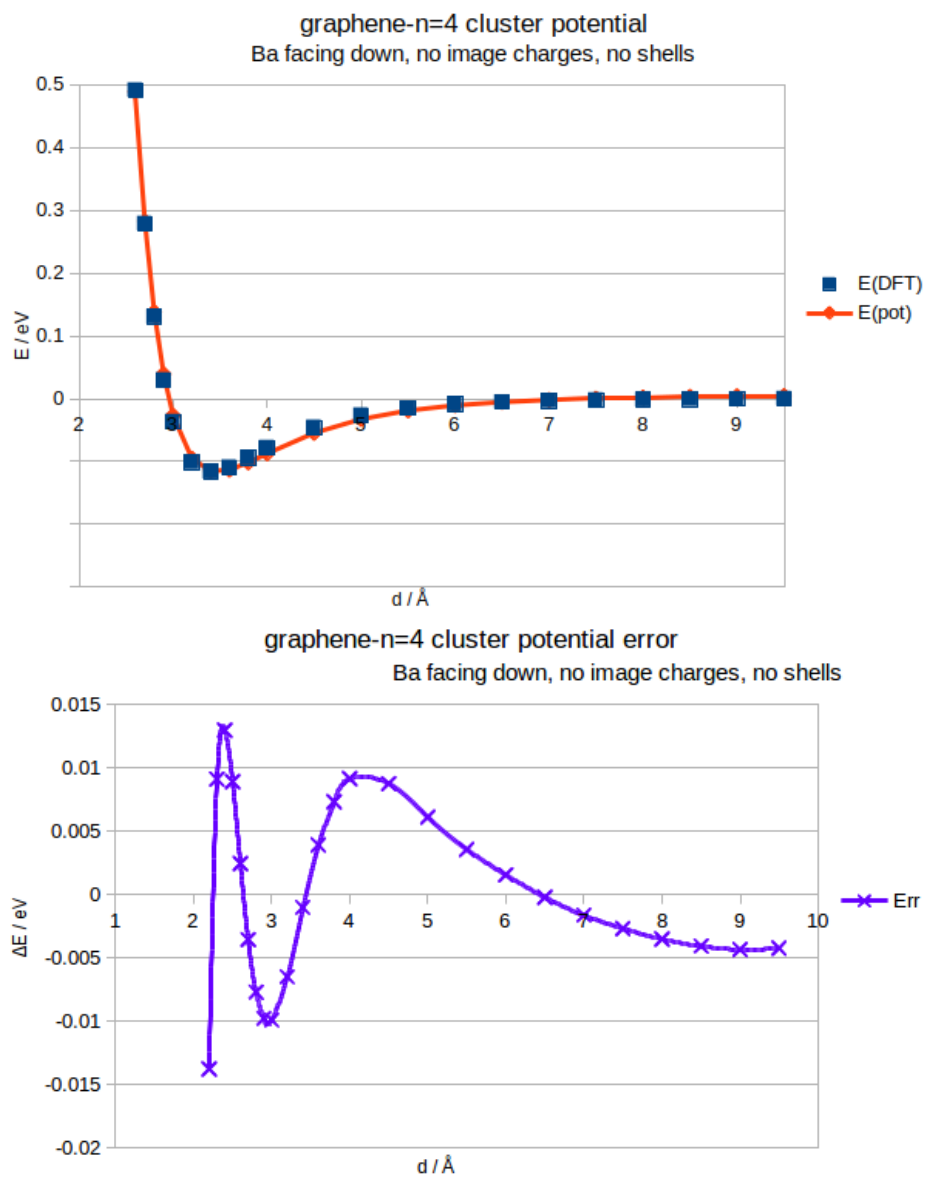
sults of this are shown in Figure 6.18. The separate potentials (where different potentials were optimised for different orientations) are indicated in green, DFT energies in blue and the final potentials which were parametrised for both directions in orange. Both with and without image charges, the difference between the two sets of potentials is dwarfed by their difference to the DFT data. When no image charges are included, the attractive well predicted by the potentials is too deep by a factor of about 3.5 and its minimum is at too short a range. With image charges, attraction is underestimated by a factor of about 8.2 and the minimum is at too long a range.

If we assume this approach to developing potentials, i.e. using the $n = 1$ stick, is sound, the answer would then lie somewhere in between, perhaps with a partial (screened) image charge. However, it is quite likely that potentials from the $n = 1$ stick simply do not have very good carryover to larger clusters. This is because the $n = 1$ stick is simply too chemically dissimilar from the other clusters to be a model for their physicochemical environment. However, these potentials give a decent starting point for refinement using larger clusters for the parametrisation – something that had been difficult to do without a first guess.

$n = 4$ Potentials

Using the $n = 1$ potentials as a starting point, a new set of potentials was developed with the $n = 4$ cluster as a basis instead of the $n = 1$ stick. The idea here was that this would be much more similar to larger clusters, especially cuboids. There are multiple orientations in which this cluster may approach the graphene surface, two of them which have been used here are shown in Figure 6.19.

First, potentials were optimised for this cluster with one of its barium atoms facing the graphene surface. The result of this is shown in Figure 6.20. The potential's energies fit the data well, with errors staying below 15 meV and a sum of squares of 0.023877.

(a) $(\text{BaO})_4$ cube, flat(b) $(\text{BaO})_4$ cube, Ba facing downFigure 6.19: $(\text{BaO})_4$ cube approaching grapheneFigure 6.20: $n = 4$ barium down potentials, and fitting errors.

The potentials optimised for the $n = 4$ cuboid with Ba facing the graphene surface were then tested on the same cluster, but approaching the surface with one of its surface planes parallel to the graphene as in Figure 6.19a. The result of this is shown in Figure 6.21. Most notable is the difference in well depth. The well depth predicted by DFT is 0.4 eV, while the well depth when using potentials is 0.2 eV. The d at which the minimum lies and other features of the plot are more accurate, but this underestimation of the attraction means that the potential needs to be improved somehow.

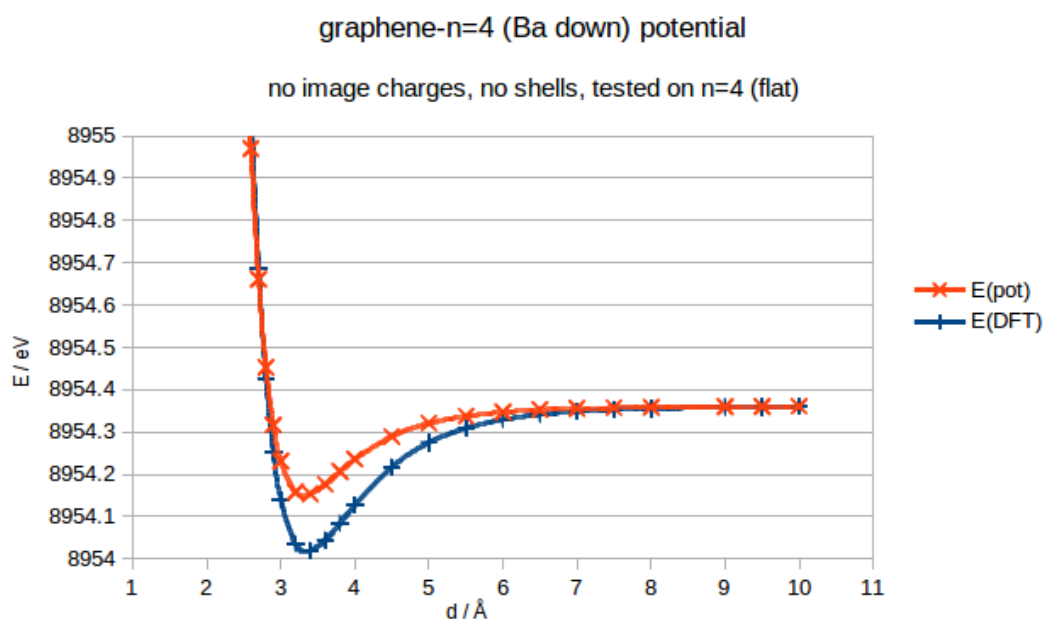


Figure 6.21: $n = 4$ potentials, optimised for $n = 4$ with barium facing the surface, tested on flat $n = 4$ cluster, no shells, no image charges.

One route toward further improvements is to include this data with the cluster approaching the surface in the "flat" configuration in the data used to parametrise the potential. This was done successfully (see Figure 6.22).

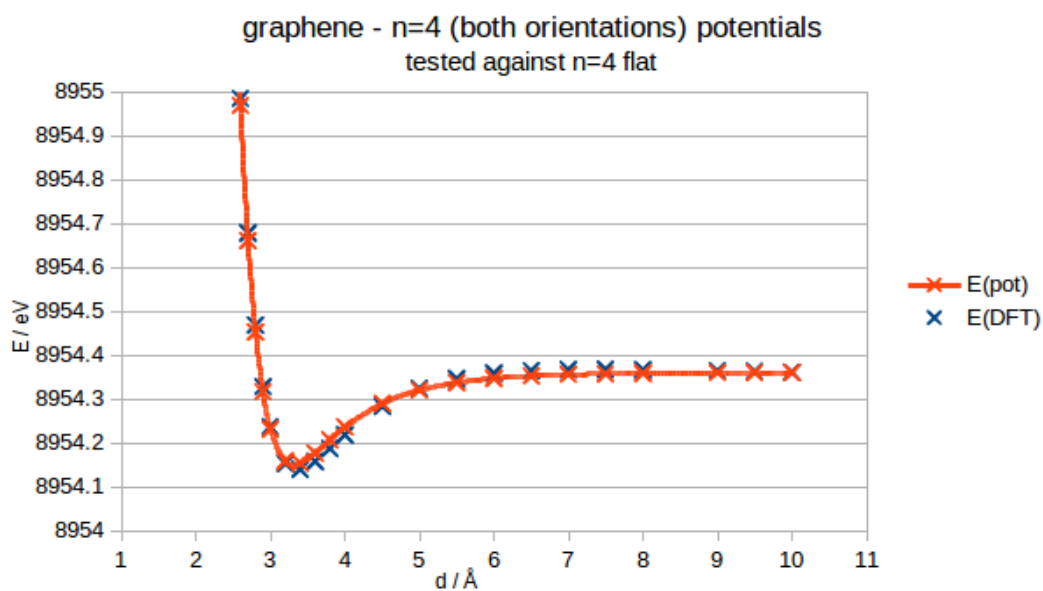


Figure 6.22: $n = 4$ potentials optimised for multiple cluster orientations, tested on the cluster flat above the surface, no shells, no image charges.

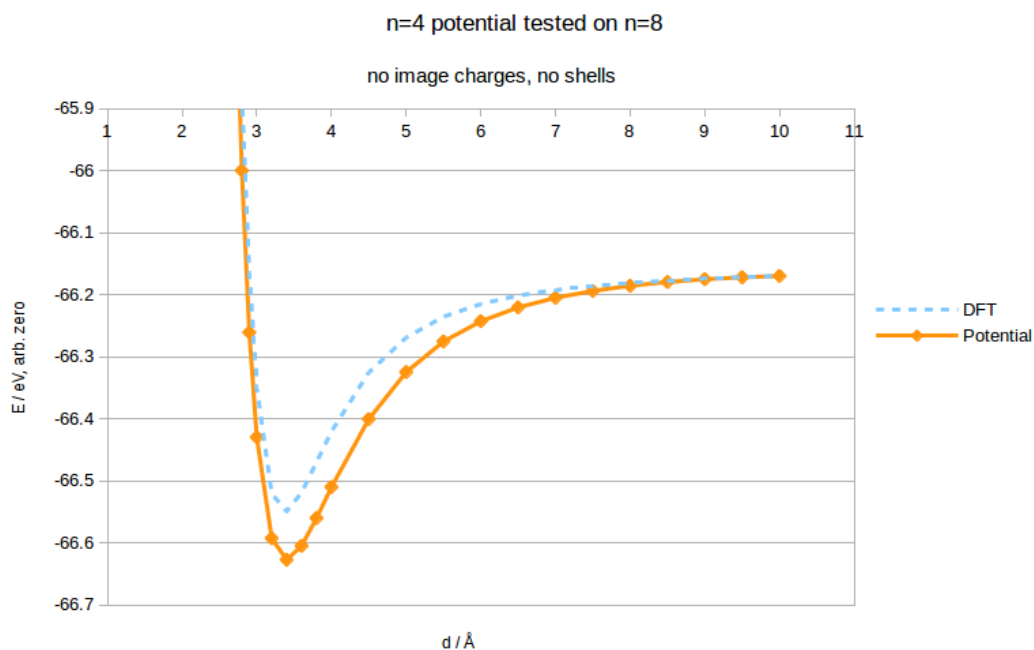


Figure 6.23: $n = 4$ potentials, tested on $n = 8$.

The new potential was tested against the $n = 8$ cuboid cluster approaching the surface (with a 4-atom face toward the surface). The result of this is shown in Figure 6.23. The well depth is overestimated – while the DFT well depth is 0.35 eV, the well depth predicted by the potential here is 0.45 eV, so the overestimation is by 29%. The energies

of this potential also approach the asymptote in the far limit too quickly. However, this still appears to be a large improvement over previous potentials.

Adding Shells to Model Polarisation

To improve upon the previous potential, the potential taken from barium facing the graphene surface was re-parametrised iteratively, this time with shells on barium and oxygen ions. Charges and spring constants were taken from the Lewis et al. potentials[109] which were used for BaO previously and are tabulated in Table 6.8.

shells		
Ba	core	9.2030
Ba	shell	-7.2030
O	core	1.0000
O	shell	-3.0000
C	core	0.0000
spring constants		
Ba		459.2000
O		41.7800

Table 6.8: Charges and spring constants for all cores & shells, as used in the shell model here.

Errors in the fit are in the same range (~ 15 meV or less, with a sum of squares of 0.030381 cf. 0.023877 without shells), similar as before (Figure 6.24), and suitably small. This was then again tested against the "flat" dataset – this is shown in Figure 6.25. This time, the potential correctly predicts the well depth and equilibrium distance between the cluster and the graphene surface, but underestimates strength of binding in the 4-6Å region. Overall, this potential performs better than that without shells, even though it is parametrised against a smaller data set.

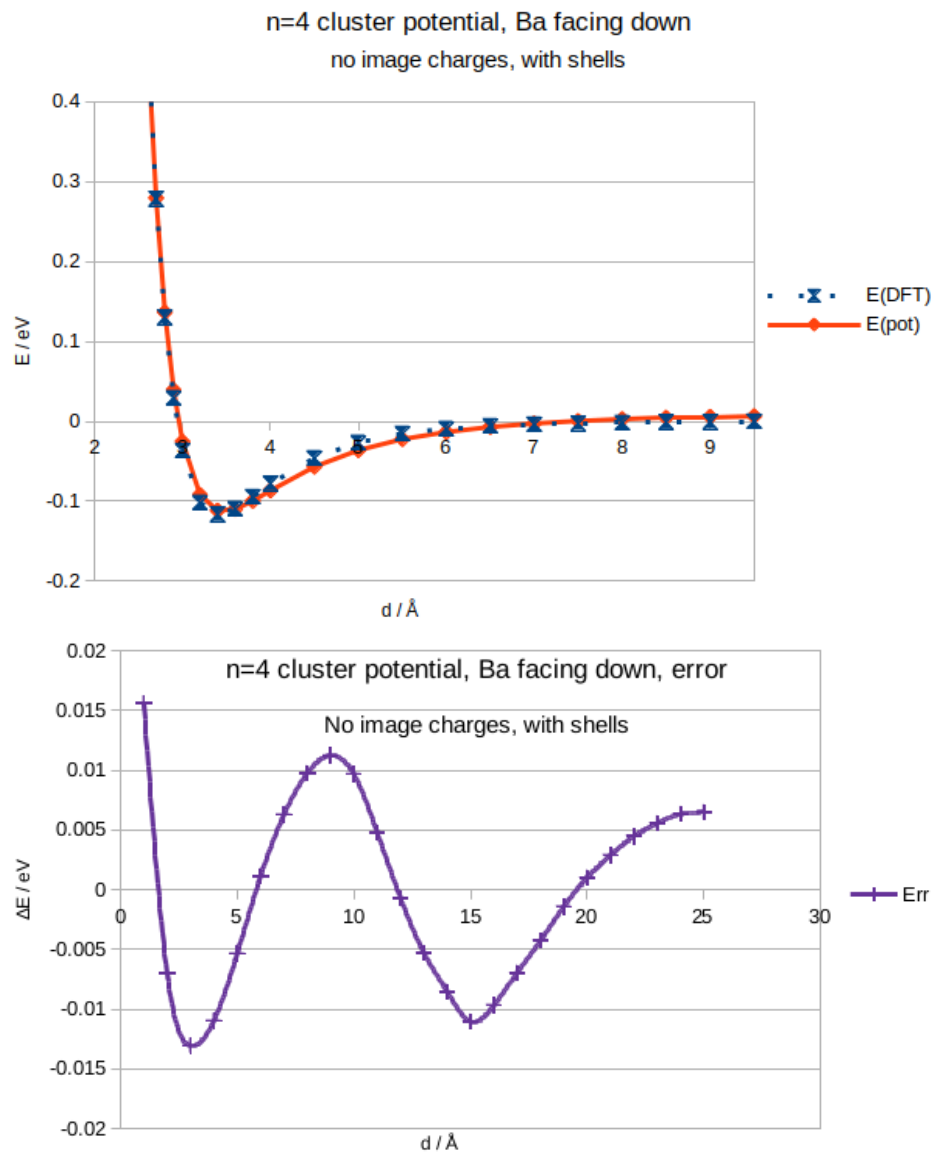


Figure 6.24: Potentials parametrised for the $n = 4$ cluster with barium facing the surface compared to DFT data, and corresponding errors.

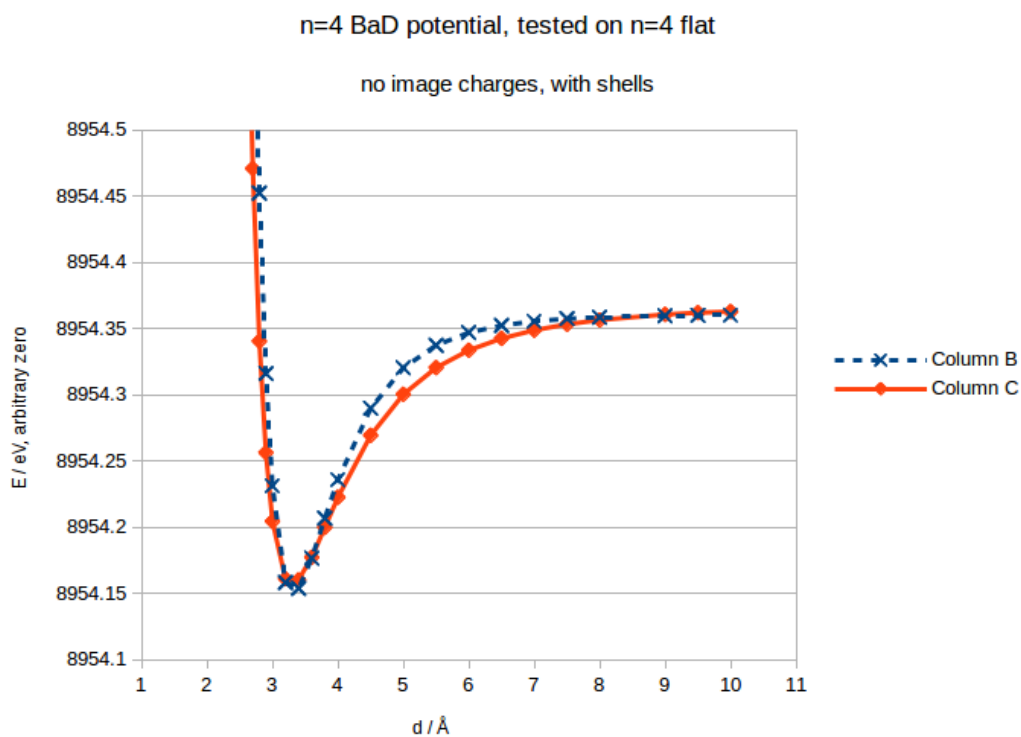


Figure 6.25: Potentials parametrised for the $n = 4$ cluster with barium facing the surface, tested on flat cluster, with shells, no image charges.

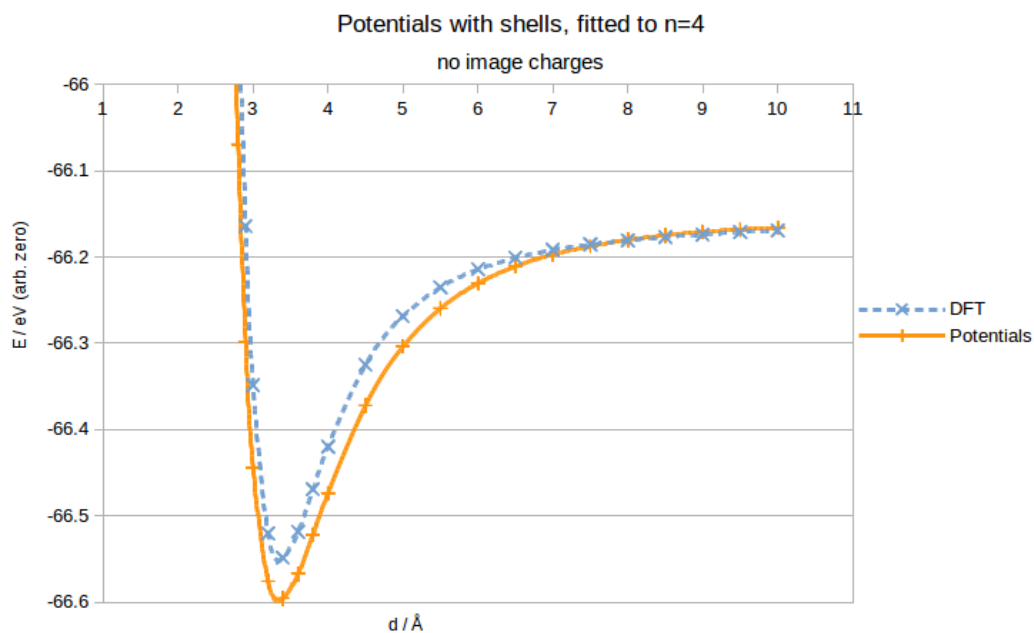


Figure 6.26: $n = 4$ potentials with shells, tested against $n = 8$ DFT data.

When this potential using the shell model is tested on the $n = 8$ cluster, we again see

an improvement: the DFT well depth is only overestimated by 13% (see Figure 6.26). This model is therefore the best model yet.

At this stage, the next logical step is to fit against $n = 4$ with image potentials included. This has been done, again first parametrising against the data set wherein barium is facing the graphene surface. At first, this potential is again parametrised using the rigid ion model, and shells will be added in the next section.

An assumption made when fitting the $n = 1$ potentials with image charges was that there is no attractive interaction between the cluster and the surface that cannot be captured by the method of image charges itself. As such, the first set of potentials that a fit was attempted for here were Born-Mayer potentials. The result of this is shown in Figure 6.27. As is visible in the plot, the well depth of the attractive interaction as modelled by image charges alone is far too shallow.

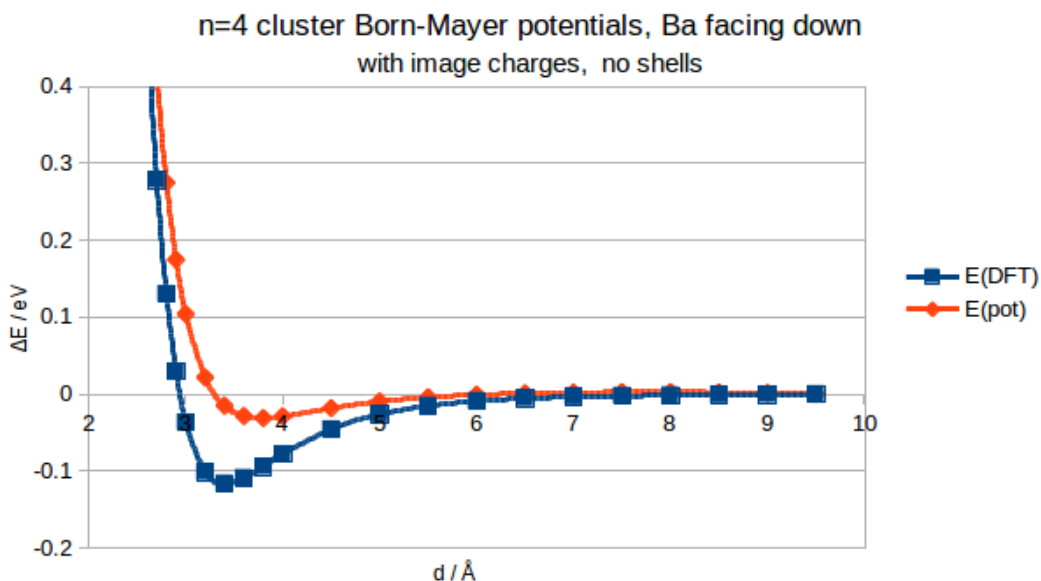


Figure 6.27: $n = 4$ barium down potentials, and fitting errors.

As such, in an attempt to improve the model, full Buckingham potentials were used. The result of this fitting as well as associated errors are shown in Figure 6.28. Errors in the fit can be spotted by the naked eye, and are indeed up to 20 meV, slightly higher than those of the equivalent potential without image charges. However, this error only exceeds 15 meV in the short, strongly repulsive range, in which accuracy is less critical

than that of the range at which attractive interactions dominate, or even the long range.

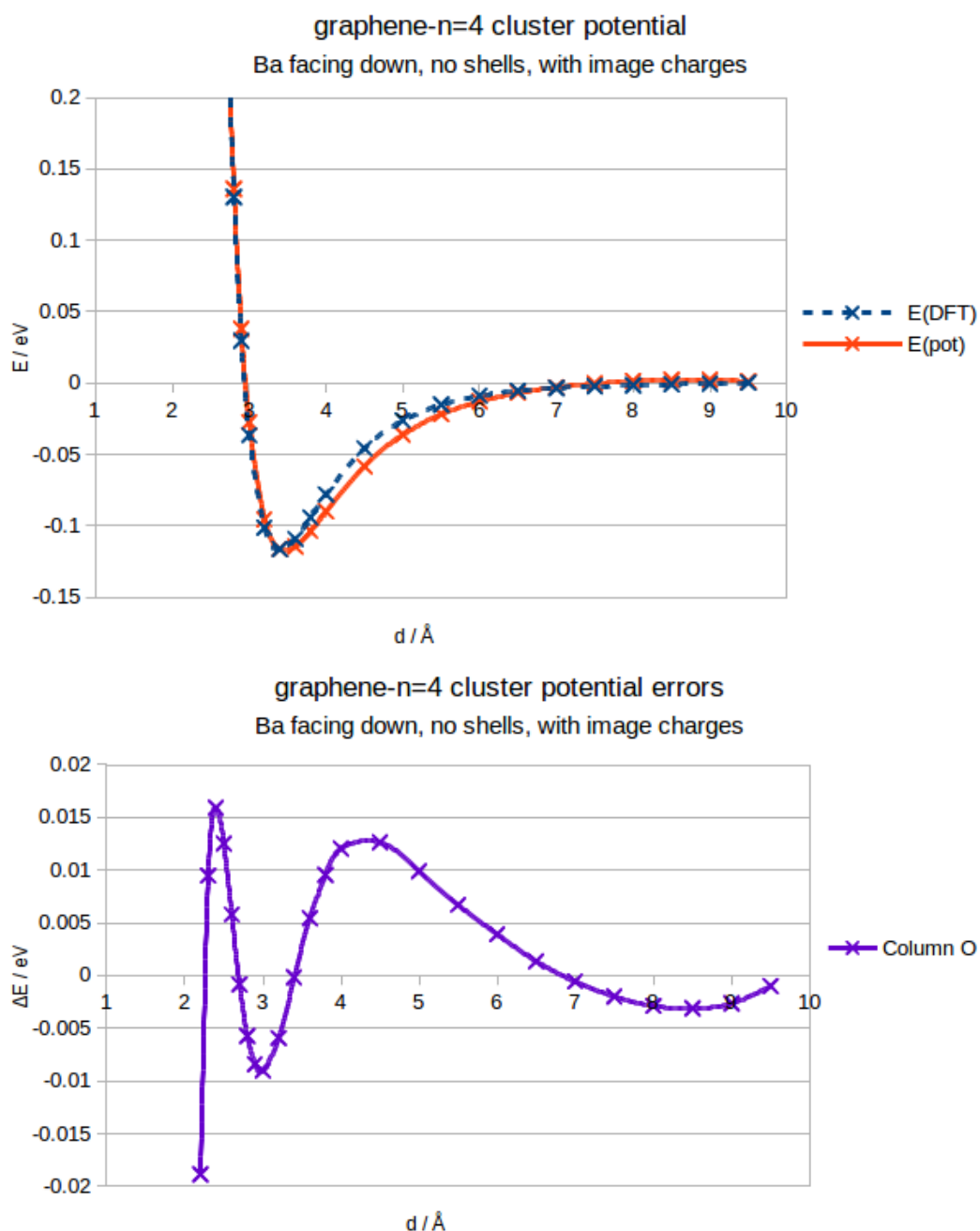


Figure 6.28: $n = 4$ barium down potentials with image charges, and corresponding fitting errors.

When this set of potentials is tested on the same cluster in the flat orientation, it accurately represents the well depth, but overestimates the equilibrium distance between the cluster and the surface marginally (Figure 6.29). Therefore, it was decided to refine parameters of the potentials against both data sets again (Figure 6.30). It turned out that

this fit actually did not improve on modelling the minima of the potential wells. Therefore, both sets of potentials (parametrised against the cluster with Ba facing the surface only, and parametrised against Ba facing the surface and flat clusters) were tested against $n = 8$.

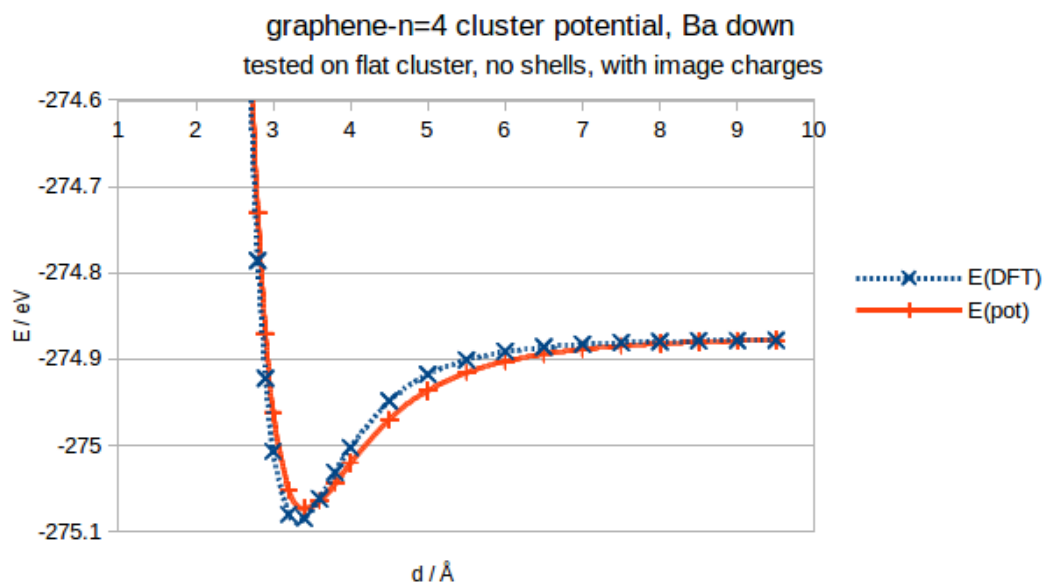


Figure 6.29: $n = 4$ barium down potentials, modelling the flat configuration.

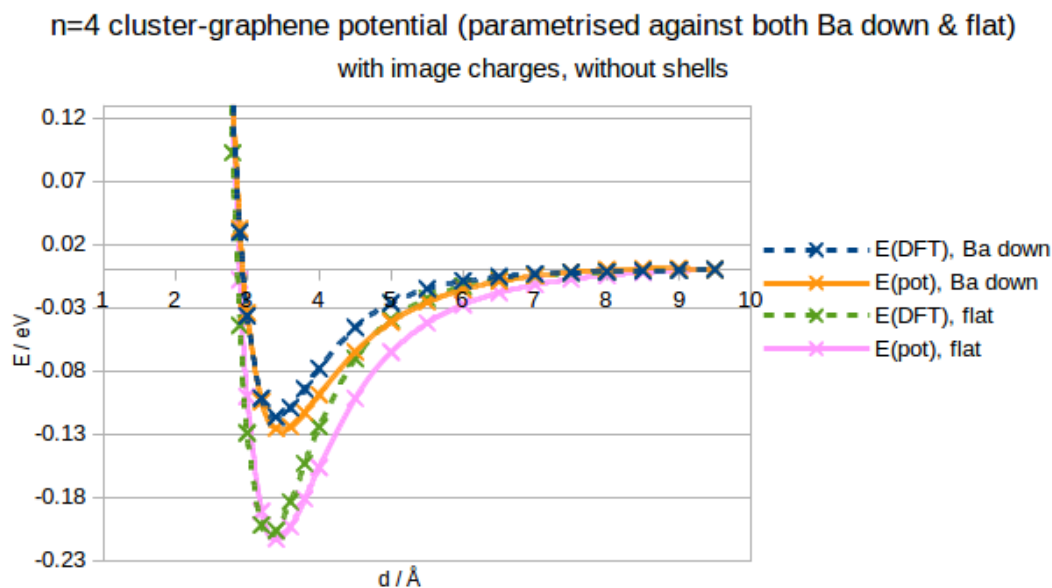


Figure 6.30: $n = 4$ potentials, parametrised against both Ba down and flat configurations.

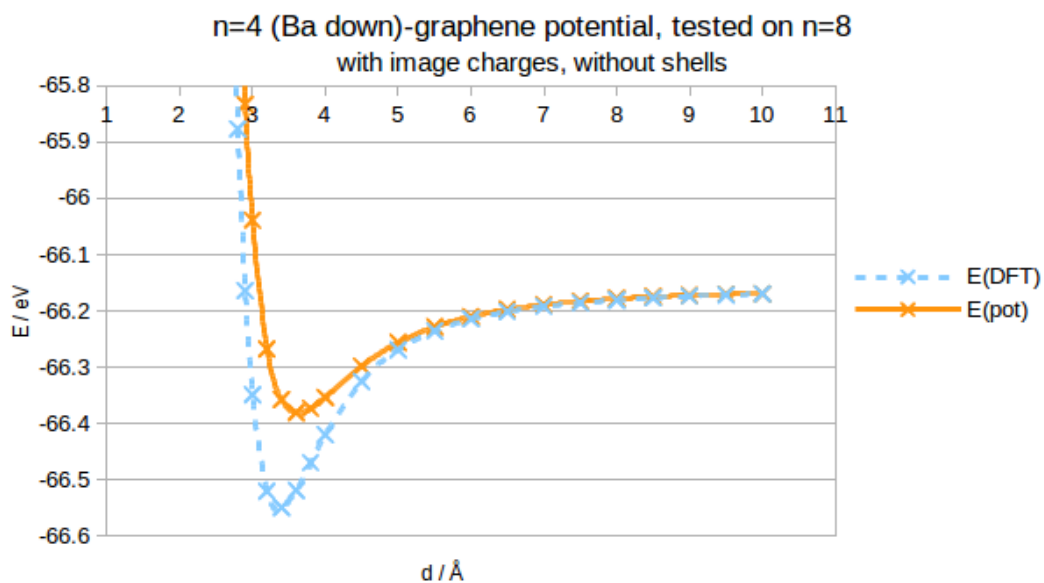


Figure 6.31: $n = 4$ potentials, parametrised against Ba down, tested on $n = 8$

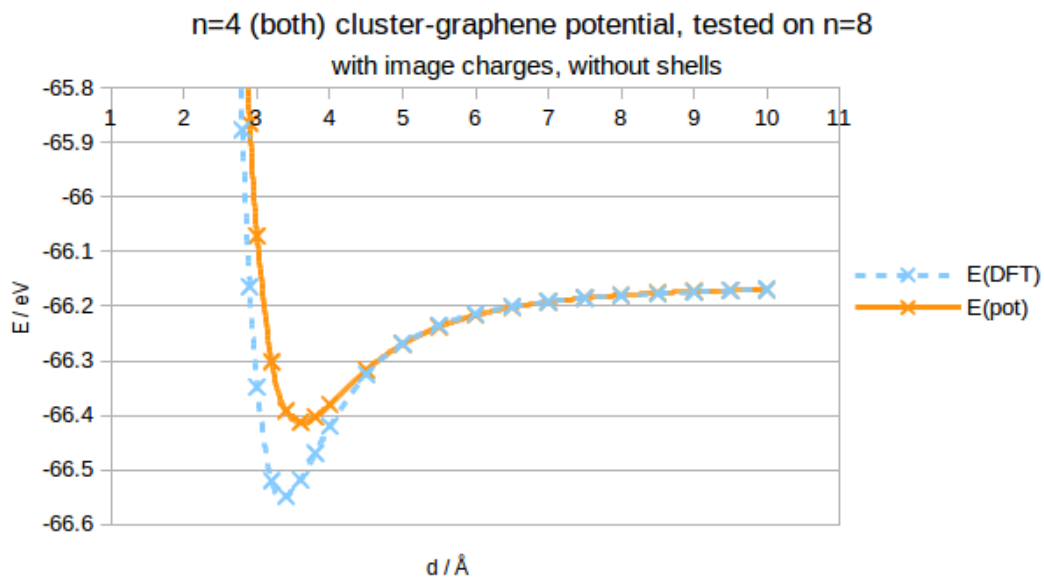


Figure 6.32: $n = 4$ potentials, optimised against both Ba down and flat configurations, tested on $n = 8$.

Figures 6.31 and 6.32 show how the two sets of potentials performed for the $n = 8$ cluster. As the $n = 1$ potentials had for $n = 4$ clusters, they again overestimate the equilibrium distance between the cluster and the surface slightly, and underestimate the well depth - this time the underestimation is by roughly 45% in the case of the Ba down potential, and 36% in the case of the potential parametrised using both orientations. Overall,

the potential parametrised against both cluster orientations performs slightly better, with a marginally deeper well and generally less of a mismatch with the DFT data.

In a last step, we added shells to this model in order to attempt a further reduction in errors. Unfortunately, the models parametrised for $n = 4$ both greatly underestimated the binding strength of the $n = 8$ cluster to graphene, with the potential set parametrised against both $n = 4$ orientations performing slightly better (Figure 6.33). Still, this set of potentials underestimated the binding strength and overestimated the equilibrium distance more so than the rigid ion equivalent set of potentials did: by 53% in the case of the Ba down potential, and by 46% in the other case.

Parameters for the two best sets of potentials are tabulated in Tables 6.9 (without image charges) and 6.10 (with image charges).

Ba shel – C core Buck		O shel – C core Buck	
A / eV	4387.488513	A / eV	1.749917
$\rho / \text{\AA}$	0.27815	$\rho / \text{\AA}$	0.307424
C / ev \AA^6	32.21478	C / ev \AA^6	0.00

Table 6.9: Parameters of the best potentials without image charges.

Ba core – C core Buck		O core – C core Buck	
A / eV	4387.488513	A / eV	1.749917
$\rho / \text{\AA}$	0.27815	$\rho / \text{\AA}$	0.307424
C / ev \AA^6	32.21478	C / ev \AA^6	0.00

Table 6.10: Parameters of the best potentials with image charges.

Overall, it appears that the answer lies somewhere in the middle: without image charges, attractive interaction strength is over- and equilibrium distance underestimated, while with image charges, the reverse happens. It is therefore reasonable to assume that a model incorporating *partial* image charges may provide a higher quality model for barium oxide nanoclusters above graphene. One way of implementing this in the future

would be to just assign charges which are a fixed fraction of the charges of the real ions to the image particles.

In fact, this is expected: the strength of the image potential above a material is proportional to

$$1 - \frac{1}{\epsilon_r}$$

ϵ_r

where ϵ_r is the dielectric constant of the material. For metals, where $\epsilon_r = \infty$, this relative strength is 1, corresponding with a 1:1 relationship of charges above the surface and image charges. For an insulating material, where $\epsilon_r = 1$, this is zero. For graphene, ϵ_r has been measured as a number of different values, generally somewhere from 2 to 15 and the image potential will vary accordingly. If we use the value of the lattice dielectric constant found in [151] which is of a graphene monolayer, and is $\epsilon_r = 2.9$, the strength of the image potential will be ~ 0.66 .

What we can glean from the development of these potentials is the following: The interaction of barium oxide clusters with pristine graphene is relatively weak (expect physisorption only). The model of image charges does not seem to adequately describe this system without modification, and in fact omitting image charges altogether seems to yield better results, but it is likely that the best result may be obtained by introducing partial image charges.

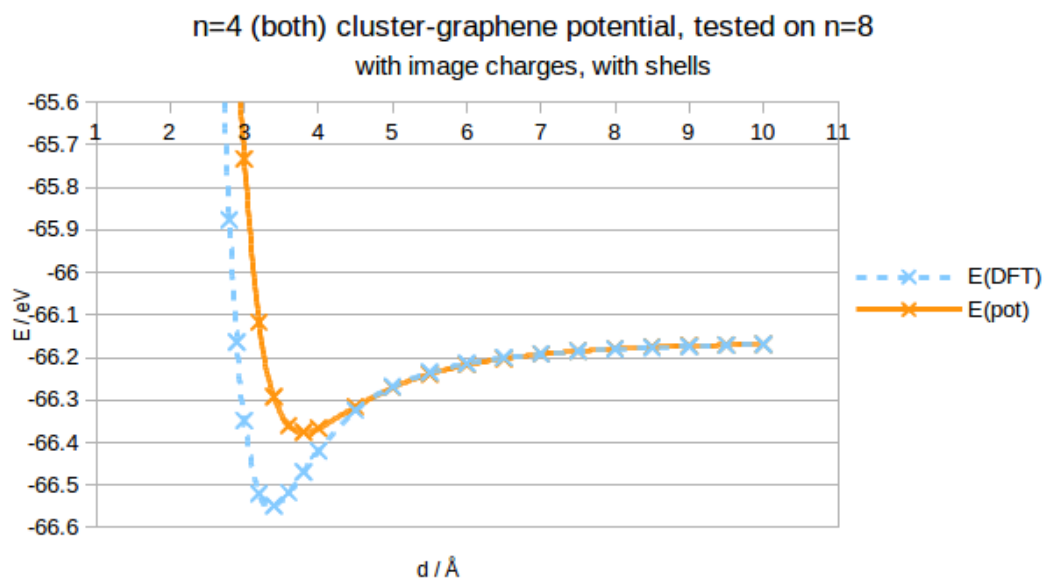


Figure 6.33: $n = 4$ potentials, optimised against both Ba down and flat configurations, tested on $n = 8$.

6.3.2 DFT Calculations of Barium Oxide Clusters on Graphene & Graphene Oxide

In order to gain more insight into the interaction of these clusters with a graphene surface, a series of DFT calculations was performed. Results of these DFT calculations of $n = 6$ and 12 clusters above a pristine graphene surface, and $n = 6$ clusters above graphene functionalised with an OH group are presented below.

Clusters of Sizes $n = 6$ and 12 Above Pristine Graphene

For the clusters of size $n = 6$, three configurations were chosen, as shown in Figure 6.34: the cuboid, which is the lowest energy configuration *in vacuo*, the barrel, which is the second lowest, and the ring, which would allow for maximal wetting if surface wetting is a dominant process. The ring was not a minimum found using DFT, so its configuration resulting from the Lewis et al. potentials[109] was used. The barrel and cuboid were deposited above the graphene surface in the orientations shown in Figure 6.34, while the ring was deposited in the configuration where the plane of the ring was parallel to

the plane of the graphene sheet. Consequently, results reported here might change if different orientations of the clusters above the graphene sheet were investigated and found to be lower in energy than the ones presented here. Additionally, once again the dispersion correction has been left out by accident, and as a consequence the cluster-surface interaction energies may not be accurate.

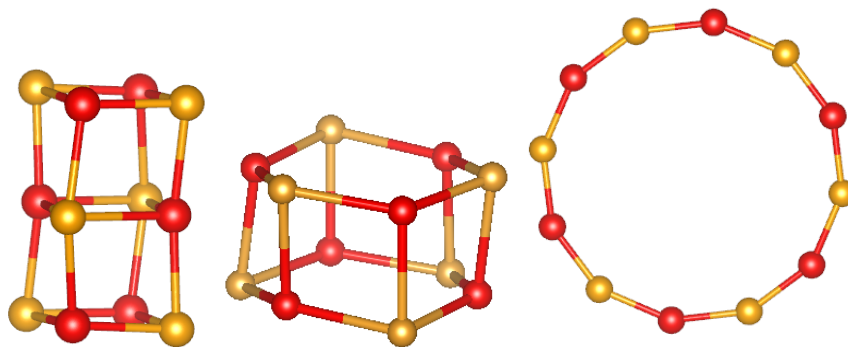


Figure 6.34: The three chosen configurations for $n = 6$: the cuboid, the barrel and the ring.

The resulting energies are shown in Table 6.11. Adsorption energies here are the differences of the total energy of the graphene-cluster system from the energies of the graphene and cluster individually. These will suffer from the lack of dispersion correction as well as from basis set superposition error and should therefore be looked at with caution. Out of the three configurations investigated here, the cuboid remains the lowest in energy. In fact, the adsorption energy appears to be strongest for the cuboid, at 213 meV stronger than that of the barrel. The "adsorption energy" for the ring is notably lower in magnitude, but is here not a true adsorption energy as it is taken from the closest DFT structure, which wasn't a ring, so it includes a definite change in configuration along with deformation above the graphene surface. Also listed are relative energies when using our new interatomic potential; for this, shells were optimised with the DFT geometries as a starting point in order to gain IP energies. Using these IPs, the barrel is predicted to be lower energy than the rocksalt cut, something that was also true with the original Lewis et al. IPs[109] *in vacuo*. The ring is correctly predicted to be much higher energy than the other two structures. However, the accuracy is impacted by the suitability of

the original BaO IPs and as such this method is not good enough to rank energies of clusters and should only be used for first guesses at structures and positions above the surface. Optimisation of both shells and cores was also attempted, however GULP did not find minima in the energy landscape in these attempts, perhaps because the original geometries were too far from actual minima for this more sensitive method to succeed.

Configuration	rel. energy (DFT)	rel. energy (IP)	adsorption energy (DFT)
cuboid	0.000	0.828	-5.415
barrel	0.347	0.000	-5.203
ring	4.279	3.892	-3.157

Table 6.11: Energies relative to the tentative GM of the cluster on the surface, and binding energies for $n = 6$ clusters above a pristine graphene surface.

Next, we will look at how the clusters deformed above the surface. The first cluster we will inspect is the cuboid, the lowest-energy structure out of the three. An illustration of this is shown in Figure 6.35. The cluster had actually re-oriented itself completely during geometry optimisation, now sitting diagonally above the graphene surface such that two barium atoms and one oxygen atom were now facing the surface. The three atoms closest to the graphene surface were all situated above "centre" sites on the surface.

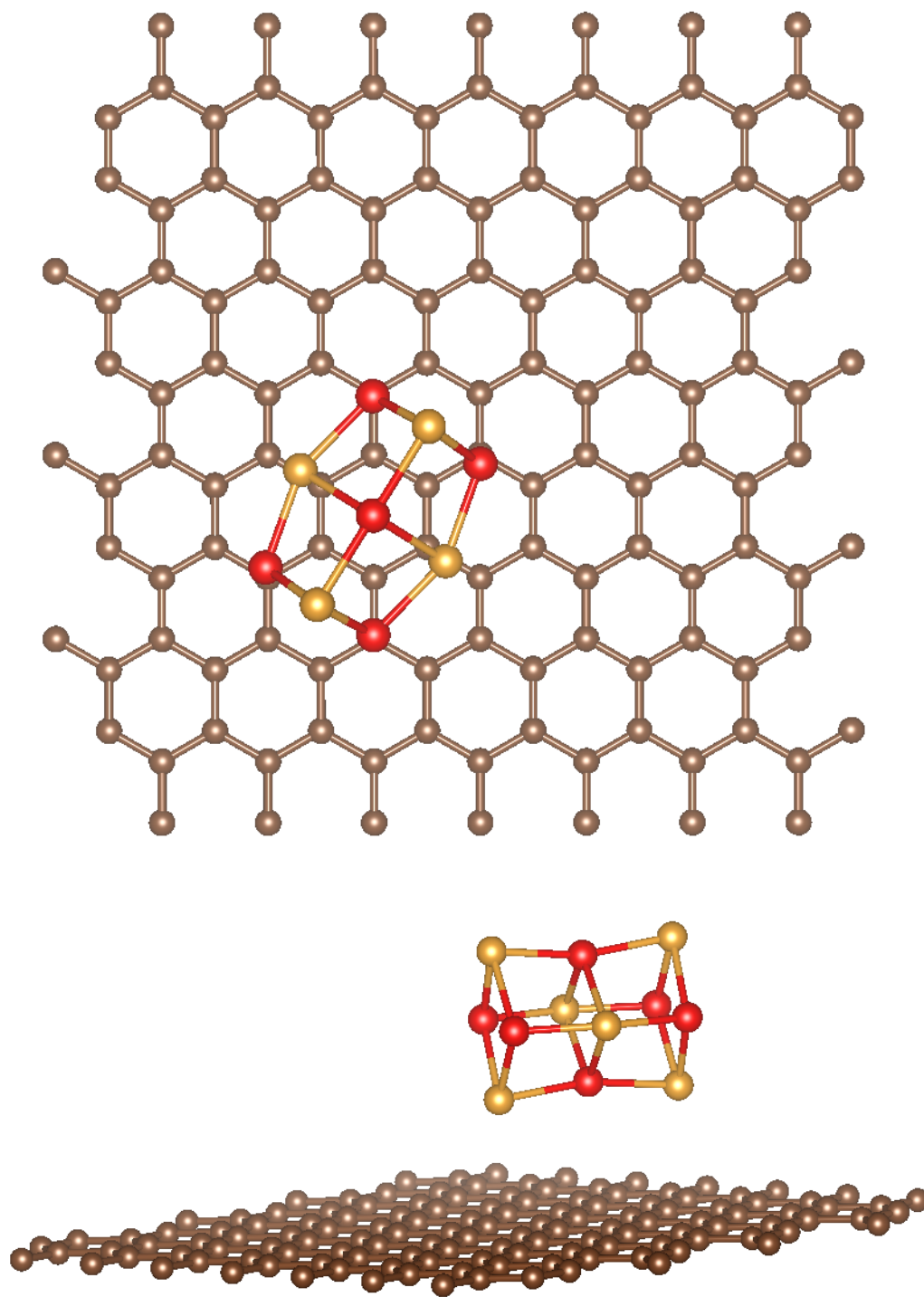
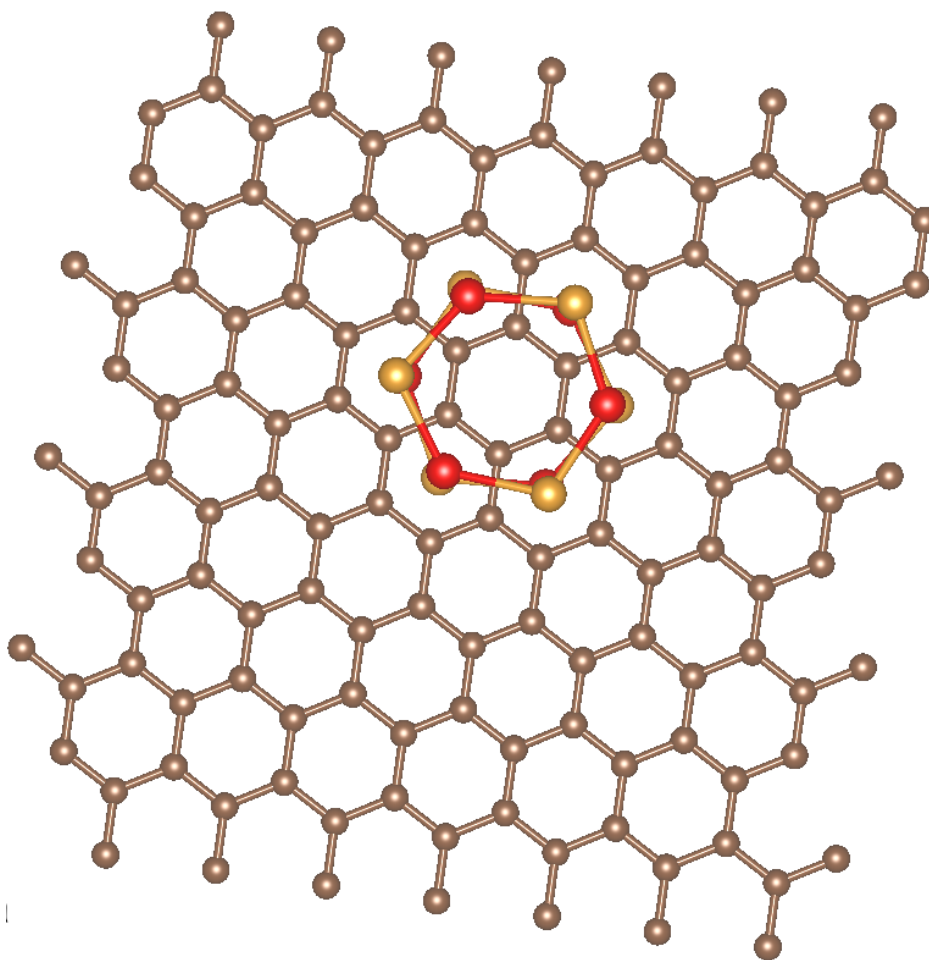


Figure 6.35: The cuboid configuration of the $n = 6$ cluster above graphene, as calculated using the PBEsol DFT functional.

Assuming that this is the lowest energy state of this configuration above the surface, there appears to be a preference of barium facing the surface as opposed to oxygen facing the surface—in line with what was observed during parametrisation of potentials

in Section 6.3.1.

The barrel configuration is the next cluster considered, as shown in Figure 6.36. Here, the cluster stayed in the orientation it was put in at the start of the geometry optimisation. However, one can see that a new puckering effect has emerged, bringing the barium atoms in the bottom layer of the cluster closer to the surface than the oxygen atoms, which in turn influenced the relative positions of the atoms in the top layer of the cluster, where the oxygen atoms are now positioned closer to the surface, but still significantly farther than the bottom layer, so the interaction will be smaller. The atoms are all situated above "centre" sites on the graphene surface.



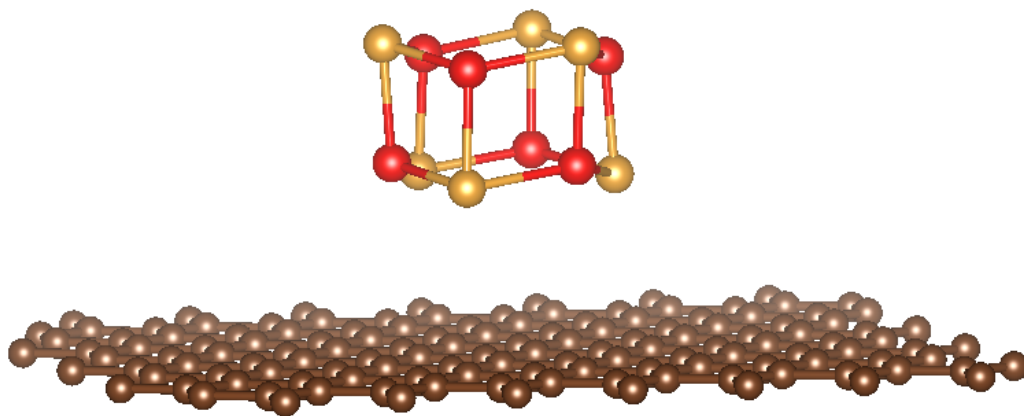


Figure 6.36: The barrel configuration of the $n = 6$ cluster above graphene, as calculated using the PBEsol DFT functional.

Finally, Figure 6.37 shows the ring configuration of the $n = 6$ nanocluster above the surface. The associated energy is much higher than that of the other two clusters, therefore we can say that wetting is not observed, at least in this fashion. The cluster is strongly puckered, with each of the oxygen atoms approx. 4.05 \AA above the surface. Half the barium atoms are closer to the surface (3.17 \AA from it) and again positioned at "centre" sites on the graphene surface, while the other half are actually markedly further from the surface, at a distance of $4.9 - 4.95 \text{ \AA}$ from it. This could be explained by a competition between the barium atoms getting closer to the surface and the oxygen atoms moving farther away from it, with this ring structure the most flexible out of the three discussed here. Indeed, looking back at the barrel structure, the closer layer of barium atoms are on average 3.40 \AA from the surface, while the closer layer of oxygen atoms are 3.78 \AA from it—the difference in distances is smaller as the structure is less free to deform. In the even more constrained cuboid, the two barium atoms closest to the graphene sheet were found to be 3.45 \AA from it, while the oxygen atom between them was 3.73 \AA from the surface, i.e. the difference in these distances was even smaller.

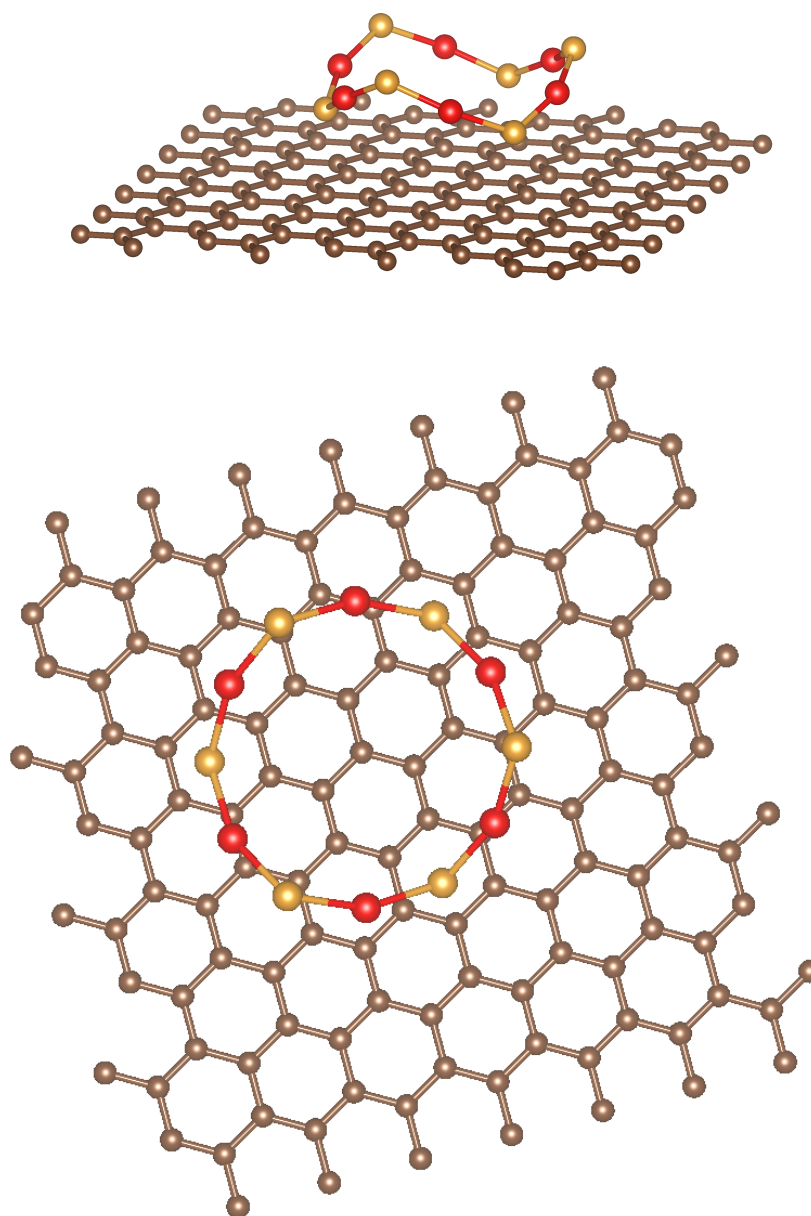


Figure 6.37: The ring configuration of the $n = 6$ cluster above graphene, as calculated using the PBEsol DFT functional.

For the $n = 12$ cluster, only two structures were investigated: the cuboid rocksalt cut and the barrel. These are shown in Figure 6.38. The ring structure was omitted because (a) there was no available starting structure and (b) from the $n = 6$ result, it is known that this type of structure is unlikely to be favoured. This time, both structures were taken from DFT. The clusters were deposited in two orientations above the surface, upright and on their side, and the lowest-energy resulting structures are reported below.

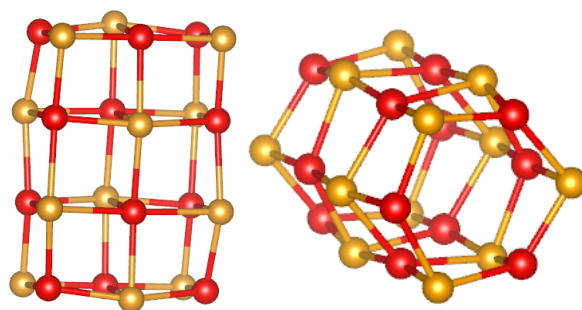


Figure 6.38: The two chosen configurations for $n = 12$: the cuboid and the barrel.

Table 6.12 shows the relative energies and adsorption energies of the two $n = 12$ structures above the graphene surface once optimised, in their lowest energy orientations. Again, the cuboid remains the lowest energy structure. However, the adsorption energy here is slightly stronger (27 meV) for the barrel, making it 320.01 meV higher in energy than the cuboid overall.

Configuration	rel. energy (DFT)	rel. energy (IP)	adsorption energy
cuboid	0.000	-9.150	
barrel	0.320	-9.177	

Table 6.12: Energies relative to the tentative GM and binding energies for $n = 12$ clusters above a pristine graphene surface.

Figure 6.39 shows the cuboid $n = 12$ structure above graphene. Unlike the $n = 6$ cuboid, this lies flat above the surface, with 6 barium and oxygen atoms each facing the surface. The central layer of atoms is again positioned above "centre" sites on the surface. However, due to lattice mismatch, the other atoms are positioned atop interstitial sites or atop atoms on the surface. There is again a puckering effect, leading to the barium atoms being closer to the surface than the oxygen atoms. The bottom layer of barium atoms are $3.40 - 3.53 \text{ \AA}$ from the surface, while the bottom layer of oxygen atoms are $3.72 - 4.05 \text{ \AA}$ above the surface. These numbers are very similar to those found for the $n = 6$ cuboid, which makes sense since the deformability of the two cuboids would be similar.

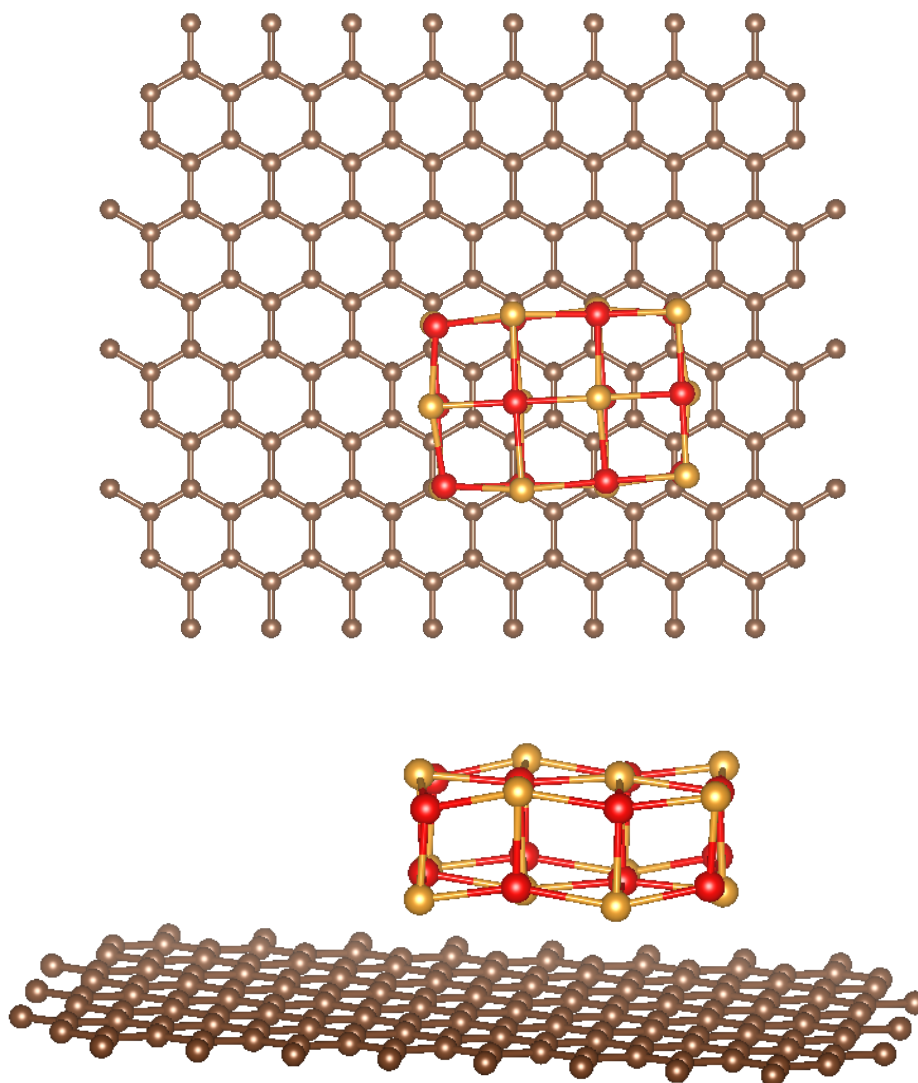


Figure 6.39: The cuboid configuration of the $n = 12$ cluster above graphene, as calculated using the PBEsol DFT functional.

Figure 6.40 shows the barrel configuration of the $n = 12$ cluster above graphene. Unlike the case of the cuboid configuration, the preferred orientation of this barrel (by 263meV) is upright above the graphene surface. Again, we observe a puckering effect. The layer of barium atoms closest to the surface is 3.32 – 3.36 Å away from the surface plane and all three barium atoms are again above "centre" positions on the surface. The closest layer of oxygen atoms is 3.59 – 3.62 Å from the surface – that is, atoms are closer to the surface than they were in the case of the $n = 6$ barrel. This may be because of attractive interactions of the surface with the further away layers of the cluster; indeed, attraction is relatively stronger than would be expected from the number of atoms directly

facing the surface.

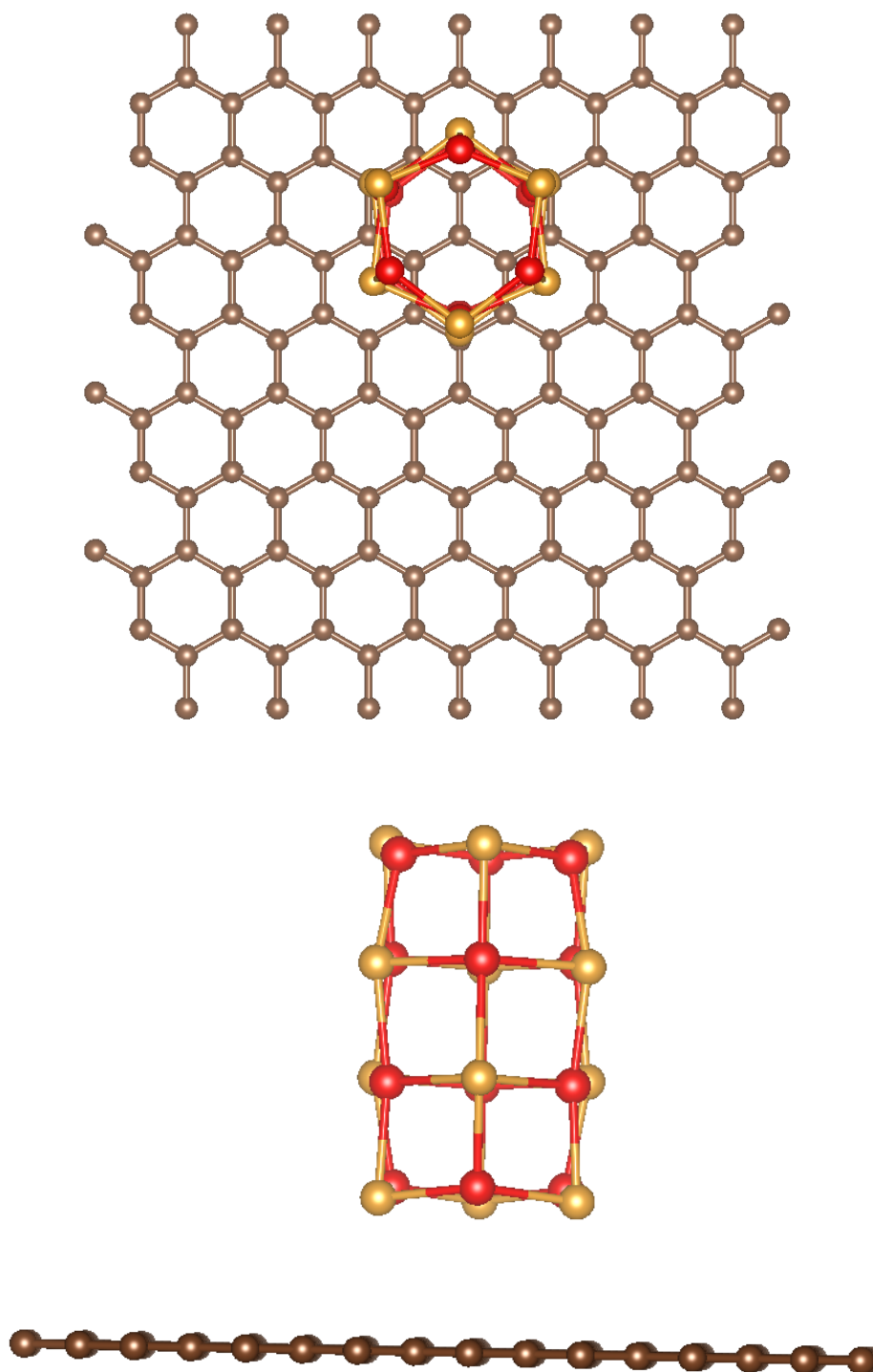


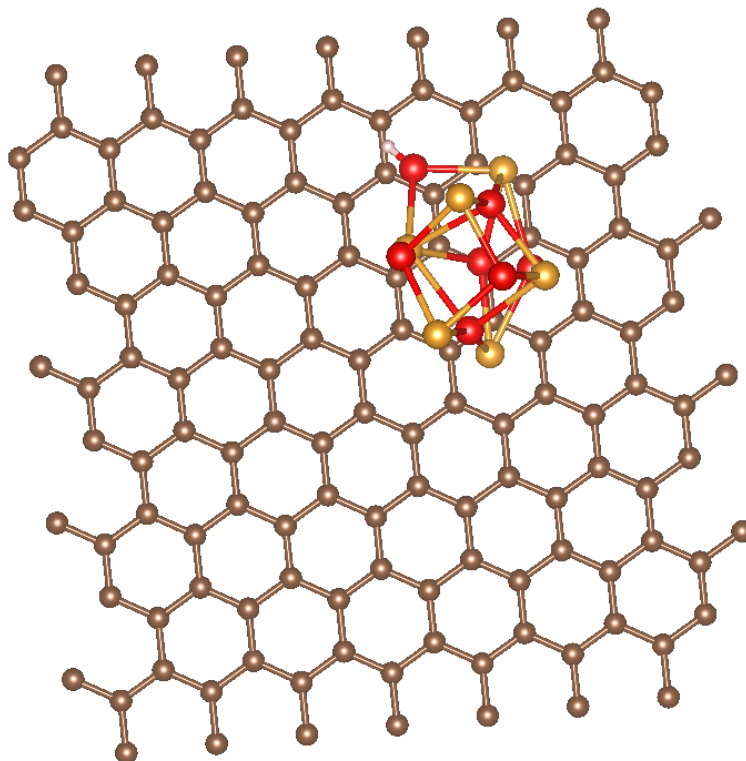
Figure 6.40: The barrel configuration of the $n = 12$ cluster above graphene, as calculated using the PBEsol DFT functional.

Overall, in these last 2 sections, the adsorption energies seem very high considering that we do not see chemisorption, and may be very wrong due to the lack of dispersion

correction, as well as due to basis set superposition error.

Clusters of Size $n = 6$ Above OH-Functionalised Graphene

Several calculations were performed optimising the two low-energy $n = 6$ structures (the barrel and the cuboid) above graphene with various defects, including vacancies, hydroxy groups and epoxy groups. However, only those above OH-functionalised graphene finished within the time of this project.



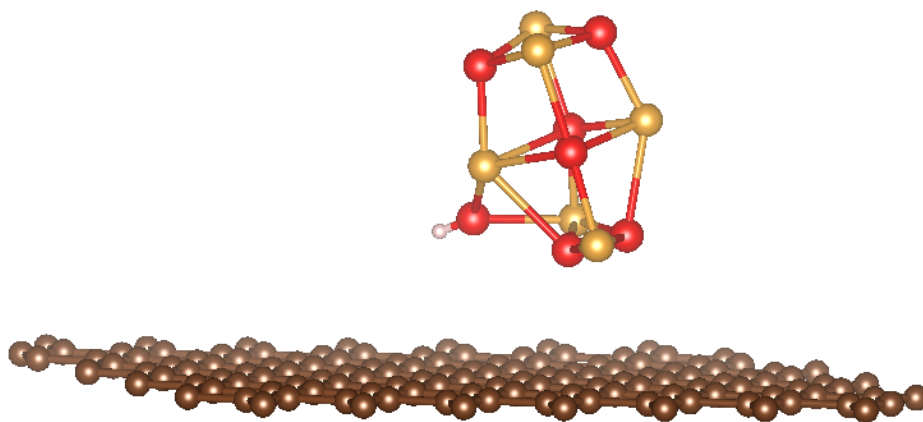


Figure 6.41: Result of optimising the cuboid configuration of the $n = 6$ cluster above OH-functionalised graphene, as calculated using the PBEsol DFT functional.

Figure 6.41 shows what happens when optimising the cuboid configuration of the $n = 6$ cluster above OH-functionalised graphene: the OH group gets incorporated into the cluster, and instead one of the other oxygen atoms is getting closer to the surface, specifically 2.8 Å from it. The cluster mostly retains its shape, with bonding in the upper half of the cluster remaining identical to that of the cluster *in vacuo*.

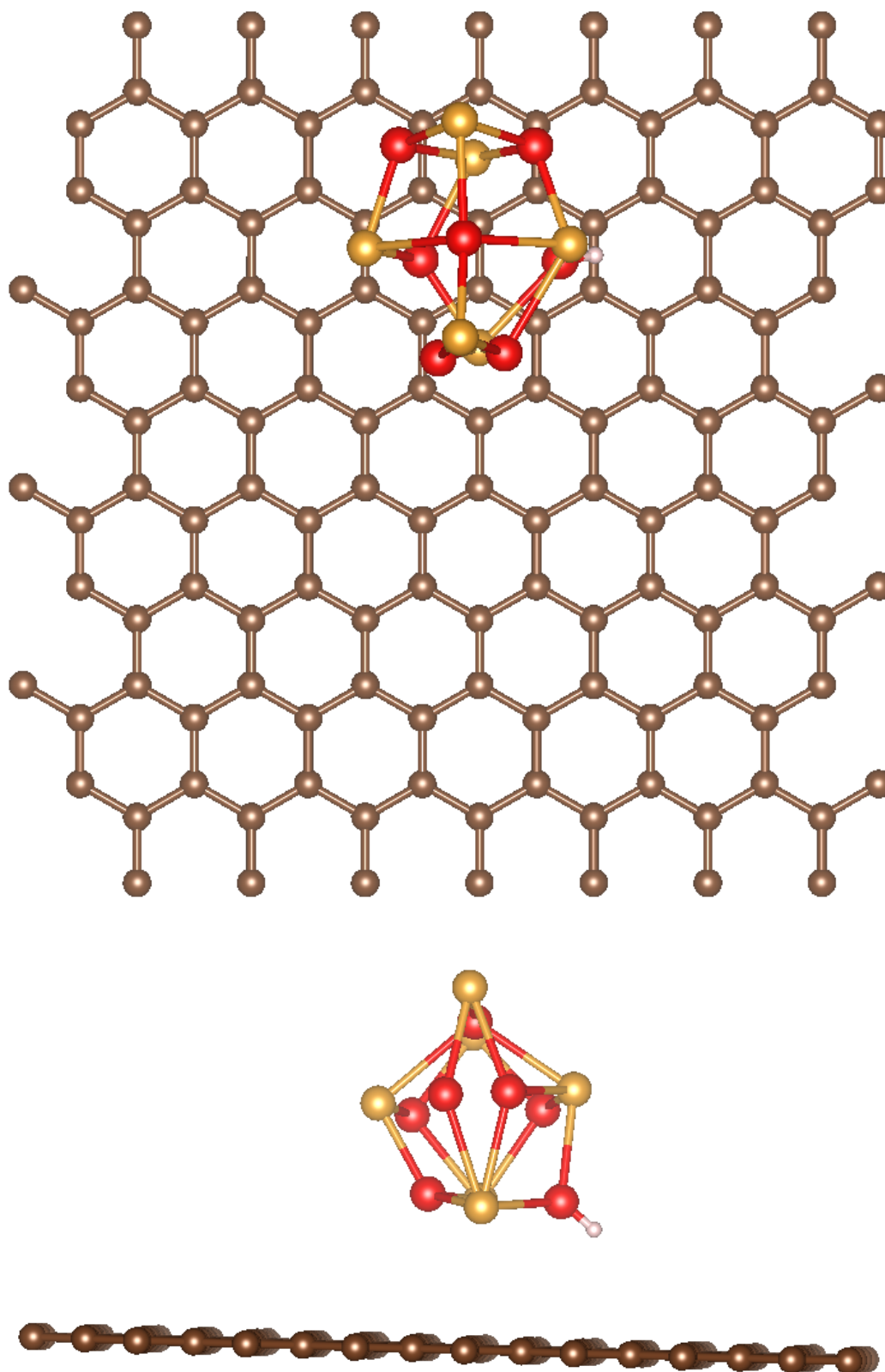


Figure 6.42: Result of optimising the barrel configuration of the $n = 6$ cluster above OH-functionalised graphene, as calculated using the PBEsol DFT functional.

In the case of the barrel (Figure 6.42), the cluster's shape changes significantly when

the OH group is incorporated into it, and it starts to resemble a rocksalt cut. Here, the (non-H) atom closest to the surface is a barium atom, at a distance of 3.00Å.

Energies of these 2 structures are tabulated in Table 6.13. The deformed cuboid remains lower in energy than the (now severely deformed) barrel, and adsorption energies are stronger than they were above pristine graphene - in line with the clusters being situated closer to the surface.

Configuration	relative energy	adsorption energy
cuboid	0.000	-8.673
barrel	0.085	-8.723

Table 6.13: Energies relative to the tentative GM and binding energies for $n = 6$ clusters above an OH-functionalised graphene surface.

6.4 Summary and Conclusions

Potential parametrisation

Interatomic potentials were parametrised to model the interaction of barium oxide nanoclusters with graphene. This was done both with and without image charges. It was found that potentials parametrised against the $n = 1$ stick were unsuitable for modelling larger nanoclusters; potentials parametrised against the $n = 4$ cuboid performed better. Generally, the potentials which did not include image charges were better at reproducing DFT results: When tested against a $n = 8$ cluster, these had an error in the well depth of about 13% compared to 36% in the model with image charges. These potentials overestimated binding strength and underestimated the equilibrium distance of the clusters from the surface, while potentials including image charges underestimated binding strength and overestimated equilibrium distances. Therefore, it is thought that the answer might lie in partial (fractional) image charges. Further work is needed to investigate this. If a good enough potential were found, a wide range of further calculation possibilities would open up. For example, one could use the new potential for global optimisation of clusters

above the surface, or MD simulations of clusters on the surface to investigate whether surface migration is a concern.

DFT calculations

DFT calculations were performed on barium oxide nanoclusters above graphene, both pristine ($n = 6$ and 12 clusters) and OH-functionalised ($n = 6$ clusters). It was found that on pristine graphene, the barium atoms moved closer to the surface than the oxygen atoms, and that the clusters deformed to accommodate this. The cuboid rocksalt cuts remained the lowest in energy. Above OH-functionalised graphene, the adsorption energy was stronger, and the clusters were found to relax to a position closer to the surface. However, instead of remaining near the graphene surface, the OH group gets incorporated into the cluster in both cases investigated here.

These results are preliminary and much further work is needed. Given more time and computational resources, we would have investigated more sizes of clusters, and more structures for each size, above pristine graphene. For graphene oxide and defective graphene, the same holds, but additionally it would be good to investigate clusters above an epoxy group, or clusters above graphene with a vacancy-type defect. Additionally, it would be advantageous to re-evaluate the existing BaO-GO results using a larger basis set.

Chapter 7

Summary and Conclusions

In this chapter, results of this thesis are summarised and suggestions for future work offered.

Throughout this thesis, several computational techniques have been used. Global optimisation has been utilised in the forms of an evolutionary algorithm and data mining to obtain tentative guess structures for $(\text{BaO})_n$ nanoclusters with $n = 1$ to 18 and 24, as measured using interatomic potentials. These structures were then refined using density functional theory to obtain more accurate energy rankings for these structures.

It was found that even- n clusters preferentially formed cuboid rocksalt cuts and were generally lower in energy than their odd- n counterparts. Cluster sizes $n = 4, 6, 8, 10$ and 16 were found to be relatively most stable, with only one exceptionally stable structure per size – all of these are cuboid rocksalt cuts.

Using the $(\text{BaO})_n$ structures gained from IP calculations as a starting point, cluster structures were then data mined for strontium, calcium and magnesium oxides by scaling them down according to ionic radii. It was found that strontium oxide and calcium oxide also show preference for cuboid rocksalt cut structures, with synthesis target sizes of $n = 8, 9, 12, 16$ and 24 for SrO and $n = 8, 9, 12, 16, 18$ and 24 for CaO. At low temperatures (100K) the $n = 14$ CaO cluster may also be a synthesis target for size-selective synthesis, and thus the only non-cuboid fulfilling the criteria.

Results for small MgO clusters look dramatically different: $n = 3k$ sizes are preferred

up to $n = 15$, and the most stable configurations for these sizes are barrel shapes, not rocksalt cuts. Synthesis target sizes are $n = 9, 18$ and 24 at 300K , and in addition to these $n = 15$ and 16 at 100K .

Next, normalised clustering energies (NCEs) of cuboid nanoclusters were taken and used to extrapolate energies of nanowires, slabs and the bulk. It was found that using a three-step approach (extrapolating from nanoclusters to nanowires, then from nanowires to slabs, then finally from slabs to the bulk) led to more accurate predictions than extrapolating directly bulk energies from those of the nanoclusters. Madelung potentials were calculated for ionic sites and there was found to be a correlation between these and relative energy rankings of clusters.

In the final chapter, barium oxide clusters on a graphene surface were investigated. First, interatomic potentials were parametrised to model the interaction of these clusters with pristine graphene. These potentials revealed that the interaction of barium oxide clusters with pristine graphene is relatively weak, and that there is likely to be a partial image charge effect on the graphene surface.

Acronyms and abbreviations

0D, 1D, 2D, 3D 0-, 1-, 2-, 3-dimensional

BFGS Broyden-Fletcher-Goldfarb-Shanno (algorithm)

BHMC Basin Hopping Monte Carlo

CASSCF Complete Active Space Self Consistent Field

DFT Density Functional Theory

EA Evolutionary Algorithm

FHI-aims Fritz Haber Institute *ab initio* molecular simulations

FSG Free-Standing Graphene

FT-IR Fourier transform-infrared spectroscopy

GA Genetic Algorithm

GGA General Gradient Approximation

GM Global Minimum

gNCE generalised Normalised Clustering Energy

GO Graphene Oxide

GULP General Utility Lattice Program

IP Interatomic Potential

KLMC Knowledge-Led Master Code

LM Local Minimum

MP2, 3 Second, Third Order Møller-Plesset Perturbation Theory

NCE Normalised Clustering Energy

NMR Nuclear magnetic resonance spectroscopy

PES Potential Energy Surface

SBU Secondary Building Unit

STEM Scanning Transmission Electron Microscopy

STP Standard Temperature and Pressure

TEM Transmission Electron Microscopy

ZORA Zeroth Order Regular Approximation

List of Figures

1.1	Examples of the three structural motifs: bubble (left), barrel (middle), rock-salt cut (right). All example structures were taken from Ref. [23]	4
1.2	A single unit cell of graphite, viewed straight from the top, and slightly side-on, with bonds and atoms beyond the unit cell shown to illustrate how it extends.	10
1.3	Graphene, functionalised with an OH group; structure optimised in FHI-aims using the PBEsol functional.	10
2.1	A charge above a surface generating an equal but opposite image charge.	26
3.1	Steps in generating optimised structures and energy rankings for barium oxide nanoclusters.	39
3.2	The $(\text{BaO})_{18}$ $4 \times 3 \times 3$ (left) and $6 \times 3 \times 2$ (right) bulk cut structures	42
3.3	The $(\text{BaO})_{24}$ bulk cut structure, the GM as predicted by PBEsol0 calculations.	44
3.4	NCEs for barium oxide clusters, as resulting from PBEsol calculations. . .	45
3.5	Second-order energies of BaO clusters ($n = 2$ to 17)	48
3.6	Dipole moments of BaO GM for $n = 4$ to 18 , as optimised with PBEsol. . .	48
3.7	Coordination numbers of BaO cluster GM for $n = 1$ to 18 , as calculated with PBEsol; bond length cutoff ~ 2.95 Å.	50
3.8	Energy as a function of the total number of bonds for $n = 16$ structures. .	51

3.9	Density of LM for BaO clusters for $n = 8$ to 18 and 24 at 100K. Blue impulses indicate cluster energy per formula unit, green lines indicate smeared energies, and red divisions mark $n - 1$ cluster energies..	52
3.10	Density of LM for BaO clusters for $n = 8$ to 18 and 24 at 300K. Blue impulses indicate cluster energy per formula unit, green lines indicate smeared energies, and red divisions mark $n - 1$ cluster energies.	54
3.11	Top 10 structure as the EA progresses (and running average energy in red)	56
3.12	Relative energy rankings of IP (left) and DFT (right) structures of $n = 13$ clusters; where structures changed significantly during the DFT geometry optimisation, the line is still drawn.	57
3.13	Relative energy rankings of IP (left) and DFT (right) structures of $n = 16$ clusters.	58
4.1	Steps in generating optimised structures and energy rankings for alkaline earth oxide nanoclusters.	62
4.4	Second-order energies of BaO, SrO and CaO GM clusters ($n = 5$ to 17). Ball-and-stick models are shown for those clusters where the second-order energies are negative, and representative SrO structures.	77
4.5	Second-order energies of MgO clusters ($n = 5$ to 17), overlaid with the second-order energies of CaO clusters to highlight the difference.	79
4.6	Deviation from ideal M–O–M angle for $n = 2$ to 4 DFT $(MO)_n$ GM configurations compared to perfectly symmetric squares, hexagons and cubes, where M labels group II cations.	82
4.7	Coordination numbers of alkali earth oxide cluster GM for $n = 1$ to 18 and 24, as calculated with PBEsol; bond length cutoffs selected appropriately for each compound.	83
4.8	Density of LM for SrO clusters for $n = 8$ to 18 and 24 at 100K (a) and 300K (b). Blue impulses indicate cluster energy per formula unit, green lines indicate smeared energies, and red divisions mark $n - 1$ cluster energies.	86

4.9	Density of LM for CaO clusters for $n = 8$ to 18 and 24 at 100K (a) and 300K (b). Blue impulses indicate cluster energy per formula unit, green lines indicate smeared energies, and red divisions mark $n - 1$ cluster energies.	88
4.10	Density of LM for MgO clusters for $n = 8$ to 18 and 24 at 100K (a) and 300K (b). Blue impulses indicate cluster energy per formula unit, green lines indicate smeared energies, and red divisions mark $n - 1$ cluster energies.	91
4.11	The four low-lying LM of $(\text{MgO})_{12}$, as resulting from geometry optimisations using the PBEsol functional.	92
4.12	Energy ranking of structures resulting from rescaling and reoptimising $(\text{BaO})_{12}$ structures, plotted with respect to change in cation. Here, the number 1 structure is the GM, with number 2 the second-lowest LM and so on.	93
4.13	Energies relative to their respective GM of structures of $(\text{MgO})_{12}$, $(\text{CaO})_{12}$, $(\text{SrO})_{12}$ and $(\text{BaO})_{12}$, as calculated using DFT (PBEsol).	95
4.14	Average bond lengths (\AA) of cuboid clusters of sizes $n = 4, 12, 16, 18$ and 24, as well as the expected asymptotes (bulk bond lengths).	96
4.15	Number of LM likely to be found in experiments at 100K for each alkali earth oxide and each cluster size.	98
4.16	Number of LM likely to be found in experiments at 300K for each alkali earth oxide and each cluster size.	99
5.1	NCEs of $2 \times 2 \times N$ cuboid clusters as a function of n .	104
5.2	NCEs of a variety of cuboid nanocluster as a function of $\frac{1}{n}$.	105
5.4	A BaO nanowire in a unit cell.	107
5.5	Extrapolation of gNCEs (from nanowire gNCEs) of slabs of thickness 2 atoms (dashed), 3 atoms (solid), 4 atoms (dotted), and 4 atoms with 4×4 data removed (dot-dashed).	109
5.6	Generalised NCEs for infinitely extending slabs, as used to extrapolate bulk energy, following the three-step method.	110

5.7	Fitting to all nanocluster energies to extrapolate bulk energy using the one-step method – the dashed lines indicate the DFT bulk energies, i.e. the limit we expect.	111
5.8	NCEs of GM clusters as a function of $\frac{1}{n}$	113
5.9	Madelung potential at the most outlying and central ion sites in chains of alternating Ba^{2+} and O^{2-} ions of different lengths, calculated using the rigid ion model in GULP.	117
5.10	Madelung potential at outlying and central ions in chains of alternating Ba^{2+} and O^{2-} ions of different lengths, as calculated using the shell model in GULP.	118
5.11	Madelung potential magnitudes at outlying and central ions in cuboid barium oxide clusters, as optimised by DFT.	119
5.12	Madelung potential magnitudes at outlying and central ions in cuboid magnesium oxide clusters, as optimised by DFT.	120
5.13	Average Madelung potential magnitudes at ionic sites in cuboid alkali earth oxide clusters, as optimised by DFT.	121
6.1	Example of a graphene cell, with large separation between graphene layers.	128
6.2	Energies of a 1×1 graphene sheet in a 3D periodic unit cell as a function of separation between sheets, as calculated using FHI-aims/PBEsol. . . .	129
6.3	Energies of a 1×1 graphene sheet in a 3D periodic unit cell, different length ranges, as calculated using FHI-aims/PBEsol.	130
6.4	Energies of a 1×1 and 5×4 graphene sheet in a 3D periodic unit cell, with the z -length varied.	131
6.5	Energies of $(\text{BaO})_1$ in a $50\text{\AA} \times y \times 50\text{\AA}$ unit cell without graphene, where y is varied	132
6.6	$(\text{BaO})_2$ square in a $50\text{\AA} \times y \times 50\text{\AA}$ unit cell, where y is varied.	133

6.7	Model of the BaO stick above graphene: (a) varying the distance between the stick and graphene (b) above one of three possible sites on graphene: "top" atop an atom (A), "int" interstitially (B), or "centre" over the centre of a ring (C).	134
6.8	Single O-C potentials generated from the Ba-O stick approaching graphene, compared to DFT data	137
6.9	Single Ba-C potentials generated from the Ba-O stick approaching graphene, compared to DFT data	138
6.10	Errors in single O-C potentials generated from the Ba-O stick approaching graphene, relative to the DFT data they were parametrised against	139
6.11	Errors in single Ba-C potentials generated from the Ba-O stick approaching graphene, relative to the DFT data they were parametrised against	140
6.12	Potentials fitted to both orientations of the Ba-O stick, as compared to DFT data for this system.	143
6.13	Single O-C potentials generated from the Ba-O stick approaching graphene, with image charges, compared to DFT data	145
6.14	Single Ba-C potentials generated from the Ba-O stick approaching graphene, with image charges, compared to DFT data	146
6.15	Errors in single O-C potentials generated from the Ba-O stick approaching graphene, with image charges, compared to DFT data	147
6.16	Errors in single Ba-C potentials generated from the Ba-O stick approaching graphene, with image charges, compared to DFT data	148
6.17	Potentials fitted to both orientations of the Ba-O stick, as compared to DFT data for this system, with image charges.	150

List of Tables

1.1	Band gaps (both from experimental data[79] and our DFT calculations using the PBEsol functional) of alkaline earth oxide bulk materials.	11
1.2	Experimental lattice parameters of BaO, SrO, CaO and MgO at STP, and calculated equivalents using FHI-AIMS/PBESOL with 8 k-points in each direction.	11
1.3	Experimental ionization energies of the alkaline earth metals.	12
3.3	Second-order energy differences of $(\text{BaO})_n$ clusters for $n = 3$ to 17.	47
3.4	Dipole moments of BaO GM for $n = 4$ to 18, as optimised with PBEsol. . .	49
4.7	Second-order energy differences for GM cluster energies of sizes $n = 5 - 17$	77
4.9	Bond lengths in bulk BaO, SrO, CaO and MgO, as well as in selected cluster sizes.	96
5.1	Generalised NCEs for infinitely long nanowires of cross-section $N_x \times N_y$, as extrapolated from plots such as in Figure 5.3	108
5.2	Generalised NCEs for infinitely extending slabs of varying thickness, as extrapolated from plots in Figure 5.5	110
5.3	Generalised NCEs for bulk materials as extrapolated from nanoclusters via the three-step method, the one-step method, and from DFT energies. . . .	111
5.4	Generalised NCEs for bulk materials as extrapolated from nanoclusters via the three-step method using cuboids, using GMs, and from DFT energies. .	112

5.5	Energies of cuboid structures of sizes $n = 24, 27$ and 28	114
5.6	Energies of cuboid structures of sizes $n = 30, 32$ and 36	115
5.7	Madelung potentials at O^{2-} sites, calculated using GULP	116
5.8	Average Madelung potentials across all ionic sites for MgO, CaO, SrO and BaO cuboids.	122
6.1	Charges of barium, oxygen and carbon in the rigid ion model	135
6.2	Sums of squares S for different single potentials of carbon interacting with oxygen and barium	136
6.3	Parameter values of single potentials (C–O and C–Ba) to model the approach of the Ba–O stick toward graphene	141
6.4	Parameters of pairs of potentials when optimised for one orientation. The potentials which are likely to be unreliable are greyed out.	141
6.5	Parameters of pairs of potentials when optimised for both orientations.	142
6.6	Absolute difference in parameters of potentials optimised for both orientations compared to those optimised for one orientation.	142
6.7	Parameters of potentials optimised for both orientations of the Ba–O stick above graphene, with image charges.	150
6.8	Charges and spring constants for all cores & shells, as used in the shell model here.	156
6.9	Parameters of the best potentials without image charges.	163
6.10	Parameters of the best potentials with image charges.	163
6.11	Energies relative to the tentative GM of the cluster on the surface, and binding energies for $n = 6$ clusters above a pristine graphene surface.	167
6.12	Energies relative to the tentative GM and binding energies for $n = 12$ clusters above a pristine graphene surface.	172
6.13	Energies relative to the tentative GM and binding energies for $n = 6$ clusters above an OH-functionalised graphene surface.	178

Bibliography

- [1] *Computational Modeling of Inorganic Nanomaterials*, ed. M. A. Z. Stefan T. Bromley, CRC Press, 2016.
- [2] R. Jin, C. Zeng, M. Zhou and Y. Chen, *Chemical Reviews*, 2016, **116**, 10346–10413.
- [3] N. Kaur, R. N. Aditya, A. Singh and T.-R. Kuo, *Nanoscale Research Letters*, 2018, **13**, 302.
- [4] X. Le Guañvel, V. Trouillet, C. Spies, G. Jung and M. Schneider, *The Journal of Physical Chemistry C*, 2012, **116**, 6047–6051.
- [5] *Private discussion*, S. Woodley, M. Zwijnenburg and R. Palmer.
- [6] A. I. Ayesh, *Journal of Nanomaterials*, 2016, **2016**, 17.
- [7] M. Hua, S. Zhang, B. Pan, W. Zhang, L. Lv and Q. Zhang, *Journal of Hazardous Materials*, 2012, **211-212**, 317 – 331.
- [8] M. Morsella, N. d'Álessandro, A. E. Lanterna and J. C. Scaiano, *ACS Omega*, 2016, **1**, 464–469.
- [9] A. L. Gajengi, T. Sasaki and B. M. Bhanage, *Advanced Powder Technology*, 2017, **28**, 1185 – 1192.
- [10] R. Kakkar, P. N. Kapoor and K. J. Klabunde, *The Journal of Physical Chemistry B*, 2004, **108**, 18140–18148.

- [11] A. Imamoglu, *Physica E: Low-dimensional Systems and Nanostructures*, 2003, **16**, 47 – 50.
- [12] K. W. J. Barnham and G. Duggan, *Journal of Applied Physics*, 1990, **67**, 3490–3493.
- [13] A. JovanoviĀŽc, M. PetkoviĀŽc, I. A. Pašti, B. Johansson and N. V. Skorodumova, *Applied Surface Science*, 2018, **457**, 1158 – 1166.
- [14] A. K. Srivastava, N. Misra and S. K. Pandey, *Journal of Cluster Science*, 2018, **29**, 57–65.
- [15] J. Zhang, S. Yan, L. Yu, X. Zhou, T. Zhou and P. Peng, *International Journal of Hydrogen Energy*, 2018, **43**, 21864 – 21873.
- [16] H. Bayat, Z. Kolahchi, S. Valaey, M. Rastgou and S. Mahdavi, *Geoderma*, 2019, **335**, 57 – 68.
- [17] F. Zamankhan, V. Pirouzfard, F. Ommi and M. Valihesari, *Environmental Science and Pollution Research*, 2018, **25**, 22889–22902.
- [18] M. Ghashghaee and M. Ghambarian, *Molecular Simulation*, 2018, **44**, 850–863.
- [19] C. R. A. Catlow, S. T. Bromley, S. Hamad, M. Mora-Fonz, A. A. Sokol and S. M. Woodley, *Phys. Chem. Chem. Phys.*, 2010, **12**, 786–811.
- [20] S. Hamad, S. M. Woodley and C. R. A. Catlow, *Molecular Simulation*, 2009, **35**, 1015–1032.
- [21] A. Marzouk, V. Ponce, L. Benitez, F. A. Soto, K. Hankins, J. M. Seminario, P. B. Balbuena and F. El-Mellouhi, *The Journal of Physical Chemistry C*, 2018, **122**, 25858–25868.
- [22] H. van Koningsveld, *Compendium of Zeolite Framework Types*, Elsevier, 2007.

- [23] M. R. Farrow, Y. Chow and S. M. Woodley, *Physical Chemistry Chemical Physics*, 2014, **16**, 21119–21134.
- [24] J. C. Schön, *Zeitschrift für anorganische und allgemeine Chemie*, **630**, 2354–2366.
- [25] J. Schön and M. Jansen, *Computational Materials Science*, 1995, **4**, 43 – 58.
- [26] F. Bawa and I. Panas, *Physical Chemistry Chemical Physics*, 2002, **4**, 103–108.
- [27] P. Batra, R. Gaba, U. Issar and R. Kakkar, *Journal of Theoretical Chemistry*, 2013.
- [28] Y. Zhang, H. S. Chen, B. X. Liu, C. R. Zhang, X. F. Li and Y. C. Wang, *The Journal of Chemical Physics*, 2010, **132**, 195104.
- [29] Y. Zhang, H. S. Chen, Y. H. Yin and Y. Song, *Journal of Physics B: Atomic, Molecular and Optical Physics*, 2014, **47**, 025102.
- [30] C. Roberts and R. L. Johnston, *Physical Chemistry Chemical Physics*, 2001, **3**, 5024–5034.
- [31] M. Chen and D. A. Dixon, *Journal of Chemical Theory and Computation*, 2013, **9**, 3189–3200.
- [32] M. Chen, A. R. Felmy and D. A. Dixon, *The Journal of Physical Chemistry A*, 2014, **118**, 3136–3146.
- [33] M. Chen, K. S. Thanthiriwatte and D. A. Dixon, *The Journal of Physical Chemistry C*, 2017, **121**, 23025–23038.
- [34] M. Chen, M. Vasiliu, S. Hu and D. A. Dixon, *The Journal of Physical Chemistry C*, 2018, **122**, 25021–25034.
- [35] A. Aguado and J. M. López, *The Journal of Physical Chemistry B*, 2000, **104**, 8398–8405.
- [36] B. Wang, S. Nagase, J. Zhao and G. Wang, *The Journal of Physical Chemistry C*, 2007, **111**, 4956–4963.

- [37] E. V. Trushin, I. L. Zilberberg and A. V. Bulgakov, *Physics of the Solid State*, 2012, **54**, 859–865.
- [38] H. Morkoç and U. Özgür, in *General Properties of ZnO*, Wiley-VCH Verlag GmbH & Co. KGaA, 2009, pp. 1–76.
- [39] F. A. Fernandez-Lima, M. A. C. Nascimento and E. F. da Silveira, *Nuclear Instruments and Methods in Physics Research Section B: Beam Interactions with Materials and Atoms*, 2012, **273**, 102 – 104.
- [40] F. A. Fernandez-Lima, O. P. VilelaNeto, A. S. Pimentel, C. R. Ponciano, M. A. C. Pacheco, M. A. C. Nascimento and E. F. d. Silveira, *The Journal of Physical Chemistry A*, 2009, **113**, 1813–1821.
- [41] F. Fantuzzi, A. Henkes and M. Nascimento, *TechConnect Briefs*, 2014.
- [42] R. D. Shannon, *Acta Crystallographica Section A*, 1976, **32**, 751–767.
- [43] A. Burnin and J. BelBruno, *Journal of Chemical Physics Letters*, 2002, **362**, 341.
- [44] Y. J. Twu, C. W. S. Conover, Y. A. Yang and L. A. Bloomfield, *Physical Review B*, 1990, **42**, 5306–5316.
- [45] A. Kasuya, R. Sivamohan, Y. A. Barnakov, I. M. Dmitruk, T. Nirasawa, V. R. Romanyuk, V. Kumar, S. V. Mamykin, K. Tohji, B. Jeyadevan, K. Shinoda, T. Kudo, O. Terasaki, Z. Liu, R. V. Belosludov, V. Sundararajan and Y. Kawazoe, *Nature Materials*, 2004.
- [46] S. Stankic, J. Bernardi, O. Diwald and E. Knözinger, *The Journal of Physical Chemistry B*, 2006, **110**, 13866–13871.
- [47] A. Sternig, S. Stankic, M. Müller, J. Bernardi, E. Knözinger and O. Diwald, *Advanced Materials*, 2008, **20**, 4840–4844.

- [48] L. K. H. Pallon, R. T. Olsson, D. Liu, A. M. Pourrahimi, M. S. Hedenqvist, A. T. Hoang, S. Gubanski and U. W. Gedde, *Journal of Materials Chemistry A*, 2015, **3**, 7523–7534.
- [49] M. Golmohammadi, J. Towfighi, M. Hosseinpour and S. J. Ahmadi, *The Journal of Supercritical Fluids*, 2016, **107**, 699 – 706.
- [50] P. Azadi, E. Afif, F. Azadi and R. Farnood, *Green Chemistry*, 2012, **14**, 1766–1777.
- [51] W. A. Saunders, *Physical Review B*, 1988, **37**, 6583–6586.
- [52] W. A. Saunders, *Zeitschrift für Physik D Atoms, Molecules and Clusters*, 1989, **12**, 601–603.
- [53] I. Katakuse, T. Ichihara, H. Ito and M. Hirai, *Rapid Communications in Mass Spectrometry*, 1990, **4**, 16–18.
- [54] X.-H. Liu, X.-G. Zhang, X.-Y. Wang and N.-Q. Lou, *Berichte der Bunsengesellschaft für physikalische Chemie*, 1997, **101**, 1071–1074.
- [55] T. P. Martin and T. Bergmann, *The Journal of Chemical Physics*, 1989, **90**, 6664–6667.
- [56] M. Azubel, J. Koivisto, S. Malola, D. Bushnell, G. L. Hura, A. L. Koh, H. Tsunoyama, T. Tsukuda, M. Pettersson, H. Häkkinen and R. D. Kornberg, *Science*, 2014, **345**, 909–912.
- [57] S. Helveg and P. L. Hansen, *Catalysis Today*, 2006, **111**, 68 – 73.
- [58] C. Chen, Z. Hu, Y. Li, L. Liu, H. Mori and Z. Wang, *Scientific Reports*, 2016.
- [59] Z. Y. Li, N. P. Young, M. Di Vece, S. Palomba, R. E. Palmer, A. L. Bleloch, B. C. Curley, R. L. Johnston, J. Jiang and J. Yuan, *Nature*, 2008, **451**, 46–48.
- [60] Y. Niu, P. Schlexer, B. Sebok, I. Chorkendorff, G. Pacchioni and R. E. Palmer, *Nanoscale*, 2018.

- [61] J. M. Thomas, P. A. Midgley, C. Ducati and R. K. Leary, *Progress in Natural Science: Materials International*, 2013, **23**, 222 – 234.
- [62] G. A. Ozin, K. Hou, B. V. Lotsch, L. Cademartiri, D. P. Puzzo, F. Scotognella, A. Ghadimi and J. Thomson, *Materials Today*, 2009, **12**, 12 – 23.
- [63] <https://web.archive.org/web/20111027064700/http://www.nanoscience.com/store/pc/viewCategories.asp>
<https://web.archive.org/web/20111027064700/http://www.nanoscience.com/store/pc/viewCategories.asp>
Accessed 13 November 2018.
- [64] J. Maier, *Advanced Materials*, 2009, **21**, 2571–2585.
- [65] K. S. Novoselov, D. Jiang, F. Schedin, T. J. Booth, V. V. Khotkevich, S. V. Morozov and A. K. Geim, *Proceedings of the National Academy of Sciences*, 2005, **102**, 10451–10453.
- [66] K. S. Novoselov, A. K. Geim, S. V. Morozov, D. Jiang, M. I. Katsnelson, I. V. Grigorieva, S. V. Dubonos and A. A. Firsov, *Nature*, 2005, 197–200.
- [67] X. Wu, Y. Hu, M. Ruan, N. K. Madiomanana, J. Hankinson, M. Sprinkle, C. Berger and W. A. de Heer, *Applied Physics Letters*, 2009, **95**, 223108.
- [68] S. Thongrattanasiri, F. H. L. Koppens and F. J. García de Abajo, *Phys. Rev. Lett.*, 2012, **108**, 047401.
- [69] A. Geim and K. Novoselov, *Nature Materials*, 2007.
- [70] C. Lee, X. Wei, J. W. Kysar and J. Hone, *Science*, 2008, **321**, 385–388.
- [71] J. Kukesh and L. Pauling, *American Mineralogist*, 1950, **35**, 125.
- [72] D. R. Dreyer, S. Park, C. W. Bielawski and R. S. Ruoff, *Chem. Soc. Rev.*, 2010, **39**, 228–240.
- [73] H. He, T. Riedl, A. Lerf and J. Klinowski, *The Journal of Physical Chemistry*, 1996, **100**, 19954–19958.

- [74] L. Lai, L. Chen, D. Zhan, L. Sun, J. Liu, S. H. Lim, C. K. Poh, Z. Shen and J. Lin, *Carbon*, 2011, **49**, 3250 – 3257.
- [75] S. Narksitipan and S. Thongtem, *Ferroelectrics Letters Section*, 2014, **41**, 94–99.
- [76] J. M. T. A. Fischer, M. Hankel and D. J. Searles, *The Journal of Physical Chemistry C*, 2015, **119**, 29044–29051.
- [77] K. Gotterbarm, C. Bronnbauer, U. Bauer, C. Papp and H.-P. Steinrück, *The Journal of Physical Chemistry C*, 2014, **118**, 25097–25103.
- [78] B. Bukowski and N. A. Deskins, *Physical Chemistry Chemical Physics*, 2015, **17**, 29734–29746.
- [79] J. A. McLeod, R. G. Wilks, N. A. Skorikov, L. D. Finkelstein, M. Abu-Samak, E. Z. Kurmaev and A. Moewes, *Physical Review B*, 2010, **81**, 245123.
- [80] R. J. Zollweg, *Physical Review*, 1955, **100**, 671–673.
- [81] R. W. G. Wyckoff, *The Structure of Crystals*, The Chemical Catalog Company Inc., 1933.
- [82] D. W. Rankin, *Crystallography Reviews*, 2009, **15**, 223–224.
- [83] M. Haertelt, A. Fielicke, G. Meijer, K. Kwapien, M. Sierka and J. Sauer, *Physical Chemistry Chemical Physics*, 2012, **14**, 2849–2856.
- [84] G. Santambrogio, M. Brümmer, L. Wöste, J. Döbler, M. Sierka, J. Sauer, G. Meijer and K. R. Asmis, *Physical Chemistry Chemical Physics*, 2008.
- [85] S. A. Shevlin and S. M. Woodley, *The Journal of Physical Chemistry C*, 2010, **114**, 17333–17343.
- [86] F. H. Stillinger, *Physical Review E*, 1999, **59**, 48–51.
- [87] J. M. Dieterich and B. Hartke, *Molecular Physics*, 2010, **108**, 279–291.

- [88] R. L. Johnston, *Dalton Transactions*, 2003, 4193–4207.
- [89] A. A. Al-Sunaidi, A. A. Sokol, C. R. A. Catlow and S. M. Woodley, *The Journal of Physical Chemistry C*, 2008, **112**, 18860–18875.
- [90] D. M. Deaven and K. M. Ho, *Physical Review Letters*, 1995, **75**, 288–291.
- [91] S. M. Woodley, *The Journal of Physical Chemistry C*, 2013, **117**, 24003–24014.
- [92] <https://hive.chem.ucl.ac.uk/>, accessed November 2016.
- [93] S. Woodley, T. Lazauskas, M. Illingworth, A. C. Carter and A. A. Sokol, *Faraday Discussions*, 2018, **211**, 593–611.
- [94] D. J. Wales and H. A. Scheraga, *Science*, 1999, **285**, 1368–1372.
- [95] J. Elliott and Y. Shibuta, *Journal of Computational and Theoretical Nanoscience*, 2009, **6**, 1443–1451.
- [96] G. G. Rondina and J. L. F. Da Silva, *Journal of Chemical Information and Modeling*, 2013, **53**, 2282–2298.
- [97] Y.-H. Yang, J.-F. Zhang, J.-B. Wang, X.-B. Xu, G.-F. Shao and Y.-H. Wen, *Physics Letters A*, 2019, **383**, 464 – 470.
- [98] L. M. Farigliano, S. A. Paz, E. P. M. Leiva and M. A. Villarreal, *Journal of Chemical Theory and Computation*, 2017, **13**, 3874–3880.
- [99] S. Kirkpatrick, C. D. Gelatt and M. P. Vecchi, *Science*, 1983, **220**, 671–680.
- [100] C. J. Pickard and R. J. Needs, *Journal of Physics: Condensed Matter*, 2011, **23**, 053201.
- [101] J. Lv, Y. Wang, L. Zhu and Y. Ma, *The Journal of Chemical Physics*, 2012, **137**, 084104.
- [102] M. D. Nelson and M. Di Vece, *Nanomaterials*, 2019, **9**, 437.

- [103] D. Mora-Fonz, T. Lazauskas, S. M. Woodley, S. T. Bromley and C. R. A. Catlow, *The Journal of Physical Chemistry C*, 2017, **121**, 16831–16844.
- [104] M. Aslan and R. L. Johnston, *European Physical Journal B: Condensed Matter Physics*, 2018, **91**, 138.
- [105] S. Tosoni and G. Pacchioni, *ChemCatChem*, 2018, **11**, 73–89.
- [106] M. M. Fogler, D. S. Novikov and B. I. Shklovskii, *Phys. Rev. B*, 2007, **76**, 233402.
- [107] R. A. Buckingham, *Proceedings of the Royal Society of London A: Mathematical, Physical and Engineering Sciences*, 1938, **168**, 264–283.
- [108] J. Jones, *Proceedings of the Royal Society of London A: Mathematical, Physical and Engineering Sciences*, 1924, **106**, 463–477.
- [109] G. V. Lewis and C. R. A. Catlow, *Journal of Physics C: Solid State Physics*, 1985, **18**, 1149.
- [110] N. H. March, *Physical Review A*, 1986, **33**, 88–89.
- [111] W. Kohn and L. J. Sham, *Physical Review*, 1965, **140**, A1133–A1138.
- [112] V. Blum, R. Gehrke, F. Hanke, P. Havu, V. Havu, X. Ren, K. Reuter and M. Scheffler, *Computer Physics Communications*, 2009, **180**, 2175 – 2196.
- [113] M. Valiev, E. Bylaska, N. Govind, K. Kowalski, T. Straatsma, H. V. Dam, D. Wang, J. Nieplocha, E. Apra, T. Windus and W. de Jong, *Computer Physics Communications*, 2010, **181**, 1477 – 1489.
- [114] J. P. Perdew, K. Burke and M. Ernzerhof, *Physical Review Letters*, 1996, **77**, 3865–3868.
- [115] J. P. Perdew, K. Burke and M. Ernzerhof, *Physical Review Letters*, 1997, **78**, 1396–1396.

- [116] J. P. Perdew, A. Ruzsinszky, G. I. Csonka, O. A. Vydrov, G. E. Scuseria, L. A. Constantin, X. Zhou and K. Burke, *Physical Review Letters*, 2008, **100**, 136406.
- [117] S. M. Woodley, *Proceedings of the Royal Society of London A: Mathematical, Physical and Engineering Sciences*, 2011, **467**, 2020–2042.
- [118] Y. Han, C. R. Stoldt, P. A. Thiel and J. W. Evans, *The Journal of Physical Chemistry C*, 2016, **120**, 21617–21630.
- [119] C. Adamo and V. Barone, *The Journal of Chemical Physics*, 1999, **110**, 6158–6170.
- [120] C. Chang, M. Pelissier and P. Durand, *Physica Scripta*, 1986, **34**, 394.
- [121] S. Faas, J. Snijders, J. van Lenthe, E. van Lenthe and E. Baerends, *Chemical Physics Letters*, 1995, **246**, 632 – 640.
- [122] K. Lejaeghere, G. Bihlmayer, T. Björkman, P. Blaha, S. Blügel, V. Blum, D. Caliste, I. E. Castelli, S. J. Clark, A. Dal Corso, S. de Gironcoli, T. Deutsch, J. K. Dewhurst, I. Di Marco, C. Draxl, M. Dułak, O. Eriksson, J. A. Flores-Livas, K. F. Garrity, L. Genovese, P. Giannozzi, M. Giantomassi, S. Goedecker, X. Gonze, O. Grånäs, E. K. U. Gross, A. Gulans, F. Gygi, D. R. Hamann, P. J. Hasnip, N. A. W. Holzwarth, D. Iușan, D. B. Jochym, F. Jollet, D. Jones, G. Kresse, K. Koepernik, E. Küçükbenli, Y. O. Kvashnin, I. L. M. Locht, S. Lubeck, M. Marsman, N. Marzari, U. Nitzsche, L. Nordström, T. Ozaki, L. Paulatto, C. J. Pickard, W. Poelmans, M. I. J. Probert, K. Refson, M. Richter, G.-M. Rignanese, S. Saha, M. Scheffler, M. Schlipf, K. Schwarz, S. Sharma, F. Tavazza, P. Thunström, A. Tkatchenko, M. Torrent, D. Vanderbilt, M. J. van Setten, V. Van Speybroeck, J. M. Wills, J. R. Yates, G.-X. Zhang and S. Cottenier, *Science*, 2016, **351**, .
- [123] C. Boothroyd, M. Moreno, M. Duchamp, A. Kovács, N. Monge, G. Morales, C. Barbero and R. Dunin-Borkowski, *Ultramicroscopy*, 2014, **145**, 66 – 73.
- [124] M. Yu, A. B. Yankovich, A. Kaczmarowski, D. Morgan and P. M. Voyles, *ACS Nano*, 2016, **10**, 4031–4038.

- [125] J. Park, H. Elmlund, P. Ercius, J. M. Yuk, D. T. Limmer, Q. Chen, K. Kim, S. H. Han, D. A. Weitz, A. Zettl and A. P. Alivisatos, *Science*, 2015, **349**, 290–295.
- [126] K. Schouteden, K. Lauwaet, E. Janssens, G. Barcaro, A. Fortunelli, C. Van Haesendonck and P. Lievens, *Nanoscale*, 2014, **6**, 2170–2176.
- [127] K.-J. Hu, S. R. Plant, P. R. Ellis, C. M. Brown, P. T. Bishop and R. E. Palmer, *Journal of the American Chemical Society*, 2015, **137**, 15161–15168.
- [128] D. Labanc, M. Šulka, M. Pitoňák, I. Černušák, M. Urban and P. Neogrády, *Molecular Physics*, 2018, **116**, 1259–1274.
- [129] J. P. K. Doye and D. J. Wales, *Physical Review B*, 1999, **59**, 2292–2300.
- [130] S. G. Escher, T. Lazauskas, M. A. Zwijnenburg and S. M. Woodley, *Computational and Theoretical Chemistry*, 2017, **1107**, 74 – 81.
- [131] A. A. Sokol, C. R. A. Catlow, M. Miskufova, S. A. Shevlin, A. A. Al-Sunaidi, A. Walsh and S. M. Woodley, *Physical Chemistry Chemical Physics*, 2010, **12**, 8438–8445.
- [132] J. C. Schön, *Zeitschrift für anorganische und allgemeine Chemie*, 2014, **640**, 2717–2726.
- [133] i. c. v. Čančarević, J. C. Schön and M. Jansen, *Physical Review B*, 2006, **73**, 224114.
- [134] T. Ziegler, J. G. Snijders and E. J. Baerends, *The Journal of Chemical Physics*, 1981, **74**, 1271–1284.
- [135] W. H. E. Schwarz, A. Rutkowski and S. G. Wang, *International Journal of Quantum Chemistry*, 1996, **57**, 641–653.
- [136] H. Coker, *The Journal of Physical Chemistry*, 1976, **80**, 2078–2084.
- [137] D. K. Kim, P. Muralidharan, H.-W. Lee, R. Ruffo, Y. Yang, C. K. Chan, H. Peng, R. A. Huggins and Y. Cui, *Nano Letters*, 2008, **8**, 3948–3952.

- [138] K. Nakane, T. Hotta, T. Ogihara, N. Ogata and S. Yamaguchi, *Journal of Applied Polymer Science*, 2007, **106**, 863–867.
- [139] Y. Feng and X. Zheng, *Nano Letters*, 2010, **10**, 4762–4766.
- [140] C. Mayousse, C. Celle, E. Moreau, J.-F. Mainguet, A. Carella and J.-P. Simonato, *Nanotechnology*, 2013, **24**, 215501.
- [141] S. Ju, K. Lee, D. B. Janes, M.-H. Yoon, A. Facchetti and T. J. Marks, *Nano Letters*, 2005, **5**, 2281–2286.
- [142] M. Curreli, C. Li, Y. Sun, B. Lei, M. A. Gundersen, M. E. Thompson and C. Zhou, *Journal of the American Chemical Society*, 2005, **127**, 6922–6923.
- [143] K. Ding, Q. Zhang, L. Wang, K. Ruan, C. Xie, X. Zhang and J. Jie, *Light, Energy and the Environment 2015*, 2015, p. JTU5A.12.
- [144] R. Kurapati, K. Kostarelos, M. Prato and A. Bianco, *Advanced Materials*, 2016, **28**, 6052–6074.
- [145] K. Levenberg, *Quarterly of Applied Mathematics*, 1944, **2**, year.
- [146] D. Marquardt, *Journal of the Society for Industrial and Applied Mathematics*, 1963, **11**, 431–441.
- [147] P.-Y. Cai, Y.-W. Huang, Y.-C. Huang, M.-C. Cheng, L.-W. Lan, C.-C. Kuo, J.-H. Wang and M.-F. Luo, *The Journal of Physical Chemistry C*, 2018, **122**, 16132–16141.
- [148] J. A. Yarmoff and C. Salvo, *Surface Science*, 2019, **681**, 59 – 63.
- [149] A. Munir, T. u. Haq, A. Qurashi, H. u. Rehman, A. Ul-Hamid and I. Hussain, *ACS Applied Energy Materials*, 2019, **2**, 363–371.
- [150] S. Ayissi, P. A. Charpentier, N. Farhangi, J. A. Wood, K. Palotás and W. A. Hofer, *The Journal of Physical Chemistry C*, 2013, **117**, 25424–25432.

- [151] W. E. Mahmoud, F. S. Al-Hazmi, A. Al-Ghamdi, F. Shokr, G. W. Beall and L. M. Bronstein, *Superlattices and Microstructures*, 2016, **96**, 174 – 178.